NBS TECHNICAL NOTE 1240

U.S. DEPARTMENT OF COMMERCE/National Bureau of Standards

NBS Reactor: Summary of Activities July 1986 Through June 1987

The National Bureau of Standards[1] was established by an act of Congress on March 3, 1901. The Bureau's overall goal is to strengthen and advance the nation's science and technology and facilitate their effective application for public benefit. To this end, the Bureau conducts research to assure international competitiveness and leadership of U.S. industry, science and technology. NBS work involves development and transfer of measurements, standards and related science and technology, in support of continually improving U.S. productivity, product quality and reliability, innovation and underlying science and engineering. The Bureau's technical work is performed by the National Measurement Laboratory, the National Engineering Laboratory, the Institute for Computer Sciences and Technology, and the Institute for Materials Science and Engineering.

The National Measurement Laboratory

Provides the national system of physical and chemical measurement; coordinates the system with measurement systems of other nations and furnishes essential services leading to accurate and uniform physical and chemical measurement throughout the Nation's scientific community, industry, and commerce; provides advisory and research services to other Government agencies; conducts physical and chemical research; develops, produces, and distributes Standard Reference Materials; provides calibration services; and manages the National Standard Reference Data System. The Laboratory consists of the following centers:

- Basic Standards[2]
- Radiation Research
- Chemical Physics
- Analytical Chemistry

The National Engineering Laboratory

Provides technology and technical services to the public and private sectors to address national needs and to solve national problems; conducts research in engineering and applied science in support of these efforts; builds and maintains competence in the necessary disciplines required to carry out this research and technical service; develops engineering data and measurement capabilities; provides engineering measurement traceability services; develops test methods and proposes engineering standards and code changes; develops and proposes new engineering practices; and develops and improves mechanisms to transfer results of its research to the ultimate user. The Laboratory consists of the following centers:

- Applied Mathematics
- Electronics and Electrical Engineering[2]
- Manufacturing Engineering
- Building Technology
- Fire Research
- Chemical Engineering[3]

The Institute for Computer Sciences and Technology

Conducts research and provides scientific and technical services to aid Federal agencies in the selection, acquisition, application, and use of computer technology to improve effectiveness and economy in Government operations in accordance with Public Law 89-306 (40 U.S.C. 759), relevant Executive Orders, and other directives; carries out this mission by managing the Federal Information Processing Standards Program, developing Federal ADP standards guidelines, and managing Federal participation in ADP voluntary standardization activities; provides scientific and technological advisory services and assistance to Federal agencies; and provides the technical foundation for computer-related policies of the Federal Government. The Institute consists of the following divisions:

- Information Systems Engineering
- Systems and Software Technology
- Computer Security
- System and Network Architecture
- Advanced Systems

The Institute for Materials Science and Engineering

Conducts research and provides measurements, data, standards, reference materials, quantitative understanding and other technical information fundamental to the processing, structure, properties and performance of materials; addresses the scientific basis for new advanced materials technologies; plans research around cross-cutting scientific themes such as nondestructive evaluation and phase diagram development; oversees Bureau-wide technical programs in nuclear reactor radiation research and nondestructive evaluation; and broadly disseminates generic technical information resulting from its programs. The Institute consists of the following Divisions:

- Ceramics
- Fracture and Deformation[3]
- Polymers
- Metallurgy
- Reactor Radiation

---

[1] Headquarters and Laboratories at Gaithersburg, MD, unless otherwise noted; mailing address Gaithersburg, MD 20899.

[2] Some divisions within the center are located at Boulder, CO 80303.

[3] Located at Boulder, CO, with some elements at Gaithersburg, MD

NBS Technical Note 1240

NBS Reactor: Summary of Activities July 1986 Through June 1987

Frederick J. Shorten, Editor

Reactor Radiation Division
Institute for Materials Science and Engineering
National Bureau of Standards
Gaithersburg, MD 20899

November 1987

U.S. Department of Commerce
C. William Verity, Secretary

National Bureau of Standards
Ernest Ambler, Director

National Bureau of Standards Technical Note 1240
Natl. Bur. Stand. (U.S.), Tech. Note 1240, 197 pages (Nov. 1987)
CODEN: NBTNAE

U.S. GOVERNMENT PRINTING OFFICE
WASHINGTON: 1987

For sale by the Superintendent of Documents, U.S. Government Printing Office, Washington DC 20402

FOREWORD

The National Bureau of Standards Reactor was built not only to serve the needs of the NBS but also those of other government agencies and outside organizations as a National Center for the application of neutron methods to problems of national interest. The Reactor Radiation Division was established to operate the reactor and to foster its scientific and technological use. Toward this end, the Division has a small nucleus of scientists experienced in the use of reactors for a wide range of scientific and technical problems. In addition to pursuing their own research and developing sophisticated experimental facilities, they actively seek out and encourage collaboration with other scientists engaged in challenging programs whose work can benefit from use of the reactor, but who as yet do not have the reactor experience necessary to take full advantage of the facilities available. The Division also provides irradiation services to a wide variety of users as well as engineering and other technical services.

The reactor operates at 20 MW and supports 25 experimental facilities ranging from intense neutron beams to extensive irradiation facilities. A major expansion of the experimental facilities is currently under way. A cold neutron source has been installed and construction of a large neutron guide hall will start this fall (November, 1987). The guide hall will accommodate fifteen new instruments served by seven neutron guides from the cold source. This will be a national user facility providing state-of-the-art instruments that are currently unavailable in the United States.

This report attempts to summarize all the work done which is dependent on the reactor including a large number of programs outside the Division. The first section summarizes the programs carried out by scientists in the Reactor Radiation Division and their collaborators. The second section summarizes NBS work originating outside NBS for which the Division provides reactor facilities and irradiation services. The remaining sections are self-explanatory.

Appreciation is extended to F. J. Shorten of the Reactor Radiation Division for his extensive contributions to the editing, organization, and preparation of this report, and K. E. Ferrel for efforts in typing manuscripts.

R. S. Carter

R. S. Carter
Chief, Reactor Radiation Division
National Bureau of Standards

ABSTRACT

This report summarizes all those programs which use the NBS reactor. It covers the period for July 1986 through June 1987. The programs range from the use of neutron beams to study the structure and dynamics of materials through nuclear physics and neutron standards to sample irradiations for activation analysis, isotope production, neutron radiography, and nondestructive evaluation.

Key words: activation analysis; crystal structure; diffraction; isotopes; molecular dynamics; neutron; cold neutrons; neutron radiography; nondestructive evaluation; nuclear reactor; radiation.

DISCLAIMER

Certain trade names and company products are identified in order to adequately specify the experimental procedure. In no case does such identification imply recommendation or endorsement by the National Bureau of Standards, nor does it imply that the products are necessarily the best available for the purpose.

TABLE OF CONTENTS

TABLE OF CONTENTS

TABLE OF CONTENTS

AMMONIA ADSORPTION BY ZEOLITE H-RHO

J. M. Nicol
(University of Maryland, College Park, MD)
and
(National Bureau of Standards, Gaithersburg, MD)

and

T.J. Udovic, R.R. Cavanagh and J.J. Rush

and

G.D. Stucky
(University of California, Santa Barbara, CA)

Previously, quasielastic (QNS) and incoherent inelastic (IINS) neutron scattering were used to characterize the deammoniation of zeolite NH_4-Rho over the temperature range 473 - 723 K, as well as the rotational dynamics of bound NH_4^+ in the cavities of this catalyst.[1] Studies have now been undertaken of the reverse process, the adsorption of ammonia by zeolite H-Rho. Ammonia was adsorbed at 295 K into the cavities of H-Rho, generated in the previous study, to loadings of 1, 3, 6 and 11 NH_3 per unit cell. The addition of NH_3 to H-Rho results in the formation of NH_4^+ ions by the coordination of the NH_3 to the H^+ cations in the zeolite framework. Figures 1 and 2 depict IINS data collected in the 34 - 190 meV and 5 - 20 meV regions as a function of NH_3 loading.

The changes visible in figure 1, namely, the rise in intensity of the peak at 45 meV, the decrease in intensity of the features at ca. 142, 131, and 93 meV and the peak formed at 180 meV indicate changes in the vibrational density of states resulting from the formation of NH_4^+ cations from NH_3 and H^+. The decrease in intensity of the proton-related features at 142,[2] 131, and 93 meV as the NH_3 loading is increased is a result of a decrease in the number of H^+ cations. The generation of NH_4^+ is seen by the appearance of the ammonium bending mode at 180 meV. The peak at 45 meV has been shown previously to be associated with adsorbate-coupled breathing (i.e., pore opening) modes of the zeolite framework.[1] The increase in the intensity of the 45 meV feature with increasing NH_3 loading is associated with an increase in the total number of H atoms in the system which are coupled to these modes. During deammoniation, a shift from 38 to 45 meV was observed. In the case of reammoniation, no corresponding shift (i.e, 45 to 38 mev) is observed.

In the 5 - 20 meV region, modes due to the hindered rotations of the NH_4^+ cations are observed at ca. 8 and 15 meV. Intensity differences are evident in data collected at 10 and 80 K. In particular, at the fullest loading of 11 NH_4^+/uc, additional baseline intensity is seen below ca. 10 meV at 80 K, which subsequently disappears on cooling the sample to 10 K. This additional intensity appears to be

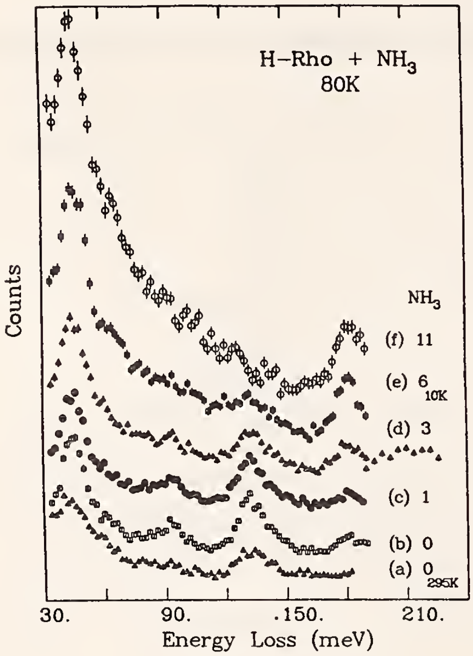

Figure 1. The IINS spectra at 80 K (except where indicated) for zeolite H-Rho as a function of NH_3 loading per unit cell.

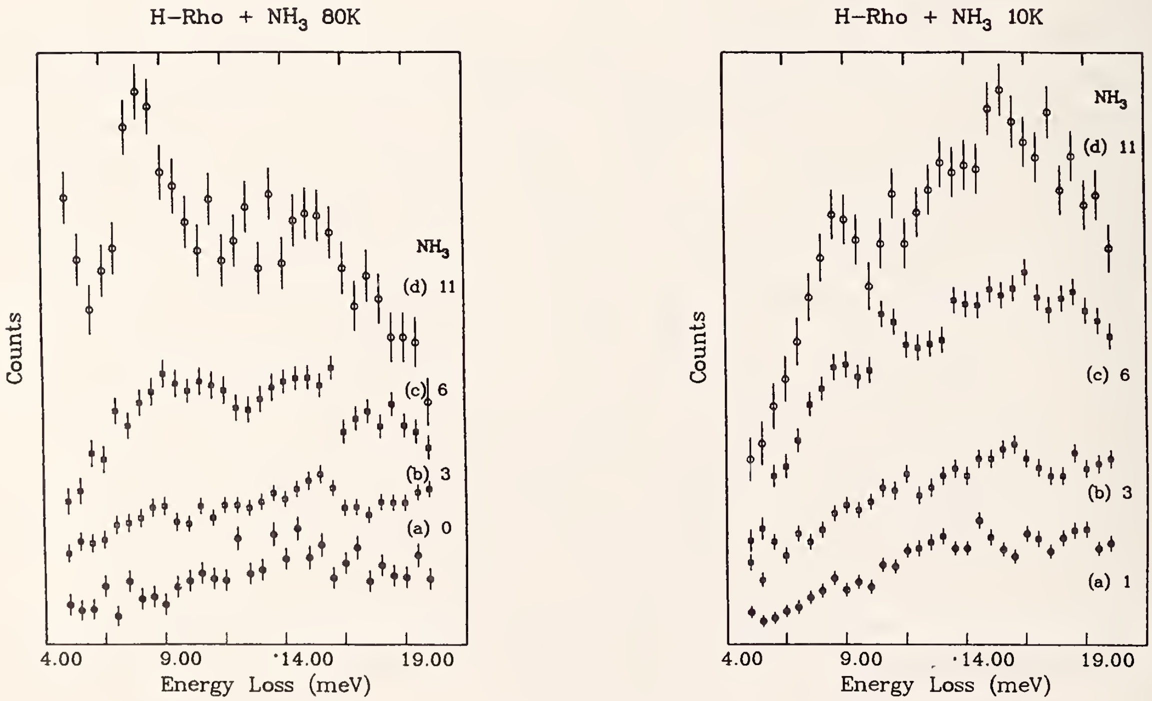

Figure 2. The low-energy IINS spectra of zeolite H-RHo as a function of NH_3 loading per unit cell: (a) data collected at 80 K and (b) data collected at 10 K.

due to a very broad quasielastic feature. The motion causing this feature is frozen at 10 K. Quasielastic data (not shown) also indicate such a weakly bound component. Currently the QES data are being analyzed to identify the mechanism and energetics of the NH_4^+ reorientational motions.

A comparison of the data of reammoniation to that collected during deammoniation will be made, in order to identify behavioral differences of the NH_4^+ cations which can be related to the differences in the catalytic properties of the two materials.

---

1. T. J. Udovic, R. R. Cavanagh, J. J. Rush, M. J. Wax, G. D. Stucky, G. A. Jones, and D. R. Corbin, J. Phys. Chem, in press.
2. M. J. Wax, R. R. Cavanagh, J. J. Rush, G. D. Stucky, L. Abrams, D. R. Corbin, J. Phys. Chem. 90, 532, 1986.

SURFACE ADSORPTION SITES OF HYDROGEN ON PALLADIUM BLACK

J.M. Nicol
(University of Maryland, College Park, MD)
and
(National Bureau of Standards, Gaithersburg, MD)

and

R. D. Kelley
(Surfaces Science Division)

and

J. J. Rush

The ability of inelastic neutron scattering (IINS) in addressing surface science problems has previously been demonstrated at NBS in studies of hydrogen and hydrocarbons adsorbed on metal powders[1,2]. This work has shown that results obtained by IINS on high-surface-area metal powders, which possess a distribution of particle sizes and are polycrystalline in nature, are generally consistent with vibrational spectroscopy results found for adsorption on single crystals.

The adsorption sites for hydrogen on the surface of palladium black (a high-surface-area Pd powder) has been investigated by a combination of IINS and normal coordinate analysis (NCA). The spectrum of H-activated Pd black is shown in figure 1. Strong scattering features are observed at 468, 760, 819 and 969 cm^{-1}. As the sample was activated under conditions where bulk hydride species should not be present all scattering features are assumed to be due to surface and/or near surface species. The 468 cm^{-1} feature has been assigned to the vibrations of subsurface H

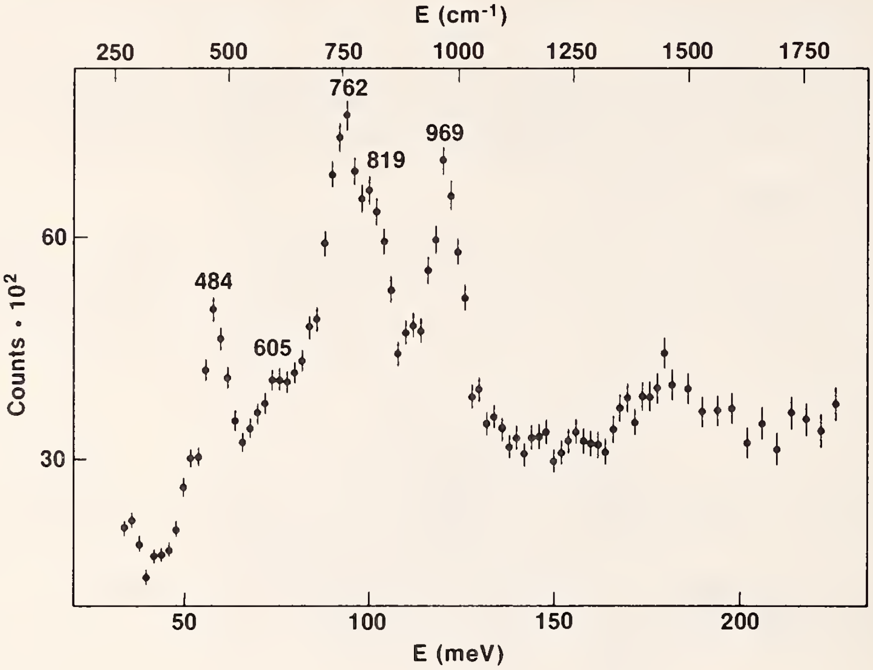

Figure 1. The IINS spectrum at 80K of hydrogen-activated palladium black.

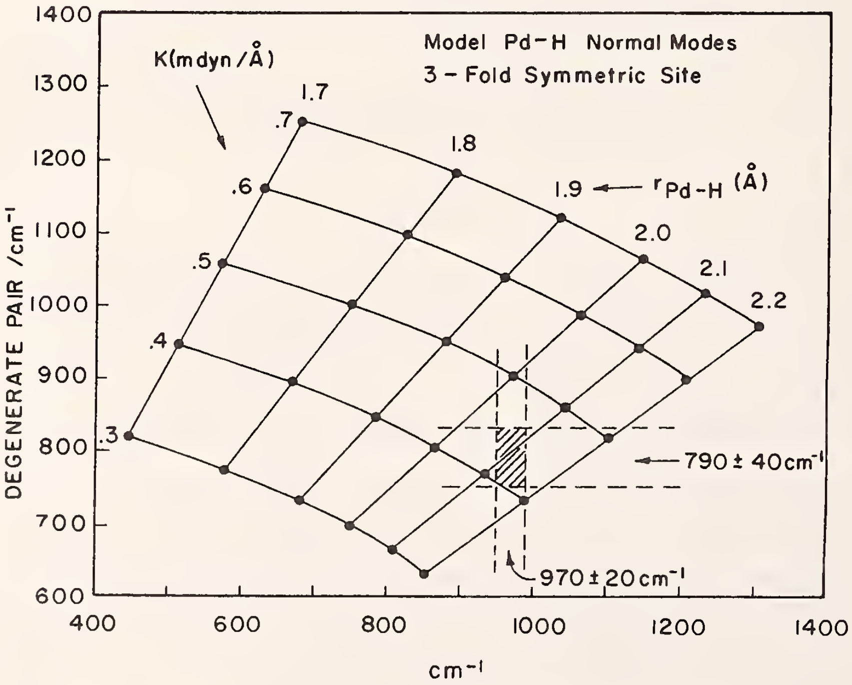

Figure 2. Vibrational modes of hydrogen on a symmetric 3-fold site as a function of force constant and Pd-H bond length calculated from normal coordinate analysis. The shaded region indicates the range of bond lengths and force constants consistent with the observed frequencies and relative intensities.

in octrahedral sites below the top most Pd surface atom plane[3]. Vibrations of H adsorbed on surface sites are responsible for the remaining feature at 760, 819 and 969 cm^{-1}. By comparing the experimental results with predicted IINS spectra obtained from NCA calculations these features were assigned to a specific surface site.

The NCA calculations employed established methods, which were previously applied to H adsorbed on Raney nickel[1]. A number of 2, 3 and 4 fold binding sites found on Pd(100) and Pd(111) surfaces (the predominant crystal planes expected on small Pd particles) were considered. The number of metal atoms considered was large enough to define the symmetry of the binding site, second layer atoms being ignored. A Pd-Pd bond length of 2.75 Å (as found in bulk Pd) and a Pd-Pd force constant of 0.35 mdym/Å were used. For all binding conditions a range of meaningful Pd-H force constants and bond lengths were considered, from which the "best fit" to the data was obtained.

While a number of models were compatible with the experimental vibrational frequencies and relative intensities, only the 3-fold site on Pd(111) was found to be physically resonable. The results of the NCA for the 3-fold site on Pd(111) is shown in figure 2. For binding in a symmetric 3-fold site one predicts a 2:1 intensity ratio for the observed spectral features, 2 degenerate modes parallel to the surface and a non-degenerate mode perpendicular to the surface. In fitting the features at 760, 819 and 969 cm^{-1} we have assumed that the degerate mode is represented by the peaks at 769 and 819 cm^{-1}, as the intensity of these modes when taken together is twice that of the mode at 969 cm^{-1}. The best fit to the data is obtained for a Pd-H bond length of 2.1 ± 0.05 Å and the force constant is 0.43 ± 0.03 mdyn/Å.

The assignment of our features to a surface 3-fold site is in good agreement with HREELS spectra of H adsorbed on Pd(111), where a vibrational energy of 759 and 1000 cm^{-1} was obtained for the degenerate parallel and perpendicular modes respectively[4].

The observed splitting of the degenerate mode can be explained by dispersion of optical phonon modes. Results of H isotope-dilution experiments confirm this observation[5].

---

1. R.R. Cavanagh, R.D. Kelley and J.J. Rush, J. Chem. Phys. 77, 1540 (1982).
2. R.D. Kelley, R.R. Cavanagh, J.J. Rush, Surface Sci. 155, 480 (1985).
3. J.M. Nicol, J.J. Rush and R.D. Kelley, Phys. Rev. B, submitted.
4. H. Conrad, M.E. Kordesch, R. Scala and W. Stenzel, J. Electron Spectrosc. Relat. Phenom. 38, 289 (1986).
5. J.M. Nicol, T.J. Udovic, R.D. Kelley and J.J. Rush, in this report.

NEUTRON SCATTERING STUDIES OF MOLECULAR HYDROGEN ADSORPTION IN CoNa-A ZEOLITE

J. M. Nicol
(University of Maryland, College Park, MD)
and
(National Bureau of Standards, Gaithersburg, MD)

and

J. Eckert
(Los Alamos National Laboratory, Los Alamos, NM)

and

J. Howard
(Imperial Chemical Industries, Wilton, England)

Inelastic incoherent neutron scattering (IINS) has been applied to the study of molecular hydrogen adsorbed in the cavities of partially cobalt-exchanged type A zeolite ($Co_{4.1}Na_{3.8}$-A). Data have been collected in the energy range 1-40 meV using the time of flight (TOF) and BT-4 spectrometers (TOF: 1-13 meV and BT-4, Be/graphite-filter configuration: 12-40 meV). Hydrogen was adsorbed to a coverage of 0.5 molecules per supercage in the fully dehydrated zeolite at 50K. Subsequently, the sample was cooled to 12K for data collection.

Figure 1 shows the TOF spectrum for H_2/CoNa-A at 12K using an incident energy of 13.8 meV and contains data for both neutron energy loss (positive E) and neutron energy gain (negative E). The spectrum has been corrected for the featureless, dehydrated zeolite background. The data points between ± 1 meV are due to less than perfect subtraction of the elastic peak. Scattering due to adsorbed hydrogen is observed at 3.8 meV. Data collected in the energy range 12-40 meV on BT-4 at 12K (neutron energy loss only) are illustrated in figure 2. The data points in the difference spectrum near 23 meV may result from incomplete subtraction of the intense 20.5 meV peak present in the bare zeolite spectrum. This peak is most likely related to a cation breathing mode coupled to residual hydrogen (probably in the form of OH groups). Two new features in the difference spectrum are observed at 15.5 and 28 meV. These features and the 3.8 meV feature in figure 1 are due hydrogen interacting with the cations (most probably the Co ions) in the zeolite framework. After annealing the sealed sample to 298K and recooling to 12K, no change was observed in the TOF spectrum. In addition, hydrogen could be reversibly evacuated from the zeolite with ease at 298K, indicative of weak physisorption. This strongly suggests that we are dealing with molecular hydrogen, and that no dissociation is occurring. Spectra collected periodically during the sample warming exhibited an unusual temperature dependence, in that very little broadening was observed with increasing temperature.

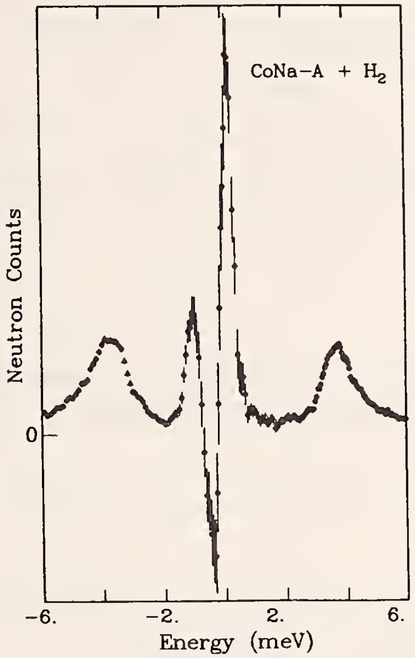

Figure 1. The time of flight spectrum at 12K of 0.5 hydrogen molecules per supercage adsorbed in dehydrated CoNa-A zeolite. The spectrum has been corrected for the dehydrated zeolite background.

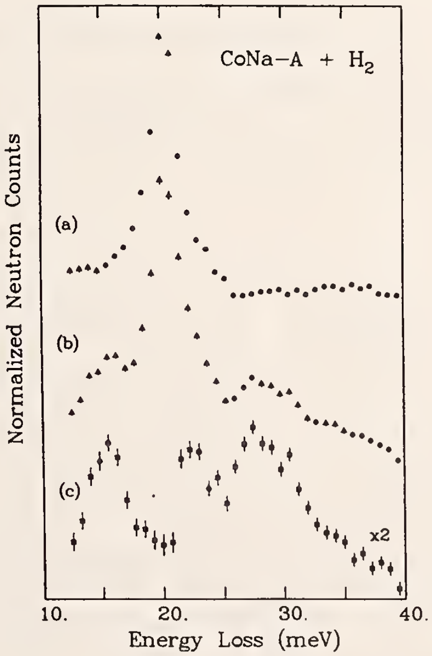

Figure 2. The Be/graphite filter spectrum at 12K of 0.5 hydrogen molecules per supercage adsorbed in dehydrated CoNa-A zeolite: (a) dehydrated zeolite background, (b) CoNa-A + 0.5 H_2 molecules per supercage and (c) difference spectrum.

Currently, the spectra are being analysed to establish the origin of the observed modes in terms of rotational and vibrational transitions of hydrogen interacting with the cobalt ions in the supercages. A number of potential force fields of different symmetry are being considered. Consideration of ortho-para hydrogen conversion at low temperature is also being made to explain the temperature dependence of the TOF spectra.

ISOTOPE DILUTION NEUTRON SPECTROSCOPY: A VIBRATIONAL PROBE OF HYDROGEN/DEUTERIUM ADSORBATE INTERACTIONS ON PALLADIUM BLACK

J. M. Nicol
(University of Maryland, College Park, MD)
and
(National Bureau of Standards, Gaithersburg, MD)
and
R. D. Kelley
(Surface Science Division)
and
T. J. Udovic and J. J. Rush

In conjunction with deuterium isotope dilution, incoherent inelastic neutron scattering (IINS) has been used to investigate the existence and degree of H-H interactions for H adsorbed on Pd black. The presence of H-H interactions can be seen clearly in IINS by the effect of isotope dilution on the vibrational density of states. Dynamic coupling between hydrogen atoms in an adsorbate layer can result in a significant dispersion of the corresponding hydrogen vibrational modes over momentum space. Although isotope dilution of H with D leaves the adsorbate layer electronically and chemically unchanged, it can somewhat change the dynamic coupling between adsorbate oscillators and, concomitantly, the degree of phonon dispersion.

The isotope dilution results are illustrated by the IINS spectrum in figure 1. The vibrational spectrum of pure H (ca. 0.7 monolayers) on Pd black is depicted for comparison in figure 1a. The assignment of the vibrational features for H/Pd black to subsurface octahedral (58 meV) and surface threefold (94, 101 and 120 meV) sites has been discussed previously.[1] In particular, the existence of H-H interactions is suggested by the broad, complex nature of the 94 meV feature assigned to the degenerate parallel stretching mode of surface H.

The spectrum of dilute H in D (ca. 0.7 monolayers, H/D ≈ 0.1) on Pd black is shown in figure 1b. In addition to the presence of H scattering features, careful

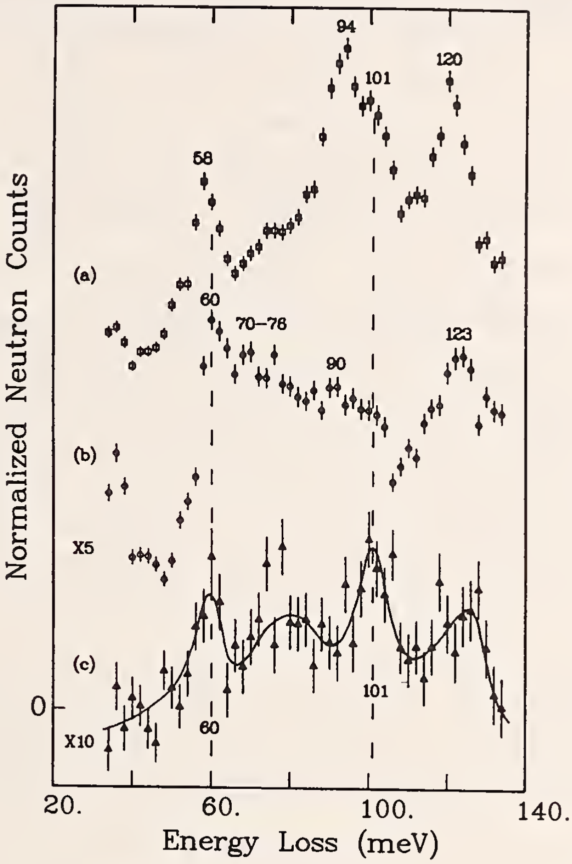

Figure 1. Neutron energy loss spectra of (a) pure H and (b) dilute H in D (0.07 H/ 0.65 D) adsorbed on Pd black. (c) Difference spectrum following the further addition of 0.04 monolayers H to the dilute H in D sample. (The solid line is intended only as a guide to the eye.)

examination of figure 1b indicates additional scattering intensity at ca. 43, 70-76 and 90 meV due to D adsorbed in the same sites occupied by H in pure H/Pd black. A comparison of figures 1a and 1b indicates that the subsurface/surface H intensity ratio is markedly higher for dilute H in D than for pure H. This suggests that, for dilute H in D, the subsurface H/D ratio is larger than the surface H/D ratio (i.e., there is preferential adsorption of H in the subsurface sites).

The difference spectrum following the further addition of 0.04 monolayers H to the dilute H in D sample is shown in figure 1c. By creation of a difference spectrum, the scattering contributions due to D are effectively eliminated, leaving a clearer representation of the scattering features due to the additional dilute H atoms. The change from a broad complex feature peaked at ca. 94 meV for pure H (figure 1a) to a sharper feature centered at ca. 101 meV for dilute H in D (Fig. 1c) corroborates the existence of dynamic H-H interactions within the pure H surface phase. These interactions cause a dispersion of the phonon optical modes similar to that for β-Pd hydride[2] and H/Pt black.[3] One can rule out mixed-site population and anharmonicity in explaining the origin of the complex feature for pure H since the presence of these factors would yield vibrational density-of-states structure that was independent of isotope dilution. Simple mass-defect theory, which has previously been used to describe the isotope dilution results for β-Pd hydride[2] and H/Pt black,[3] predicted a value of 101 meV for the H local mode energy of dilute H in D on Pd black, in good agreement with the observed value.

The overlap of scattering contributions from subsurface H overtone vibrations in the vicinity of the 120 meV feature (assigned to the perpendicular stretching mode of surface H) precludes any definite conclusions to be drawn about this dilute H feature in figure 1c. Moreover, except for the small shift to higher energy, there appears to be little effect of isotope dilution on the density of states assigned to subsurface H at 58 meV. This is consistent with the lower total concentration (ca. 0.1 ML as suggested by the relative scattering intensities) and degree of H dilution (H/D $\approx$ 0.4) in the subsurface phase compared to the surface phase.

The present results again illustrate the potential of isotope dilution neutron spectroscopy for probing the interactions of hydrogenous adsorbates in polycrystalline materials such as catalysts. Future experiments are planned to more quantitatively investigate the effects of isotope dilution on the phonon density of states for surface H on Pd black.

---

1. J.M. Nicol, J.J. Rush and R.D. Kelley, in this publication.

2. J.J. Rush, J.M. Rowe and D.Richter, Phys. Rev. B 31, 6102 (1985).

3. J.J. Rush, R.R. Cavanagh, R.D. Kelley and J.M. Rowe, J. Chem. Phys. 83, 5339 (1985).

NEUTRON SCATTERING STUDIES OF THE STRUCTURE AND DYNAMICS OF POTASSIUM-AMMONIA INTERCALATED GRAPHITE

D. A. Neumann and J. J. Rush

and

H. Zabel
(University of Illinois, Urbana, IL)

and

Y. B. Fan and S. A. Solin
(Michigan State University, East Lansing, MI)

Potassium-ammonia intercalated graphite is an ideal system for the study of the structure and dynamics of a simple two-dimensional (2D) molecular liquid. In addition, the intercalant layer forms a 2D analog of the widely studied[1] metal-ammonia solutions. We have therefore performed extensive elastic, quasielastic, and inelastic neutron scattering studies which probe the structure and dynamics of these compounds.

The elastic scattering results have shown that the intercalant layer in the stage 1 system, $KC_{24}(ND_3)_{4.3}$, does indeed form a two-dimensional liquid at room temperature. It has also been shown that the data can be best described using a

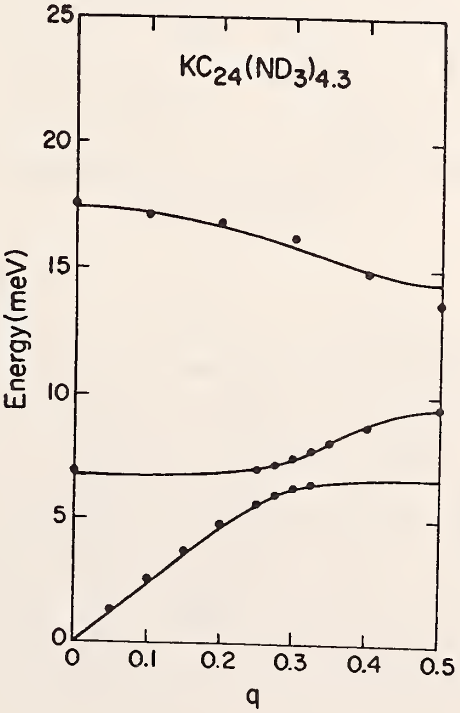

Figure 1. [001] L phonon dispersion of stage 1 $KC_{24}(ND_3)_{4.3}$ at room temperature.

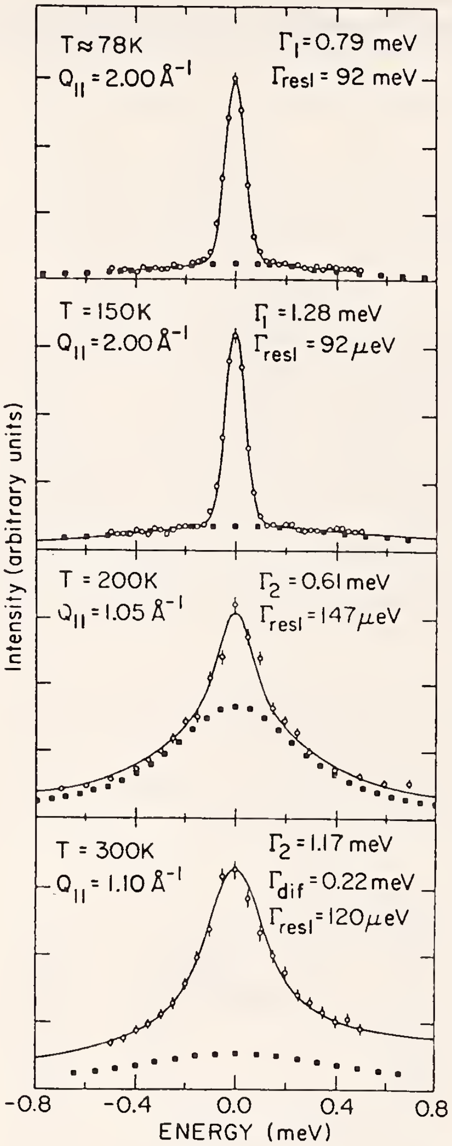

Figure 2. a) Quasielastic spectrum at 78 K. The open circles are the experimentally measured points, the solid line is a fit to a δ-function plus a Lorentzian, both convoluted with the Gaussian instrumental resolution, and the solid squares represent the Lorentzian contribution to the scattering. A scattering function of this type is indicative of a rotational motion of the ammonia molecules. b) Quasielastic spectrum at 150 K. This shows the broadening of the Lorentzian component of the scattering function. The activation energy of this motion is estimated to be 3 - 5 meV. c) Quasielastic spectrum at 200 K (above the intercalant melting transition). Here the previously observed Lorentzian has broadened into a flat background. However the peak still includes both a δ-function and a Lorentzian component due to the appearance of a different reorientational motion. d) Qualielastic spectrum at room temperature. The elastic component has also been broadened due to translational motion of the ammonia molecules.

model in which four ammonia molecules are clustered about a single K ion. It was not found necessary to include in the model any modulation of the liquid imposed by the graphite bounding layers. Scans along the c^*-axis have shown that adjacent intercalant layers are uncorrelated and that the graphite layers stack in an eclipsed configuration. It was also discovered that upon cooling the K-ammonia layer freezes into a solid phase at a temperature of about 185 K. The structure of this phase has not yet been determined, but it is currently believed to be discommensurate and based on a 3 x 3 commensurate structure.

The measured c-axis phonon dispersion of this compound is shown in figure 1. The most striking feature is the existence of three modes due to the splitting of the acoustic branch by an additional excitation having an energy of 6.7 meV. The solid line represents the results of a model calculation in which the phonon dispersion of the stage 1 compound is described by a 1D Born-von Karmen model consisting of a single force constant and two masses, one for the carbon sheet and the other for the K-ammonia layer. The additional mode is then included as an Einstein oscillator and the hybridization follows from a coupling term. Similar results have also been observed for the stage 1 compound $KC_{22}(ND_3)_{3.1}$ although the value of the coupling constant is reduced by an amount consistent with the reduction in the ammonia concentration. The physical motion corresponding to the additional excitation is however, still not clear. Models which describe it as a libration of a single molecule all suffer from the fact that the potential barrier required for a 7 meV excitation is so small that at room temperature, the splitting should be completely destroyed by anharmonicity. It is therefore probable that this motion corresponds to a collective excitation of the molecules associated with a single K ion.

The quasielastic scattering results, shown in figure 2, were performed on samples made with hydrogenated ammonia in order to increase the incoherent scattering cross section. Below the intercalant melting transition these results display a two-component peak, one component of which is resolution limited. This lineshape is typical of a single rotational motion, which in this case has been identified as spinning of the ammonia molecule about its three-fold symmetry axis. Above the melting transition, two other motions are observed. The first corresponds to reorientations of the molecular complexes about the graphite c-axis while the second is due to translation motions of the ammonia molecules.

---

1. J. C. Thompson, Electrons in Liquid Ammonia, (Clarendon, Oxford, 1976).

INELASTIC AND QUASIELASTIC NEUTRON SCATTERING STUDIES OF PELLICULAR ZIRCONIUM HYDROGEN PHOSPHATE, $Zr(HPO_4)_2.H_2O$

R.C.T. Slade
(University of Exeter, England)
and
(National Bureau of Standards, Gaithersburg, MD)

and

G. Alberti
(University of Perugia, Italy)

and

J.M. Nicol

Zirconium hydrogen phosphate (ZRP) is of interest as an inorganic ion-exchanger and also as a protonic solid electrolyte. Pellicular ZRP (sheets made up of platelets all with their c-axes nearly normal to the sheets) is of contemporary interest and was first synthesised in Perugia. The Exeter Solid State Chemistry Group has an on-going collaborative research programme probing structure and dynamics in protonic electrolytes.

The incoherent inelastic neutron scattering spectrum of pellicular ZRP confirmed that it is correctly chemically formulated, the P-O-H bending mode being observed at ca. 1100 cm^{-1} together with librational modes of H_2O at lower frequencies.

Investigation of the incoherent quasielastic neutron scattering spectrum of ZRP on the time-of-flight spectrometer (incident wavelength 5 Å) revealed broadening at 90^oC with a width (FWHM) for the Lorentzian component of 390 μeV. Examination of ZRP at 70^oC on the triple-axis spectrometer showed Q-independent broadening (measurements at $Q/Å^{-1}$ = 1.34 and 2.00 avoiding Bragg scattering) with a width for the Lorentzian component of 150 μeV. The Q-independence of the broadening characterises the motion reponsible as a reorientation (of H_2O).

INELASTIC AND QUASIELASTIC NEUTRON SCATTERING STUDIES OF HYDROGEN OXIDE BRONZES

R.C.T. Slade
(University of Exeter, England)
and
(National Bureau of Standards, Gaithersburg, MD)

and

H.A. Pressman and A. Ramanan
(University of Exeter, England)

and

J.M. Nicol

Hydrogen oxide bronzes, H_xMO_n, are nonstoichiometric insertion compounds of transition metal oxides MO_n and of interest in catalysis and as mixed (electronic/protonic) conductors. In such systems H is believed to be attached to O (as -OH and, sometimes, as $-OH_2$ coordinated to M) and rapid hydrogen self-diffusion may be observed. The Exeter group has an ongoing collaborative programme investigating hydrogen oxide bronzes.

The inelastic neutron scattering scattering spectrum of the compound $H_{18}V_9Mo_6O_{40}$ was recorded, completing the vibrational spectroscopy of the optically dark phases $H_xV_9Mo_6O_{40}$ (x = 8, 18). The presence of hydroxyl was confirmed by the observation of the M-O-H deformation at 1040 cm^{-1} (and no peak at ca. 1600 cm^{-1} characteristic of $-OH_2$). In the higher x value phase a broad band at lower energies (centered at 640 cm^{-1}) is attributed to H being carried by oxygen in the breathing modes of the MO_6 octrahedra.

The single phase $H_{2.0}MoO_3$ was studied on the time-of-flight spectrometer at $\lambda_o = 5$ Å. At 60 °C Q-dependent broadening of the spectrum was observed. Grouping detectors known from the diffraction pattern to be free of Bragg contamination, the width (FWHM) of the Lorentzian component was 150 ± 7 μeV at $Q^{el}_{mean} = 1.3$ Å^{-1} and 250 ± 22 μeV at $Q^{el}_{mean} = 2.0$ Å^{-1}. The Q-dependence of the broadening confirms a diffusive motion of H is being observed. The percentage of the total proton population undergoing diffusion is, as would be anticipated, Q-independent at 42 ± 2 %.

CONCENTRATION DEPENDENCE OF THE LOCAL MODE SPLITTING FOR HYDROGEN IN YTTRIUM

T. J. Udovic, J. J. Rush, J. M. Rowe, N. F. Berk

and

I. S. Anderson
(Swiss Institute for Nuclear Research, Villigen, Switzerland)

Recently, incoherent inelastic neutron scattering measurements of the local mode frequencies in single-crystal samples of $YH(D)_{0.18}$[1] demonstrated a highly unusual potential which is much softer and anharmonic along the c axis than in the basal plane. The observation of a vibrational frequency which is reduced by ca. 25 % along the c axis is surprising since the T sites have nearly cubic local symmetry with a c/a ratio that is only 3 % less than the ideal value. Low temperature results with improved energy resolution showed a novel splitting of the c axis mode which was interpreted in terms of the known H pairing in this system.

We have performed high resolution measurements of the local mode frequencies of hydrogen in yttrium as a function of concentration and isotopic dilution in order to

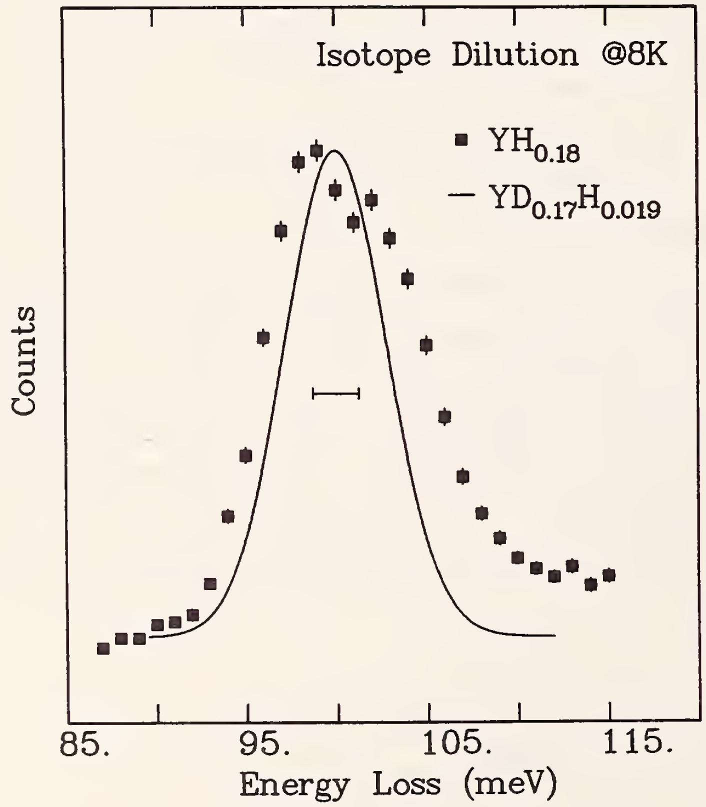

Figure 1. Comparison of the vibrational features for the H local mode polarized along the c direction in single-crystal $NH_{0.18}$ and $YD_{0.17}H_{0.019}$ at 8 K.

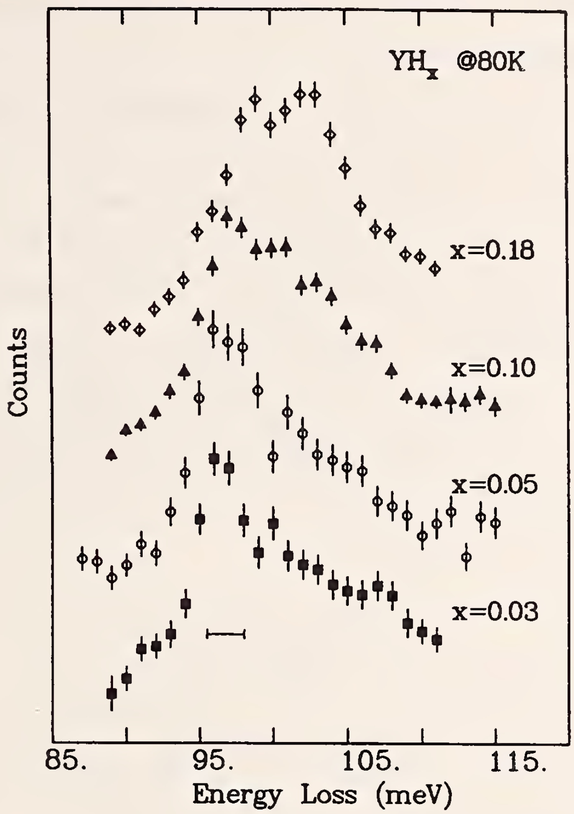

Figure 2. Concentration dependence of the vibrational features for the H local mode polarized along the c direction in polycrystaline YH$_x$ at 80 K.

separate the effect of interactions between H atoms at higher concentrations from the metal-hydrogen interactions.

Figure 1 shows the spectrum taken from the single crystal of YH$_{0.18}$ at 8 K, together with the data taken from the same crystal with composition YD$_{0.17}$H$_{0.019}$. The spectrum for YH$_{0.18}$ shows two distinct peaks of roughly equal intensity centered at 99 and 103 meV, respectively. This observation of a splitting in the local mode frequency polarized along the c direction for hydrogen parallels the earlier measurements of a similar splitting for YD$_{0.18}$. However, the spectrum taken from the isotopically diluted hydrogen shows a single peak, centered at 100 meV, whose full width (6 meV) is considerably narrower than the full width (~11 meV) of the doublet measured for the pure hydrogen sample. This observation clearly favors a model of dynamical coupling as an explanation of local mode splitting.

A simple phenomenological model based on an elementary pair of coupled harmonic oscillators relates the peaks at 99 and 103 meV to local "acoustic" and "optic" vibrational modes of hydrogen pairs. Such a model also predicts a single peak for the isotope diluted case, with a small upward shift in energy compared to the nominal isotopic fundamentals, in good agreement with the experimental observations.

The concentration dependence of the local mode frequencies from a polycrystalline sample is shown in figure 2. The essential features are an overall shift of the spectrum to lower energy as the concentration is decreased, together with a broadening and collapse of the high-energy peak. In terms of the above model, these observations may be explained by a relaxation of long-range, strain-induced ordering present at high concentrations. This relaxation would result in a distribution of coupling constants, responsible for the behavior of the high-energy peak. At the same time, the loss of long-range order would allow metal atom displacements, otherwise hindered at high concentration due to the ordering of H atom pairs, which give rise to an overall shift of the local mode spectrum to lower energy.

---

1. I. S. Anderson, J. J. Rush, T. J. Udovic and J. M. Rowe, Phys. Rev. Lett. 57 (1986) 2822.

INVESTIGATION OF HYDROGEN TRAPPING IN $PdSc_{0.02}$

T. J. Udovic and J. J. Rush

and

I. S. Anderson
(Swiss Institute for Nuclear Research, Villigen, Switzerland)

and

H. Schone
(College of William and Mary, Williamsburg, VA)

Preliminary incoherent inelastic neutron scattering (IINS) experiments were performed using the BT-4 triple-axis spectrometer to investigate the effect of Sc impurity atoms on the vibrational density of states of H absorbed in Pd. Figure 1 shows the H vibrational spectrum of $PdSc_{0.02}H_{0.02}$ as a function of temperature after subtraction of the $PdSc_{0.02}$ background spectrum using the Be-filter detector (with a resolution of ca. 6 meV below 100 meV). Normally, the local modes of α- and β-phase Pd-H occur at 69 and 58 meV, respectively. Indeed, the spectrum at 295 K shows a broad local mode distribution peaking at 69 meV, suggesting the presence of α-phase H. However, upon cooling to 80 K, a marked change in the spectrum is seen, with a broad feature peaking at ca. 60 meV and a shoulder at ca. 80 meV. Although it appears that some α-phase H is still present at 80 K, the vibrational distribution indicates that the Sc atoms perturb the main fraction H atoms that would otherwise

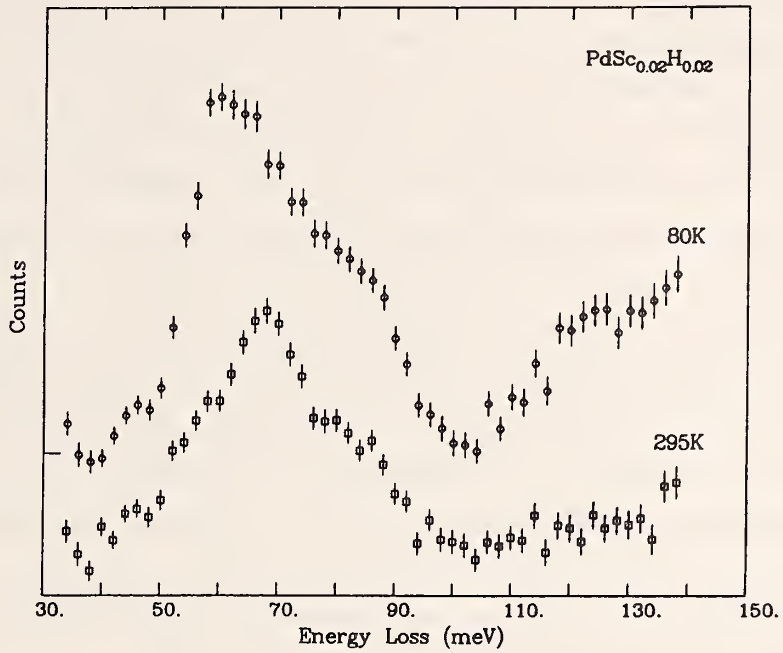

Figure 1. Temperature dependence of the H vibrational spectrum for $PdSc_{0.02}H_{0.02}$ (minus the $PdSc_{0.02}$ background spectrum) using the BT-4 triple-axis spectrometer in the Be-filter detector configuration.

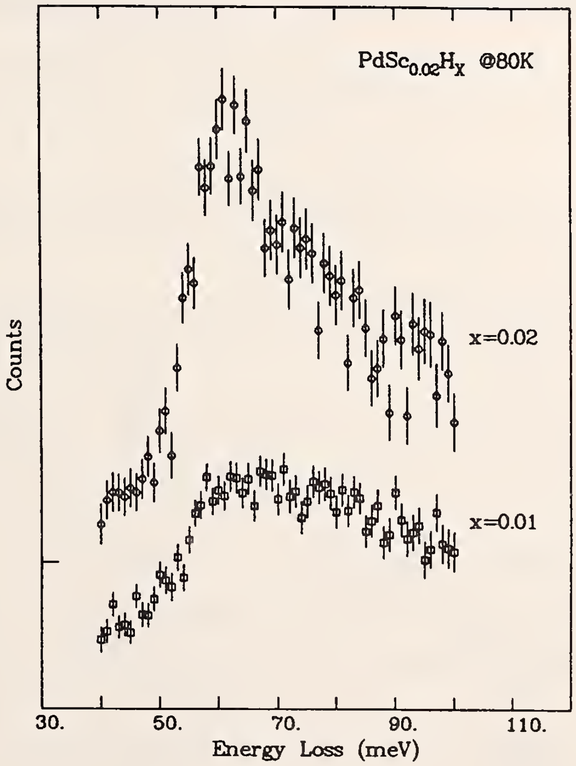

Figure 2. Hydrogen concentration dependence of the H vibrational spectrum for $PdSc_{0.02}H_x$ (minus the $PdSc_{0.02}$ background spectrum) using the BT-4 triple-axis spectrometer in the composite Be/graphite-filter detector configuration.

populate the β-phase within the pure Pd matrix. The 2 meV shift from the expected β-phase position suggests that the Sc atoms actually trap at least some of the H atoms, resulting in a perturbed site location compared to α- or β-phase H. The spectra can be explained by an ad-mixture of β-phase and trapped H.

A higher-resolution configuration (i.e., the composite Be/graphite filter detector with a resolution ranging from 2 to 5 meV over the energy regime scanned) was used to explore the 80 K spectrum of $PdSc_{0.02}H_x$ as a function of H concentration. Figure 2 illustrates the results for x = 0.01 and 0.02. The spectrum for $PdSc_{0.02}H_{0.02}$ is similar to that in Fig. 1, and no features have been more clearly resolved. The spectrum for $PdSc_{0.02}H_{0.01}$ illustrates a more unusual vibrational distribution with little evidence for β-phase H. This suggests that, for lower H concentrations, all the H is, indeed, trapped by the Sc atoms, yielding significant vibrational contributions centered at higher energy.

Future experiments will focus on investigating this trapping phenomenon more thoroughly as function of temperature and H concentration.

PHONON DENSITY OF STATES OF $La_{1.8}Sr_{0.2}CuO_4$ AND La_2CuO_4

J. J. Rhyne and J. A. Gotaas

and

L. Toth and S. Lawrence
(Ceramics Branch, Naval Research Laboratory, Washington, DC)

and

S. Wolf, M. Osofsky, and D. U. Gubser
(Metal Physics Branch, Naval Research Laboratory, Washington, DC)

The system $La_{2-x}Sr_xCuO_4$ was the first of the new "high-T_c" superconductors, with transition temperatures in the range of 30-40K,[1] and it is believed that the superconductivity in this system may still be of the BCS type, and hence mediated by phonons. Detailed knowledge of the phonon dispersion would require single crystals of sufficient size to perform inelastic scattering experiments on, but useful information can be garnered by measuring the phonon density of states, which requires only powdered samples. We have used BT-4 in both triple-axis and Be filter modes to measure inelastic scattering in the superconductor $La_{1.8}Sr_{0.2}CuO_4$ and the non-superconducting end compound La_2CuO_4 in an effort to identify key features in the phonon spectrum. To obtain the density of states from the inelastic scattering, we have used the incoherent approximation, which has been shown to be reasonably accurate even for predominantly coherent scatterers.[2] This yields the neutron-weighted density of states, since the scattering from any mode depends on the atoms participating in it according to the ratio of the total scattering amplitude over the atomic mass. This will tend to weight modes involving oxygen atoms more heavily than the other atoms, but that will be the same for both systems studied, and furthermore it is believed that the oxygen atoms are crucial to the superconductivity in these compounds.

In order to cover the energy range from 5 to 95 meV, data were taken in three overlapping modes, which were then scaled to form a single density of states, after correcting the data for background and other energy factors that convert the measured scattering to the double differential cross section. The resulting density of states was normalized so that the integrated intensity was unity, to make comparison between the two samples easier.

Figure 1 displays the neutron weighted density of states (DOS), $\bar{g}(\omega)$, for $La_{1.8}Sr_{0.2}CuO_4$ at T = 10K. The line through the data is simply a guide to the eye. There is a typical ω^2 dependence to the DOS at low energies, followed by a peak (or shoulder) in the vicinity of 12 meV, increasing to the largest feature in the scattering, a peak at approximately 20 meV. There is a slight drop to form a valley, then an increase to a second peak at about 30 meV. There is a deeper valley in the scattering at 35 meV, followed by another peak at 40 meV, another at 55-60 meV, then

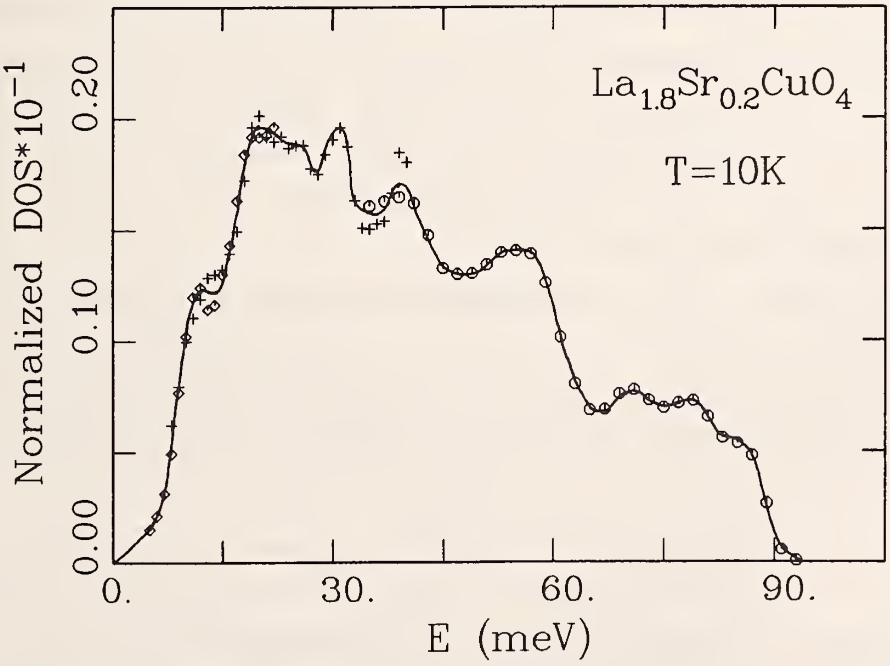

Figure 1. Neutron-weighted phonon density of states for $La_{1.8}Sr_{0.2}CuO_4$ at 10K.

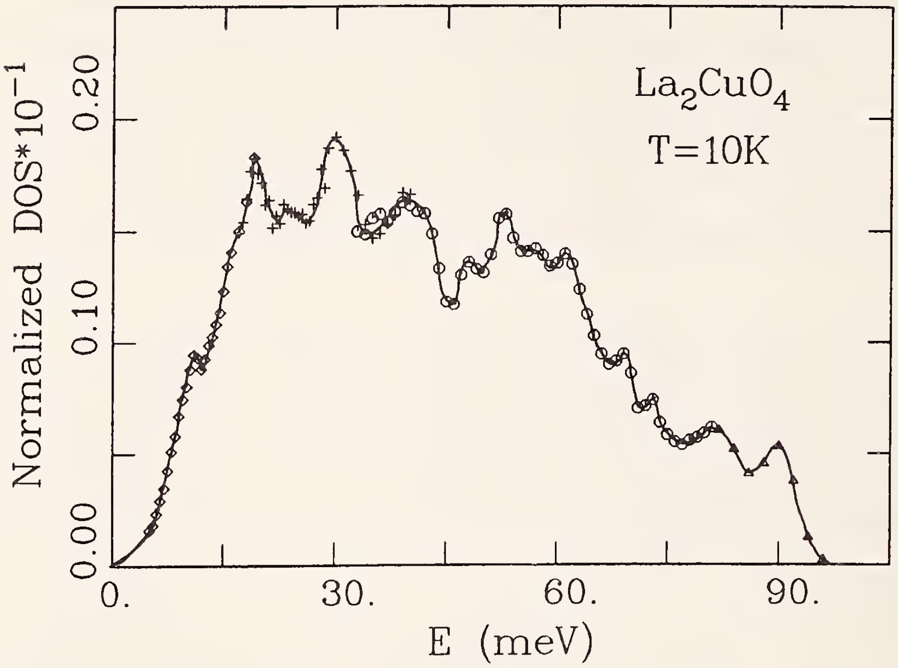

Figure 2. Density of states for non-superconducting La_2CuO_4 at 10K. Scattering above 45 meV is shifted upward by approximately 5 meV with respect to the spectrum seen in Fig. 1.

a sharp drop before a broad collection of peaks between 65 and 85 meV. The intensity then drops to zero in the vicinity of 90 meV.

Figure 2 shows the same data range for the non-superconducting compound La_2CuO_4. The general features of the DOS are clearly similar, with the differences that the shoulder at 12 meV is less pronounced, and the valley between the peaks at 20 and 30 meV is deeper. Otherwise, the most significant change is that the intensity at energies between 45 and 90 meV has shifted substantially upward in the non-superconductor, as though the entire scattering pattern had been shifted toward higher energies by approximately 5 meV.

The comparison between the two DOS spectra suggests a general softening of the phonon spectrum for the superconducting compound, but it is difficult to single out a given feature that may be closely coupled to the superconducting mechanism. Further interpretation requires some sort of detailed lattice dynamical model to fit the observed DOS.

---

1. J. G. Bednorz and K. A. Muller, Z. Phys. B64, 189 (1986).

2. P. F. Miceli, S. E. Youngquist, D. A. Neumann, H. Zabel, J. J. Rush and J. M. Rowe, Phys. Rev. B34, 8977 (1986).

PHONON DENSITY OF STATES OF $YBa_2Cu_3O_7$ AND $YBa_2Cu_3O_6$

J. J. Rhyne, D. A. Neumann, J. A. Gotaas, and F. Beech
and
L. Toth and S. Lawrence
(Ceramics Branch, Naval Research Laboratory, Washington, DC)
and
S. Wolf, M. Osofsky, and D. U. Gubser
(Metal Physics Branch, Naval Research Laboratory, Washington, DC)

We have used inelastic neutron scattering to probe the vibrational modes in the high temperature superconductor $YBa_2Cu_3O_7$[1] and in the non-superconducting but crystallographically equivalent compound $YBa_2Cu_3O_{6.05}$, to examine possible phonon effects contributing to the superconducting mechanism in these compounds. The vibrational density of states (DOS) was obtained from the inelastic neutron scattering data using the incoherent approximation.[2] The measurements yield the neutron-weighted phonon DOS, since the scattering from different species is weighted by the values of the total scattering cross section divided by the mass. For O, Cu, Ba, and Y these values are 0.26, 0.12, 0.043, and 0.08 (barns/amu) respectively. Thus ≈80% of the observed scattering will be due to vibrations of the oxygen atoms.

The data were collected on BT-4; low energy data ($\omega \leq 25$ meV) were taken in the constant-Q mode (E_f=13.8 meV) at several values of the scattering vector between 3.3 and 5.0 $Å^{-1}$ and averaged to improve the incoherent approximation. Higher energy data (> 20 meV) were taken using the Be-graphite-Be filter analyzer. After making all background corrections and converting the measured intensities to $\bar{g}(\omega)$, we used the overlapping energy regions to scale the DOS obtained in the three different energy ranges to obtain a single DOS, which was then normalized so that the integrated DOS was unity. Previous studies of the DOS of coherent scatterers[2] suggest that any effects due to coherent scattering will only be manifested in the relative intensities of the various features and will be of the order of the size of the error bars in our case.

The neutron-weighted phonon DOS of $YBa_2Cu_3O_7$ at 120 K is shown in figure 1. Below 9 meV, the DOS displays the ω^2-dependence typical of three dimensional systems. The small shoulder at about 12 meV is probably due to a zone boundary interlayer shear mode. The DOS then increases, reaching a large maximum at 19-20 meV, followed by another maximum at roughly 25 meV before dropping sharply to a minimum at 28-30 meV. There is a broad feature centered at about 34 meV, followed by a narrower, less intense maximum at about 44 meV. Above 50 meV, the DOS increases to a shoulder at

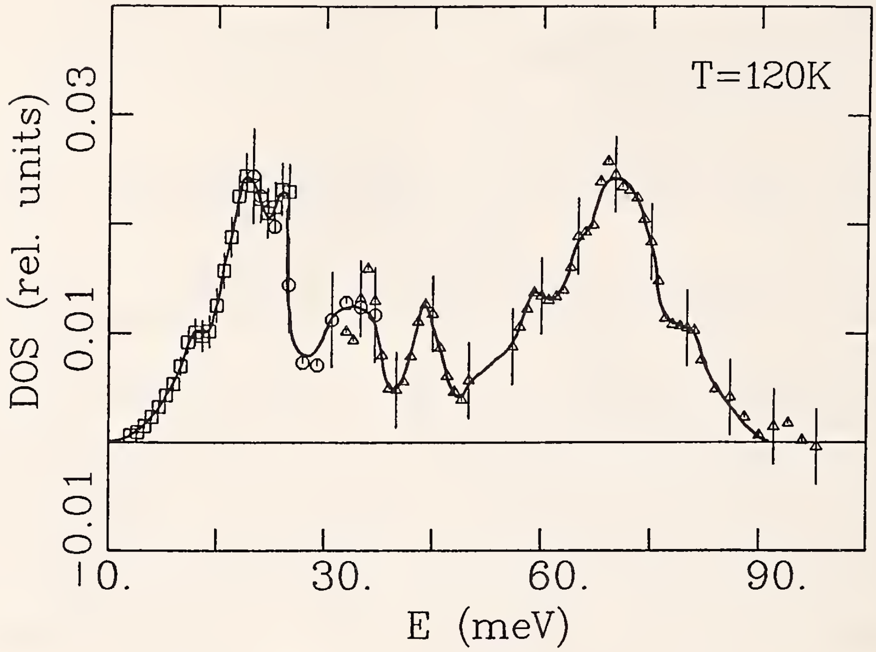

Figure 1. Vibrational density of states as measured by inelastic neutron scattering scattering at 120 K. The largest spectral weight is contained in peaks involving oxygen vibrations (see text).

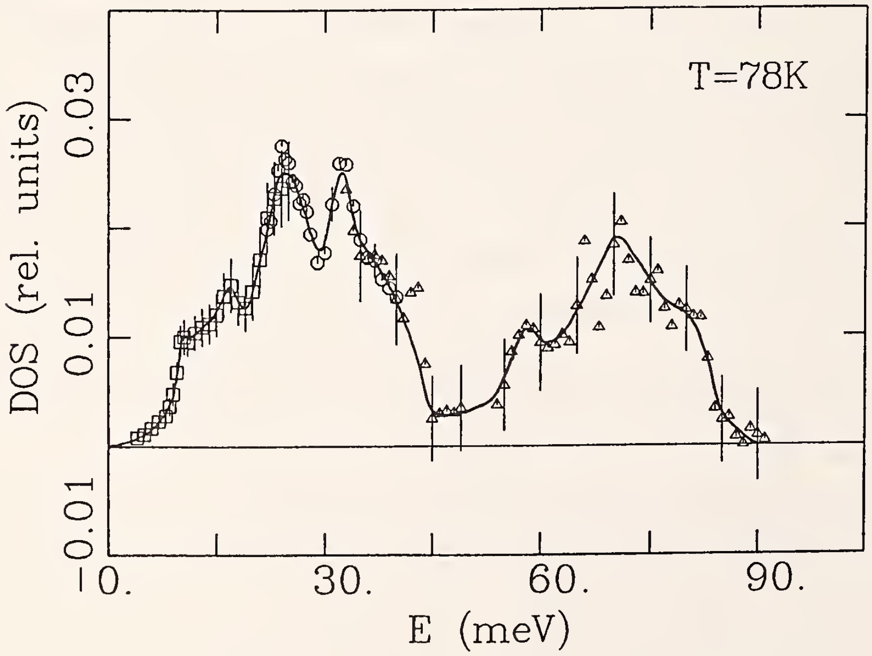

Figure 2. Vibrational density of states for the non-superconducting control compound $YBa_2Cu_3O_6$ measured at 78 K. The scattering above about 45 meV is essentially unchanged from the superconducting material, while that at lower energies shows significant changes in relative weights of the peaks.

about 60 meV and then a peak at 70 meV before dropping to zero at about 90 meV. The rather unusual relative intensities of the low- and high-energy DOS peaks is due to the degree of O atom participation in the modes in these energy regions.

We have also measured the DOS in the superconducting state at T=12K. The only clearly discernible difference was a slight shift of (½-1 meV) in the energy range of 10-20 meV, which can be explained by typical anharmonic effects.

The DOS of the non-superconducting (semiconducting) $YBa_2Cu_3O_6$ compound is significantly different, particularly in the relative weights of the peaks in the energy range below about 45 meV. As observed in figure 2, the feature at ≈ 70 meV is essentially the same for the non-superconducting compound as for the $YBa_2Cu_3O_7$, and thus probably represents vibrational states associated with the planar and tetrahedral oxygen sites (O(1), O(2), and O(3)) which have not changed their occupancy. The double peak structure at 19-25 meV is dramatically different in the non-superconducting material, for which the relative height of the DOS feature at 19 meV has been strongly reduced compared to that at 25 meV. The scattering minimum near 30 meV is common to both materials, however the broad relatively weaker feature around 34 meV in the superconductor has become a dominant peak in the non-superconductor with a shoulder extending out to include the peak near 44 meV. Another minimum occurs around 47 meV in both materials. It is thus suggestive that the scattering between about 25 meV and 45 meV reflects optic modes involving the copper and oxygen atoms with polarization vectors in the plane, since these would certainly be affected by the removal of oxygen atoms from the O(4) site.

In the absence of a complete model calculation, a definitive assignment of specific vibrational modes to the observed peaks in the DOS cannot be made. However, as stated above, the overall spectrum is dominated by oxygen atom modes, and those arising from the O(4) linear chain site contribute to the lower energy peaks in the spectrum and do not contribute strongly to the major features above 45 meV, which remain unaffected by removal of more than 90 per cent of the oxygen from the O(4) site.

---

1. R. J. Cava, B. Batlogg, R. B. van Dover, D. W. Murphy, S. Sunshine, T. Siegrist, J. P. Remeika, E. A. Rietman, S. Zuhurah, and G. P. Espinosa, Phys. Rev. Lett. 58, 1676 (1987).

2. P. F. Miceli, S. E. Youngquist, D. A. Neumann, H. Zabel, J. J. Rush, and J. M. Rowe, Phys. Rev. B 34, 8977 (1986).

THE FLOPPY TO RIGID TRANSITION IN GLASSY GeSe AND SiTe ALLOYS

W. A. Kamitakahara
(Ames Laboratory, Ames, IA)

and

R. L. Cappelletti
(Ohio University, Athens, OH)

and

P. Boolchand
(University of Cincinnati, Cincinnati, OH)

and

D. A. Neumann

Some years ago Phillips introduced the notion of overconstrained and underconstrained glasses.[1] In an underconstrained glass the number of degrees of freedom per atom, N_d (3 in three dimensions) is greater than the number of mechanical constraints imposed by bond-stretching and bond-bending forces, N_c, while in an overconstrained system the opposite is true. More recently, Thorpe has developed this idea by showing that in an underconstrained glass it is possible to have displacements without the atoms being subjected to a restoring force.[2] These deformations can then be thought of as zero-energy "excitations" which have been termed "floppy" modes. (When van der Waals and dihedral angle forces are included the floppy modes actually occur at non-zero energies as of course they must.) Thus by adjusting the number of constraints per atom one can observe both floppy and rigid behavior. In practice this can be achieved by varying the ratio of Se or Te ($N_c = 2$) to Ge or Si ($N_c = 4$) in a glassy alloy and then looking for an excess of low energy modes in the vibrational density of states. We have therefore performed inelastic neutron scattering studies of these systems in an attempt to directly observe the floppy modes.

The results of these measurements do indeed show a large feature in the vibrational density of states of amorphous Se at an energy of about 4 meV. Upon alloying with Ge this peak rapidly becomes less prominent, in qualitative agreement with the concept of a floppy to rigid transition. However the observed concentration dependence of the integrated intensity does not quantitatively agree with simple rigidity percolation models. In addition, the temperature dependence of this feature has been measured for the pure Se sample. These results show only slight differences from those obtained at room temperature. No unambiguous evidence for floppy modes was observed for the SiTe samples; however pure glassy Te samples, which would have the highest fraction of floppy modes, were not available.

---

1. J. C. Phillips, J. Non-Cryst. Solids 34, 153 (1979); 43, 37 (1981).

2. M. F. Thorpe, J. Non-Cryst. Solids 57, 355 (1983).

MAGNETIC STRUCTURE OF Dy-Y SUPERLATTICES

R. W. Erwin and J. J. Rhyne
and
M. B. Salamon, J. Borchers, S. Sinha, R. Du, J. E. Cunningham and C. P. Flynn
(University of Illinois, Urbana, IL)

Recent advances in the technologies required to manufacture superlattices and multilayers have not only greatly expanded the control of materials properties, but just as significantly opened new avenues for the investigation of microscopic interactions. For many superlattices interdiffusion can now be limited to be between only two growth planes, so that one has nearly arbitrary control over the stacking sequence of atoms. These sharp chemical boundaries provide an ideal milieu for studies of dimensionality and interface effects, and the control of layer thickness makes it possible to study the details of interactions propagating through the interlayers. We have been focusing on rare-earth magnetic interactions by studying single-crystal rare-earth-metal superlattices grown by molecular beam epitaxy.[1]

We have shown by neutron diffraction that it is possible to characterize the magnetic structures in single-crystal superlattices by means of a simple model for the superlattice structure factors. In the Dy-Y superlattices investigated here the measurements show that the magnetic structure is modulated by the separate magnetic properties of each layer type. This is shown in figure 1 where we plot the turn angles obtained in the Dy and Y layers for $[Dy_{16}|Y_{20}]_{89}$, $[Dy_{15}|Y_{14}]64$ and $[Dy_{16}|Y_{9}]_{100}$. The helimagnetic turn angle in the Y layers is consistent with the 52° value obtained in dilute alloys and other superlattices[2] as well as band-structure calculations.[3] The turn angle in the Dy layers is qualitatively similar to that of bulk Dy, with an apparent trend towards larger values as the relative amount of Y is increased. This may be evidence that magnetoelastic effects are perturbing the Dy turn angle. The most salient difference between the superlattices and bulk Dy is the suppression of the ferromagnetic transition.[4]

In figure 1 is also shown the total magnetic phase shift across the Dy and Y layers between the nominal interfaces. The phase shift across the Y layers is clearly not a multiple of π radians so that the coupling cannot be simply scalar as obtained for Gd-Y superlattices.[2]

We have also obtained the magnetic coherence length by deconvoluting the instrumental width and chemical coherence length from the observed magnetic superlattice linewidths. These results are shown in figures 2 and 3, and it is

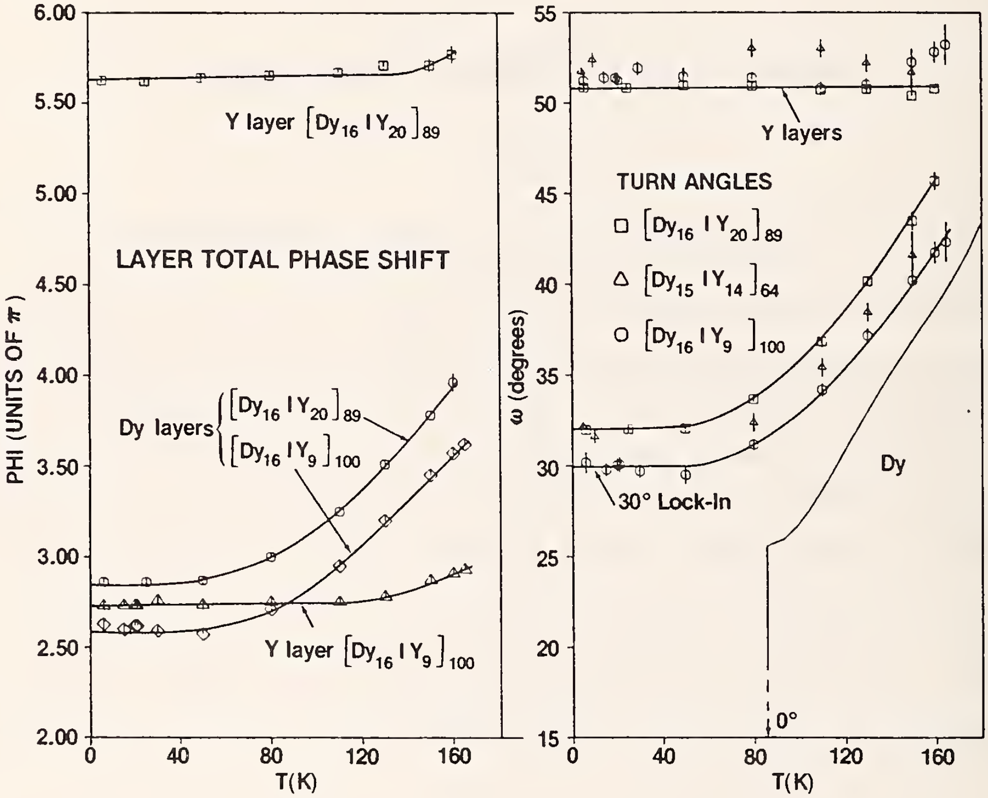

Figure 1. Left-hand side: Total phase shift of spin-density wave across Y layers and Dy layers as a function of temperature for $[Dy_{16}|Y_{20}]_{89}$ and for $[Dy_{16}|Y_9]_{100}$. Note the Y phase shift is not a multiple of π. Right-hand side: Temperature dependence of the interplane turn angles for Y layers and Dy layers in $[Dy_{16}|Y_{20}]_{89}$ $[Dy_{15}|Y_{14}]_{64}$ and $[Dy_{16}|Y_9]_{100}$. Note the 30° lock in at low T for the sample with the small number of Y planes. $[Dy_{16}|Y_9]_{100}$. The turn angle of bulk Dy, which drops to 0° at the 85 K ferromagnetic transition, is shown for comparison.

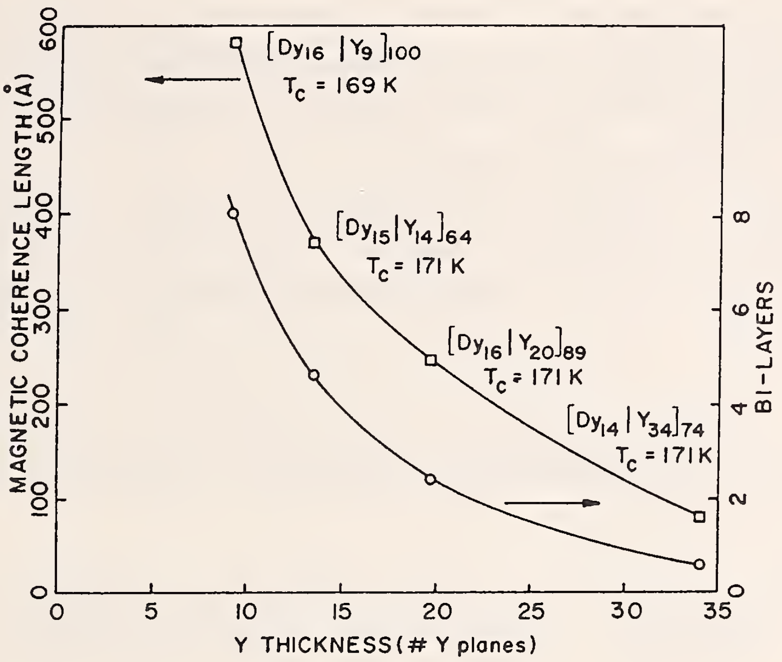

Figure 2. Magnetic correlation length (in both Å and in number of complete bilayers) obtained from the intrinsic Q width of the magnetic satellite peaks as function of the Y thickness (number of atomic planes) for the three samples.

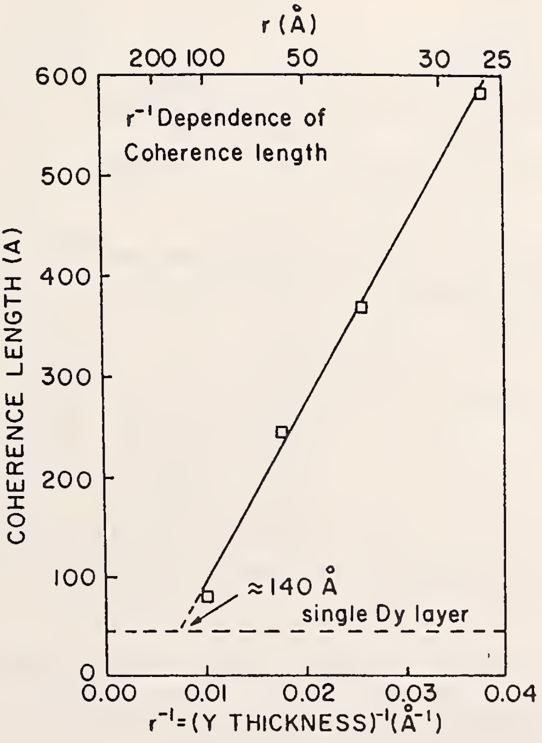

Figure 3. Magnetic correlation length plotted against the inverse of the Y thickness showing 1/r dependence.

found that the coherence length falls off as the inverse of the Y layer thickness. Note that the coherence falls below two bilayers at about 28 atomic planes of Y. If the coherence in the chirality of the helical order were lost we would expect the coherence range to be below two bilayers.

In conclusion, the nature of the magnetic structure in the Dy-Y superlattices, including the phase and chirality coherence, suggests that the order is propagated via a spin-density wave in the Y conduction bands stabilized by the Dy 4f spins.

---

1. J. Kwo, D. B. McWhan, M. Hong, E. M. Gyorgy, L. C. Feldman and J. E. Cunningham, in Layered Structures, Epitaxy, and Interfaces, Materials Research Society Symposia Proceedings No. 37, edited by J. H. Gibson and L. R. Dawson (Materials Research Society, Pittsburgh, 1985), p. 509.

2. C. F. Majkrzak, J. W. Cable, J. Kwo, M. Hong, D. B. McWhan, Y. Yafet, J. V. Waszczak and C. Vettier, Phys. Rev. Lett. 56, 2700 (1986); L. E. Wenger, G. W. Hunter, J. A. Mydosh, J. S. Gotaas and J. J. Rhyne, Phys. Rev. Lett. 56, 1090 (1986); B. D. Rainford, H. B. Stanley and B. V. B. Sarkissian, Physica 130B, 388 (1985).

3. S. H. Liu, R. P. Gupta and S. K. Sinha, Phys. Rev. B 4, 1100 (1971).

4. R. W. Erwin, J. J. Rhyne, M. B. Salamon, J. Borchers, Shantanu Sinha, R. Du, J. E. Cunningham and C. P. Flynn, Phys. Rev. B 35, 6808 (1987).

MAGNETIZATION PROCESS IN Dy THIN FILMS AND Dy-Y SUPERLATTICES

R. W. Erwin and J. J. Rhyne
and
J. Borchers, M. B. Salamon, R. Du and C. P. Flynn
(University of Illinois, Urbana, IL)

The epitaxial growth of single crystal rare-earth superlattices by molecular beam techniques provides a unique method of studying the interactions responsible for the intricate magnetic structures found in the constituent elements. We have shown that the helimagnetic phase of Dy remains intact in Dy-Y superlattices (and thin Dy films) with a coherence of both phase and chirality through the magnetically 'dead' Y interlayers.[1] In this report we describe how the ferromagnetic phase is suppressed in Dy-Y superlattices and also perturbed in Dy thin films. We will also discuss the field effects on the coherence of the helimagnetic state in order to obtain an estimate of the coupling strength across the Y interlayers.

The suppression of ferromagnetism in $[Dy_{13}|Y_{50}]_{40}$, $[Dy_{15}|Y_{34}]_{74}$, $[Dy_{16}|Y_{20}]_{89}$, $[Dy_{15}|Y_{14}]_{64}$ and $[Dy_{16}|Y_{9}]_{100}$ is clearly deduced from the temperature independence of the nuclear Bragg peaks observed in the neutron diffraction patterns.[1] It is evident that this effect is not simply the result of exchange dilution, since the Neel temperatures of the superlattices are within 5 to 10 percent of the value for bulk Dy (180 K). Instead it is predominantly caused by the decreased magneto-elastic energy density when non-moment bearing Y atoms are placed in the lattice. We can calculate this effect by making the approximation that the basal plane orthorhombic distortion, the ϵ^γ mode, is completely clamped in the superlattice. Experimentally we have shown this to be the case by observing the temperature and field dependence of basal plane nuclear reflections. The only allowed strains occur along the c-axis so that the magneto-elastic energy density can be expressed as

$$f_{me} = \frac{1}{2}c^z(\epsilon^z)^2 - A^z(\cos\omega)(\epsilon^z)$$

where

$$c^z = c^\alpha_{11} + \frac{1}{3}c^\alpha_{22} \quad \text{and} \quad A^z = c^\alpha_{11}\lambda_1 + \frac{1}{\sqrt{3}}c^\alpha_{22}\lambda_2 .$$

The strains λ_1 and λ_2 are defined in Ref. 2, c^α_{11} and c^α_{22} are the symmetry elastic constants and ω is the magnetic helix turn angle. Solving for the equilibrium

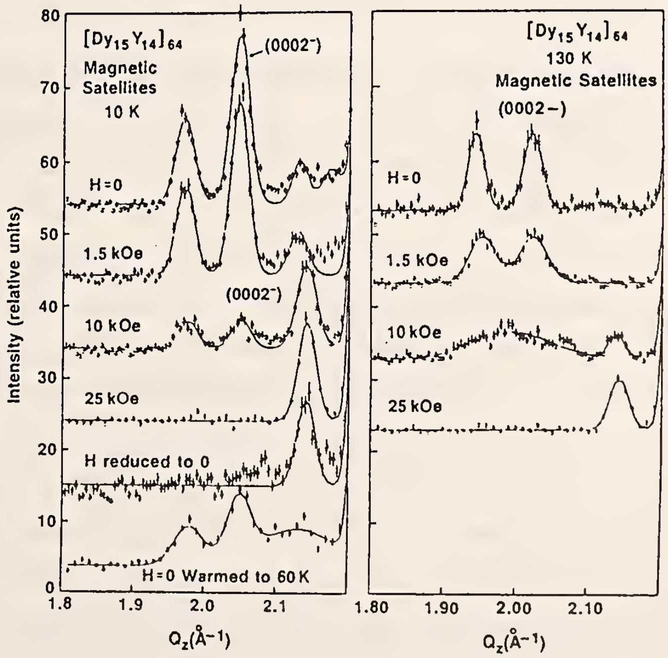

Figure 1. The field dependence of the magnetic satellites is compared at 10 K and at 130 K for [Dy$_{15}$|Y$_{14}$]$_{64}$. A second order transition to the ferromagnetic state is observed at low temperature with a considerable remanence. At high temperature the magnetization process is initiated by a breakdown of the helimagnetic coherence due to pseudo-random field effects. This allows an estimate of the coupling strength across the Y layers of 1 K per Dy layer per basal-plane atom.

strains in the superlattice results in the expression for the magnetoelastic driving energy for ferromagnetism:

$$\Delta f_{me} = \frac{1}{2}(\sin^2\omega)(A^z)^2/c^z \ .$$

At T = 10 K in ferromagnetic bulk Dy $\lambda_1 = 0.0009$ and $\lambda_2 = 0.0049$, while the elastic constants are $c_{11}^{\alpha} = 4.2\text{x}10^{11}$ ergs/cm^3 and $c_{22}^{\alpha} = 13.1\text{x}10^{11}$ ergs/cm^3.[3,4] Using $\omega = 30°$ we find that Δf_{me}(10K) = 0.6 K/atom, favoring ferromagnetism. Therefore, even at low temperatures the magnetoelastic energy is not sufficient to overcome the exchange-energy barrier of -1.0 K/atom in any Dy thin film elastically constrained so that the γ-mode is completely clamped.

In a 4000 Å thick Dy film grown on the same Nb and sapphire substrate as the superlattices the temperature of the ferromagnetic transition is reduced to just below 80 K on cooling, and a 20 K temperature hysteresis is observed. An orthorhombic distortion is observed in a saturating field along the easy a-axis, although its value is about 1/4 of the γ-mode strain in bulk Dy. The Nb buffer layer is found to be unstrained suggesting that the magnetic film can slip on the substrate when the magnetoelastic energy is sufficient. This would explain the observed partial suppression of the ferromagnetic phase in the Dy film including the hysteresis.

The effect of an applied field on the superlattice helimagnetic state is shown in figure 1. At low temperature (10 K in the figure) intensity is gradually transferred from the helimagnetic superlattice peaks to the main Bragg peak (not shown in the figure). The peak positions and widths are field independent. This second order transition is, however, irreversible in most of the superlattices studied, due to the large basal plane anisotropy. These anisotropy barriers can be reduced and the helimagnetic phase regained upon warming the temperature to about 40 to 60 K, although the degree of coherence is less than in the zero-field-cooled state.

At high temperatures the magnetization process is qualitatively different than at 10 K. Upon applying a magnetic field of 1.5 kOe, the magnetic satellites are observed to broaden. The full width of the most intense magnetic peak has been plotted for two superlattices in figure 2. This rapid destruction of the coherence has not been observed in any bulk helimagnets, and must therefore be a consequence of the weak interlayer coupling of the Dy spins, along with the rapid decrease of basal-plane anisotropy as the temperature is raised. Our data analysis gives an

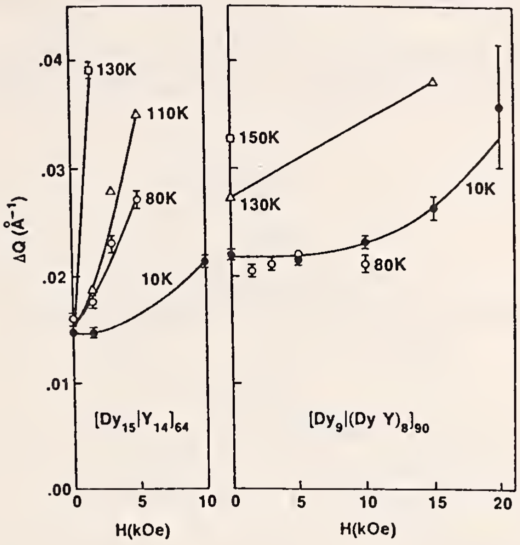

Figure 2. The intrinsic width of the magnetic satellites is plotted against the applied field for several temperatures and for two different superlattices. This width should increase as a power law of the applied field when random-field theory applies, as is observed at high temperatures.

uncompensated magnetic moment per layer of Dy of $5.4\mu_B$ at 130 K due to the mismatch of the helix wavelength with the Dy-layer thickness for the sample shown in figure 1.[1] We suggest that the Zeeman energy of the external magnetic field coupled to this excess magnetic moment per layer is sufficient to break the weak interlayer coupling between Dy spins. This is a random-field effect since the net layer moments are in pseudo-random directions relative to the external field. We can approximate the strength of the interlayer coupling at 130 K as 5 kOe × $5.5\mu_B \approx 1$ K per Dy layer per basal-plane atom. This is orders of magnitude larger than estimates of the exchange coupling in rare-earths at a distance equivalent to the interlayer spacing, which is additional evidence in support of the formation of an incipient spin density wave in Y in the presence of magnetic moments.

---

1. J. J. Rhyne, R. W. Erwin, J. Borchers, S. Sinha, M. B. Salamon, R. Du and C. P. Flynn, J. Appl. Phys. 61, 4043 (1987); R. W. Erwin, J. J. Rhyne, M. B. Salamon, J. Borchers, S. Sinha, R. Du, J. E. Cunningham and C. P. Flynn, Phys. Rev. B35, 6808 (1987).

2. W. E. Evenson and S. H. Liu, Phys. Rev. 178, 783 (1969).

3. J. J. Rhyne and S. Legvold, Phys. Rev. 138, A507 (1965); F. J. Darnell and E. P. Moore, J. Appl. Phys. 34, 1337 (1963).

4. M. Rosen and H. Klimer, Phys. Rev. B1, 3748 (1970).

SPIN DYNAMICS IN DILUTE MAGNETIC SEMICONDUCTORS $Cd_{1-x}Mn_xTe$ AND $Zn_{1-x}Mn_xTe$

T. M. Giebultowicz and J. K. Furdyna
(University of Notre Dame, Notre Dame, Indiana)

and

J. J. Rhyne

and

W. Y. Ching
(University of Missouri, Kansas City, MO)

and

D. L. Huber
(University of Wisconsin, Madison, WI)

The dilute magnetic semiconductors $Cd_{1-x}Mn_xTe$ and $Zn_{1-x}Mn_xTe$ are often referred to as "frustrated" antiferromagnets. This term is supposed to describe a system in which the energies of all pairs of antiferromagnetically bonded spins cannot be minimized simultaneously. A prototypical example of a frustrated antiferromagnet is a FCC array of spins, each interacting antiferromagnetically only with its nearest neighbors. In $Cd_{1-x}Mn_xTe$ and $Zn_{1-x}Mn_xTe$ the magnetic ions Mn^{++} form site-dilute FCC lattices, and the antiferromagnetic interactions between these ions are extremely short-range ($J_{NNN} \approx 0.1J_{NN}$). Thus, both these compounds are a very close realization of this idealized model. As follows from many recent theoretical analyses and model studies[1], the consequences of the frustration of the spin lattice are far reaching in the context of the magnetic properties of such systems. For example, the ground state of the system is highly degenerate, there is no long-range spin order in three dimensions, and the mechanism of spin excitations becomes very complex. Frustration may also result in a spin glass behavior of the system in the case of site-diluted lattices. $Cd_{1-x}Mn_xTe$ and $Zn_{1-x}Mn_xTe$ show, indeed, many of the characteristic features of a spin glass at low temperatures. It is not clear, however, whether these systems belong to the same universality class as, for example, <u>Cu</u>Mn or <u>Au</u>Fe.

As with other spin glasses, the characterization of the spin dynamics in $Cd_{1-x}Mn_xTe$ and $Zn_{1-x}Mn_xTe$ at low temperatures and in the vicinity of the spin freezing temperature is a problem of considerable importance. Recent model studies[2] of spin dynamics in dilute FCC Heisenberg antiferromagnets have indicated that quasiharmonic magnons may exist in these systems despite the absence of the long-range spin order. In order to verify these findings, we have carried out a series of inelastic neutron scattering experiments on single crystals of $Cd_{0.33}Mn_{0.67}Te$ and $Zn_{1-x}Mn_xTe$ with x = 0.65 and 0.41. The inelastic scattering spectra were compared

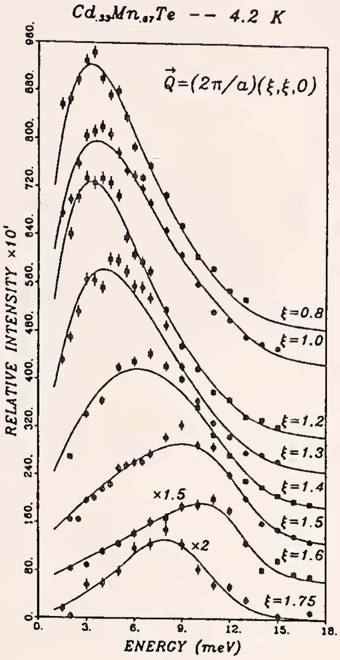

Figure 1. Fit of the theoretical lineshapes to the inelastic magnetic neutron scattering spectra in $Cd_{0.33}Mn_{0.67}Te$ measured for several Q-vectors along the <ξ,ξ,0> direction.

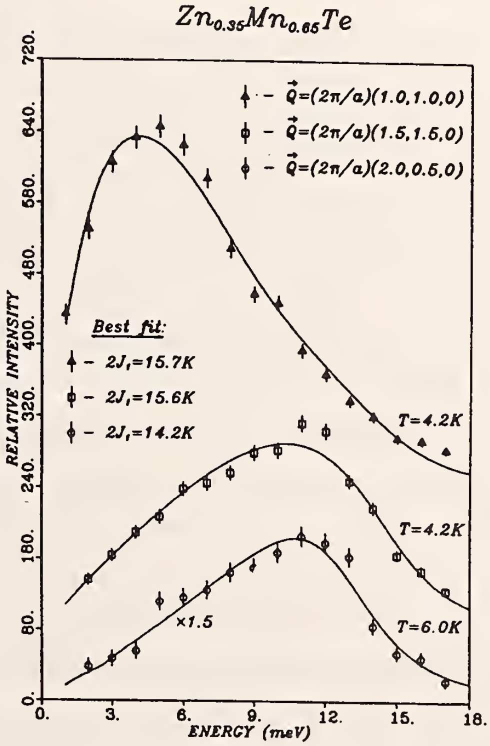

Figure 2. Examples of the same fit as in figure 1 for three different Q-points in $Zn_{0.35}Mn_{0.65}Te$.

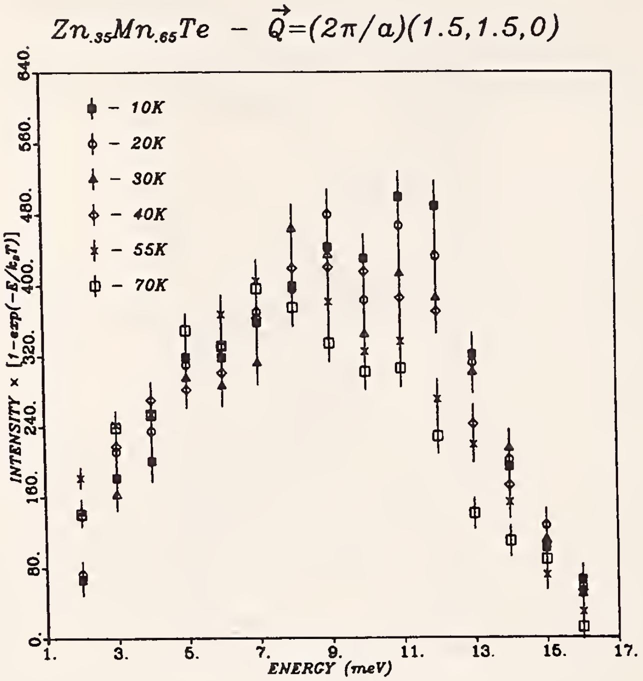

Figure 3. The inelastic magnetic scattering spectra normalized by the detailed balance factor $[1 - \exp(-E/kT_B)]^{-1}$ measured in $Zn_{0.35}Mn_{0.65}Te$ at $\vec{Q} = (2\pi/a)(1,1,0)$ for several different temperatures.

with the dynamic structure factors $S(\vec{Q},E)$ obtained from the model. The calculations were performed for systems with the same fraction of site occupancy as in the measured samples, and with Heisenberg NN and NNN interactions. The ratio of the exchange constants was assumed to be $J_{NN}/J_{NNN} = 0.1$. Examples of the fits of the theoretical curves to the experimental data obtained for the samples with high Mn concentration are shown in figure 1 and 2. The results of this analysis show that the model provides a very good description of the spin dynamics in the systems studied for most of the Brillouin zone. Certain discrepancies were found to occur only for Q-points close to the magnetic reflection center $(1,\frac{1}{2},0)$. This fact may suggest that there is an additional interaction mechanism in the real systems not accounted for by the model (e.g., one such possibility may be the Moriya-Dzialoshinsky anisotropy).

The variation of spin dynamics with temperature was studied in detail for the $Zn_{0.35}Mn_{0.65}Te$ sample. As indicated by the static spin-spin inverse correlation range $\kappa(T)$, and by the energy distribution in quasielastic magnetic scattering measured vs. T, a transition from the low-temperature short-range ordered magnetic phase to the paramagnetic state occurs in this system at $T_0 \approx 43$ K. Surprisingly, for certain $\vec{Q}$-vectors the dynamic structure factor does not exhibit significant changes up to temperatures as high as 70K (see figure 3), indicating that magnon modes occur in the system even in the thermally disordered phase.

---

1. For review of these works see, e.g., K. Binder and A. P. Young, Rev. of Mod. Physics 58, 801 (1987)

2. W. Y. Ching, D. L. Huber, Phys. Rev. B25, 5761, and B26, 6164 (1982)

MEASUREMENTS OF PHASE TRANSITIONS WITH NEUTRON SPIN ROTATION

J. W. Lynn, Q. Li, W.-H. Li and S. Sun-Mack
(University of Maryland, College Park, MD)
and
(National Bureau of Standards, Gaithersburg, MD)

and

R. W. Erwin

We have been employing a technique of measuring the magnetic properties of systems by monitoring the change in phase of a neutron caused by changes in the magnetization of the sample.[1,2] In essence the phase angle $\vec{B}\cdot d\vec{x}$ is measured along the path of the neutron, and any changes in $\vec{B}$ as a function of temperature or applied field are then observed. The qualitative behavior of the sample can be determined directly, and quantitative information can be obtained if the thickness and shape of the sample are known and care is taken to eliminate return fields from the path of the neutron outside the sample.[2] We have used this technique to make measurements on ferromagnets such as U_2NiSn and Zr_5Sb_3Fe, reentrant ferromagnetic spin glass materials such as $(Fe_xNi_{1-x})_{75}P_{16}B_6Al_3$, superconductors such as Nb and $YBa_2Cu_3O_7$, and magnetic superconductors such as $(Er_{1-x}Ho_x)Rh_4B_4$ and $Tm_2Fe_3Si_5$.

The measurements were made on the BT-2 triple-axis polarized beam spectrometer. A monochromatic polarized beam is directed towards the sample, the polarization state can be manipulated with flat-coil spin rotators placed before and after the sample, and the final polarization is analyzed with a Heusler alloy analyzer. At the position of the first flipper the spin of the neutron is rotated by $\pi/2$ so that $\vec{B} \perp \vec{P}$. The spin then begins to precess with the classic Larmor precessional frequency as it travels through the sample to the second flipper coil. The total phase angle along the path is

$$\phi = \frac{\gamma_L}{v} \int \vec{B}\cdot d\vec{x}$$

where $\gamma_L = 2.916$ kHz/Oe and v is the velocity. The instrument is set at one particular value for ϕ, for example in the paramagnetic state of the sample where B_{sample} is zero, and then changes in B can be readily detected. Figure 1 shows such a measurement for $(Fe_{0.15}Ni_{0.85})_{75}P_{16}{}^{11}B_6Al_3$, a sample which is just on the ferromagnetic side of the paramagnetic-ferromagnetic-spin glass phase diagram.[3] We observe a change in the phase angle below ~50 K as the system enters the ferromagnetic state, but then the ferromagnetic component is lost at low

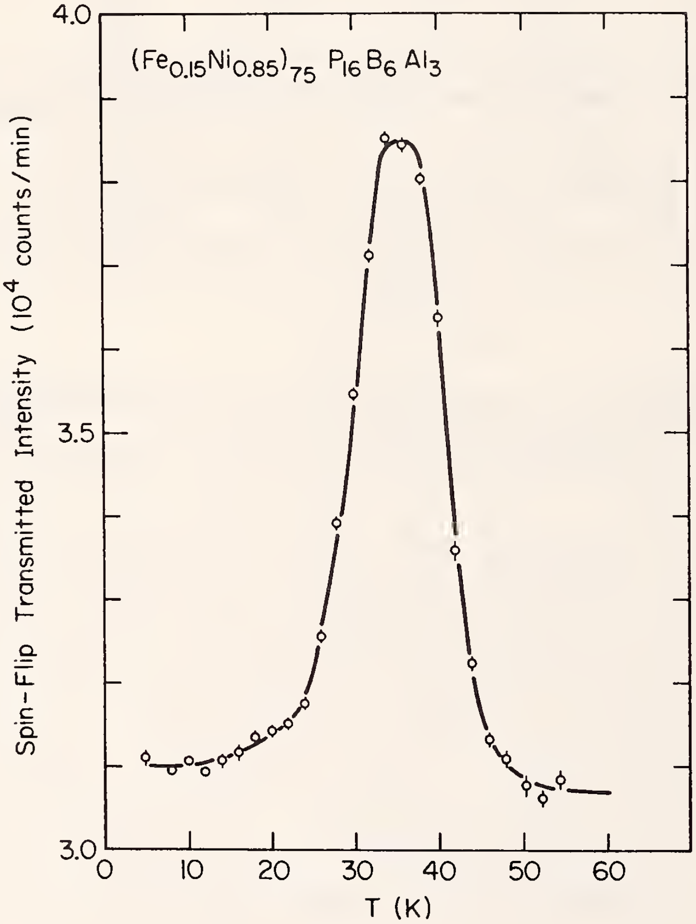

Figure 1. The observed intensity for neutrons which have undergone a spin rotation of π. The increase in intensity an cooling signals the onset of ferromagnetism, while the decrease at low temperature indicates the destruction of the ferromagnetic state as the spin glass state develops.

temperatures as the spin glass state develops.[4] These measurements were taken in an applied field of ~2 Oe. One advantage of this technique is that intensity is no problem since we are observing the transmitted intensity of the primary beam, and hence measurements can be made on very small samples. The data in figure 1 were taken on a sample weighing ~4 mg. Another advantage of the method is that the measurements can be carried out with the identical sample and under the identical experimental conditions as conventional neutron measurements, which facilitates comparison of the measured properties. We have found this quite useful in the case of some of our results on magnetic superconductors[5] since this is the only neutron technique where the superconducting phase transition can be observed directly.

---

1. J. W. Lynn, Q. Li, and R. W. Erwin, Bull. Am. Phys. Soc. 32, 922 (1987).
2. N. Stüsser, M. Th. Rekveldt, and T. Spruijt, Phys. Rev. B31, 5905 (1985); ibid 31 6423 (1986).
3. See, for example, M. A. Manheimer, S. M. Bhagat and H. S. Chen, J. Magn. Magn. Mat. 38, 147 (1983).
4. R. W. Erwin, J. W. Lynn, and A. Magerl, J. Magn. Magn. Mat. 54, 101 (1986).
5. J. W. Lynn, J. A. Gotaas, R. N. Shelton, H. E. Horng and C. J. Glinka, Phys. Rev. B31, 5756 (1985).

MAGNETIC FIELD-INDUCED STATE IN $Y_{1-x}Gd_x$

J. A. Gotaas and J. J. Rhyne

and

L. E. Wenger
(Wayne State University, Detroit, MI)

and

J. A. Mydosh
(Kammerlingh Onnes Lab, Rijksuniversiteit Leiden, The Netherlands)

We have previously studied the magnetic phase transition in single crystals of $Y_{1-x}Gd_x$ in both zero-field and in magnetic fields up to 7 Tesla.[1,2] A new sample ($x = 0.044$) has been used to achieve a more favorable scattering geometry which permitted measurements of the basal plane reflection (100) and its magnetic satellite, as well as the (002) and its satellite. The modulated magnetic state produces reflections which are satellites of the allowed nuclear reflections with indices ($h\ k\ \ell\pm\delta$), where the modulation wave vector $\delta = 0.28c^*$. The intensity of the observed peaks depends on the structure factor of the nuclear reflection, the absorption, the magnetic form factor, and a spin structure factor which depends on the relative orientation of the spin directions and scattering vector.[3] If all other factors affecting the intensity are removed, this spin orientation factor will then lead to the satellite of the (100) being only half as intense as the satellite of the (002) in a helical phase.

Figure 1 displays data taken on this sample in a field applied along a basal plane direction perpendicular to the scattering vector. The zero-field peak intensities have been normalized to reflect the intensity ratio of 0.51 between the (100$^+$) and (002$^-$) satellites, which facilitates the direct comparison of their field dependence. The field dependence of the (002$^-$) satellite intensity is as observed earlier, with a sharp decrease in intensity at H_c.[2] In contrast, the (100$^+$) satellite shows no such drop, but rather a uniform gradual decrease with field. Note that the (002$^-$) satellite contains contributions from the full basal plane magnetic moment, but the (100$^+$) satellite is only sensitive to the moment components which are transverse to Q, or in this case parallel to the applied magnetic field. These data therefore suggest that the sudden drop in intensity at H_c results from a disordering of the helical moment components perpendicular to the applied field.

The different behavior of the two reflections under the applied field can be understood more precisely with the help of the spin density wave concept. In addition to the possibility of helical spin density waves (HSDW), there can also

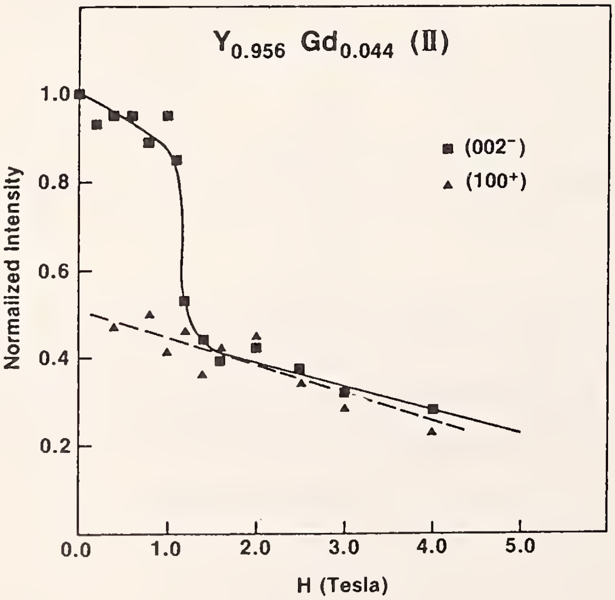

Figure 1. Normalized peak intensities of (002$^-$) [■] and (100$^+$) [▲] satellites as function of applied field at 4.4 K.

exist linear spin density waves (LSDW).[4] In zero field, the linear state is energetically unfavorable in the absence of basal plane anisotropy. However, the application of the magnetic field can serve to destabilize the helical state in favor of the linear state, where moments lying in the basal plane have their magnitude modulated along the c axis. This is not a reduction of the actual physical 4f spin of the magnetic ions, but only a reduced configurational average at each of the appropriate sites. Thus the LSDW represents a state with disordered transverse components.

Since the average moment per site in the basal plane (and hence perpendicular to Q) is smaller in the LSDW state, the scattered intensity will be reduced at the $(002^{\pm})$ satellites. We can calculate that the average moment in the LSDW state is reduced to $(1/\sqrt{2})$ of the moment in the HSDW state. Since the scattering intensity is proportional to the square of the moment, this leads to a reduction by a factor of two in the peak intensity at the (002^{-}) satellite on conversion of the HSDW to a LSDW, precisely as observed in the measurements.

For the (100^{+}) reflection the LSDW state could have moments either parallel or perpendicular to Q. In the former case, there will be essentially no scattering from the LSDW state at the (100^{+}) satellite position, while in the latter case there will be essentially the same scattering from either a HSDW or a LSDW. The identical intensities observed for the (100^{+}) reflection and the collapsed (002^{-}) peak suggest that the field-induced transition is from the helical state to a linear state transverse to Q and hence parallel to the applied field in this geometry.

The neutron diffraction data presented here demonstrate that the field-induced magnetic transition in these dilute Y(Gd) alloys is a modification of the spin structure from a simple helical spin density wave to a superposition of a linear spin density wave and a ferromagnetic component, with the linear state moments parallel to the applied field but modulated in magnitude along the c axis.

---

[1] J.A. Gotaas, J.J. Rhyne, L.E. Wenger and J.A. Mydosh, J. Magn. and Magn. Mater. 54-57, 93 (1986).

[2] L.E. Wenger, Gary W. Hunter, J.A. Mydosh, J.A. Gotaas and J.J. Rhyne, Phys. Rev. Lett. 56, 1090 (1986).

[3] Stephen W. Lovesey, Theory of Neutron Scattering from Condensed Matter, Vol 2. (Oxford, 1984) Chap. 12.

[4] A.W. Overhauser, Phys. Rev. 128, 1437 (1962).

MAGNETIC PHASE TRANSITION IN $Y_{0.97}DY_{0.03}$

J. A. Gotaas and J. J. Rhyne
and
L. E. Wenger
(Wayne State University, Detroit, MI)
and
J. A. Mydosh
(Kamerlingh Onnes Lab, Rijksuniversteit Leiden, The Netherlands)

As part of a systematic investigation of the magnetic states in dilute alloys of rare earth ions in yttrium, we have carried out neutron diffraction measurements on a single crystal of the dilute alloy $Y_{0.97}Dy_{0.03}$. We have verified that in zero applied magnetic field, the system orders into a modulated state at $T_N = 9K$. In these dilute alloys, the propagation vector lies along the c axis and has magnitude $\delta = 0.28c^*$, with the magnetic moments lying in the basal plane of the hexagonal lattice. Within experimental error, the full free-ion moment is found for the Dy and the temperature dependence is consistent with that of the Brillouin function for $J=15/2$. At T = 6K, a magnetic field applied in the basal plane causes no shift in the value of the modulation wave vector of the magnetic satellite (000^+) and there is no additional broadening of the diffraction peak, similar to the behavior observed in the Y(Gd) system.[1] As shown in figure 1, when the magnetic field is increased, the scattered intensity at 0.28c* drops continuously, with the helical phase being completely suppressed in a field of 3 T. On reducing the field, there is hysteresis in the peak intensity at 0.28c*, with only 79% of the original intensity being recovered at H=0. This residual intensity grows slowly with time, increasing to approximately 82% of the original value over a period of one hour. This behavior differs from that of the Y(Gd) system,[1] which shows no hysteresis and displays a sharp transition between helical and sinusoidal phases. The difference presumably is due to the presence of the crystal field anisotropy in the case of Dy, in contrast to the S-state Gd ion. Further experiments as a function of both field and Dy concentration are planned to clarify this.

---

[1] J. A. Gotaas, J. J. Rhyne, L. E. Wenger and J. A. Mydosh, NBS Technical Note 1231, 33 (1986).

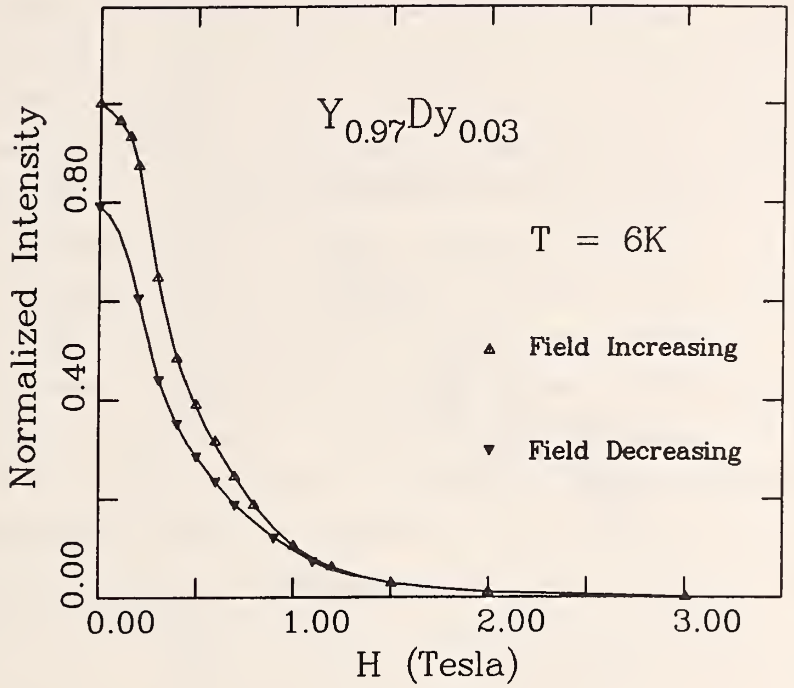

Figure 1. Normalized peak intensity of (000^{+}) magnetic satellite as a function of applied magnetic field, showing smooth suppression of modulated state and hysteresis on reducing field at T = 6K.

ABSOLUTE MEASUREMENT OF THE ORDERED MAGNETIC MOMENT IN HOLMIUM RICH $(Er_{1-x}Ho_x)Rh_4B_4$

Q. Li, J. W. Lynn and J. A. Gotaas
(University of Maryland, College Park, MD)

and

(National Bureau of Standards , Gaithersburg, MD)

$HoRh_4B_4$ is an Ising-like ferromagnet (T_M = 6.5 K) where the ordered magnetic moment is locked along the tetragonal c-axis.[1] A crystal-field model predicts[2] a ground-state doublet with a saturation magnetic moment of 10.0 μ_B. However, from our previous neutron diffraction studies[1] it appeared that the ordered moment was substantially less than the full 10 μ_B value. A similar discrepancy has also been noted for $ErRh_4B_4$. New powder neutron diffraction measurements were performed on $(Er_{1-x}Ho_x)Rh_4B_4$ for concentrations x = 1.0, 0.89, 0.84 and 0.75 in order to investigate the possible origin of these discrepancies.

The usual method to determine the magnetic moment is to place the magnetic intensities on an absolute basis by comparison with the nuclear intensities. However, in the case of $HoRh_4B_4$ the structure factors for the low angle nuclear peaks happen to sum to very small values, so that even small uncertainties in the coherent nuclear scattering amplitudes are greatly amplified in the calculated nuclear structure factor. At larger angles, on the other hand, one has to rely on calculated free-ion values of the magnetic form factor to extract the moment $<\mu^z>$, which may introduce inaccuracies in the determined value. We therefore decided to make a determination of the magnetic moment which was independent of the nuclear scattering intensities of the samples by employing an independent (copper powder) diffraction standard. We have also measured the magnetic form factor in order to determine if the observed reduced value of the magnetic scattering might be attributed to a moment on the rhodium sublattice rather than a reduction of the holmium moment. The data were taken with a combined sample of 25 % (by weight) $HoRh_4B_4$ and 75 % Cu. Use of the mixed sample substantially reduced the error introduced by absorption corrections of Cu and $HoRh_4B_4$ since the absorption factors are the same. Thus within experimental error the necessity of an absorption correction was averted with this method.

The measurements in the ordered state were taken at T = 1.7 K, which was sufficiently low to obtain the full ordered moment. The magnetic component of the intensity can be obtained by subtracting the scattering observed well above the ordering temperature from the low temperature data. We have also made a measurement of the magnetic form factor of $HoRh_4B_4$ by measuring the intensities of eight powder reflections. The results are shown in figure 1. The solid curve is the spherical component of the free-ion calculation, and it is seen to agree quite closely with the measurements. Thus we can conclude that there are no anomalies in the form factor, and there is no obvious Rh contribution to the magnetic scattering amplitudes. The final value of the magnetic moment was

$$<\mu^z> = (8.61 \pm 0.06)\ \mu_B.$$

Our diffraction results for the other concentrations of $(Er_{1-x}Ho_x)Rh_4B_4$ yield the same value for the ordered moment of holmium, within experimental error. This value is significantly reduced from the value of 10 μ_B expected from a single-ion crystal field model, and indicates that a more elaborate calculation is warranted.

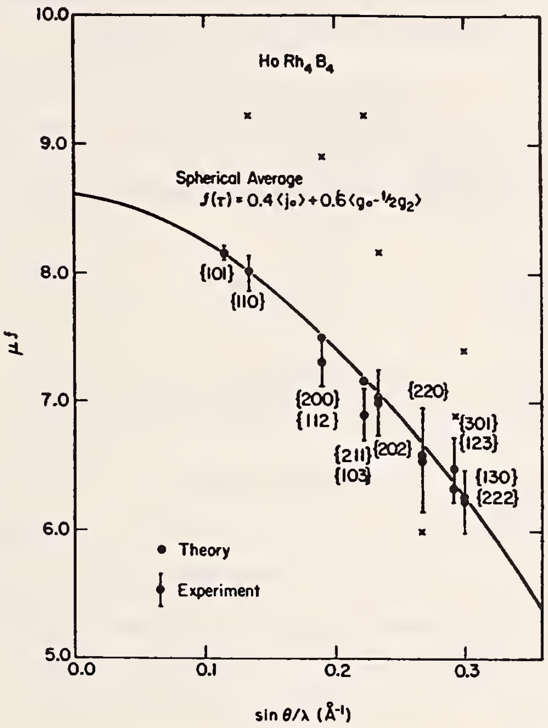

Figure 1. Magnetic form factor for $HoRh_4B_4$. The observations are in good agreement with the calculated free-ion spherical form factor for Ho^{3+} (solid curve). The theory points O include a small aspherical correction for the holmium form factor. The X's show how the form factor would appear assuming a substantial rhodium moment. The rhodium moment is actually determined to be zero within the experimental uncertainty of 0.07 μ_B.

---

1. J. W. Lynn, J. A. Gotaas, R. N. Shelton, H. E. Horng, and C. J. Glinka, Phys. Rev. B<u>31</u>, 5756 (1985). Additional experimental details and discussion can be found here.

2. B. D. Dunlap, L. N. Hall, F. Behroozi, G. W. Crabtree, and D. G. Niarchos, Phys. Rev. B<u>29</u>, 6244 (1984), and references therein; B. D. Dunlap and J. W. Lynn (to be published).

NEUTRON SCATTERING STUDY OF THE SPIN DYNAMICS OF AMORPHOUS $Fe_{78}B_{13}Si_9$ ALLOY

S. C. Yu, J. W. Lynn
(University of Maryland, College Park, MD)
and
(National Bureau of Standards, Gaithersburg, MD)

and

J. J. Rhyne

and

G. E. Fish
(Allied Signal Inc., Morristown, NJ)

In order to obtain a better understanding of the magnetic properties of amorphous alloys at high temperature,[1] we have started a neutron study of the spin dynamics of the high transition temperature amorphous ferromagnetic alloy $Fe_{78}B_{13}Si_9$ (Metglas 2605S2).[2] The amorphous nature of the system required that measurements be taken near the forward (000) beam position. A fixed incident energy of 13.5 meV was used and a pyrolytic graphite (PG) filter was placed after the PG (002) monochromator to suppress high order wavelength contaminations. Nominal soller slit horizontal collimators of 10′-10′-10′-10′ were used to produced a FWHM energy resolution of 0.35 meV at the elastic position. Well defined spin waves were observed over the entire accessible wave vector range of $0.06\ \text{Å}^{-1} \leq q \leq 0.12\ \text{Å}^{-1}$, for temperatures between 473 K (0.67 T_c) and 705 K (0.99 T_c). At lower temperatures the spin wave energies were outside the range of accessible (q,E) due to neutron kinetic restrictions which apply to structurally amorphous materials.

In analyzing the data, the spin-wave energies and linewidths were obtained by convoluting a theoretical cross-section with the instrumental resolution and least-squares fitting to the observed spectra, after subtraction of the background scattering. The spectral weight function used in the convolution was a double Lorentzian.[3]

The spin wave dispersion relation exhibits the conventional quadratic relationship $E = D(T)\ q^2 + \Delta$ typical of an isotropic ferromagnet, where the small energy gap Δ of 0.05 meV is attributed primarily to the dipole-dipole interaction. The spin-wave stiffness constant D obtained from such data is shown in figure 1 as a function of temperature. An estimate of the T = 0 value of $D \approx 156$ meV-Å^2 was obtained from a plot of D(T) versus T extrapolated to low temperatures, while the Curie temperature of 710 K was obtained from the extrapolation of D(T) to zero at

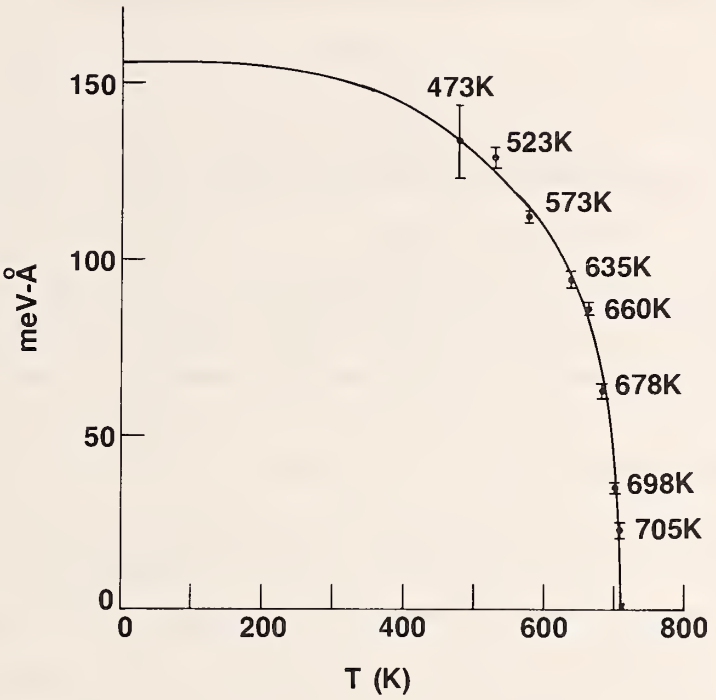

Figure 1. Temperature dependence of the spin-wave stiffness constant.

high temperatures. At room temperature D has attained 93 % of the saturated low-temperature value. Thus we do not expect much change in the dynamic susceptibility in going from room temperature to low temperatures; the primary effect for the observed scattering will be due to the change in the thermal population of the magnetic excitations of the system. The temperature range over which the spin waves were accessible was too high for the spin wave renormalization to be proportional to $(T/T_c)^{5/2}$. Spin wave linewidth data for $T/T_c \approx 0.95$ showed the q^4 wave-vector dependence expected for magnon-magnon interactions.

The overall results indicate that conventional hydrodynamic spin wave theory provides an appropriate description of the long wavelength magnetic excitations in amorphous $Fe_{78}B_{13}Si_9$, with a value of $D/T_c \approx 0.22$ meV-Å^2/K consistent with that found for other amorphous transition metal ferromagnets.[1]

---

1. J. W. Lynn and J. J. Rhyne, in Spin Waves and Magnetic Excitations, ed. by A. S. Borovik Romanov and S. K. Sinha (North Holland, 1988), Chap. 15.

2. A. K. Bhatnagar and N. Ravi, Phys. Rev. B 28(1) 359 (1983).

3. R. W. Erwin, J. W. Lynn, J. J. Rhyne and H. S. Chen, J. Appl. Phys. 57, 3473 (1985).

MAGNETIC STRUCTURE OF CUBIC $Tb_{0.3}Y_{0.7}Ag$

J. A. Gotaas

and

M. Said and J. S. Kouvel
(University of Illinois, Chicago, IL)

and

T. O. Brun
(Argonne National Laboratory, Argonne, IL)

The cubic compound TbAg has an ordered antiferromagnetic state below T_N = 106K, with the (ππ0) structure.[1] The (ππ0) structure is made up of alternating ferromagnetic (110) planes which are antiferromagnetically aligned, so that the basic magnetic unit cell is tetragonal with the basal plane dimensions doubled with respect to the nuclear cell.[2] In the case of TbAg, the moments have been shown to lie along the c-axis.[1] On diluting the magnetic Tb ions by non-magnetic Y ions, the transition temperature decreases linearly with decreasing Tb concentration. For concentrations below 50% Tb, magnetization measurements begin to show typical spin glass properties, such as a time dependent thermoremanence, which suggests the coexistence of antiferromagnetism with a spin-glass state. We have used neutron diffraction to investigate the nature of this mixed phase in the compound $Tb_{0.3}Y_{0.7}Ag$. For this composition, T_N = 36K as determined by low-field magnetization measurements. We have taken complete diffraction patterns at 60K and 4.5K. At 60K, the pattern arises from the crystallographic structure and is of the CsCl-type, with a lattice parameter of 3.612Å. At 4.5K, we have additional peaks appearing of two types.

The first type appears at the expected positions for the (ππ0) structure, but is a broadened peak instead of being resolution limited. If we interpret the broadening as due to a finite correlation range of the (ππ0) structure, it yields a value of approximately 20Å, or roughly 3 times the expanded magnetic unit cell. The second type of peak is much narrower, and corresponds to satellites of the (ππ0) structure. Detailed modeling remains to be done, but the data is qualitatively consistent with the type of structure observed in HoAg and TmAg, which is a modulated structure based upon the (ππ0) antiferromagnetic structure.[3] It can be described as a structure made up of two sublattices, each of which is modulated in magnitude along the propagation vector in the lattice. The modulation wave vector in these compounds is along a cube edge (100)-type direction. If we assume the same type of modulation here, the modulation wavelength would be approximately 60Å, or on the order of nine magnetic unit cells, although the structure is likely incommensurate.

Preliminary temperature dependent measurements have been made on these peaks, showing a similar temperature dependence for both types, with an ordering temperature apparently between 37 and 40K, with some intensity persisting to above 45K. The apparent discrepancy in ordering temperature may be partially due to differences in thermometry. Further work is planned, including more detailed temperature dependences, higher-resolution measurements to study the peak structure more carefully, field-dependent measurements and the investigation of other compositions.

---

1. J. W. Cable, W. C. Koehler and E. O. Wollan, Phys. Rev. 136, A240 (1964).
2. H. A. Gersch and W. C. Koehler, Phys. Chem Solids 5, 180 (1958).
3. P. Morin, D. Schmitt and C. Vettier, J. Phys. (Paris) 46, 9 (1985).

RECENT PROGRESS ON BT-2 TRIPLE-AXIS POLARIZED SPECTROMETER

W-H. Li and J. W. Lynn
(University of Maryland, College Park, MD)
and
(National Bureau of Standards, Gaithersburg, MD)

BT-2 is now operational as a variable incident energy three-axis polarized neutron spectrometer. The monochromator is composed of five Heusler alloy (Cu_2MnAl) crystals, each of which measures 2.955 x 0.675 x 0.15 inch^3, and are mounted in reflection geometry on a vertically curved[1] aluminum frame between two Nd-Fe-B permanent magnets. The use of Nd-Fe-B magnets instead of $SmCo_5$ reduces the radiation hazard of the magnet assembly. The analyzer is a flat Heusler alloy assembly in reflection geometry. A pyrolytic graphite filter, or cold beryllium filter, can be automatically placed in the reactor beam for filtering purposes. Guide fields of ~ 130 Oe are built into the beam paths before and after the sample. Flat-coil spin flippers can be used to rotate the polarization before and after scattering as dictated by experimental requirement. New non-magnetic Söller slit collimators have been constructed, with a minimum divergence of 5′ (FWHM). Be-Cu blades coated with Cd are used, and can be removed to coarsen the divergence as required. The collimators were found to function within specifications at 14.8 meV.

Before the shut down of the reactor for installation of the cold source, we have carried out the following experiments to test the operation of the spectrometer.[1] Spin-flip and non-spin-flip incoherent scattering cross sections from vanadium were measured,[2] spin rotation transmition measurements were conducted on U_2NiSn and Zr_5Sb_3Fe to detect ferromagnetic phase transitions. Clear phase transitions starting at temperature around 50 K and 270 C for quasi-crystal U_2NiSn and ferromagnetic Zr_5Sb_3Fe, respectively, were observed.[3] Preliminary inelastic scattering of high-Tc superconductor $YBa_2Cu_3O_7$ and amorphous metglas $Fe_{40}Ni_{40}P_{14}B_6$ were also performed. The results show that BT-2 is now capable of carry out inelastic scattering.

One of the difficulties with using Heusler alloy crystals for polarized beam research is the very high reflection of these crystals for $\lambda/2$ sections. We therefore plan to replace these crystals with pyrolytic graphite monochromator and analyzer crystals, and to obtain the polarization by use of multilayer devices.[2,3] We expect to have this upgrade completed within the next year.

---

1. A. Freund, R. Pynn, W. G. Stirling, and C. M. E. Zeyen, Physica, 120B, 86 (1983).

2. J. W. Lynn, J. K. Kjems, L. Passell, A. M. Saxena, and B. P. Schoenborn, J. Appl. Cryst., 9, 454 (1976).

3. C. F. Majkrzak and L. Passell, Acta Cryst., A41, 41 (1985).

X-RAY DIFFRACTION STUDIES OF AMORPHOUS $Ni_{71.12}Cr_{19.00}Si_{7.30}B_{1.50}C_{0.08}$ ALLOY

S. C. Yu and J. W. Lynn
(University of Maryland, College Park, MD)
and
(National Bureau of Standards, Gaithersburg, MD)

The low cost metallic glass brazing foils provide strength and ductility which are comparable to that obtained using gold-nickel foils.[1] The flexibility of the ribbon is related to its atomic structure; it is amorphous, or glassy, rather than crystalline. We have begun an investigation of the Ni rich brazing filler metal system by probing the atomic structure of the Ni-Cr based amorphous alloy with a conventional reflection type x-ray diffraction technique.

The sample used for this study is a metallic glass alloy with weight percent composition of $Ni_{72.12}Cr_{19.00}Si_{7.30}B_{1.50}C_{0.08}$, a commercial product labeled MBF-50A by Allied Signal. The scattered intensity was measured in step-scan mode at intervals of 0.05° over an angle range $2\theta = 12° \rightarrow 160°$. The Mo K_α ($\lambda = 0.7107$ Å) radiation was filtered, and the wide-angle vertical scan x-ray diffractometer was equipped with a pyrolytic graphite monochromator. The observed intensity distributions, $I(2\theta)$, were converted to scattering intensity distribution, $I(K)$, as a function of scattering wave vector, $K = 4\pi \sin \theta/\lambda$, over the range from 1.85 $Å^{-1}$ to 17.41 $Å^{-1}$. All data were collected at room temperature.

The basic experimental and analytical techniques used in this study were taken from Cargill.[2] We obtained the total interference function (or structure factor) $I(K)$ from the resulting normalized coherent scattering intensity. From this total interference function, the atomic distribution function in real space, $W(r)$, was obtained by Fourier inversion.[3]

The coordination number (CN) is estimated from the area under the first peak of the radial distribution function located between $r = 0$ and the first minimum r_{min} in the radial distribution function (RDF) which is defined by $4\pi r^2 \rho(r)$:

$$CN = \int_0^{r_{min}} 4\pi r^2 \rho dr.$$

The density of this metallic brazing foil sample, which was required to obtain the radial distribution function, was taken to be 7.86 g/cm^3.[4] The atomic percentage of the sample (i.e., $Ni_{61.45}Cr_{18.28}Si_{13.00}B_{6.94}C_{0.33}$) is used for the analysis instead of the weight percentage.

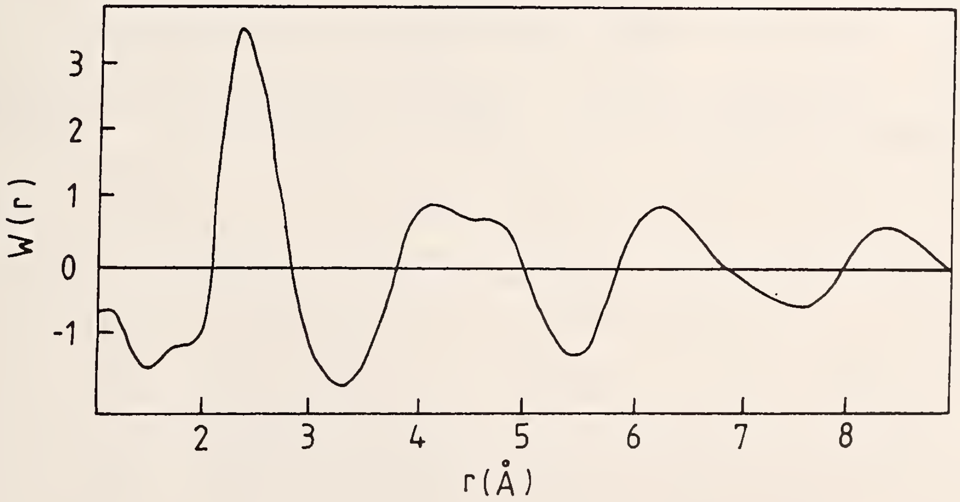

Figure 1. Atomic distribution function of the Ni-Cr based amorphous alloy.

The atomic distribution function W(r) of the amorphous alloy is shown in figure 1. In this distribution, a shoulder is observed in the peak at r = 4.66 Å, which is often the case in amorphous alloys.[5] The spurious ripples present at r values less than about 2 Å are due to the relatively small remaining errors in the determination of the normalization constant. Such errors, however, do not affect the peak positions of the distribution function. The first peak occurs at r = 2.47 Å which is followed by a split double peak at 4.18 Å and 4.66 Å and other smaller peaks at larger r. For the present alloy, the nearest neighbor distance and the coordination number were found to be 2.47 Å and 12.23, respectively.

If we assume that each of the atoms in the sample is packed with 12 nearest neighbors (pseudo-dodecahedral-type structure), the nearest neighbor distance should be the statistical average of the 12 contact distances, which is the sum of the neighboring atomic radii as given by Teatum et.al.[6] The differences between the nearest neighbor distance obtained from the first peak position of W(r) and the calculated nearest neighbor distance (2.51 Å) from the atomic radii of each element for CN = 12, using the above model, are only 1.6 %.

---

1. D. Bose, A. Datta and N. DeCristofaro, Welding Journal <u>60</u>(<u>10</u>) (1981) 29.

2. G. S. Cargill III, <u>Solid State Physics</u>, vol. <u>30</u>, eds. F. Seitz, D. Turnbull and H. Ehrenreich (Academic Press, N.Y., 1975) p. 227.

3. C. N. J. Wagner, J. Non-Cryst. Solids <u>31</u> (1978) 1-40.

4. METGLAS data sheets, Allied Signal Inc.

5. S. Steeb and P. Lamparter, J. Non-Cryst. Solids <u>61</u> & <u>62</u> (1984) 237.

6. E. Teatum, K. Gschneidner, and J. Waber, 1960, LA-2345, U.S. Department of Commerce, Washington, D. C.

TWO-DIMENSIONAL ORDERING IN $ErBa_2Cu_3O_7$

J. W. Lynn, W-H. Li, and Q. Li
(University of Maryland, College Park, MD)
and
(National Bureau of Standards, Gaithersburg, MD)

and

H. C. Ku, H. D. Yang, and R. N. Shelton
(Iowa State University, Ames, IA)

The discovery[1] of superconductivity in $YBa_2Cu_3O_7$ has generated unprecedented excitement in the physics community both because of the possible new fundamental phenomena this class of systems represents as well as the enormous potential for applications. The substitution of the heavy rare-earth elements for yttrium has little if any detrimental effect on the superconducting transition temperature,[2,3] and hence these are ideal materials to investigate the interplay between magnetism and superconductivity.[4] We find that the Er moments exhibit a two-dimensional ordering (or long range correlations) which is driven by the dipolar coupling of the moments. The configuration of spins is such that chains form which are aligned ferromagnetically, but with adjacent chains antiparallel.

The diffraction data were taken with a wavelength of 2.3509 Å and a pyrolytic graphite monochromator and filter, in a pumped He-3 cryostat. Powder x-ray diffraction patterns were indexed on an orthorhombic unit cell (Pmmm), with room temperature lattice parameters of (3.845, 3.884, 11.53) Å. A minor amount (< 5 %) of a secondary ternary oxide phase was barely detectable in the x-ray pattern, although it was easily detected with neutrons when the impurity ordered magnetically ($T_M \sim 12$ K). Magnetization measurements showed an onset temperature for superconductivity of 95 K, with a Meissner exclusion of 75 % at low temperatures.

To isolate the magnetic scattering in $ErBa_2Cu_3O_7$ we have employed the subtraction technique.[5] Well above any magnetic ordering temperature the magnetic moments will be completely uncorrelated, and the diffraction pattern will consist of coherent nuclear Bragg peaks and "background". At low temperatures, on the other hand, magnetic peaks will develop in the scattering due to magnetic order or correlations, which will appear in addition to the nuclear Bragg peaks. A subtraction of the high temperature data from the data at low T then isolates the magnetic response. Such a subtraction is shown in the top portion of figure 1. We see a rapid rise in the scattering, with a maximum at an angle of 17.8°, and then a long tail of scattering which extends towards larger angles. The position of the peak coincides with a {1/2,0,0} type reflection, so that we can determine immediately that the scattering is antiferromagnetic in nature. Note also that the net scattering at the lowest angles is negative, which simply reflects the sum rule on the magnetic response; in some regions of q the magnetic scattering must decrease in order to produce peaks elsewhere. The pronounced asymmetry of the observed peak is a classic profile of a two-dimensionally ordered system.[6] To understand the origin of this behavior we note that there is only one Er ion per unit cell, so that the Er sublattice is simple orthorhombic. The lattice parameters then show that the separation of the Er ions along the a and b lattice directions is nearly the same, while the distance along the c axis is about three times longer. Hence the dipolar interactions will be very much smaller along this direction, and two dimensional correlations seems likely. If the spin structure is collinear, then there are only two possible spin configurations. The first is where the nearest neighbors are antiparallel, while the next nearest neighbors are parallel as shown in the inset to the figure. The unit cell will be doubled along one direction, and this will give rise to peaks like (1/2,0), (1/2,1), etc., and is consistent with the data in figure 1. Note that the spins form chains along the b axis which are parallel, while adjacent chains along the a axis are antiparallel. The other possible spin configuration is obtained by reversing all the next nearest neighbors along the b direction, so that the unit cell doubles along both directions. The lowest order peak in this model is the (1/2,1/2) peak, which is inconsistent with the data.

To quantitatively fit these data we have employed a model which assumes that the scattering originates from a Bragg line. We remark that since the orthorhombic distortion of this system is small and the scattering profile from a 2-d powder is quite broad, we cannot unambiguously determine if the peak is a (1/2,0) or (0,1/2) type reflection. The solid curve in the figure is a least squares fit, assuming there is no intrinsic width to the Bragg line, and no correlations along the line. The fit is excellent, and hence we conclude that there are strong correlations in the a-b plane, while the correlation length along the c-axis is small. Of course for a powder it is difficult to determine whether the system is truly long range ordered (viz. 2d Ising model), or whether it is simply highly correlated. Additional measurements at lower temperatures would be useful.

The bottom portion of the figure shows the temperature dependence of the intensity at the peak position. We see that the scattering is still increasing rapidly down to 0.3 K, which is the lowest temperature we could achieve. Comparing the magnetic intensity with the (001) nuclear intensity establishes that the ordered magnetic moment $<\mu^z>$ is already 2.9 μ_B. We would expect the intensity to continue

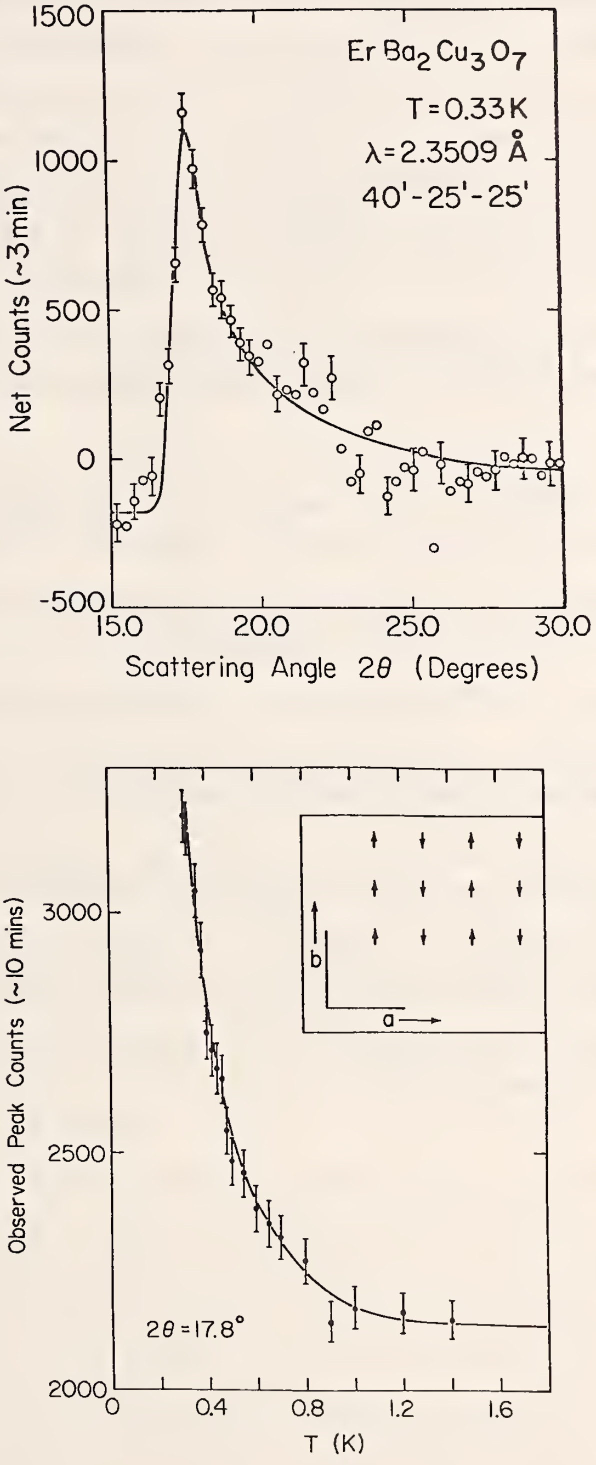

Figure 1. a) Magnetic intensity observed at low temperatures. The solid curve is a least squares fit of the data to the two-dimensional model as described in the text. The data were taken with an simple collimation (FWHM) of 40', and 25' before and after the sample. b) Temperature dependence of the peak intensity. The solid curve is a guide to the eye. The inset shows the magnetic configuration of spins.

to increase until the full ground state moment is obtained, and then become independent of temperature. At sufficiently low temperatures the peak intensity would presumably start to increase again as 3-d order eventually sets in, with the data in figure 1 narrowing into a set of resolution limited Bragg peaks. The only related system which has been investigated so far is La_2CuO_4, where the Cu moments exhibit 3-d order ($T_N \approx 220$ K) with a similar doubling of the unit cell.[7] In the present system we would also expect a 3-d type of order if the Cu ions aligned since nearest neighbor spacings are comparable in all three directions. However, we have no evidence in the present experiments that the Cu ions order.

---

1. M. K. Wu, J. R. Ashburn, C. J. Torng, P. H. Hor, R. L. Meng, L. Gao, Z. J. Huang, Y. Q. Wang and C. W. Chu, Phys. Rev. Lett. 58, 908 (1987).
2. P. H. Hor, R. L. Meng, Y. Q. Wang, L. Gao, Z. J. Huang, J. Bechtold, K. Forster, and C. W. Chu, Phys. Rev. Lett. 58, 1891 (1987).
3. Z. Fisk, J. D. Thompson, E. Zirngiebl, J. L. Smith and S-W. Cheong (preprint).
4. For a review see Topics in Current Physics, edited by O. Fischer and M. B. Maple (Springer-Verlag, New York, 1983), Vols. 32 and 34.
5. Additional details can be found in J. W. Lynn, J. A. Gotaas, R. N. Shelton, H. E. Horng and C. J. Glinka, Phys. Rev. B31, 5756 (1985).
6. See, for example, J. K. Kjems, L. Passell, H. Taub, J. G. Dash, and A. D. Novaco, Phys. Rev. B13, 1446 (1976), and references therein.
7. D. Vaknin, S. K. Sinha, D. E. Moncton, D. C. Johnston, J. Newsam, C. R. Safinya, and H. E. King, Jr. (preprint).

SUPPRESSION OF SUPERCONDUCTIVITY BY ANTIFERROMAGNETISM IN $Tm_2Fe_3Si_5$

J. A. Gotaas

and

J. W. Lynn
(University of Maryland, College Park, MD)
and
(National Bureau of Standards, Gaithersburg, MD)

and

R. N. Shelton and P. Klavins
(Iowa State University, Ames, IA)

$Tm_2Fe_3Si_5$ is of great interest because it orders antiferromagnetically at ambient pressure with T_N = 1.1 K, while the application of pressure drives the system superconducting.[1,2] The most interesting feature is that the superconducting phase is suppressed once the antiferromagnetic ordering takes place. If the ordered magnetic state is purely antiferromagnetic, then this represents a unique experimental observation of the destruction of superconductivity by antiferromagnetism in rare earth ternary compounds. We have previously examined $Tm_2Fe_3Si_5$ via neutron diffraction under applied pressures up to 5.8 kbar and temperatures down to 0.3 K.[3,4] We have now extended this to a pressure of 8.2 kbar, at which point the superconducting phase transition occurs at T_c = 3 K.

The crystallographic structure of $Tm_2Fe_3Si_5$ is primitive tetragonal with space group P4/mnc,[5] and remains unchanged under application of pressures up to 8 kbar, as we have determined by high resolution neutron diffraction patterns taken on BT-1 at room temperature and 78 K. The magnetic pattern at 8.2 kbar is also the same as that found at ambient pressure.

It is essential to determine if there is any ferromagnetic component (at any pressure) which might be responsible for the destruction of the superconductivity. As a result of the multi-sublattice magnetic structure there is magnetic intensity at virtually all the nuclear peak positions, which complicates the detection of a possible ferromagnetic component. Two peaks which have no antiferromagnetic contribution ({200} and {002}) were examined carefully and found to have no ferromagnetic contribution, but the experimental precision was only $1.5\mu_B$. To improve the precision of this important result, an additional experiment was carried out with polarized neutrons at BT-2. If a polarized neutron beam is transmitted through a sample which orders ferromagnetically, the local magnetization will tend to rotate the polarization of the beam; the polarized beam transmission measurement thus serves as a sensitive indicator of any ferromagnetic ordering in a system.[6] No change was observed in the beam polarization as a function of temperature in $Tm_2Fe_3Si_5$ at 8.2 kbar and we estimate from these data that any ferromagnetic component must be $\lesssim 0.1\mu_B$. A careful search for ferromagnetic fluctuations or possible oscillatory magnetic states was made around the forward beam and at the nuclear peaks in the vicinity of the transition, but no evidence was found for such additional effects which might accompany the destruction of the superconducting phase.

The theories which have been developed for antiferromagnetic superconductors generally predict that the magnetic and superconducting states will coexist, with some modifications of the superconducting properties (particularly H_{c2}) in the magnetically ordered state.[7,8] Machida et al.[8] do explicitly consider a choice of parameters in which the superconducting state is destroyed by the antiferromagnetic transition, but then the superconducting state would be expected to reemerge at lower temperatures. We have examined $Tm_2Fe_3Si_5$ at 8.2 kbar via ac susceptibility measurements down to 40 mK, and find no evidence for such an additional transition.

Our neutron diffraction measurements show that there is no ferromagnetic component in the ordered state, and no change in the nature of the antiferromagnetic ordering under increased pressure. This is the first direct experimental observation of the quenching of superconductivity by purely antiferromagnetic order, and should place strict constraints on the various theories which have been applied to antiferromagnetic superconductors.

---

1. C. B. Vining and R. N. Shelton, Phys. Rev. B28, 2732 (1983).
2. C. B. Vining and R. N. Shelton, Solid State Commun. 54, 53 (1985).
3. J. W. Lynn, J. A. Gotaas and R. N. Shelton, NBS Technical Note 1217, 58 (1985).
4. J. A. Gotaas, J. W. Lynn and R. N. Shelton, NBS Technical Note 1231, 30 (1986).
5. A. R. Moodenbaugh, D. E. Cox and C. B. Vining, Phys. Rev. B32, 3103 (1985).
6. J. W. Lynn, Q. Li and R. W. Erwin, Bull. Am. Phys. Soc. 32, 922 (1987).
7. A general review of theory is given by P. Fulde and J. Keller, in Topics in Current Physics, edited by Ø. Fischer and M. B. Maple (Springer-Verlag, New York, 1983), Vol 34, Chapter 9.
8. Kazushige Machida, Kazuo Nokura and Takeo Matsubara, Phys. Rev. B22, 2307 (1980).

CRYSTAL STRUCTURE OF THE HIGH-TEMPERATURE SUPERCONDUCTOR $La_{1.85}Sr_{0.15}CuO_4$ ABOVE AND BELOW T_c

A. Santoro

and

R. J. Cava, D. W. Johnson, Jr., and W. W. Rhodes
(AT&T Bell Laboratories, Murray Hill, NJ)

This material has been shown[1] to support bulk superconductivity at temperatures on the order of 40 K. They have also been shown to undergo a second-order structural phase transition from tetragonal to orthorhombic symmetry on cooling. This transition occurs at approximately 200 K for x = 0.15. The crystal structure of $La_{1.85}Sr_{0.15}CuO_4$ has been determined at 300, 60, and 10 K by neutron-diffraction powder profile analysis.

The ambient temperature crystal structure has tetragonal symmetry, space group I4/mmm, and is of the undistorted K_2NiF_4 type whereas the crystal structure at 60 and 10 K has orthorhombic symmetry.

The orthorhombic distortion causes a doubling in the volume of the crystallographic unit cell, with the relation between the orthorhombic (O) and tetragonal (T) cells given by $(a,b,c)_0 = (1,1,0/-1,1,0/0,0,1)\ (a,b,c)_T$.

The major change in the structure in the tetragonal to orthorhombic phase transition involves the buckling of the copper-oxygen bipyramidal planes present in both phases. The crystal structure of the orthorhombic phase is not significantly different above and below T_c. Whilst the copper-oxygen coordination polyhedron changes shape in a subtle manner at the tetragonal-to-orthorhombic phase transition, it is unchanged at T_c.

---

1. R. J. Cava, R. B. Van Dover, B. Batlogg, and E. A. Rietman, Phys. Rev. Lett. 58, 408 (1987).

THE STRUCTURE AND PROPERTIES OF $Ba_2YCu_3O_6$

A. Santoro
and
S. Miraglia
(Laboratoire de Cristallographie, CNRS, Grenoble, France)
and
F. Beech
(Imperial College, University of London, UK)
and
S. A. Sunshine, D. W. Murphy, L. F. Schneemeyer, and J. V. Waszczak
(AT&T Bell Laboratories, Murray Hill, NJ)

Recently, there have been several reports of variability in the oxygen stoichiometry for the material $Ba_2YCu_3O_x$, with superconductivity being maximized near x = 7. Elucidation of the nature of the oxygen nonstoichiometry is crucial to a detailed understanding of the electronic properties, including superconductivity. Gallagher, et al.[1] showed that the basic perovskite framework of cations is maintained for $7.0 \geq x \geq 6.0$. A reversible transformation was observed for $x \approx 6.5$ from the orthorhombic symmetry Pmmm observed for values of x close to 7.0 to the tetragonal symmetry and space group P4/mmm.

The structure of $Ba_2YCu_3O_6$ has been determined by neutron diffraction powder profile analysis. The cell is tetragonal P4/mmm with a = 3.8570(1)Å and c = 11.8194(3)Å. The cations are in a perovskite type arrangement, with Ba and Y ordered on the A site to give a cell tripled along c. The oxygens occupy only 2/3 of the perovskite anion sites and are ordered such that 1/3 of the Cu is two-fold coordinated and 2/3 is five-fold coordinated. This configuration can be derived from that of the superconductor $Ba_2YCu_3O_7$ by removing the oxygen atoms along the b axis at the (0,1/2,0) position.

This model is consistent with the results of Beech et al.[2] who found that oxygen vacancies in $Ba_2YCu_3O_{6.8}$ occur only in the O(4) sites i.e., in the chains extending along the b-axis of the orthorhombic cell.

A pressed pellet of the material exhibited semi-conducting behavior with a band gap of 0.21 eV from 125 - 300 K. Magnetic measurements suggest that the compound can be described as $Ba_2YCu^{1+}Cu_2^{2+}O_6$.

---

[1] P. K. Gallagher, H. M. O'Bryan, S. A. Sunshine, and D. W. Murphy, MRB <u>22</u> 995 (1987).

[2] F. Beech, S. Miraglia, A. Santoro, and R. S. Roth, Phys. Rev. <u>B</u> 8778 (1987).

SYNTHESIS AND STRUCTURE REFINEMENT IN THE NON-STOICHIOMETRIC SOLID SOLUTIONS $Ba_2Re_4[Ba_xRe_{2/3 - 2/3x}]Ti_9O_{27}$ (RE = Nd, Sm)

F. Beech
(Imperial College, University of London, London, UK)

and

A. Santoro and R. S. Roth

and

P. Davis
(University of Pennsylvania, PA)

and

J. L. Soubeyroux
(ILL, Grenoble, France)

and

M. Zocchi
(University of Milan, Milan, Italy)

The multiphase composition at $BaO:Sm_2O_3:5TiO_2$ is important since it finds application in microwave filter devices due to its high dielectric constant, very low dielectric loss and zero temperature coefficient of the dielectric constant. The aim of this project is to isolate the active single phase material and investigate its structure and inherent electrical properties. The Neodynium analogues are somewhat lossy compared to the Samarium system however they are more amenable to neutron investigation since Sm has a high neutron absorbance.

A small "single" crystal was obtained from a partially melted specimen of $10BaO:15.5Nd_2O_3:74.5TiO_2$ which was investigated by x-ray techniques. The structure analysis suggested a formulation for the single phase material of $Ba_2Nd_4[Ba_xNd_{2/3-2/3x}]Ti_xO_{27}$ with $x \approx 0$. Solid state synthesis of compositions containing this formula show that a single phase solid solution exists with x varying from 1.0 to 0 and the composition in equilibrium with TiO_2 contains x slightly greater than 0.25. This composition with a small amount of Rutile (TiO_2) and $Nd_4Ti_9O_{24}$ will always be present in a solid state preparation of the ideal composition $BaO:Nd_2O_3:5TiO_2$.

It was discovered in the course of this investigation that conventional ceramic techniques were applicable only to the synthesis of small (<1 gm) batches of the single phase material. Due to the low diffusion lengths in this system very high temperature (>1500° C) processing is required, unfortunately any inevitable inhomogeneity in the firing mixture results in the low temperature formation of $Nd_4Ti_9O_{24}$ which melts at 1350° C.

In order to circumnavigate this problem the molecular level mixing offered by Sol-Gel techniques has been utilized. Synthetic routes to the single phase materials have been devised and the $x = 0,1$ end members of the Nd system and the $x = 0$ composition in the Sm system have been isolated. Work is in progress on the $x = 1$ Sm composition.

Powder neutron diffraction data has been taken on BT1 for both the Nd materials. Analysis of the data using the Rietveld technique for the $x = 0$ material has lead to a structure based on corner shared groups of perovskite-like molecules of $[Nd_4Ti_9O_{27}]^{6-}$ containing three kinds of tunnels, pentagonal Ba^{2+}, diamond shaped $[Ba_xNd_{2/3-2/3}x]^{2+}$ and vacant triangular sites. The analysis of the $x = 1$ Nd composition is in progress.

High resolution electron microscopy lattice images taken down the c axis show a "herring bone weave" pattern, with angles near 60°. All postulated structures based on the 1:1:5 compositions show calculated lattice images with 90° angles. However, calculated images based on the neutron refined structure agree with the observed pattern.

The current structural thrusts of this project center on the elucidation of the $x = 1$, Nd compound. We are also investigating the Samarium structure using synchrotron radiation at the NSLS Brookhaven National Laboratory. Measurements on the inherent electrical characteristics of the single phase materials are in progress.

NEUTRON POWDER DIFFRACTION STUDY OF $Ba_2YCu_3O_{6.5}$

S. Miraglia and D. Tran Qui
(Laboratorie de Cristallographic, CNRS, Grenoble, France)
and
F. Beech
(Imperial College, University of London, London, UK)
and
(National Bureau of Standards, Gaithersburg, MD)
and
A. Santoro

1. Introduction

The compound $Ba_2YCu_3O_\delta$ has been prepared with oxygen content varying from $x \simeq 6.0$ to $x \simeq 7.0$.[1] Within this range of compositions the structure of the material can be described as a three-layered oxygen-deficient perovskite[2] and exhibits a tetragonal (P4/mmm) to orthorhombic (Pmmm) phase transition associated with ordering of the oxygen atoms. The orthorhombic structure of $Ba_2YCu_3O_7$ and its relationship to the atomic arrangement of perovskite are illustrated in figure 1.

The phase transition is induced by changes in oxygen stoichiometry which is, in turn, a function of the temperature and of the oxygen partial pressure in the sample container.[3] The orthorhombic, superconducting phase exists for values of δ comprised between ~ 6.5 and 7.0, while for $\delta < 6.5$ the symmetry of the compound is tetragonal. The transition occurs for values of δ of about, or slightly higher than, 6.5 depending on the temperature of the experiment and the sample preparation.[1,3-6] The oxygen atoms which are removed from the structure or introduced in it are those present in the basal plane of the unit cell[7,8] and they are labeled O(4) and O(5) in figure 1.

The variation of oxygen content of $Ba_2YCu_3O_\delta$ is directly related with the existence of the one-dimensional chains of near-squares of CuO_2 extending along the b-axis of the unit cell and considered to be the factor responsible for the enhanced value of T_c.[9] In fact, the value of T_c is a function of the oxygen stoichiometry, the highest value of this temperature corresponding to a value of δ slightly less than 7.0.[9] It seems important, therefore, to know the structural details of the material and to determine the subtle structural changes that occur when the oxygen content is varied. For this reason we have refined the structure of the compound $Ba_2YCu_3O_{6.5}$ at room temperature with the profile method applied to neutron diffraction powder data. The results of this study are reported in this paper together with a comparison of the structural details obtained for the other compositions analyzed so far.

2. Experimental

The neutron diffraction measurements were made at room temperature with the high resolution five counter diffractometer at the National Bureau of Standards Reactor, using the experimental conditions shown in table 1. The structure was refined using the Rietveld method[10] adapted to the multicounter diffractometer and modified to include the background parameters.[11] In the final refinement all the structural, lattice, and profile parameters were varied simultaneously and the results are given in table 2. In table 3 are shown the relevant bond distances found for $Ba_2YCu_3O_{6.5}$ and they are compared with those obtained for other compositions of the system $Ba_2YCu_3O_\delta$ ($6 \le \delta \le 7$).

3. Discussion

One of the important structural features of the system $Ba_2YCu_3O_\delta$ is that the coordination of the ions Ba^{2+} is ten-fold for $\delta = 7$ and eight-fold for $\delta = 6$. This point can be easily comprehended by reference to figure 2. An analysis of the data reported in table 3 shows that the distances Ba-O(1) and Ba-O(4) increase with decreasing oxygen content, while the distances Ba-O(2) and Ba-O(3) decrease. This means that the Ba^{2+} ions move away from the plane formed by atoms O(1), being 0.301 Å above this plane in $Ba_2YCu_3O_7$ and 0.513 Å in $Ba_2YCu_3O_{6.06}$.[8] Correspondingly, their distance from average plane formed by atoms O(2) and O(3) decreases from 2.263 to 2.174 Å. In other words, they move towards that part of the original cuboctahedron of perovskite that is left after the removal of the atoms O(4).

The coordination of ions Y^{3+}, on the contrary, does not change with the oxygen content, and the coordination polyhedron (a near-rectangular prism) does not vary significantly in going from x = 0 to x = 1.

In $Ba_2YCu_3O_7$ the ions Cu(1) are four-coordinated and they are located at the center of near rectangles connected by vertices and forming chains along the b-axis. In $Ba_2YCu_3O_6$ these ions are two-coordinated, suggesting for this compound the formulation $Ba_2YCu^{1+}Cu_2^{2+}O_6$, where $Cu^{1+} \equiv Cu(1)$ and $Cu^{2+} \equiv Cu(2)$.[8] The distances Cu(1) - O(1) and Cu(1) - O(4) decrease continuously as the oxygen is removed from the (0,1/2,0) sites. The description of the Cu(1) coordination for compositions comprised between these extremes is rather complex. A simple statistical distribution of the oxygen on the (0,1/2,0) sites would result in three-fold oxygen coordination for the copper ion. This coordination for copper has, to our knowledge, never been reported[12] and therefore we must consider the possible existence of very small domains (of the order of only a few unit cells), with no long range coherence or order, in each one of which the vacant sites are distributed so that the coordination of Cu(1) is either four or two. This assumption is consistent with the rather large temperature factors of Cu(1) and O(1) that are observed experimentally and with the fact that these temperature factors increase with decreasing x values.

Also the environment of Cu(2) changes significantly with the oxygen content. The distance Cu(2) - O(1) increases continuously (from 2.295 to 2.469 Å) in going from x = 0 to x = 1 and, correspondingly, the distance of Cu(2) from the average plane of the atoms O(2) and O(3) decreases (from 0.269 to 0.217 Å). This shift shows that the coordination of Cu(2) tends to be more and more square-planar with decreasing oxygen content.

As mentioned previously, the oxygen atoms O(4) show a large temperature factor. This feature has been observed in all compositions analyzed so far[7,8] and has been reported by other groups as well.[13,14] In addition, it has been found that this factor does not decrease significantly with temperature,[7] thus indicating the presence of static disorder. This is not surprising considering that this atom is relatively weakly bonded in the structure. The results given in table 2 show that O(4) is highly anisotropic in the direction of the a-axis (similar results have been obtained also for $Ba_2YCu_3O_7$ and $Ba_2YCu_3O_{6.8}$). Based on the above observations, an attempt has been made to refine the structure with the oxygen atom O(4) split over the two positions ($\pm$x,1/2,0) (position 2k of space group Pmmm) instead of the constrained (0,1/2,0) position. The results of this refinement do not differ significantly from those reported in table 2, but the value of the atomic coordinate x (x = -0.053(4)) can be considered to be significantly different from zero. In addition, with this assignment, the isotropic temperature factor of O(4) becomes 1.1 $Å^2$. The statistical test developed by Prince[15] was applied in order to determine if the model with O(4) at ($\pm$x,1/2,0) (model 2) gives a better fit to the experimental data than the model with O(4) at (0,1/2,0) (model 1). The slope of the regression line showed that model 2 fits the data significantly better than model 1. With this configuration of the oxygen atoms O(4) the near-squares of copper and oxygen forming the chains along the b-axis become buckled much in the same way observed for the two-dimensional distributions of Cu-O atoms extending horizontally at $z \simeq 0.36$. However, a definitive answer to the problem of the location of the atoms O(4) would

Table 1. Experimental conditions used to collect the intensity data.

Monochromatic beam:	reflection 220 of a Cu monochromator
Wavelength:	1.548 (1) Å
Horizontal divergences:	10, 20, 10′ of arc for the in-pile, monochromatic beam, and diffracted beam collimators, respectively
Sample container:	vanadium can of about 10mm diameter
2Θ angular range:	10° - 120°, steps: 0.05°

Measurements made at room temperature.

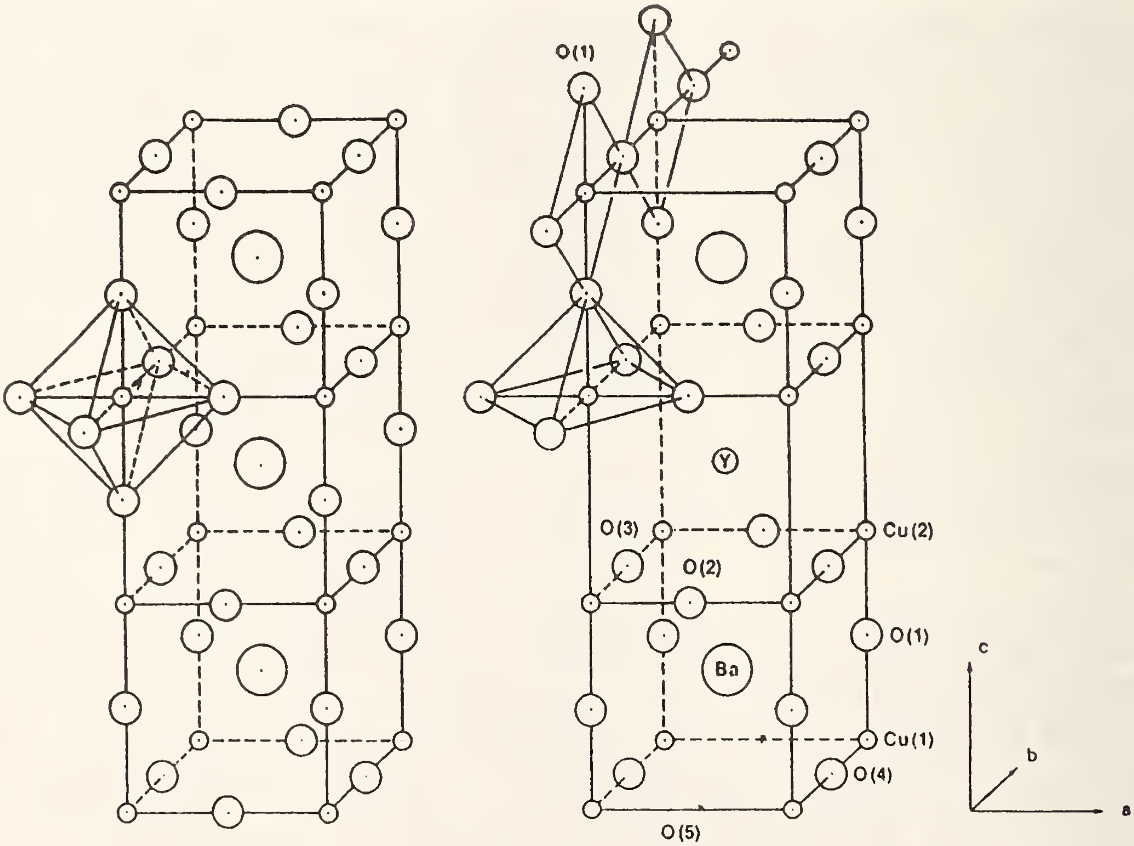

Figure 1. (a) Crystal structure of perovskite ABX_3. Large and small circles represent the A and B cations, respectively. The circles of intermediate size are the X anions. Three unit cells of perovskite are stacked together along the c-axis. (b) Idealized crystal structure of $Ba_2YCu_3O_7$. Note that the perovskite oxygen atoms at (0,0,1/2) and (1/2,0,0) are missing in this compound.

Table 2. Refined structural parameters of $Ba_2YCu_3O_{6.5}$

Space group Pmmm - a = 3.8468(1), b = 3.8747(1), c = 11.7466(5)

Atom	Position	x	y	z	B	n
Ba	2t mm	1/2	1/2	0.1917(2)	0.42(7)	1.0
Y	1h mmm	1/2	1/2	1/2	0.65(6)	0.5
Cu(1)	1a mmm	0	0	0	1.07(7)	0.5
Cu(2)	2q mm	0	0	0.3596(2)	0.46(4)	1.0
O(1)	2q mm	0	0	0.1528(3)	1.48(7)	1.0
O(2)	2s mm	1/2	0	0.3788(4)	0.42(7)	1.0
O(3)	2r mm	0	1/2	0.3767(4)	0.70(7)	1.0
O(4)	1e mmm	0	1/2	0	(*)	0.25

(*) $B_{11} = 4.7(4)$, $B_{22} = 1.7(4)$, $B_{33} = 0.3(5)$

$R_N = 5.65$, $R_P = 6.20$, $R_W = 8.20$, $R_E = 5.34$, $X = 1.54$

Table 3. Relevant bond distances in $Ba_2YCu_3O_{7-x}$.

		$x = 0^{(*)}$	$x = 0.2^{(*)}$	$x = 0.5^{(**)}$	$x = 0.94^{(***)}$
Ba - O(1)	x4	2.7408(4)	2.7470(8)	2.7690(8)	2.7751(5)
Ba - O(2)	x2	2.984(2)	2.972(3)	2.930(4)	2.905(1)
Ba - O(3)	x2	2.960(2)	2.938(6)	2.902(4)	
Ba - O(4)	x2	2.896(2)	2.922(4)	2.956(2)	
Y - O(2)	x4	2.409(1)	2.403(3)	2.404(3)	2.4004(8)
Y - O(3)	x4	2.386(1)	2.389(2)	2.408(3)	
Cu(1) - O(1)	x2	1.846(2)	1.843(3)	1.795(3)	1.795(2)
Cu(1) - O(4)	x2	1.9429(1)	1.9428(1)	1.9374(1)	
Cu(2) - O(1)	x1	2.295(3)	2.323(4)	2.429(4)	2.469(2)
Cu(2) - O(2)	x2	1.9299(4)	1.9305(6)	1.9366(6)	1.9406(3)
Cu(2) - O(3)	x2	1.9607(4)	1.9585(8)	1.9478(6)	

(*) From ref. (7). The distances reported are those obtained for the samples at room temperature. (**) This work. (***) Ref. (8).

require the collection of more data at low temperatures and, for this reason, we report as an interim structure the model with the atom O(4) located at (0,1/2,0).

The background modulation mentioned previously in the angular range of 2Θ between 10° and 21° can be related to the presence of short range ordering of the oxygen vacancies along the b-axis. Attempts to detect long range ordering, however, were unsuccessful. No evidence of super-lattice lines could be found in the powder pattern of $Ba_2YCu_3O_{6.5}$, and doubling of the b-axis and ordering of vacancies did not result in an improvement of the agreement between observed and calculated intensities.

---

1. P. K. Gallagher, H. M. O'Bryan, S. A. Sunshine, D. W. Murphy. Mat. Res. Bull. 22, 995 (1987).

2. T. Siegriest, S. Sunshine, D. W. Murphy, R. J. Cava, and S. M. Zahurak. Phys. Rev. B, 35, 7137 (1987).

3. G. S. Grader and P. K. Gallagher. Preprint.

4. J. D. Jorgensen, M. A. Beno, D. G. Hinks, L. Soderholm, K. J. Volin, R. L. Hitterman, J. D. Grace, I. K. Schuller, C. U. Segre, K. Zhang, and M. S. Kleefisch. Preprint.

5. P. K. Gallagher. Preprint.

6. H. M. O'Bryan and P. K. Gallagher. Preprint.

7. See e.g. F. Beech, S. Miraglia, A. Santoro, and R. S. Roth. Phys. Rev. B, 35, 8778 (1987).

8. A. Santoro, S. Miraglia, F. Beech, S. A. Sunshine, D. W. Murphy, L. F. Schneemeyer, and J. V. Waszczak. Mat. Res. Bull., 22, 1007 (1987).

9. F. Herman, R. V. Kasowski, and W. Y. Hsu. Preprint.

10. H. M. Rietveld. J. Appl. Cryst. 2, 65 (1969).

11. E. Prince. U.S. Tech. Note 1117 (F. J. Shorten, Ed.) p. 8.

12. R. D. Shannon. Acta Cryst. A32, 751 (1976).

13. W. I. F. David, W. T. A. Harrison, J. M. F. Gunn, O. Moze, A. K. Soper, P. Day, J. D. Jorgensen, D. G. Hinks, M. A. Beno, L. Soderholm, D. W. Capone, I. K. Schuller, C. U. Segre, K. Zhang, and J. D. Grace. Nature, 327, 310 (1987).

14. M. A. Beno, L. Soderholm, D. W. Capone, D. G. Hinks, J. D. Jorgensen, and I. K. Schuller. (1987) Appl. Phys. Lett. 51 57 (1987).

15. E. Prince. Acta Cryst. B38, 1099 (1982).

STRUCTURAL DISTORTION IN $La_{1.85}Ba_{0.15}CuO_4$

F. Beech
(Imperial College, University of London, London, UK)
and
(National Bureau of Standards, Gaithersburg, MD)

and

S. Miraglia
(Laboratoire de Cristallographie, CNRS, Grenoble, France)

and

A. Santoro

The structure of the 33 K superconductor $La_{1.85}Ba_{0.15}CuO_4$ has been reexamined at 300 and 10 K. At room temperature the tetragonal I4/mmm structure (similar to K_2NiF_4) is confirmed.[1] However, at low temperature the compound has been found to exhibit orthorhombic symmetry. The low temperature phase can be described by adopting space group Cmca and using the orthorhombic cell related to the room temperature tetragonal cell by means of: $(abc)_0 = (11, -110, 001)\ (abc)_T$. These results are similar to those found for $La_{1.85}Sr_{0.15}CuO_4$.[2] The powder pattern of the material contains two very weak peaks not yet accounted for, and refinements are still in progress in order to characterize the structural details.

---

1. J. D. Jorgensen et al., Phys. Rev. Letters 58, 1024 (1987).

2. R. J. Cava, A. Santoro, D W. Johnson, and W. W. Rhodes, Phys. Rev. B35, 6716 (1987).

NEUTRON STUDY OF THE CRYSTAL STRUCTURE AND VACANCY DISTRIBUTION OF THE SUPERCONDUCTOR $Ba_2Y\ Cu_3O_{9-\delta}$

F. Beech
(Imperial College, University of London, London, UK)
and
(National Bureau of Standards, Gaithersburg, MD)

and

S. Miraglia
(Laboratoire de Cristallographie, CNRS, Grenoble, France)

and

A. Santoro and R. S. Roth

Two samples of the high temperature superconductor $Ba_2Y\ Cu_3O_{9-\delta}$ with $\delta = 2.0$ and 2.2, have been studied at room temperature and at 10 K, with the neutron powder diffraction method and profile analysis. The structure of the compound is orthorhombic.

The oxygen atoms are located on four sets of sites and not on five sets as reported earlier in x-ray diffraction studies. Of the two sets of copper atoms, one is surrounded by four oxygen atoms at distances 1.9299(4)A and 1.9607(4)A. This arrangement forms a two-dimensional framework of Cu-O atoms that extends indefinitely along the a- and b- axis. A fifth oxygen atom is located at 2.295(3)A from the copper atom, giving a pyramidal configuration. In the other set, the Cu atoms are also surrounded by four oxygen atoms, with distances 1.9429(1)A and 1.846(2)A. In this case, however, the oxygen atoms form rectangles connected by vertices, and resulting in chains along the b-axis.

In the compound with $\delta = 2.0$ all oxygen sites are fully occupied. When $\delta = 2.2$ there are oxygen vacancies, but these are confined to one set of positions only, specifically to the oxygen atoms of the chains, located on the b-axis.

No detectable change of the structure has been observed between room and low temperature.

NEUTRON AND SYNCHROTRON X-RAY POWDER STUDIES OF A HIGH IONIC CONDUCTOR SOLID SOLUTION: $Li_{1+x}Ti_{2-x}In_xP_3O_{12}$

D. Tran Qui
(Laboratoire de Cristallographie, CNRS, Grenoble-Cedex, France)

and

E. Prince

and

Soubeyroux
(Institut Laue Langevin, Grenoble, France)

and

D. Cox
(Brookhaven National Laboratory, Upton, NY)

Recently (1) it was reported that Li^+ exhibits high mobility in the $Li_{1+x}Ti_{2-x}In_xP_3O_{12}$ system. On the basis of x-ray powder patterns, it was suggested that, for moderate substitution of Ti^{4+} for In^{3+} ($0 \le x \le 0.4$) an $R\bar{3}c$, NASICON-type structure is formed in $Li_{1+x}Ti_{2-x}In_xP_3O_{12}$ and further substitution ($x \ge 0.4$) of In^{+3} induces, similar to the NASICON system, a distortion leading to monoclinic symmetry. More detailed electrical measurements performed on carefully sintered pellets have shown that the conductivity curve of this solid solution actually has two maxima, one, 2.10^{-2} $(\Omega cm)^{-1}$, at $x \approx 0.35$, and another, $8.10^{-3} (\Omega cm)^{-1}$, at $x \approx 1.8$ (1,2). Structural studies using single crystals of different compositions have unambiguously shown that insertion of In in the solid solution induces much more complicated structural changes in its framework than previously stated. $Li_{1+x}Ti_{2-x}In_xP_3O_{12}$ compounds adopt, depending on x value, three structure types, corresponding to three different phases: phase I, $0 \le x \le 0.4$, is rhombohedral (or may be slightly monoclinic); phase II, $0.4 < x \le 1.0$ is orthorhombic, Pbca; and phase III, $1.0 < x \le 2.0$ is monoclinic $P2_1/n$. In contrast with the NASICON system, the transitions from phase I to phase II and from phase II to phase III correspond to structural reorganisation in the framework. Only the rhombohedral $R\bar{3}c$ structure in phase I is NASICON-type (3,4).

In order to better understand the influence of the framework on the Li mobility in $Li_{1+x}Ti_{2-x}In_xP_3O_{12}$ solid solutions, two series of structural studies have been performed by using the high resolution powder diffractomer at the NBS research reactor (5,6):

a - Distortion of the $[Ti_{2-x}In_xP_3O_{12}]$ framework as a function of x.

Neutron powder refinements of highly conducting, polycrystalline samples with nominal compositions $x = 0.25$, 0.40 and 0.45 indicate that lithiums in the large eight-coordinated sites are in a highly disordered configuration, occuping only 6% of the site capacity, while the low energy octahedral sites are 95% filled (7).

b - Thermal expansion of the $[Ti_{2-x}In_xP_3O_{12}]$ framework.

Such a site distribution, which is unfavorable for fast ion diffusion, may change in the highly conducting state: transfer of Li ions from octahedral sites into the large cavities is therefore expected at high temperature.

Refinements of the $[Ti_{2-x}In_xP_3O_{12}]$ framework at 40, 200, 600 and 800 K, have fully confirmed this expectation, and the observed expansion of this framework is consistent with the reported electrical conductivity behaviour of this materials (1).

Neutron studies have in addition suggested the existence of a parasitic phase in the $Li_{1+x}Ti_{2-x}In_xP_3O_{12}$ solid solution. This parasitic phase has been confirmed by a high resolution a synchrotron x-ray diffraction pattern of $Li_{1.25}Ti_{1.75}In_{0.25}P_3O_{12}$ which showed 26 extra reflections, well resolved from the expected lines. Rietveld refinement applied to the x-ray pattern confirms a neutron observation that the observed Ti/In ratio is substantially lower than it should be according to the chemical analysis. These extra reflections are indexed, and a space group and a solution of the crystal structure of this unwanted phase is identified as $LiInP_2O_7$.

---

1. S. Hamdoune, D. Tran Qui and E.J.L. Schouler. (1986) Solid State Ionics 19 587-591.
2. S. Hamdoune, M. Gondrand and D. Tran Qui Mater. Res. in press
3. S. Hamdoune, Relation between structure and Transport Properties in Solid Solution: $Li_{1+2}Ti_{2-x}In_xP_3O_{12}$, These, Laboratoire de Cristallographie CNRS Grenoble July 1986
4. D. Tran Qui, S. Hamdoune Acta. Cryst. C43 397-399.
5. E. Prince and A. Santoro, National Bureau of Standards, U.S. Tech Note No. 1117, p. 11 (1980).
6. E. Prince, National Bureau of Standards, U.S. Tech Note 1117, p.87. D. Tran Qui, S. Hamdoune, J.L. Soubeyroux and E. Prince, Journal of Solid State Chemistry in press.

NEUTRON POWDER DIFFRACTION STUDY OF $V_9Mo_6O_{40}$

R.C.T. Slade
(University of Exeter, England)
and
(National Bureau of Standards, Gaithersburg, MD)

and

A. Ramanan
(University of Exeter, England)

and

E. Prince

The phases in the system V_2O_5-MoO_3 are being investigated because of their importance in catalysis. The single phase $V_9Mo_6O_{40}$ has a monoclinic unit cell and systematic absences in x-ray powder diffraction studies consistent with the space group C2.

The room temperature powder diffraction pattern was analysed using Rietveld procedures in the space group C2. All peaks were accounted for. The final model shows disorders about special positions for one metal atom and one oxygen atom, equivalent to those proposed by Eick and Kihlborg [1] for the phase V_2MoO_8. All sites are fully occupied. The distribution of V and Mo atoms between metal atom sites was determined. An alternative model with anisotropic temperature factors for those atoms on special positions lead to physically unrealistic values for those parameters. Table 1 presents the final model. The work is being prepared for publication.

---

1. H.A. Eick and L. Kihlborg, Acta Chem. Scand., 20, 1658 (1966)

Table 1. Refined model for $V_9Mo_6O_{40}$ in space group C2.

Atom	Position	X	Y	Z	B	N
M1*+	4c	0.0001(8)	0.0260(112)	0.0901(29)	2.75(31)	0.314(7)**
M2*	4c	0.1856(6)	0.0267(165)	0.0824(31)	1.99(34)	0.286(7)**
O1	4c	0.0987(2)	0.0261(51)	0.0024(15)	1.22(9)	1.000
O2	4c	0.2079(2)	0.5257(53)	0.9992(12)	0.52(8)	1.000
O3	4c	0.1885(2)	0.0329	0.4927(14)	1.10(10)	1.000
O4	2b	0.0000	0.0697(62)	0.5000	2.86(25)	0.500
O5+	4c	0.9994(7)	0.5282(86)	0.0685(19)	1.23(19)	0.500

$R_n = 9.19$ $R_p = 6.77$ $R_{wp} = 8.74$ $R_e = 6.09$

a = 19.3611(7) Å, b = 3.6250(1) Å, c = 4.1215(2) Å
$\beta = 90.617(3)^\circ$

* Mo/V sites.
** N(Mo) shown.
\+ Disorder about special (2a) position.

NEUTRON POWDER DIFFRACTION STUDY OF ANHYDROUS LITHIUM EXCHANGED ZEOLITE X

R.C.T. Slade
(University of Exeter, England)
and
(National Bureau of Standards, Gaithersburg, MD)

and

E.K. Andersen and I.G. Andersen
(Odense Universitet, Denmark)

and

E. Prince

Zeolite X is a synthetic molecular sieve with an aluminosilicate framework isomorphous with the mineral faujasite. In its alkali metal forms, the framework Si/Al ratio in zeolite X is such that there are more exchangeable cations than available sites within the sodalite units that link to form the framework. Previous studies of alkali-exchanged faujasites have identified cation sites within the sodalite units and the hexagonal prisms linking them. Sites for the excess alkali metal within the supercages have been suggested, but never definitively located.

Lithium exchanged zeolite X was prepared by potentiometric titration of the ammonium form with lithium hydroxide. Exchange was > 93%.

The room temperature powder diffraction pattern was analysed using Rietveld procedures in the space group Fd3m. The final model locates all of the atoms in the structure. Lithium atoms occupy sites of three types: (1) at the windows linking sodalite units and hexagonal prisms (Lithium coordinated by three oxygens in a nearly planar configuration), (2) at the windows linking sodalite units and the supercage (fully occupied, also with 3-coordination) and (3) at sites III′ on the walls of the supercage (above an approximate square of oxygens). The values obtained are presented in table 1. The work is being prepared for publication.

Table 1. Refined model for anhydrous lithium zeolite X in space group Fd3m.

Atom	Position	X	Y	Z	B	N
Tet*	192i	0.1242(4)	0.9495(3)	0.0377(4)	0.43(12)	1.000
O1	96g	0.1779(3)	0.1779(3)	0.9785(3)	1.83(19)	0.500
O2	96g	0.1712(3)	0.1712(3)	0.3235(4)	1.60(21)	0.500
O3	96g	0.2506(3)	0.2506(3)	0.1517(4)	2.27(22)	0.500
O4	96h	0.1015(3)	0.8985(3)	0.0000	2.97(28)	0.500
Li1	32e	0.0465(11)	0.0465(11)	0.0465(11)	2.2±1.4	0.138(15)
Li2	32e	0.2220(12)	0.2220(12)	0.2220(12)	4.8±1.6	0.167(17)
LiIII′	96g	0.0938(22)	0.0938(22)	0.8896(34)	0.8±1.9	0.115(15)

$R_n = 10.18$ $R_p = 7.96$ $R_{wp} = 10.16$ $R_e = 9.41$ a = 24.6715(10) Å

*Si/Al

PHASE EXTENSION BY MAXIMUM ENTROPY

E. Prince
and
L. Sjölin and R. Alenljung
(Chalmers University of Technology, Göteborg, Sweden)

The intensities measured in a neutron diffraction experiment depend on the amplitudes of the Fourier transform of the contents of the unit cell at points of the reciprocal lattice. The diffraction data contain no phase information, so it is not, in general, possible to perform the inverse transform to obtain the distribution of scattering matter in the unit cell. Hauptman and Karle,[1] in the work for which they were awarded the 1985 Nobel Prize in chemistry, showed how to make use of the facts that crystals are composed of atoms and that electron density is everywhere positive to determine the most probable values of the phases of many reflections given the amplitudes of all reflections and the phases of some of them. Although the direct methods of Hauptman and Karle are very powerful for determining crystal structures when these unit cells contain no more than a few hundred atoms, they have not been particularly successful for biological macromolecules, where the cell contents may be many thousands of atoms.

Building on information theory, as developed by Shannon[2] and Jaynes,[3] Gull and Daniell[4] developed a method for extending the inverse Fourier transform that can be described conceptually as a process of generating, by a random process, enormous numbers of trial density maps and considering the most frequently occurring of those that are consistent with the data to be the best solution. Their method consists of dividing the map into a large number of cells, called pixels, and finding the maximum of a function of the form

$$s = - \sum p_k \, \ell n \, p_k ,$$

where p_k is the mean density in the k th pixel, subject to one or more constraints that face the Fourier transform of the distribution p(t) to be consistent with the data. Because of the resemblance of this function to the entropy function of statistical mechanics, the method has become known as the method of maximum entropy.

A Fourier sum computed with a limited number of amplitudes and previously determined phases gives a density distribution under the highly unrealistic assumption that the amplitudes of all terms not included in the sum are exactly zero. There is no assurance that this map will not have negative regions and other physically nonsensical features. A maximum entropy distribution will necessarily be positive everywhere, and replaces the zero terms by values that are "most likely", or, perhaps, "least surprising." The maximum entropy distribution has the form

$$p_k = (N/V)\ F(000)\ \exp(Z_k x) / \sum_{j=1}^{N} \exp\ (Z_j x),$$

where V is the volume of the unit cell, N is the number of pixels, F(000) is the total number of electrons in the unit cell, and

$$x = \ell n\ (p_2/p_1),$$

where p_1 and p_2 are the densities in any two pixels such that $p_1 \neq p_2$. Z_k is a function of the densities in the low resolution map:

$$Z_k = (p'_k - p'_1)/(p'_2 - p'),$$

where

$$p'_k = \sum |F| \cos\ (2\pi h \cdot r_k - \delta),$$

and the sum is over the reflections used in the low resolution map. The distribution access with the data used in the low resolution map if $\sum p_k p'_k = \sum (p'_k)^2$, and the sum on the left is a well behaved function of x that can be set equal to the sum on the right by standard, numerical methods.

Repeated application of maximization entropy at progressively higher resolution, in each case using the observed amplitudes with calculated phases, will eventually lead to an everywhere-positive density distribution that is in agreement with all observed data. There is no assurance, however, that the solution will be unique. Further control over the nature of the solution can be gained by making use of the fact that a protein crystal is typically divided by a smooth envelope into two continuous regions, one of which contains the protein molecule, while the other contains solvent whose density is essentially constant. At each step the solvent is flattened,[5] while entropy maximization is applied to the protein.

Figure 1 shows portions of three density maps calculated from data taken from ribonuclease A. Figure 1a is a map at 2 Å resolution with phases taken from the

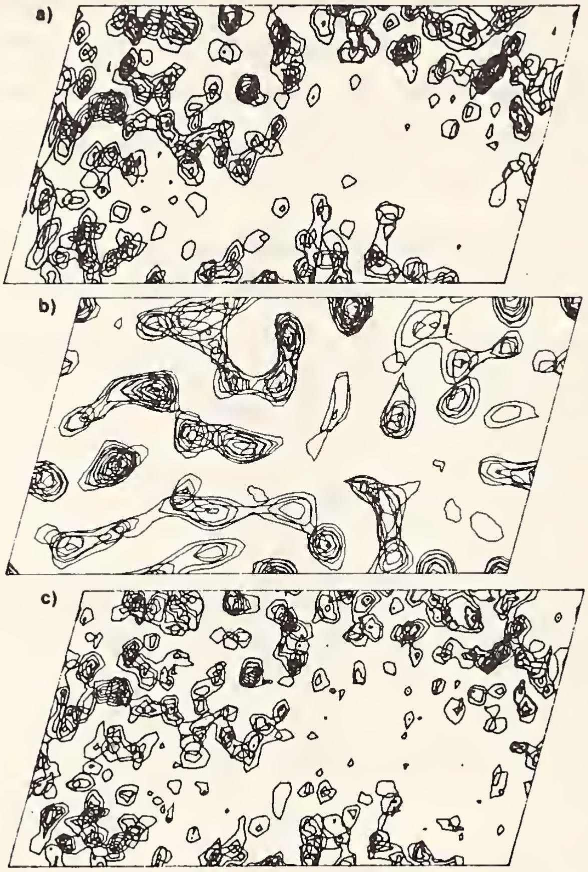

Figure 1. Several overlaid sections of Fourier density maps of ribonuclease A: a) Density map at 2 Å resolution with phases from the refined structure; b) Density map truncated at 5 Å resolution; c) Map at 2 Å resolution with phases extend from 5 Å to 2 Å by the maximum entropy/solvent flattening procedure.

refined structure.[6] Figure 1b is the map with the series truncated at 5 Å resolution. In figure 1c the phases of all reflections with resolution higher than 5 Å have been treated as unknown, but extended using the maximum entropy and solvent flattening procedure back to 2 Å. The close similarity between a and c indicates that the refined structure has been very closely reproduced.

---

1. J. Karle in Structure & Statistics in Crystallography, A. J. C. Wilsen, ed. pp. 7-22 (1985).
2. C. E. Shannon. Bell Syst. Tech. J. 379-423 (1948).
3. E. T. Jaynes, in The Maximum Entropy Formalism, R. D. Levine & M. Tribus, eds. pp. 15-118 (1979).
4. S. F. Gull & G. J. Daniell. Nature (London) 272, 686-690 (1978).
5. B. C. Wang. Methods in Enzymology. 114. Diffraction Methods in Biological Macromolecules, H. W. Wycoff, C. H. W. Hus & S. N. Timasheff, eds. pp. 114-167 (1985).
6. A. Wlodawer & L. Sjölin. Biochemistry, 22, 2720-2728 (1983).

SUB-SURFACE RESIDUAL STRESS MEASUREMENTS BY MEANS OF NEUTRON DIFFRACTION

H. J. Prask and C. S. Choi
(ARDEC, Picatinny Arsenal, Dover, NJ)
and
(National Bureau of Standards)

Neutron diffraction is a measurement technique which closely parallels x-ray diffraction in methodology and analytical formalism. However, in the normal diffraction wavelength range neutrons are, in general, about a thousand times more penetrating than x-rays. In addition the coherent scattering cross-section for neutrons varies in a random manner with atomic number in contrast to the essentially monatonically increasing dependence of x-rays. We have made use of these neutron properties to nondestructively determine sub-surface residual stress in a variety of samples, utilizing energy dispersive neutron diffraction (EDND) to improve resolution and because it appears to reduce anomalous peak shifts in textured samples. We have examined aluminum and steel calibration samples to test the technique,[1] and have applied the technique to the characterization of sub- and near-surface residual stresses in two types of armament-system components: U-0.75 wt % Ti cylindrical rods and 7075-T6 aluminum alloy ogives.[2]

U-0.75wt % Ti ("U-0.75Ti") is an alloy of considerable importance in certain military applications. In order to improve performance and decrease production costs, fabrication-process changes are dictated which can affect desired material properties such as yield strength, ultimate strength, ductility, and susceptibility to stress-corrosion cracking (SCC). These properties depend in varying degrees on the residual stress distribution produced by the fabrication method which includes gamma-phase solutionizing, quenching, aging, and cold work. Two different types of samples were studied. For convenience, the residual stress determinations were made on 10 cm long pieces cut from the mid-point of 46 cm long, 3.3 cm (starting) diameter rods. However, with slight modification of the instrument uncut rods could also be examined. One group was γ-phase solutionized in a vacuum furnace, water-bath quenched, and rotary straightened ("mild" cold work). Of these, some were machined to the final 2.5 cm diameter, and one was moderately cold worked and machined to the final 2.5 cm diameter. In addition, one sample was solutionized in an induction furnace and water-spray quenched, aged, rotary straightened and machined to the final diameter. In all cases aging after quenching was 1-2 hours at 400° C or less.

We utilize the overall equilibrium conditions required by elasticity theory to determine d_0. That is, since the body is static with no external force applied, residual stresses normal to any plane must balance and at any surface the stress orthogonal to that surface must vanish. Stresses inferred from measured strains can be adjusted, by adjusting d_0, to fulfill the equilibrium conditions.[2] Employing the (112) reflection we have determined strains in the mid-point r-θ plane of the 10 cm long DU pieces. Determination of stresses was made using Eqs. 2 - 4 of ref. 2 and recently determined values of Poisson's Ratio (0.267) and the elastic modulus (176600 MPa) for α'-DU. We find that the results for all of the mildly cold-worked samples, including the induction-furnace solutionized/spray-water quenched sample, exhibit stress distributions of the type shown in figure 1a. The moderately cold-worked specimen exhibits a stress distribution which is quite different as shown in Figure 1b.

In the past few years several failures have occurred during ballistic acceptance testing of the 155 mm M483A1 projectile. The purpose of this projectile is to deliver submunitions. An ogive at the forward end, that contains a small explosive charge, is threaded to the projectile body and sealed from it by a pusher plate. The aft end is sealed by a shear plate. At detonation, the pressure developed in the ogive cavity creates an aft directed force that acts on the pusher plate transmitting it through the submunitions to the aft-end shear plate. For effective operation, the force must be sufficient to fracture the shear plate and accelerate the submunitions, thus scattering the submunitions behind the forward traveling projectile body. The malfunctions occurred when the ogive body failed before the aft-end pusher plate.

The ogive is manufactured from 7075-T6 aluminum and is pictured in figure 2. Production ogives are manufactured by two different suppliers, A and B, who use somewhat different manufacturing methods.In full-scale tests the primary failure mode, exclusive to the B-type ogive, is a circumferential fracture at the first loaded thread. A single failure of an A-type ogive, by longitudinal fracture in the conical region, has also been reported. One ogive of type B and one ogive of type A were studied by EDND employing six 4mm x 4mm x 4mm beam spot positions, three at each end of one diameter in the plane of the potential failure site. Overall equilibrium was also used to determine d_0. It was assumed that the average of the 0° and 180° data was representative of the full circumference. Theoretical diffraction elastic constants were used for (200) in the stress/strain calculations.

In figure 3, final absolute residual stress values are shown for both ogive types for 0° and 180° positions at the first thread position. In contrast to previous measurements, the nondestructive EDND stress determination indicates very

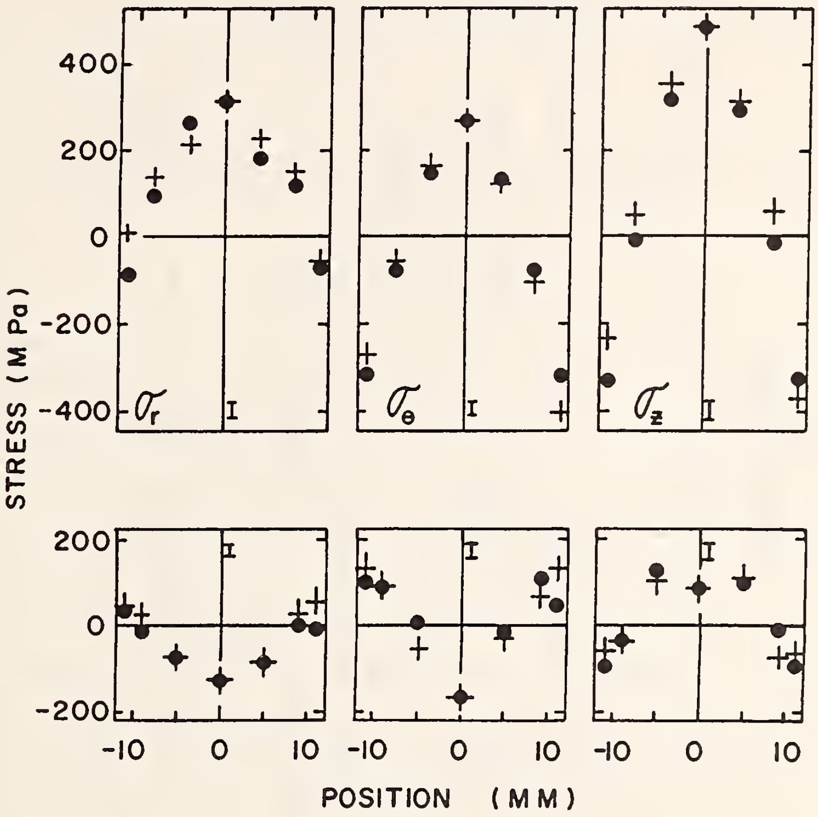

Figure 1. EDND determined residual stress distributions for (1a) mildly cold-worked U-0.75Ti specimens (typical), and (1b) the moderately cold-worked specimen. The crosses and solid circles correspond to measurements along the two orthogonal diameters at the mid-plane of 10 cm long by 2.5 cm diameter rods. Representative standard deviations are shown near the centerline of each stress distribution.

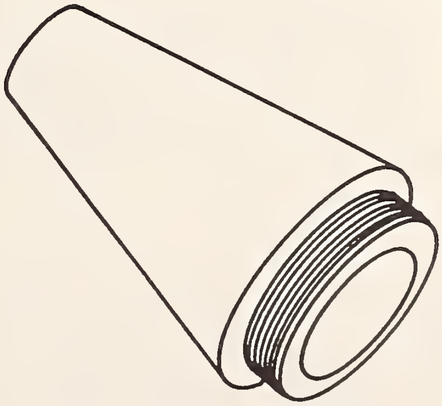

Figure 2. M483A1 ogive with forward end at upper right. Overall length is 19.3 cm, ID at aft end is 4.7 cm. The region of interest is under the most forward thread shown, 8.6 mm thick.

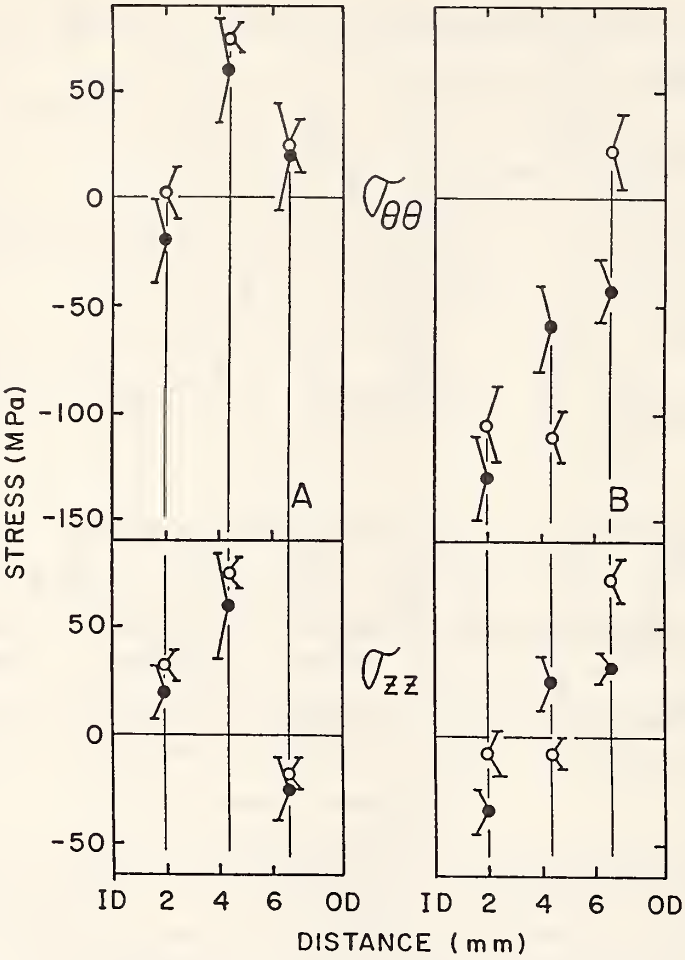

Figure 3. $\sigma_{\theta\theta}$ and σ_{zz} residual stress distributions of the A and B type gives as determined by EDND. "OD" corresponds to the thread-root position. The open and closed circles correspond to measurements made 180° apart.

significant differences in the two ogive types. In the A-type ogives it is found that just below the thread root ("OD") the σ_{zz} stresses are about -20 MPa (compressive) whereas the B-type show +30 to +70 MPa (tensile) stresses. This is completely consistent with the principal failure mode differences that have been observed.

---

1. H. J. Prask and C. S. Choi, J. Nucl. Matls. 126, 124-131 (1984).

2. H. J. Prask and C. S. Choi, "Residual Stress Measurements in Armament System Components by Means of Neutron Diffraction", Proceedings of ASM's 1987 Conference on Residual Stress - In Design, Process and Materials Selection, Cincinnati, Ohio, April 1987, in press.

3. H. J. Prask, C. S. Choi and K. A. Hardman-Rhyne, "Residual Stress Characterization of Al_2O_3/SiC (Whiskers) Using Neutron Diffraction Techniques", presented at Amer. Cer. Soc. Conf., Pittsburgh, April 1987.

RESIDUAL STRESS CHARACTERIZATION OF Al_2O_3/SiC (WHISKERS) USING NEUTRON DIFFRACTION TECHNIQUES

H. J. Prask and C. S. Choi
(ARDEC, Picatinny Arsenal, Dover, NJ)
and
(National Bureau of Standards, Gaithersburg, MD)

and

K. R. Hardman-Rhyne
(Ceramics Division)

Neutron diffraction is a measurement technique which closely parallels x-ray diffraction in methodology and analytical formalism. However, in the normal diffraction wavelength range neutrons are, in general, about a thousand times more penetrating than x-rays. In addition the coherent scattering cross-section for neutrons varies in a random manner with atomic number in contrast to the essentially monatomically increasing dependence of x-rays. We have made use of these neutron properties to nondestructively determine sub-surface residual stress in metallurgical samples, described in another contribution to this report. We have also made use of neutron diffraction to partially characterize residual stresses in each constituent of an Al_2O_3-25wt % SiC(whisker) ceramic composite.

The composite was prepared elsewhere by hot-pressing a dried powder mixture of SiC whiskers (diameters $\leq 1\ \mu m$, lengths $\leq 80\ \mu m$) and alumina into a 13 mm thick slab. The neutron sample was a cube, 13 mm on a side, cut from the edge of the slab. Energy dispersive neutron diffraction was used to measure strains along the fourfold axis perpendicular to the slab-edge surface, as shown in figure 2, employing a 4mm x 4mm x 4mm beam spot. Details of the technique are given in reference 1. The pertinent region of the neutron diffraction pattern ($\lambda = 1.54$Å) is shown in figure 1. The specific peaks examined were Al_2O_3(300) and SiC(114), the latter being the "cleanest" SiC peak of reasonable intensity in the pattern. A profile for the envelope of intensity around this peak, excluding Al_2O_3(125), was obtained from a sample of SiC whiskers.

In these initial measurements several simplifying assumptions were made. Isotropic bulk values were used to calculate the diffraction elastic constants (Al_2O_3: E = 386 GPa, $\mu = 0.23$; SiC: E = 406 GPa, $\mu = 0.22$) and shear stresses were assumed to be zero. The d_o's for each component were obtained from measurements on a block identical to the sample specimen, crushed in a mortar and pestle. The beam-spot centers for the measurements are indicated in figure 2, where Y = +6.5mm corresponds to the slab edge and the hot pressing was along the Z-direction.

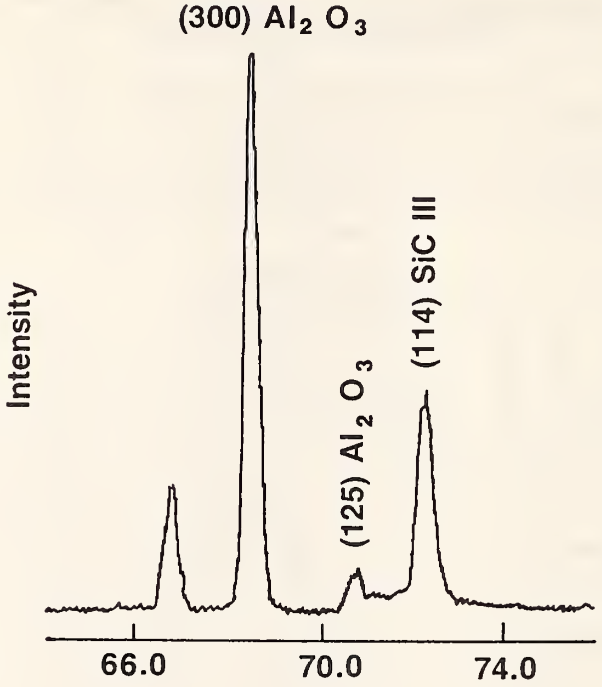

Figure 1. The region of the neutron diffraction pattern of the Al_2O_3/SiC sample examined in the residual stress measurements.

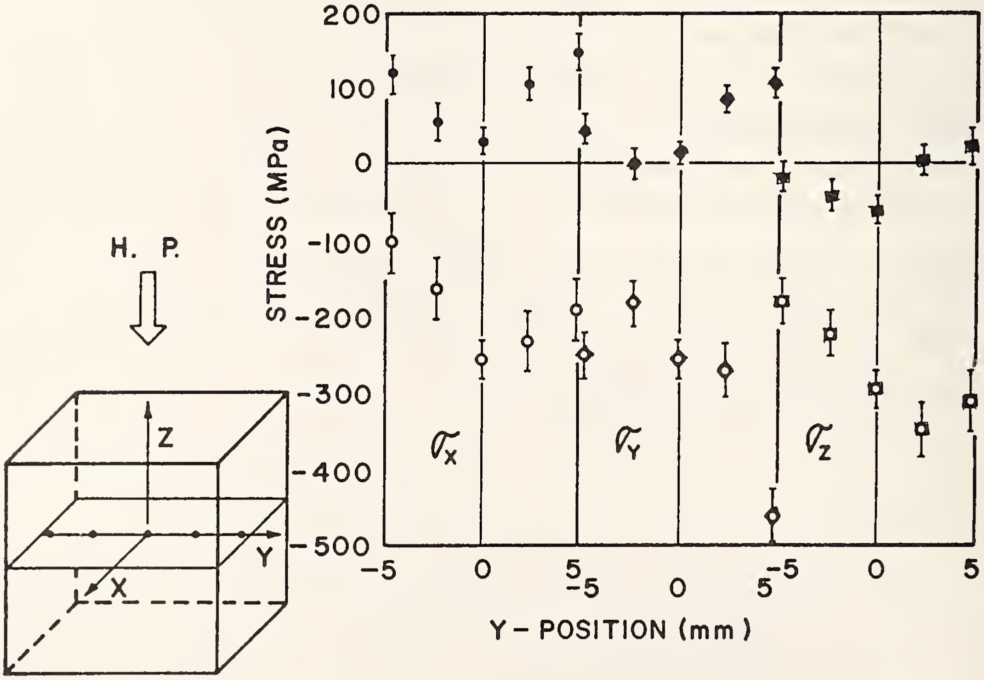

Figure 2. A schematic of the ceramic block (13 mm on a side) with measurement points indicated, and the three residual stress components for each constituent as a function of position along the Y-axis (SiC = open symbols).

Strains were measured in five directions at each point. Under the assumptions described above, the three stress components obtained at each measurement point are shown in figure 2, for each constituent. Overall, it is clear that the alumina is either in tension or slightly compressed, while the SiC is in definite compression for this sample.

---

1. H. J. Prask and C. S. Choi, J. Nucl. Matls. 126, 124-131 (1984).

FIBER TEXTURE AND NEUTRON POWDER DIFFRACTION PATTERN

C. S.Choi and H. J. Prask
(ARDEC, Picatinny Arsenal, NJ)
and
(National Bureau of Standards, Gaithersburg, MD)

In recent years, Rietveld profile refinement of neutron powder diffraction data has been widely used for the crystallographic study of crystalline powder samples, but not for polycrystalline solid samples because of the effect of texture. The Rietveld method determines not only the structural parameters but also the peak widths, and hence is particularly attractive for the microstructural study of a polycrystalline solid. The purpose of the present study is two-fold: characterization of the crystallite orientation distribution in fiber-textured samples by means of a simple distribution function; and its application in Rietveld profile refinements for the correction of texture effects.

The pole density distributions of fiber textured samples exhibit axial symmetry, and hence show concentric intensity distributions about the symmetry axis. For simplicity, we assume that the pole density distribution is Gaussian. In general, a crystal lattice (except the triclinic case) has multiple equivalent lattice planes, each with different tilt angles. Then, the observed pole density distribution as a function of tilt angles, $P(\rho)$, can be described by a superposition of Gaussian peaks centered at respective tilt angle, such that

$$P(\rho) = S\Sigma(N_i/W\sin\rho_i)\exp\text{-}A(\rho-\rho_i)^2/W^2 \qquad (1)$$

where, S is the scale factor, N_i is the number of superimposed peaks (including the equivalent reflections) at the tilt angles (ρ_i), and $A = 4\ln 2$. For multi-axis fiber texture, the pole density distribution can be expressed by a superposition of each fiber texture.

Table 1. Summary of the Rietveld profile refinement for 60 % swaged samples, 6E 6G 6H, and 75 % swaged samples 7A and 7B. The calculated profiles were corrected for the duplex fiber texture models. In the Table, Axis refers to the fiber axis, and width to the FWHM of the fiber axis distributions.

Sample	6E	6G	6H	7A	7B
a	2.8599(1)	2.8607(1)	2.8599(2)	2.8624(2)	2.8618(1)
b	5.8335(4)	5.8325(4)	5.8346(6)	5.8293(6)	5.8345(5)
c	4.9611(2)	4.9618(2)	4.9613(2)	4.9632(2)	4.9623(2)
U	5532(58)	5552(60)	6010(82)	5815(77)	5855(57)
W	1626(16)	1669(16)	1646(23)	1709(24)	1743(18)
Rb	4.96	4.96	6.46	8.09	6.88
Rp	7.44	7.27	8.56	9.11	6.94
Rw	9.64	9.77	11.39	11.73	8.64
Re	6.52	6.40	8.92	9.24	4.58
Axis-1	[252]	[252]	[252]	[252]	[252]
Width	31	31	31	22	23
Ratio	.45	.44	.44	.40	.37
Axis-2	[041]	[041]	[041]	[051]	[051]
Width	29	30	30	23	24
Ratio	.55	.56	.56	.60	.63

A generalized crystallite orientation distribution may be obtained by considering the total number of poles $F(\rho,hkl)$ for individual lattice points instead of the pole density $P(\rho)$ for a group of equivalent reflections as shown in the eq.(1), and expressing the tilt angle ρ_i with reciprocal lattice vectors. Then eq.(1) can be rewritten:

$$F(\rho,hkl) = (K/W)\exp-A\{(\rho-\alpha)/W\}^2 \qquad (2)$$

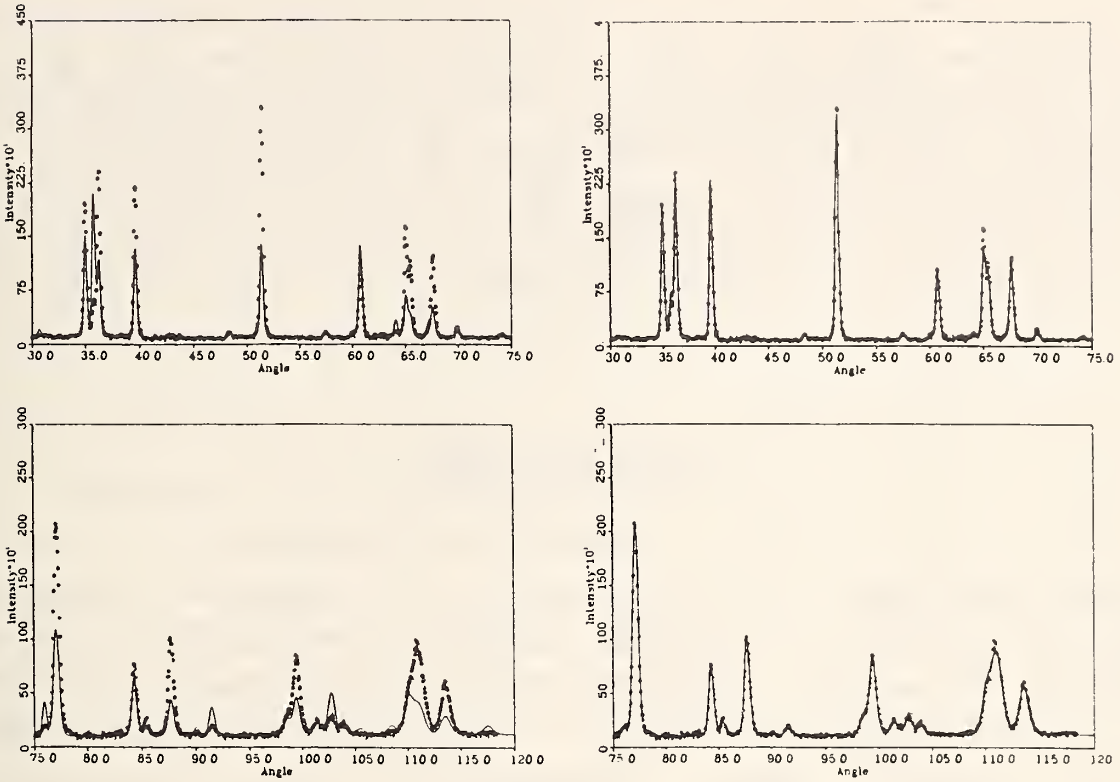

Figure 2. The results of the Rietveld profile refinements of the swaged uranium alloys (60% area reduction), without texture corrections (top) and with the corrections (bottom). The observed neutron diffraction data are indicated by the circles.

where $\alpha = \mathrm{acos}(b_0.b)$ and b_0 and b are the unit reciprocal lattice vectors for the fiber axis and (hkl) pole, respectively. This function represents both the pole figure of a given (hkl) reflection (by fixing the hkl) and the crystallite orientation distribution or inverse pole figure for a given scattering vector (by fixing the tilt angle). If we know the crystal structure of the sample, the crystallite orientation distribution can be converted to the powder diffraction pattern by multiplying $F(\rho,hkl)$ by the corresponding integrated reflectivity. Therefore, the crystallite orientation distribution can be used as a correction factor for the texture effect in the Rietveld refinement, or vice versa. We have modified our Rietveld program to include a general type of fiber texture and for all crystal symmetries by adding several subroutines.

The diffraction patterns of four swaged uranium alloys were measured with the high-resolution powder diffractometer at the NBS reactor with the fiber-axis direction oriented perpendicular to the diffraction plane. The pole figures of four reflections, (020) (111) (112) and (131), were measured for each sample, using the single crystal diffractometer. Duplex fiber texture pole density distribution functions (eq. 1) with fiber axes [041] and [252] were found from the four observed pole density curves. The $p(\rho)$, eq. (1), were converted to $F(\rho,hkl)$, eq.(2), with $\rho=90^0$ in this case. Then, the texture correction factor for the above powder patterns are given by $F(\rho,hkl)/\sin(\rho_i)$. Since the crystal structure of the samples was well known, only the profile parameters and the texture parameters were refined by using the modified Rietveld program. The results of the profile refinements were quite satisfactory and are given in table 1. The observed and calculated diffraction profiles with the texture correction and without the corrections are shown in figure 1.

CRYSTAL DATA CENTER

V. L. Himes, A. D. Mighell, and J. K. Stalick

The NBS Crystal Data Center is concerned with the collection, evaluation and dissemination of data on solid-state materials. The Data Center maintains a comprehensive database with chemical, physical and crystallographic information on all types of well characterized substances. These materials fall into the following categories: inorganics, organics, organometallics, metals, intermetallics, and minerals. During the year, the database and specially designed scientific software have been made available to the scientific community in three distinct modes: 1) NBS CRYSTAL DATA Distribution Package (1987); 2) International Online Search System; 3) Specialized Database for Electron Diffractionists.

1. NBS CRYSTAL DATA Distribution Package (1987)

This product includes NBS CRYSTAL DATA, a FORTRAN program (NBS*SEARCH), and accompanying documentation. NBS CRYSTAL DATA contains up-to-date crystallographic data on more than 115,000 materials. Each entry consists of the reduced cell and volume, crystal system, space group symbol and number, chemical name, chemical formula, literature reference and other data. For convenience, NBS CRYSTAL DATA is provided in both full and abbreviated formats. The Database formats and contents are described in detail in NBS Technical Notes <u>CRYSTAL DATA: Version 1.0 Database Specifications</u> (Stalick and Mighell, 1986) and <u>NBS*SEARCH: A Program to Search NBS CRYSTAL DATA</u> (Himes and Mighell, 1987). NBS*SEARCH software has been designed to be used in conjunction with the 1-line Search File for the characterization and identification of crystalline materials. Selected data for each entry from NBS CRYSTAL DATA have been used to create a 1-line Search File in which each record of 132 characters corresponds to the data for one crystalline compound.

2. Online Dissemination of NBS CRYSTAL DATA

The NBS Crystal Data Center and CISTI's CAN/SND Scientific Numeric Database Service (Canada) have collaborated to make the data available through CRYSTDAT. CRYSTDAT is an online, state-of-the-art database search system that can easily be accessed by scientists worldwide. Within CRYSTDAT, especially designed scientific, database management and computer systems software have been integrated to form a unified analysis system. During the year the system has been extensively upgraded with respect to data (~115,000 entries) and software. Currently over 110 institutions, including most major US industrial companies have signed up to use CRYSTDAT. Over the past months, CRYSTDAT has been intensively used in conjunction with the development of technologically important materials. In the synthesis of new optical materials, for example, space group and point group frequencies for special classes of compounds have proved invaluable. In the design of lasers and superconductors, the database has been systematically searched for candidate compounds with the appropriate lattice parameters, space group and chemical composition.

3. Database for Electron Diffractionists

A new product, designed specifically for electron diffractionists, has been prepared. This product allows the experimentalist to identify materials using such typical electron diffraction data as elemental information and d-spacings. The database for electron diffractionists was prepared in three basic steps. First, an augmented NBS CRYSTAL DATA was prepared. To generate this derivative database, d-spacings (3.6 million) were calculated for all inorganic compounds in NBS CRYSTAL DATA using cell and space group information. Second, selected data items for 60,000 entries were extracted from the augmented database. These data were then combined with similar data on 10,000 entries from the Powder Diffraction File. Third, a streamlined database, formatted for rapid searching, was built with d-spacings and elemental data for ~ 70,000 inorganic compounds. Search software has been written to be used in conjunction with the streamlined database. The product can be integrated with software associated with commercial electron microscopes or used independently. Extensive tests using observed electron diffraction data have proved that the product provides a major new analytical tool for electron diffractionists. The generation of this new product was carried out as a collaborative effort between the NBS Crystal Data Center and Dr. Martin Carr of the Sandia National Laboratories.

A MATRIX APPROACH TO SYMMETRY

V. L. Himes and A. D. Mighell

In the collection of crystallographic diffraction data the initial sequence of steps is directed towards defining the lattice and the crystal symmetry. In doing so, the experimentalist traditionally relies on familiar or standard orientations to guide both the collection and the evaluation of data. On the diffractometer, for example, a conventional unit cell (as defined by the magnitudes of the cell parameters) is determined and the assumed Laue symmetry is verified by taking specially oriented films or by checking the intensities of equivalent (h,k,l)'s listed for standard orientations. There are many valid reasons for choosing conventional cells and orientations in the latter stages of experimental work. However, by choosing specific or familiar orientations in the initial stages, assumptions are made that influence what data is collected and, consequently, mistakes are more likely to be made. The lattice and its symmetry need not be expressed with respect to a standard cell. The properties of the lattice are reflected in <u>any</u> primitive cell because translation of the primitive unit cell generates the entire lattice. The matrix approach to symmetry[1] represents a powerful new strategy in which the emphasis is shifted from standard cells and standard orientations to matrices.

In the matrix approach to symmetry, the matrices that transform the lattice into itself are generated. This group of symmetry matrices defines the holohedry of the lattice. The metric symmetry (and any pseudosymmetry) of the lattice is determined simply by counting the number of matrices. However, the experimentalist need not rely solely on metric information. The group of matrices generated in this way may be viewed as sets of equivalent (h,k,l)'s represented in matrix form. Thus the Laue symmetry may be readily analyzed <u>without</u> transformation to standard familiar orientations. Furthermore, using extremely simple mathematics, the nature and the direction of each symmetry operation of the lattice may be calculated. This information may, in turn, be used to obtain a transformation matrix to a conventional or standard cell of the lattice.

By providing the conceptual and practical framework required to perform experimental procedures in a logical and general manner, the matrix method should revolutionize the automation of diffractometers. New theory and computer algorithms have been developed that permit the determination and interpretation of symmetry using any cell of the lattice. Symmetry can be directly analyzed in the most general way possible without relying on assumptions, conventions and standard cells. The method is precisely what the experimentalist needs as it permits the efficient measurement of exactly the data required to establish the Laue group. In applying the technique, the experimentalist is always aware of the highest possible symmetry, all pseudosymmetries and the interaction of experimental error and symmetry. The symmetry for an unknown crystal is determined through a straightforward sequence of steps, discussed in the following sections, as soon as a cell defining the lattice has been determined.

1. Generation of the Symmetry Matrices

The basis of the matrix approach to symmetry is to generate the matrices that relate any primitive cell of the lattice to itself. Although any method that will generate the required matrices will suffice, it has been found that the B-matrix algorithm (Santoro, Mighell & Rodgers, 1980) is efficient and reliable. With the algorithm, the matrices B in the following equation are determined:

$$ai = \sum_j Bij\ aj\ (i,j = 1, 2, 3)$$

where ai and aj define two primitive triplets of noncoplanar translations (a triplet is called <u>primitive</u> when it defines a primitive cell). When using the B-matrix algorithm for the analysis of symmetry, one selects a primitive cell and generates a set (or sets) of symmetry matrices. Only B-matrices with integer elements and a determinant of +1 are considered. The treatment of experimental error using the matrix method is conceptually very simple. Generated with each symmetry matrix ia a 'tolerance' matrix. The tolerance matrix represents the tolerances in the unit cell parameters required to transform the cell into itself by the specified matrix. Suppose Cell 1 is defined by lattice parameters a, b, c, α, β, γ. If, when applied to Cell 1, the matrix procedure yields the matrix B with the tolerance matrix

$$\begin{pmatrix} \text{tol } a & \text{tol } b & \text{tol } c \\ \text{tol } \alpha & \text{tol } \beta & \text{tol } \gamma \end{pmatrix}$$

then the transformation of Cell 1 by the matrix B will give Cell 2 having lattice parameters

$$\begin{array}{lll} a' = a + \text{tol } a & b' = b + \text{tol } b & c' = c + \text{tol } c \\ \alpha' = \alpha + \text{tol } \alpha & \beta' = \beta + \text{tol } \beta & \gamma' = \gamma + \text{tol } \gamma \end{array} .$$

Thus, the matrix procedure enables a direct comparison of the calculated errors with the experimental errors for the refined unit cell. The computer program based on the B-matrix algorithm is very fast even when analyzing highly skewed unit cells.

In addition, the computer time is essentially independent of the magnitudes of the tolerances specified for the unit cell parameters.

2. Determination of the Metric Lattice Symmetry

By relating the lattice to itself, all the symmetry operations of the lattice are obtained. The metric lattice symmetry is then determined by counting the number of matrices. The greater the number of matrices found, the higher the symmetry. Using the B-matrix algorithm, the numbers of matrices for the seven lattice metric symmetries are: triclinic, 1; monoclinic, 2; orthorhombic, 4; rhombohedral, 6; tetragonal, 8; hexagonal, 12; and cubic, 24.*

An important feature of the matrix approach is that one can determine the highest possible metric symmetry within any specified tolerance of the unit cell parameters, and that all possible pseudosymmetries are immediately apparent. By initially assuming very large experimental errors, a menu of all possible symmetries is obtained. Thus, to determine metric symmetry using the matrix procedure, one sets large limits for the tolerances (such as 1.0 and 6.0 for the cell edges and angles, respectively) and analyzes the set(s) of symmetry matrices and tolerance matrices obtained. Theoretically, it is the nature of the matrices themselves that defines the sets to be analyzed (i.e., those defining a symmetry group). Practically, however, the usual result is that the tolerance matrices alone clearly define the groups and all that is required to determine the metric lattice symmetry and pseudosymmetry is to count.

---

*To obtain a complete group of symmetry operations using the B-matrix algorithm, multiply the matrices by -1 to generate a set twice the size.

When the symmetry matrices are used to transform an experimentally determined unit cell, metrically similar unit cells are generated (refer to the definition of tolerance matrices). If the lattice symmetry elements correspond to crystallographic symmetry elements, then these metrically similar cells are symmetrically equivalent and the observed metric differences are due to experimental errors. The matrix approach to symmetry provides an ideal way to evaluate the experimental errors by simply averaging the set of tolerance matrices. The resulting 'error' matrix (= averaged tolerance matrix) may be compared directly to the e.s.d.'s for the refined unit cell, or it may be applied to the refined cell to calculate an idealized cell reflecting the exact metric symmetry. In either case, the extent to which the refined cell parameters deviate from the exact metric symmetry is easily established.

3. Determination of the Laue Symmetry

The symmetry operations of the lattice may be generated using the B-matrix algorithm by transforming the lattice into itself. The transformation of Cell 1 to Cell 2 can be represented by the equation:

$$\left(\begin{matrix} a2 & & & a1 \\ b2 & = & B & b1 \\ c2 & & & c1 \end{matrix}\right)$$

where (ai,bi,ci), i=1m2 represents the basis vectors in direct space and

$$B = \begin{pmatrix} b11 & b12 & b13 \\ b21 & b22 & b23 \\ b31 & b32 & b33 \end{pmatrix}$$

The same matrix, B, can be used to transform the values of the (h,k,l)'s for the setting defined by Cell 1 to the setting defined by Cell 2. Thus, the B-matrices also may be viewed as matrix representations of equivalent (h,k,l)'s. With the matrix approch to symmetry, the metric symmetry may be determined to within any specified tolerance of the unit cell parameters, and the same group of B-matrices may be used to experimentally determine the Laue symmetry. The metric lattice symmetry, the Laue symmetry and all possible pseudosymmetries can be readily evaluated without transformation to standard or familiar orientations. In practice, the Laue symmetry may be determined by evaluating the intensities of equivalent reflections. A more theoretical proof of the Laue symmetry, as well as an analysis of all possible subgroups, is obtained by analyzing the B-matrices themselves.

The symmetry operations of the lattice are represented by the B-matrices. The values of the elements in each matrix depend upon the kind and orientation of the element with respect to the coordinate system chosen. Because the B-matrix algorithm generates matrices with a determinant of +1, the nature of the symmetry axis is found by calculating the trace of the matrix: $\mathrm{tr}(B) = b11 + b22 + b33$. The trace of the matrix is invariant under similarity transformations; that is, it is independent of the basis chosen. The symmetry axis is an n-fold rotation axis where $n = 1,2,3,4,6$ for $\mathrm{tr}(B) = 3,-1,0,1,2$, respectively. The direction of the axis is given by the solutions $\underset{\sim}{q}$ of a linear algebraic equation of the form $(B - \underset{\sim}{1})\underset{\sim}{q} = 0$, where $\underset{\sim}{1}$ is the identity matrix.

4. Practical Symmetry Determination

A primitive unit cell with

$a = 13.8102(21)$ $b = 13.8091(22)$ $c = 16.6620(28)$ Å

$\alpha = 89.994(13)$ $\beta = 89.993(13)$ $\gamma = 89.980(13)$ °

was determined for the complex C56 H60 Cu5 N22. The group of B-matrices generated from this unit cell is given in table 1. The metric lattice symmetry is tetragonal since eight symmetry matrices were found. When evaluating symmetry using the matrix method, the experimentalist need not rely solely on metric information. The group of B-matrices may be viewed as sets of equivalent (h,k,l)'s represented in matrix form. Once a reflection has been found on the diffractometer, the equation

$$\left[\begin{pmatrix} h \\ k \\ l \end{pmatrix}_{eq} \right]_i = Bi \begin{pmatrix} h \\ k \\ l \end{pmatrix}$$

may be used to generate sets of reflections that should have equivalent intensities if the metric and crystal symmetry agree. Substitution of the B-matrices from table 1 into the above equation, where $i = 1,\ldots 8$ for the tetragonal system, generates the following set of (h,k,l)'s:

(-h,-k,l) (-h,k,-l) (-k,-h,-l) (-k,h,l)
(k,-h,l) (k,h,-l) (h,-k,-l) (h,k,l)

This is the familiar set used for the tetragonal system since the primitive cell used to generate the symmetry matrices reflected the conventional metric conditions consistent with the highest possible symmetry of the lattice (i.e., in the tetragonal system, a cell with $a = b \neq c$ and $\alpha = \beta = \gamma = 90°$ as oppposed to a primitive cell with $a \neq b \neq c$ and $\alpha \neq \beta \neq \gamma \neq 90°$). For sets of general (h,k,l)'s, it was found that the intensities for all eight reflections in the sets were equivalent, indicating 4/mmm Laue symmetry for the complex. This observation was confirmed by a full structure determination (Himes, Mighell & Siedle, 1981).

Using the matrix approach, the Laue symmetry and any pseudosymmetry, metric or crystal, may be determined from any cell defining the lattice. A second unit cell was determined for the complex C56 H60 Cu5 N22 and refined on a diffractometer:

$a = 19.5263(27)$ $b = 42.4583(59)$ $c = 30.8742(45)$ Å

$\alpha = 29.242(13)$ $\beta = 18.442(13)$ $\gamma = 23.106(12)°$

As expected, the matrix procedure predicted tetragonal symmetry since eight B-matrices were generated (table 2). The group of matrices used to determine the metric symmetry also were used to evaluate the Laue symmetry from this skewed unit cell. For example, when the (5,6,7) reflection was multiplied by each of the B-matrices from table 2, the following set of (h,k,l)'s was predicted and subsequently found, to have equal intensities:

(-1, -6, -4)	(-1, 2, 1)	(-5, -14, -7)	(-5, -6, -8)
(5, 14, 8)	(1, -2, 4)	(1, 6, -1)	(5, 6, 7)

Once the symmetry has been evaluated, these same matrices may be used to obtain a transformation matrix to a conventional or standard cell.

5. Concluding Remarks

The matrix approach to symmetry has been used routinely to determine symmetry for all types of compounds from small molecules to proteins. This approach, which deals with symmetry in its most abstract form, provides the conceptual and practical framework required to perform experimental procedures in the most logical and general manner possible. Unlike techniques currently in use in modern diffractometry, automated procedures based on this new method will determine

Table 1. Symmetry matrices found for C56 H60 Cu5 N22. Program limits of 1.0 and 6.0 were used for the cell edges and angles, respectively.

$$(1)\begin{pmatrix}-1 & 0 & 0\\ 0 & -1 & 0\\ 0 & 0 & 1\end{pmatrix}\quad (2)\begin{pmatrix}-1 & 0 & 0\\ 0 & 1 & 0\\ 0 & 0 & -1\end{pmatrix}\quad (3)\begin{pmatrix}0 & -1 & 0\\ -1 & 0 & 0\\ 0 & 0 & -1\end{pmatrix}\quad (4)\begin{pmatrix}0 & -1 & 0\\ 1 & 0 & 0\\ 0 & 0 & 1\end{pmatrix}$$

$$(5)\begin{pmatrix}0 & 1 & 0\\ -1 & 0 & 0\\ 0 & 0 & 1\end{pmatrix}\quad (6)\begin{pmatrix}0 & 1 & 0\\ 1 & 0 & 0\\ 0 & 0 & -1\end{pmatrix}\quad (7)\begin{pmatrix}1 & 0 & 0\\ 0 & -1 & 0\\ 0 & 0 & -1\end{pmatrix}\quad (8)\begin{pmatrix}1 & 0 & 0\\ 0 & 1 & 0\\ 0 & 0 & 1\end{pmatrix}$$

Table 2. C56 H60 Cu5 N22: Symmetry matrices calculated from a skewed cell. Program limits of 1.0 and 6.0 were used for the cell edges and angles, respectively.

$$(1)\begin{pmatrix}-3 & 0 & 2\\ -8 & 1 & 4\\ -5 & 0 & 3\end{pmatrix}\quad (2)\begin{pmatrix}-3 & 0 & 2\\ -4 & -1 & 4\\ -4 & 0 & 3\end{pmatrix}\quad (3)\begin{pmatrix}-1 & 0 & 0\\ -4 & 1 & 0\\ 0 & 0 & -1\end{pmatrix}\quad (4)\begin{pmatrix}-1 & 0 & 0\\ 0 & -1 & 0\\ -3 & 0 & 1\end{pmatrix}$$

$$(5)\begin{pmatrix}1 & 0 & 0\\ 4 & -1 & 0\\ 3 & 0 & -1\end{pmatrix}\quad (6)\begin{pmatrix}3 & 0 & -2\\ 4 & 1 & -4\\ 5 & 0 & -3\end{pmatrix}\quad (7)\begin{pmatrix}3 & 0 & -2\\ 8 & -1 & -4\\ 4 & 0 & -3\end{pmatrix}\quad (8)\begin{pmatrix}1 & 0 & 0\\ 0 & 1 & 0\\ 0 & 0 & 1\end{pmatrix}$$

symmetry without risk of error as the technique does not rely on assumptions, conventions, or standard cells. A FORTRAN program, NBS*LATTICE, has been written to analyze lattice relationships and is available for distribution. The present version of NBS*LATTICE performs several functions including the determination of metric lattice symmetry.

---

1. Himes, V.L. & Mighell, A.D., Acta Cryst. A43. 375-384, (1987).
2. Himes, V.L. & Mighell, A.D. & Siedle, A.R.. J. Am. Chem. Soc. 103, 211-212, (1981).
3. Santoro, A., Mighell, A.D. & Rodgers, J.R. Acta Cryst. A36, 796-800, (1980).

SMALL ANGLE NEUTRON SCATTERING RESEARCH AT NBS

J. A. Gotaas and C. J. Glinka

Until the reactor shutdown for the installation of the cold source, the SANS instrument was utilized by experimenters for more than 98% of the available beam time, including scientists from universities (20), industry (10), government laboratories (3) and six NBS divisions and NBS-Boulder (16). The areas of experiments included polymers (44%), chemistry and physics (16%), magnetism (15%), ceramics (9%), metallurgy (7%) and biology (6%). A brief review of some of this work follows; much of it is described more completely elsewhere in this report.

As can be seen from the distribution of beam time given above, research in polymers is one of the most active programs on the SANS, with scientists from the Polymers Division playing a key role. C. Han (Polymers Division), with a number of collaborators from university, industry and NBS, has continued detailed studies of the conformations of a variety of polymer blends, of the critical behavior of low density polymer materials, and has examined the phase diagram and interaction parameters of rubber/rubber mixtures. In collaboration with V. Soni (Shell), Han has also used SANS to characterize the formation of micelles in block copolymers for emulsion and oil recovery applications. W. Wu and B. Bauer (Polymers Division) have continued their extensive studies of epoxy networks, determining the fractal dimension of networks and the intranetwork form factor as a function of molecular weight, as well as elucidating molecular mechanisms for the growth and deformation of epoxy networks. B. Bauer and R. Briber (Polymers Division) have studied the phase diagram of crosslinked polymer blends. Finally, M. Landry (Kodak) has used SANS to characterize both bulk polystyrene and polystyrene blends in the vicinity of the glass transition temperature.

The most active research effort from industry has been that of Exxon, which has involved a number of Exxon scientists along with collaborators from universities and NBS, and has formed a substantial part of the research in chemistry and physics. S. Sinha and J. Huang (Exxon) with H. Stanley (U. Maryland) have studied the phase separation of binary fluids, including the effects of adsorption on surfaces, and have characterized the structure of heavy oils. R. Overfield (Exxon) and H. Stanley have studied the thermal dissociation of heavy oils. W. Dozier (Exxon) has used SANS to study the structure of microemulsions. J. Gregory (Mobil) and C. Glinka (Reactor Radiation Division) have examined the structure of hydrogen-implanted silicon, a material useful for solar cells. H. Hanley and G. Straty (NBS-Boulder) have studied concentrated latex solutions and supercooled glycerol. C. Glinka and

L. Sander (Center for Analytical Chemistry) have continued their study of the structure of bonded phases in porous silica. R. Slade (U. Exeter, England) used SANS as a tool to study the porosity of clay materials.

SANS has continued to prove a vital tool for probing the microscopic structure of amorphous magnetic systems. J. Rhyne (Reactor Radiation Division) and M. Spano (Naval Surface Weapons Center) have studied a wide range of concentrations of various amorphous rare earth-iron systems, examining the competition between exchange and anisotropy which leads to the formation of an intriguing low temperature state, the correlated spin glass. Rhyne and G. Fish (Allied Corporation) have measured the short correlation ranges in amorphous Fe-Zr resulting from the competition between ferromagnetic and antiferromagnetic exchange interactions. In an international collaboration, Rhyne and B. Barbara (CNRS, France) have probed the critical behavior resulting from the presence of random exchange and anisotropy fields in amorphous $Dy_xGd_{1-x}Ni_2$ alloys. In a different area, J. Lynn, W.-H. Li and Q. Li (U. Maryland) have examined the new high temperature superconductor $ErBa_2Cu_3O_7$ (T_c=95K) and found evidence for the screening of paramagnetic fluctuations by the superconducting electrons, the first such observation in a superconducting rare earth system.

K. Hardman-Rhyne (Ceramics) continued to take advantage of the non-destructive interaction of neutrons with samples to evaluate the structures of calcinated Green State alumina and alumina powder, as well as the porosity of a variety of systems, including slipcast alumina sheets and, with T. Coyle (Ceramics), sol-gel networks. Hardman-Rhyne also used SANS to study the effects of stress in causing microcracks in composites and creep cavitation in siliconized SiC.

SANS has also been of great utility in the characterization of metallurgical samples, as B. Mozer (Reactor Radiation Division) and R. Shull (Metallurgy) have compared the microstructures of amorphous metallic alloys prepared by different techniques. E. Case (Michigan State U.) has examined the microstructure of boron-doped Ni_3Al as part of an investigation of embrittlement mechanisms. R. Fields (Fracture and Deformation Division) and R. Reno (U. Maryland) have also used SANS to study the precipitation of Cu-rich particles and austenite in aged A710 steel. Finally, R. Odette, J. Fint and D. Klingensmith (U. California-Santa Barbara) made strenuous efforts to push the background of the SANS instrument to record-low levels in their attempt to observe small structural changes corresponding to embrittlement in irradiated steels.

Finally, several research groups have taken advantage of SANS to study the structure of biological systems. D. Engelman and J. Flanagan (Yale U.) examined the unfolded states of proteins with altered amino acid sequences in order to understand how one-dimensional amino acid chains fold to produce three-dimensional proteins. As part of a continuing program, S. Krueger (U. Maryland) and R. Nossal (National Institutes of Health) have studied neurosectretory vesicle systems in an effort to understand the role of proteins and protein interactions in their function.

As usual, the demand for beam time on the SANS instrument continued to be greater than the amount available, leaving a number of experiments for the future. The increased flux resulting from the new cold source may be expected to ameliorate this situation somewhat, but will certainly be partially counteracted by the desire of researchers to perform ever more demanding experiments.

CURVATURE PROPERTIES OF A MODEL BICONTINUOUS STRUCTURE WITH A WELL DEFINED LENGTH SCALE

N. F. Berk

We have shown previously[1,2] that an algorithm originally invented by Cahn[3] to simulate morphology influenced by spinodal decomposition in isotropic 2-phase systems can be adapted to the description of the scattering properties of microdispersed and microporous systems distinguished by a morphology with a well defined length scale, including microemulsions and controlled pore glasses.

Cahn's scheme associates an interface between two material phases of uniform density with a level-set (contour) of a random standing wave, $S_N(\vec{r})$, composed of N sinusoids having <u>fixed</u> <u>wavelength</u>, λ, but random directions, $\hat{k}_n$, phase constants, ϕ_n, and amplitudes, A_n:

$$S_N(\vec{r}) = \frac{1}{\sqrt{N\langle A^2\rangle}} \sum_{n=1}^{N} A_n \cos(k\hat{k}_n \cdot \vec{r} + \phi_n), \quad (1)$$

where $k = 2\pi/\lambda$ and $\langle A^2\rangle$ is the mean square sinusoid amplitude. For example, for an isometric partition, a 2-phase interface coincides with the 0-set of $S_N(\vec{r})$--the set $\{\vec{r}\}$ on which $S_N(\vec{r}) = 0$--since over a large space (1) is positive as often as it is negative. Numerical simulations of this process are remarkably evocative of the morphology of phase separated glasses, as imaged by micrographic techniques; the model structure is highly interconnected, even well away from volume fraction isometry.

The character of the morphology is further elucidated by its curvature properties.[2] If κ_1 and κ_2 are the local principal curvatures[4] on a β-set, the local mean curvature, $H = (\kappa_1+\kappa_1)/2$, may be computed from $H = \vec{\nabla}\cdot\hat{n}/2$, where $\hat{n}(\vec{r})$ is the unit normal vector field generated by $S(\vec{r}) = -S_N(\vec{r})$ of (1). Then, on a β-set $H(\vec{r}) = (k^2\beta+S''(\vec{r}))/2S'(\vec{r})$, where (′) denotes the normal derivative. For $N = 50$, numerical simulation gives $\langle H\rangle \approx 0.7k\beta$, where $\langle\cdot\rangle = \int\cdot d\Sigma/\Sigma$ here denotes the average over the surface Σ, so that $\langle H\rangle = 0$ on a 0-set, the surface separating isometric bulk partitions. For a family of parallel surfaces (constant $S'(\vec{r})$), the local Gauss curvature, $K = \kappa_1\kappa_2$, satisfies $K(\vec{r}) = 2H(\vec{r})^2-|H'(\vec{r})|$. With $S'=D$, one then has $H = k^2\beta/2D$ and $K = k^4(\beta^2-D^2/k^2)/2D^2$; for $\beta = 0$, in particular, $H = 0$ and $K = -k^2/2$, independent of D. Such a surface is saddle-like everywhere and satisfies formal requirements for nonplanar minimum area. The actual β-sets of (1) are not a parallel family[2], but on average the 0-set has qualities of a minimal surface, with simulations giving $D \approx \langle S'\rangle = k/\sqrt{2}$ and $\langle H^2\rangle \approx 0.04k^2$, so that $\langle K\rangle \approx -k^2/2$.

---

1. N.F. Berk, NBS Technical Note 1231, ed. F.J. Shorten, National Bureau of Standards, (Gaithersburg), p. 77 (1986).

2. N.F. Berk, Phys. Rev. Lett., 58, 2718 (1987).

3. J. W. Cahn, J. Chem. Phys., 42, 93 (1965).

4. T. Y. Thomas, Concepts from Tensor Analysis and Differential Geometry, Academic Press, (New York) (1961).

INTERPRETATION OF SMALL ANGLE NEUTRON DATA FROM POROUS GLASS USING CAHN'S MORPHOLOGY

N.F.Berk and C.J.Glinka

and

H.B. Stanley
(University of Maryland, College Park, MD 20742)
and
(National Bureau of Standards, Gaithersburg, MD)

Despite intensive recent experimental investigation in many laboratories, the detailed internal structure of microporous glass has not yet been theoretically understood. We have applied a morphological model[1,2] based on Cahn's theory of spinodal decomposition[3] that appears to describe the bulk pore structure. This model implicitly assumes that the internal pore surfaces are smooth, although we are investigating methods to incorporate roughening effects. In fact, the nature of the internal surfaces is still the subject of considerable controversy, with claims both for smooth and rough surfaces in nominally similar commercial glasses.

The basic model is described elsewhere[2]. The essential idea is that interfaces for random, interpenetrating structures with a well defined length scale can be modelled mathematically as isometric contours of a stochastic function having random Fourier components with a common wavenumber $k = 2\pi/\lambda$. Scattering from this morphology is characterized by four distinctive features: (a) a sharp diffraction line at $q = k$, where q is the scattering wavevector; (b) a divergent contribution going as $1/q$ for $q \to 0$; (c) a sharp step at $q = 2k$; and (d) Porod law behavior, $1/q^4$, as $q \to \infty$, as required of scattering from smooth bodies. The relative strengths of the "singular" features, (a) - (c), depend on composition (the volume fractions of the spatial partitions generated by the model) and contrast conditions of the experiment being modelled.

In applying the model to real controlled pore glasses one can expect on physical grounds that the wavenumber, k, of the morphology will be distributed about a modal value, k_0, with some effective width, Δk, according to a distribution P(k). Such k dispersion can be incorporated in the model[2] and is found to moderate the various singular features of the scattering associated with the nondispersed morphology: the peak at $q \approx k_0$ is broadened, the hyperbolic divergence at $q = 0$ is cured, while the step at $q \approx 2k_0$ is rounded off. The relative changes in these features brought about by dispersion are sensitive to the actual shape of P(k). For example, increasing the width of P(k) not only rounds off the shoulder at $q = 2k_0$, but it can also cause it to be masked by scattering from the broadened peak at $q =$

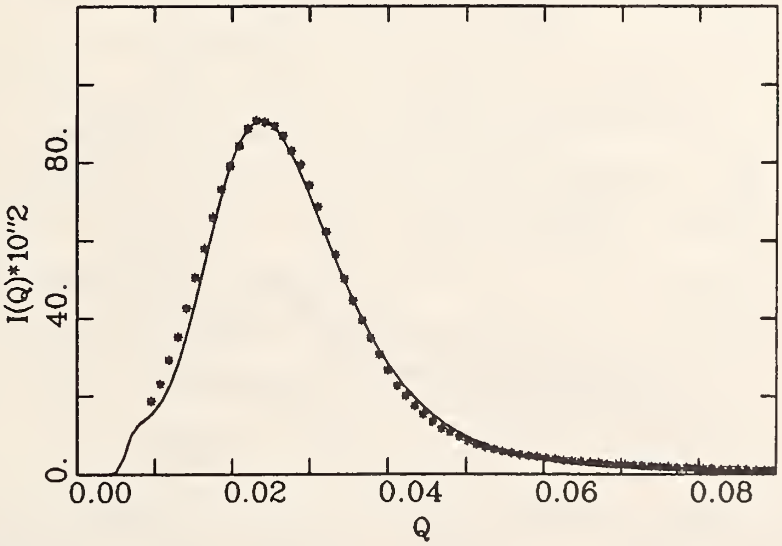

Figure 1. Small angle neutron scattering from dry controlled pore glass. The solid line is a fit using the model discussed in the text and incorporating the k dispersion of Eqn. (2). The fit accounts for instrumental resolution and a beam stop.

k_0. The scattering near $q = 0$ is also sensitive to the shape of $P(k)$. The scattering formula for the small q "singular" features for given $P(k)$ is

$$J(q) = \frac{\pi}{2} C_1 \frac{P(k)}{k^2} + \frac{\pi}{4q} C_2 \int_0^\infty \frac{dq'}{q'} P(q') \int_{|q' - q|}^{|q' + q|} \frac{dq''}{q''} P(q''). \qquad (1)$$

where C_1 and C_2 depend on composion and contrast[2]. Thus, the scattering observed near $q = 0$ depends not only on the degree to which the $1/q$ divergence is moderated in the second term of (1) but also on the behavior of $P(k)$ near $k = 0$ in the first term. It particular, the broadened peak will contribute zero intensity at the origin only if $P(k) \to 0$ faster than k^3.

We have found that our measured scattering from various samples of controlled pore glasses are well described by the model at small q assuming a $P(k)$ of the normalized inverse Gaussian (Wald) type,

$$P(k) = \sqrt{\nu/(2\pi k^3)}\, e^{-\nu(k-\mu)^2/2\mu^2}, \qquad (2)$$

for $k>0$, where ν and μ are free parameters, and $\langle k\rangle = \mu$ and $\langle(k - \langle k\rangle)^2\rangle = \mu^3/\nu = (\Delta k)^2$. The mode, k_0, is given by $k_0 = \mu\{(1 + 9\mu^2/4\nu^2)^{1/2} - 3\mu/2\nu\}$. Figure 1 illustrates the scattering from a typical sample of commercially available glass, which was carefully cleaned and dried, compared to the scattering predicted by the model. The data show a characteristic peak centered at $q_0 = 0.024$ A^{-1} and a non-Porod power law decay, $1/q^m$, with $m \approx 3.5$, for $q \gg q_0$. The solid line is a model fit incorporating (1) and terms not shown here and using (2) with $k_0 = 0.025$ A^{-1} ($\langle k\rangle = 0.033$ A^{-1}) and $\Delta k = 0.03$ A^{-1}. The effects of instrumental resolution have also been included. The model fits well in the region of the peak, but fails in the tail, as it must without incorporating a means of describing the apparent roughness indicated by the scattering at high q. The choice of distribution (2) is arbitrary, but it does reflect the apparent need for a $P(k)$ that falls sharply as $k \to 0$.

We are investigating the structural implications of the shape of the $P(k)$ that appears to best fit the data, including a method to produce computer simulations of the corresponding morphology.

---

1. N.F. Berk, NBS Technical Note 1231, ed. F.J. Shorten, National Bureau of Standards, (Gaithersburg), p. 77 (1986); See also N.F. Berk elsewhere in this Summary of Activities.
2. N.F. Berk, Phys. Rev. Lett., 58, 2718 (1987)
3. J. W. Cahn, J. Chem. Phys., 42, 93 (1965).

PHASE SEPARATION OF A BINARY FLUID IN POROUS GLASS

H.B. Stanley
(University of Maryland, College Park, MD)
and
(National Bureau of Standards, Gaithersburg, MD)

and

S.K. Sinha
(Exxon Research and Engineering Co., Annandale, NJ)

and

S.K. Satija
(University of Delaware, Newark, DE)

and

C.J. Glinka

The critical behavior of a binary fluid mixture confined in a porous medium is thought to be dramatically different from that in the bulk, especially if one of the two phases preferentially wets the medium[1]. We have investigated the phase separation of a critical concentration of 2,6 lutidine and water by means of small angle scattering at the NBSR and observe for the first time, the development of critical fluctuations. Data were taken with a neutron wavelength of 8A for momentum transfers $.009 < q < .125\ A^{-1}$. The porous glass used (trade-name VYCOR) has an

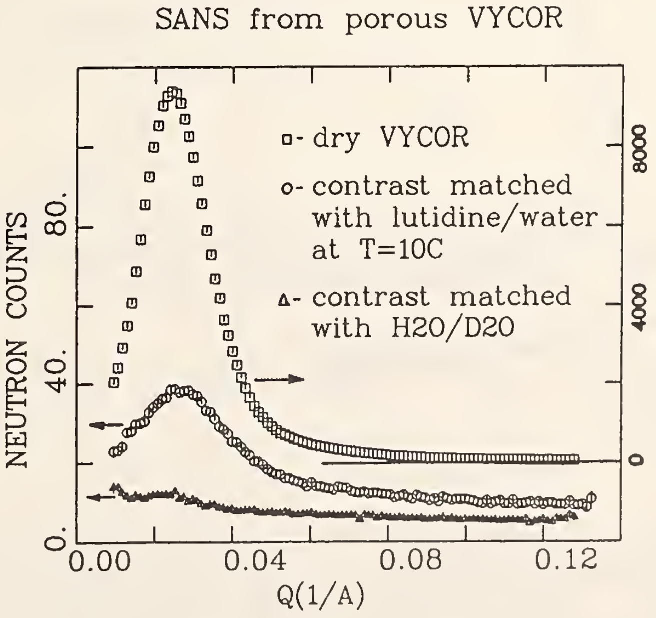

Figure 1. Comparison of the small angle scattering from dry VYCOR porous glass with that from VYCOR saturated with contrast matching solutions of H_2O/D_2O (lower curve) and lutidine/water (middle curve). Notice the 100-fold change of scale between the dry and wetted VYCOR scattering curves.

average pore size of the order of 100A and a well defined inter-pore distance as indicated by the distinctive sharp peak in the scattering cross-section (see figure 1). The manufacturing process involves quenching a borosilicate glass-forming melt into a separated mixture of SiO_2-rich and B_2O_3-rich phases. The latter is leached out, leaving the fully connected internal pore space.

The scattering from the pore structure itself could be reduced by a factor of about 500 by imbibing a contrast matching solution of H_2O/D_2O, as shown in figure 1. When imbibed with a contrast matching solution of lutidine plus H_2O/D_2O, at the critical concentration of 28% lutidine, some residual scattering remained (see figure 1) even well below the bulk phase separation temperature of 31C which is likely due to preferential wetting of the pore surfaces by one of the components of the fluid mixture.

In figure 2 we illustrate the scattering from lutidine/water, at the critical composition, in VYCOR as a function of temperature. We notice that the scattering reflects the pore structure of the dry glass, but is not due simply to changing contrast even at the lowest temperatures measured (5 C), because the peak shape is significantly broader (see figure 1). As the temperature is raised a second

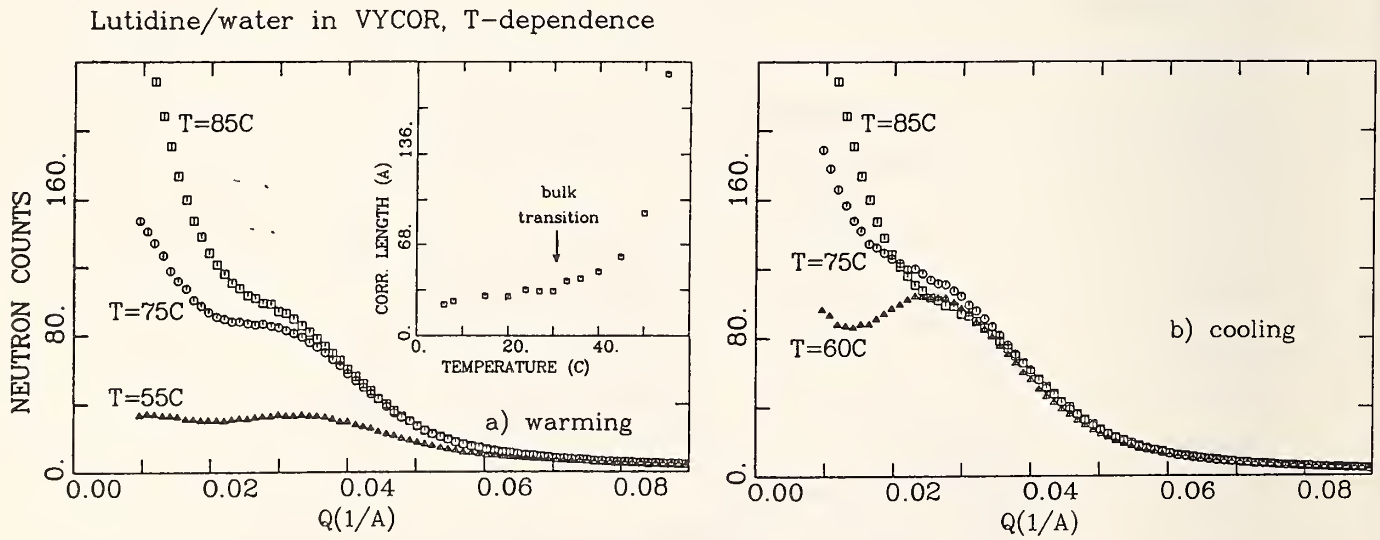
Lutidine/water in VYCOR, T-dependence

Figure 2. a)Temperature dependence of the scattering from VYCOR imbibed with a contrast matching solution of lutidine/water at the critical point composition. The correlation range derived from the lorentzian tails of the scattering curves appears to diverge between 50 to 60C, well above the bulk transition temperature of 31C. b)Once heated above the phase separation temperature, the scattering is irreversible on cooling (compare with a).

component centered at q=0 becomes dominant, and cooling shows the changes to be largely irreversible (at least on a time scale of several hours) as illustrated by figure 2b. The scattering for wavevector transfers greater than about .07 A^{-1} follows an Ornstein-Zernike form from which estimates of the correlation lengths of the fluctuations could be made. These are illustrated inset in figure 2a for the data taken on warming. It can be seen that no anomaly occurs at the bulk transition temperature (around 31 C), but that there is a divergence at higher temperature indicating a phase separation between 50 and 60 C, in agreement with light scattering data[2]. After heating and phase separation we see no time dependence over a period of an hour, but we do have evidence for changes over a period of weeks, indicating that slow diffusion may be needed to regain the low temperature homogeneous equilibrium state. Even after several weeks at room temperature, however, the sample did not return to its original state.

A theoretical study of these wetting and phase separation processes in porous media is currently in progress, based on the formulation of J.W. Cahn[3] as extended by N. Berk.[4]

---

1. M.C. Goh, W.I. Goldburg and C.M. Knobler Phys. Rev. Letts. 58 1008 (1987).
2. S.B. Dierker and P. Wiltzius, Phys, Rev. Lets. 58, 1865 (1987).
3. J.W. Cahn, J. Chem Phys. 42, 93 (1965).
4. N.F. Berk, Phys. Rev. Letts. 58, 2718 (1987).

DETERMINATION OF BONDED PHASE ADSORBATE THICKNESSES BY SMALL ANGLE NEUTRON SCATTERING

C. J. Glinka
and
L. C. Sander
(Center for Analytical Chemistry)

We have been using SANS to characterize the structure of linear hydrocarbon chains chemically grafted to the internal pore surfaces of microporous silica particles. The aim of this work has been to relate the structure of the bonded adsorbate layers to the performance of chemically modified microporous particles used in chemical separation (e.g. in high performance, reverse-phase liquid chromatography) and processing.

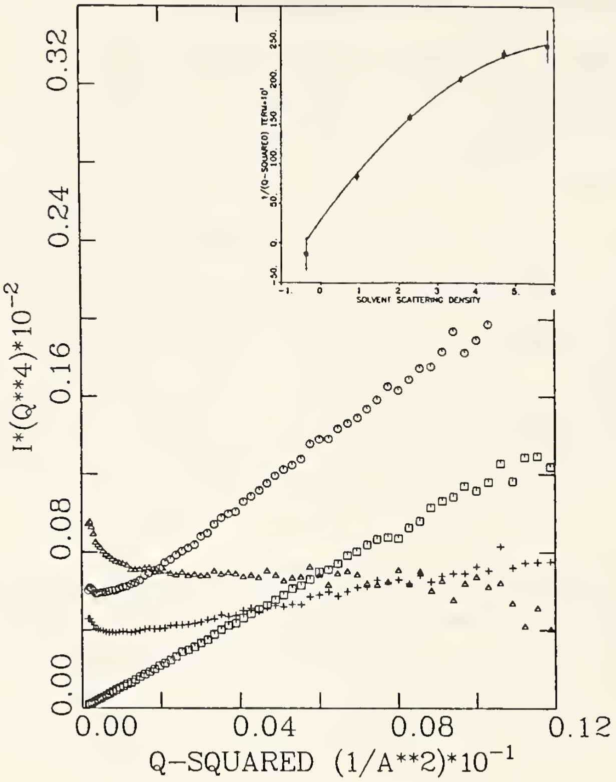

Figure 1. IQ^4 versus Q^2 plots of the small angle scattering from a porous silica gel with C18 alkyl chains grafted to the internal pore surfaces and imbibed with various mixtures of deuterated and protonated methanol (Δ 100 % MEOH, + 79 % MEOH, □ 36 % MEOH and o 18 % MEOH). The slopes of the linear portions of the curves can be fit tp a model (inset) which gives the thickness and scattering ensity of the bonded phase layer.

Our most recent measurements[1] have focused on the outer (i.e. larger Q) portion of the SANS patterns observed from such systems where the distance scale probed is commensurate with the thickness of the bonded phase layers and where the details of the pore structure have no effect on the scattering. The only scattering from the pore structure which is observed at larger Q's is the Q^{-4}, Porod law, scattering from the pore-silica interfaces, and this scattering can be suppressed by filling the pores with a solution (a mixture of protonated and deuterated methanol in our case) which matches the scattering density of silica. By so doing, the signal from the bonded phase layers is accentuated.

If the thickness of the bonded phase is much smaller than the size of the pores, then in the pore masked condition the scattering should exhibit the Q^{-2} dependence characteristic of thin sheets. This is indeed what is typically observed as illustrated in figure 1 (squares) which shows the scattering from C18 alkyl chains bonded to a large pore (1000 Å) silica gel. The intensity of the Q^{-2} scattering (the slope of the linear region in figure 1) is proportional to the square of the product of the thickness and the scattering density of the bonded layer. Although not separable in a single measurement, both of these quantities can be obtained by carrying out a series of measurements in which the contrast with the pore filling solution is varied. Figure 1 shows such contrast variation series from which the average thickness of the C18 layer was determined to be 16 ± 2 Å (compared to a fully extended chain length of 25 Å). This represents the first direct measurement of bonded phase thickness in such materials.

We have carried out similar measurements on bonded phases of alkyl chains ranging from C4 to C30. The SANS results are being used to develop correlations between the bonded phase morphology and chromatographic trends observed when these phases are used to separate solute mixtures of polycyclic aromatic hydrocarbons.

---

1. L. C. Sander, C. J. Glinka and S. A. Wise, (submitted to Analytical Chemistry).

SANS STUDY OF ORGANOPHILIC BENTONITE DISPERSED IN TOLUENE

R.C.T. Slade
(University of Exeter, England)
and
(National Bureau of Standards, Gaithersburg, MD)

and

C.J. Glinka

Organophilic bentonites (montmorillonite clays) are additives used in preparing thixotropic marine paints. The normally organophobic clays are made organophilic by exchange to incorporate quaternary ammonium cations in the interlayer region. Studies of aqueous suspensions of alkali-exchanged montmorillonites by SANS[1] revealed suspended platelets and gave details of the platelet constitution for various exchange cations. No studies of suspensions of organophilic bentonites in organic solvents have been made previously.

Organophilic Claytone 40 (English China Clays International) was suspended in mixtures of toluene/d^8-toluene. Sols were prepared with 0.75% and 1.50% clay by mass.

Small angle scattering of neutrons ($\lambda = 5$ Å) was observed for all samples. Plots of ln(I) versus ln(Q) were linear in the region 0.015-0.05 $Å^{-1}$. The gradients of such plots were, however, solvent composition dependent, ranging (for 1.5% sols) from -2.3 (100% toluene) to -3.1 (100% d^8-toluene). The pattern was similar for the lower concentration (0.75%) sols.

The results of this preliminary study are not consistent with a model of individual clay sheets or composite platelets in suspension (anticipated gradients in ln(I) versus ln(Q) plots would be -2). The scattering is more indicative of globular, composite particles with dimensions far larger than those observed in aqueous suspensions of alkali-exchanged clays.[1] Further studies will be made at longer wavelength to probe the observed region of linear dependence of ln(I) on ln(Q) in detail.

---

1. D. J. Cebula, R. K. Thomas, and J. W. White, J.C.S. Faraday I, 76, 314-321 (1980).

SMALL ANGLE SCATTERING STUDY OF THE SUPERCONDUCTING TRANSITION IN $ErBa_2Cu_3O_7$

J. W. Lynn, W-H. Li, and Q. Li
(University of Maryland, College Park, MD)
and
(National Bureau of Standards, Gaithersburg, MD)

and

H. C. Ku, H. D. Yang, and R. N. Shelton
(Iowa State University, Ames, IA)

The discovery of superconductivity[1] above the boiling point of liquid nitrogen in the oxide compounds such as $YBa_2Cu_3O_7$ has created tremendous excitement not only because of the possible new fundamental superconducting mechanism in this class of systems but also because of the enormous potential for applications. The substitution of the heavy rare-earth elements for yttrium has little if any detrimental effect on the superconducting transition temperature,[2,3] and hence these are ideal materials to investigate the interplay between magnetism and superconductivity.[4] In the low T_C systems this coupling is thought to be primarily electromagnetic in origin, but the direct London screening of the long wavelength magnetic fluctuations by the superconducting electrons has so far eluded detection. Our present small angle neutron scattering results show that the intensity at small wave vectors q does in fact decrease when the sample becomes superconducting. Furthermore, the overall amplitude, temperature dependence, and q-dependent shape of this change in the scattering is consistent with the expected suppression effect.

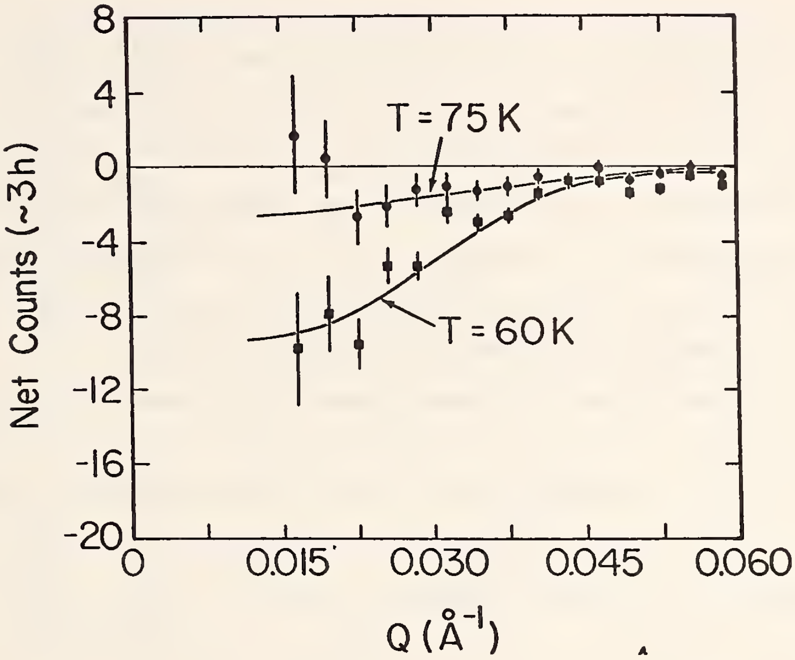

Figure 1. Wave vector dependence of the net intensity for two temperatures below T_C.

However, this interpretation would require a London penetration depth λ_L which is much smaller than expected, and suggests that either another length scale might be relevant to describe the magnetic screening, or the observation represents a new aspect common to this class of superconductors.

The SANS data were obtained with a neutron wavelength of 6.0 Å using the high resolution focusing beam configuration. We would expect to observe a paramagnetic signal, which would be superposed on metallurgical scattering which rises steeply at very small q. Since the ordering temperature is so low, the magnetic correlations caused by the Er magnetism will be negligible in the vicinity of the superconducting transition. Above T_C the magnetic scattering will then be independent of q, which means that fluctuations of all wavelengths are equally likely to occur. Below T_C, however, it will cost additional energy to make fluctuations with wavelengths which are comparable to or larger than the London penetration depth, and hence we would expect the fluctuations for $q \lesssim 1/\lambda_L$ to be suppressed in amplitude. Subtracting the data above T_C from the data below T_C will then emphasize any changes in the observed scattering, while the metallurgical scattering should cancel.[5] Some difference data at two temperatures are shown in figure 1. Above T_C we did not detect any change in scattering, while at 75 K we see a small effect which is statistically significant; all the data points are below zero or within one standard deviation of zero. Reducing the temperature to 60 K clearly decreases the scattering further, while little additional change was found at lower T. We remark that one important check is to compare the magnitude of the decrease in the scattering at small Q with the observed intensity of the raw data at large Q where the nuclear scattering is small and the paramagnetic scattering dominates. For the paramagnetic suppression interpretation to be valid, we can certainly not reduce the scattering at small q more than the paramagnetic intensity that was originally there, so that the intensity at large Q places an upper bound on the overall size of the possible effect.[5] The data of figure 1 are well within this bound.

The results for the temperature dependence of the scattering are shown in the top portion of figure 2. The data at each Q exhibit the same T dependence, so we have summed the data over a range of wave vectors from 0.023 to 0.037 $Å^{-1}$ to improve the statistics. The intensity clearly decreases below the superconducting transition temperature, and exhibits behavior which is quite similar to the behavior of the magnetization as shown in the bottom portion of the figure. Here the cooling data were taken in an applied field of 100 Oe, while the warming data were obtained by cooling in zero field, and then applying a field of 100 Oe.

Experimentally we have demonstrated that the SANS scattering decreases below the superconducting transition. If it is correct to interpret this change as due to magnetic screening, then we can use the data of figure 1 to estimate the magnetic screening length in this material. The screening in real space should be described by an exponential, which yields a squared Lorentzian scattering function with $\lambda_L = [\sqrt{2} - 1]^{1/2}/q_{hw}$. A fit to this functional form yields $\lambda_L \sim 22$ Å, which would be a very small London length. We can compare this value to the related oxide superconductor $La_{1.85}Sr_{0.15}CuO_4$, where λ_L has been measured[6,7] to be 2000 → 2500 Å. This range is typical for a strong type-II superconductor, and suggests that our screening length is not a direct measure of λ_L. Another relevant length scale is of course the superconducting coherence length ξ_0, which is the correct order of magnitude. A second possibility is that the screening in these magnetic superconductors occurs on the length scale of $(\gamma\lambda_L)^{1/2}$, where γ is the magnetic stiffness parameter.[4] This is the quantity which controls the size of the oscillatory wave vector in the "low T_C" magnetic superconductors, and is also the correct order of magnitude. A more interesting possibility, however, is that the change we observe originates from another property of these oxide superconductors unrelated to the Er magnetism. It would be very useful to have a direct measurement of the London penetration depth of this material.

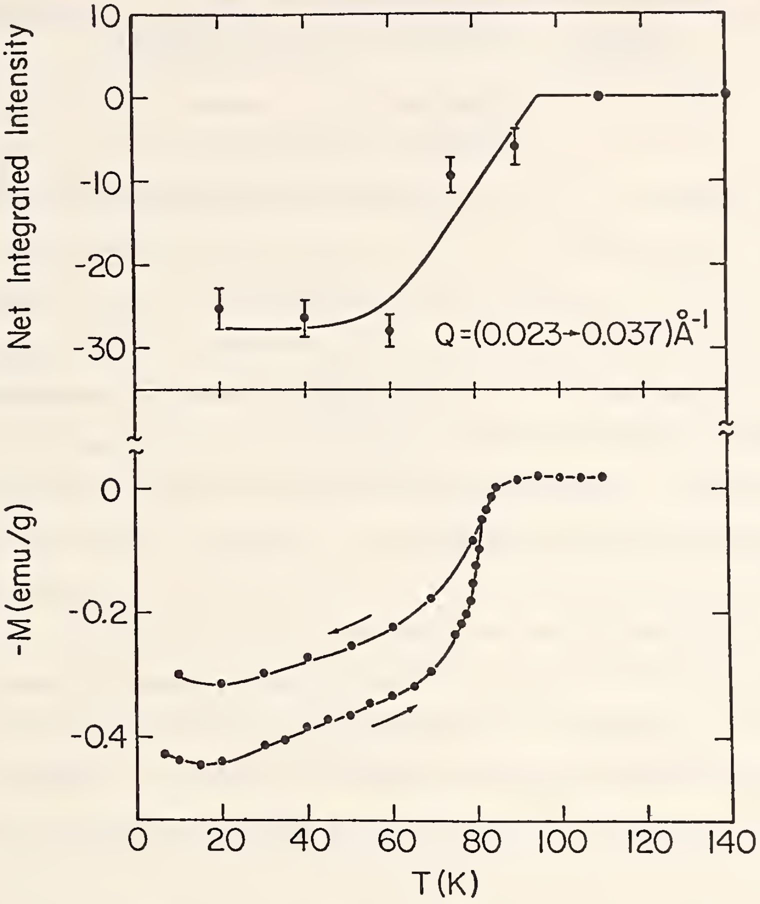

Figure 2. a) Temperature dependence of the scattering, integrated over the Q range of 0.023 to 0.037 $Å^{-1}$. b) Temperature dependence of the magnetization.

---

1. M. K. Wu, J. R. Ashburn, C. J. Torng, P. H. Hor, R. L. Meng, L. Gao, Z. J. Huang, Y. Q. Wang and C. W. Chu, Phys. Rev. Lett. 58, 908 (1987).

2. P. H. Hor, R. L. Meng, Y. Q. Wang, L. Gao, Z. J. Huang, J. Bechtold, K. Forster, and C. W. Chu, Phys. Rev. Lett. 58, 1891 (1987).

3. Z. Fisk, J. D. Thompson, E. Zirngiebl, J. L. Smith and S-W. Cheong (preprint).

4. For a review see Topics in Current Physics, edited by O. Fishcer and M. B. Maple (Springer-Verlag, New York, 1983), Vols. 32 and 34.

5. Additional experimental details are given by J. W. Lynn, Physica 136B, 117 (1986).

6. G. Aeppli, R. J. Cava, E. J. Ansaldo, J. H. Brewer, S. R. Kreitzman, G. M. Luke, D. R. Noakes, and R. F. Kiefl, Phys. Rev. B35, 7129 (1987).

7. W. J. Kossler, J. R. Kempton, X. H. Yu, H. E. Schone, Y. J. Uemura, A. R. Moodenbaugh, M. Suenaga and C. E. Stronach, Phys. Rev. B35, 7133 (1987).

NETWORK FORMATION OF THERMOSETTING POLYMERS - A SMALL ANGLE NEUTRON SCATTERING STUDY OF EPOXIES

W-L. Wu and B. J. Bauer
(Polymers Division)

The crosslink process of long chain molecules in bulk up to its gelation point has been simulated successfully in the classical theory by Flory & Stockmayer (FS). Their model is equivalent to a Bethe tree in which no closed loops are allowed. On the other hand, the results of a percolation model which allows for closed loops have been applied successfully in the crosslink of many systems e.g. silica gel and colloidal particles. It is the goal of this work to determine which model does the cure of thermoset follow. Intuitively, one expects that the percolation model will prevail due to the size of the thermoset monomers. However, there is an obvious difference between the percolation model and the cure of thermoset; there are two types of bonds in a cured thermoset, one is the monomer chain by which the reaction ends are originally connected and the other is that formed between the reacted ends. These two bonds are different in length for most cases. In the percolation model, however, only one type of bond is considered. It is, therefore, of interest to determine whether any of these two models will adequately describe the curing of thermoset.

Epoxy was chosen as the model system for thermoset and all the cure was conducted in the bulk state instead of in solution. More specifically, diglycidal ether of Bisphenol A (DGEBA) was cured with di- and tri amines connected with polypropylene chain (Jeffamine D-230 & T-403 respectively). All the curing was conducted at 60° C in the early stage and followed by a 23° C cure as the gel point was approached. The reason for lowering the cure temperature in the later stage was to capture samples with a small undercure, ϵ, defined as the distance to reach the critical degree of cure P_c. The extent of cure was monitored by both infrared spectroscopy (IR) and viscosity. As the cure precedes, specimens of different degree of cure were removed from the reaction bath and dissolved in deuterated THF. For each specimen, solutions of 3 to 5 levels of concentration were prepared; the lowest concentration was in the range of 0.2 % by volume. All these solutions were kept at -5° C throughout the whole experiment and no further cure was detected in any of the solutions. Small angle neutron scattering (SANS) results on these solutions were extrapolated to zero angle and zero polymer concentration to obtain the values of molecular weight (M_w) and radius of gyration (R_g) of the crosslinked polymer chains at various degrees of cure.

Since all the scattering measurements were carried out in solution, the excluded volume effect must be included in the data interpretation. Furthermore, we are dealing with a polydispersed system in terms of the size of the crosslinked molecules. One should not, therefore, expect to observe a simple fractal type scattering exemplified by the following relation

$$I(q) \propto q^{-D}$$

where q is the magnitude of the scattering vector and D is the mass fractal dimension by which the value of M_w and R_g are related through the simple relation $M_w \propto R_g^D$. After taking into account both the polydispersity and the excluded volume effects, the effective value for D is 1.64 for the percolation model and 1.0 for the F-S model.

The results of the epoxy cured with di-amine yield the value 1.15 for the exponent D which is close to what is predicted by F-S. This is a rather surprising result because the monomer sizes of the epoxy as well as the di-amine are far shorter than a long chain. Furthermore, the crosslink reaction is confined at the chain ends of the monomers instead of randomly distributed along the chains. A plausible explanation is that the primary amine reacts much faster than the secondary one as observed by other investigators, hence, linear chains of significant length are formed in the beginning of the cure. The later stage of cure is the crosslink of these linear long chains via the reaction of the secondary amines along the backbone chains. Such a two-stage reaction is expected to conform to F-S theory. In order to test the hypothesis mentioned above, tri-amine was included in this study. In this case even though the primary amine reacts much faster than the secondary one, a three dimensional network will still prevail over a linear chain. The SANS results on T-403 cured epoxy yield a value for the exponent D of 1.67 which is almost identical to what is predicted by percolation. To further test the percolation result, a high molecular weight specimen of tri-amine cured epoxy with a narrow size distribution was prepared through a solution fraction method. A typical fractal scattering behavior is observed in the SANS result and the fractal dimension is about 2.1. This value is close to that predicted by the percolation theory and is called "animal-like" behavior.

In summary, the results indicate that the crosslinking of thermoset in the bulk state follows the percolation process. However, in certain cases some specific chemical reaction mechanisms can modify the process towards what is predicted in F-S theory.

SANS STUDIES OF CROSSLINKED POLYMER BLENDS

B. J. Bauer, R. M. Briber, and C. C. Han
(Polymers Division)

P. G. de Gennes[1] has developed a theory describing the scattering function of crosslinked polymer blends. He makes an analogy with a dielectric medium. In a dielectric medium the separation of + and - charges is counteracted by an electrostatic force. In a polymer blend separation of the polymers causes chains to stretch so it is counteracted by elastic forces. He assumes that the blend components demonstrate "good miscibility" when crosslinked, and that crosslinks are present between the two different polymer types.

Equation (1) is the scattering function for a blend of equal amounts of two polymers with n_c units between crosslinks of step size b, χ_0 is the spinodal value of the interaction parameter of the uncrosslinked blend, and χ is the interaction parameter at the temperature of the scattering experiment. C is a coefficient of internal rigidity which is roughly estimated as $C = 36\ n^{-2}b^{-2}$.

$$I^{-1} = C/q^2 + (\chi_0 - \chi) + b^2q^2/24 \qquad (1)$$

This predicts that a plot of intensity versus q should have a maximum that varies as the inverse square root of n. There also should be no zero angle scattering. As the spinodal is approached, the peak will increase in intensity, but not change position. The single phase region will be greatly extended compared to the uncrosslinked blend.

Blends of high molecular weight polystyrene-d8 (PSD) and polyvinylmethyl ether (PVME) were made and were crosslinked by exposure to gamma irradiation at 45 C. Table 1 gives characterization of the samples studied. Scattering experiments were carried out from 120 C to 180 C.

Figure 1 shows corrected scattering intensity for blend crosslinked with 125 Mrad irradiation. As the temperature is increased a shoulder appears at 0.025 A^{-1}. The form of the scattering differs from the de Gennes prediction by not going to zero at $q = 0$. The problem seems to lie in the assumption that upon crosslinking the polymers have "good miscibility", indicating a flat baseline. Previous studies[2] have shown that low temperature scattering is weak, but has non zero low angle scattering.

To account for this non-zero baseline, a scattering experiment was performed at 45 C, the crosslinking temperature. When this is subtracted from the data of figure

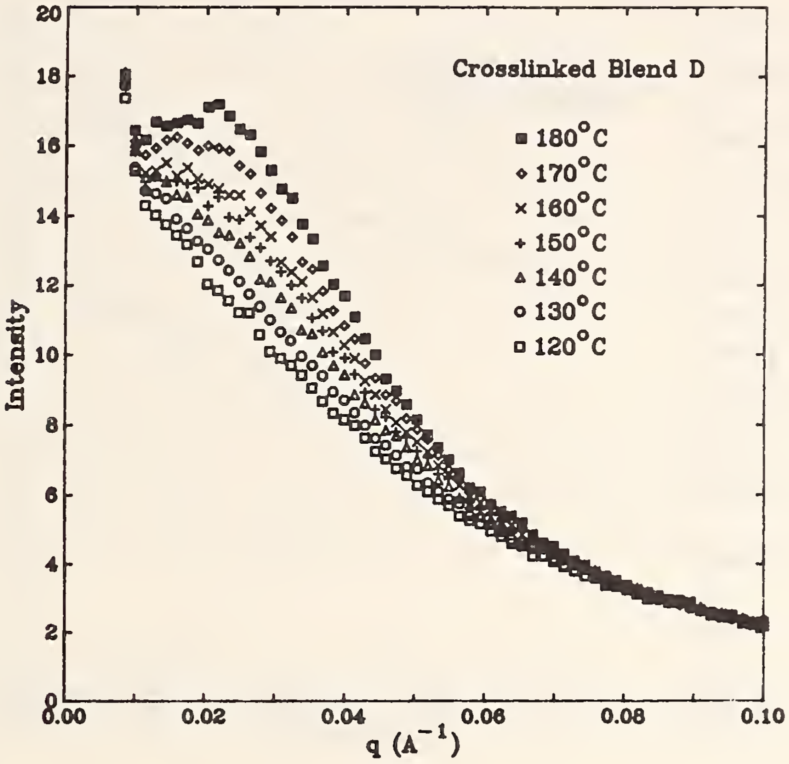

Figure 1. I versus q for sample D, 125 Mrad.

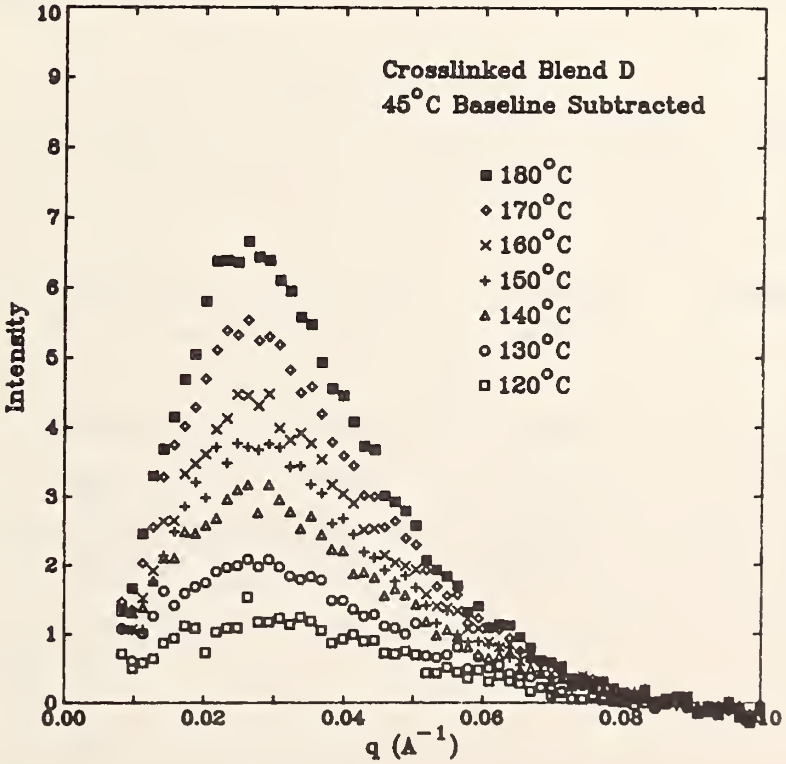

Figure 2. I versus q for sample D, 125 Mrad minus I versus q for sample A, 0 Mrad, 45 C.

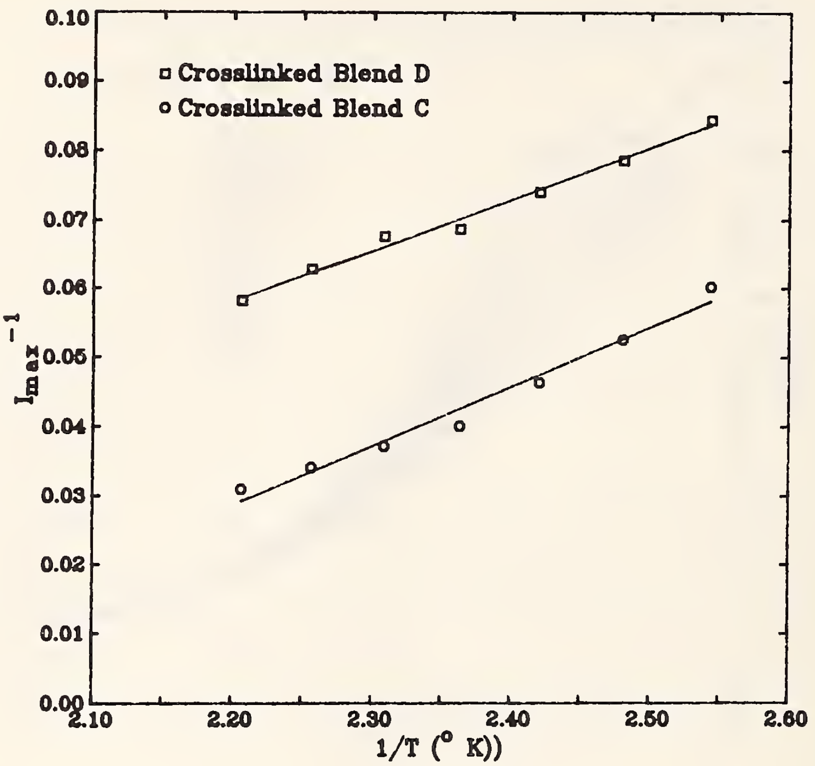

Figure 3. I_{max}^{-1} versus T^{-1} for samples C and D.

Table 1. Crosslinked polymer blends. Starting PVME Mw = 1.7 x 10^6, PSD Mw = 6.2 x 10^6, Φ_{PSD} = 0.3.

Sample	Dose (Mrad)	M_c-PSD	N_c-PSD	M_c-PVME	N_c-PVME
A	0	-------	----	-------	----
E	5	160,000	1450	380,000	6520
B	25	32,000	290	76,000	1300
C	50	16,000	145	38,000	652
D	125	6,500	58	15,000	261

1, figure 2 results. This is qualitatively what is predicted, a prominent peak increasing with increasing temperature, and intensity dropping to zero as q → 0. The peak position changes as the inverse square root of the irradiation time as is expected, but the coefficient of internal rigidity appears smaller than predicted.

The spinodal temperature is reached when the peak goes to infinity. Figure 3 is a plot of inverse scattering intensity versus inverse temperature for the samples with 50 and 125 Mrad exposure. There is only a weak dependence on temperature, extrapolations give spinodal temperatures of 260 C and 423 C, while for the uncrosslinked blend it is 150 C.

Qualitatively, de Gennes' prediction of the scattering from a crosslinked polymer blend is good when the non-zero baseline is accounted for. The scattering has prominent peaks that vary in position with the crosslink density and go to zero as q → 0. Crosslinking greatly extends the one phase region of the blend.

---

1. P. G. de Gennes, J. Physique Lett., 40, L-69 (1979).

2. C. C. Han, M. Okada, Y. Muroga, B. J. Bauer, and Q. Tran-Cong, Poly. Eng. Sci., 26, 3 (1986).

SANS STUDIES OF SINGLE PHASE INTERPENETRATING POLYMER NETWORKS

B. J. Bauer, R. M. Briber, and C. C. Han
(Polymers Division)

Interpenetrating Polymer Networks (IPN's) are systems in which one of the the polymeric components is polymerized in the presence of the other, with one or both being crosslinked to itself. In virtually every case phase separation takes place during the polymerization, giving a two phase morphology.[1] We have succeeded in polymerizing samples of semi-IPN's where one component is linear (polyvinylmethyl ether, PVME) and the other is crosslinked (polystyrene-d8, PSD). IPN's were formed without phase separation taking place giving single phase samples that can be studied by SANS in a way similar to blends of uncrosslinked linear polymers.[2]

Binder and Frisch[3] have studied the thermodynamics of weakly crosslinked IPN's. They add terms to the free energy of the blend due to the elastic contributions of the network. The second derivative of the free energy with respect to composition is given in equation (1).

$$\partial^2 \Delta F/\partial \Phi^2 = (B - 1/3)/(n_c \Phi_0) + 1/n(1 - \Phi_0) - 2_\chi \qquad (1)$$

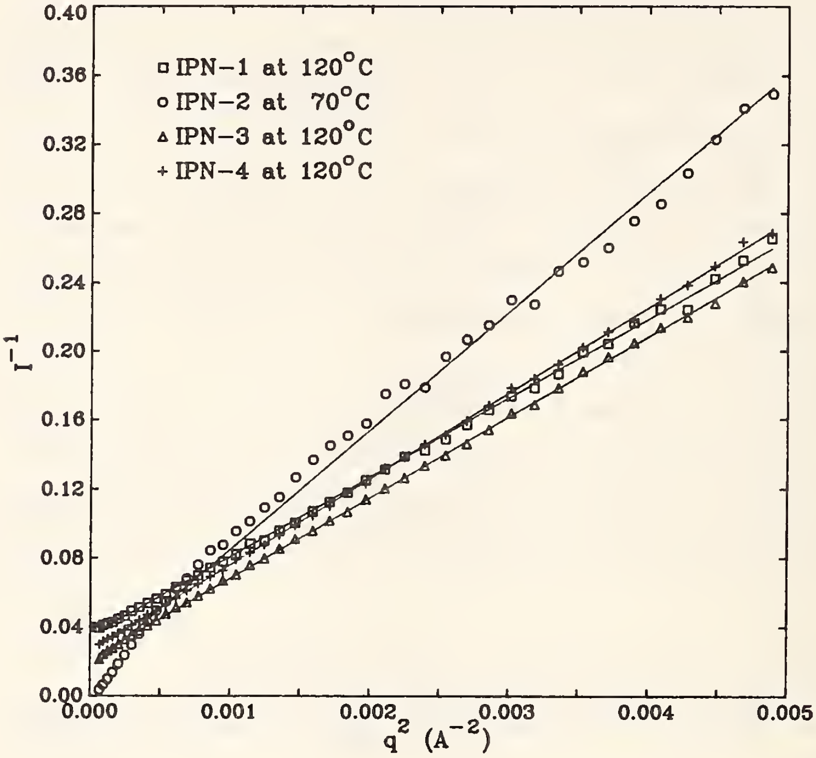

Figure 1. I^{-1} versus q^2 for samples 1,3, and 4 at 120 C and sample 2 at 75 C.

n is the degree of polymerization of the PVME, n_c is the number of units between crosslinks in PSD, Φ_0 is the volume fraction PSD, and χ is the interaction parameter. B is from rubber elasticity theory and can vary from 0 to 1 depending on the particular theory. The last two terms are identical to those of an uncrosslinked polymer blend. If $B > 1/3$ then the crosslinks should cause enhanced single phase stability, and $B < 1/3$ should destabilize the single phase region.

Table 1 gives the parameters of the IPN's in this study. Figure 1 is a plot of inverse scattering intensity versus q^2. Samples 1, 3, and 4 are linear as is true for an uncrosslinked blend. Sample 2, however, has a large amount of excess low angle scattering, indicating phase separation. In the process of polymerizing, the most densely crosslinked sample phase separated while the lower crosslink density ones did not.

Figure 2 is a plot of inverse zero angle scattering intensity versus inverse temperature. In uncrosslinked blends this gives a linear relationship and extrapolation to zero gives the spinodal. Samples 1 and 4 fit this well giving spinodals of 151 C and 146 C. Sample 2 has a pronounced curvature, indicating a different exponent.

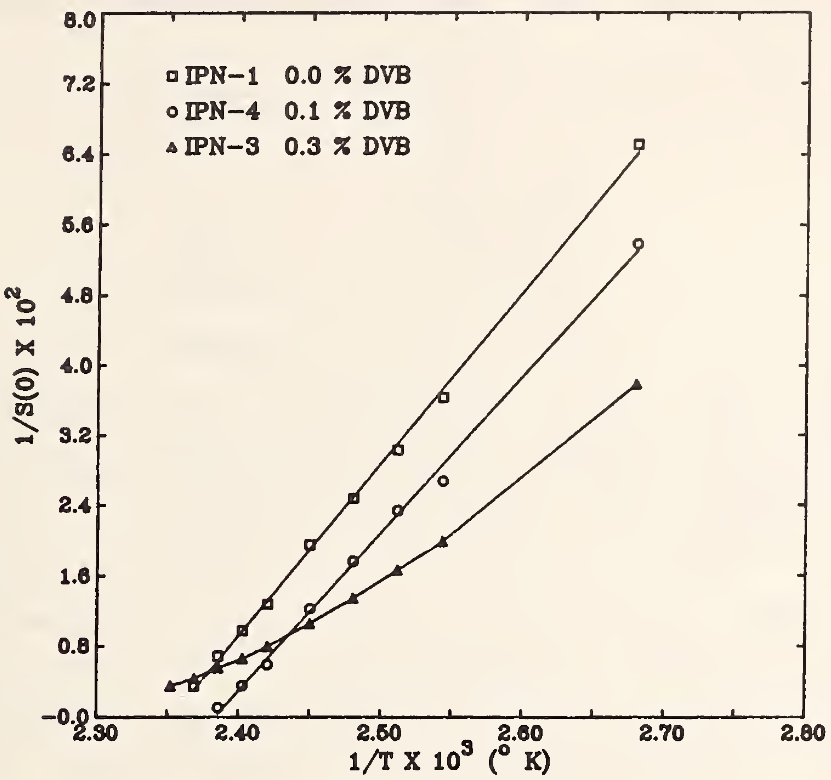

Figure 2. $S(0)^{-1}$ versus T^{-1} for samples 1, 3, and 4.

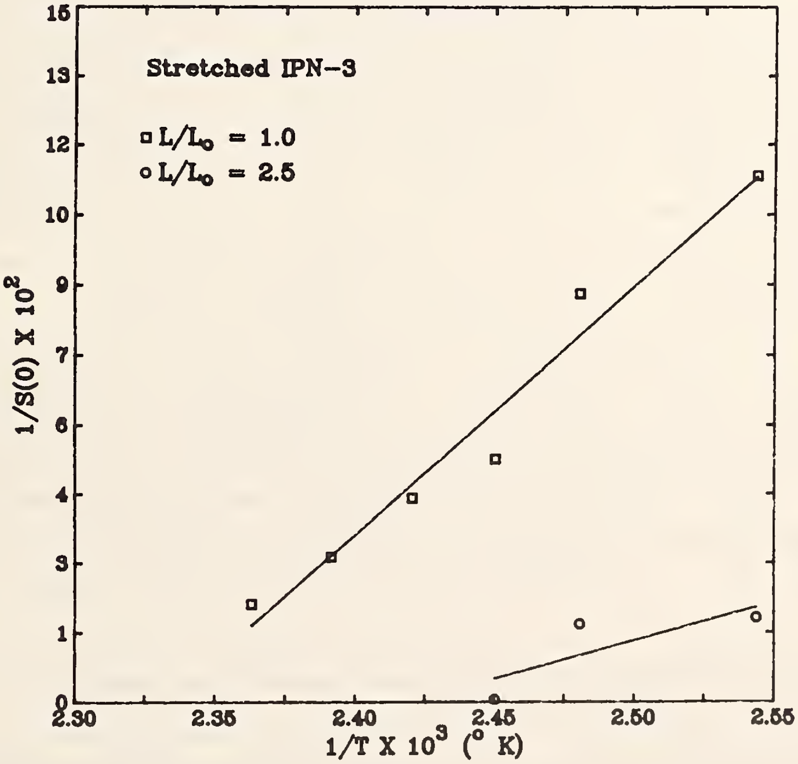

Figure 3. $S(0)^{-1}$ versus T^{-1} for deformed sample 3 parallel and perpendicular to the deformation direction.

Table 1. IPN's of PSD/PVME. Linear PVME Mw = 633,000.

Sample		M_c	n_c
IPN-1	0.57	-------	----
IPN-2	0.49	17,000	150
IPN-3	0.56	56,000	500
IPN-4	0.45	190,000	1700

At temperatures close to 70 C, the polymerization temperature, the sample with no crosslinking is furthest from the spinodal. As crosslink density increases, one gets closer to the spinodal until at the highest crosslink density, phase separation has occurred. As the temperature is increased, however, the lines cross over, with sample 3 having a higher crosslink density being further from the spinodal.

Sample 3 was also studied in a deformed state. The sample was placed in a holder with a groove cut into it. When compressed, the sample deformed in one direction only, the dimension perpendicular to it remained constant. The sample was stretched a factor of 2.5 in one direction and 1.0 in the other. The scattering pattern was asymmetric and averages were made of 15° sectors along the stretch and perpendicular to it. Zero angle scattering intensities from lorentzian plots are shown in figure 3. The two plots extrapolate to zero at different temperatures, indicating that the blend is destabilized along the direction of deformation. Because of the narrow sector, the statistics are poor and the exact shape of the curves cannot be determined. For the three highest temperatures, inverse intensity versus q^2 gave good fits perpendicular to the direction of deformation, but along the direction of deformation, the plots gave negative intercepts.

In conclusion, at the temperature of synthesis, the presence of crosslinker decreases the single phase stability, causing phase separation at the highest concentration. As the temperature is increased, however, the crosslinks inhibit phase separation. Upon deformation the sample is destabilized along the direction of deformation, causing different spinodal temperatures along the two directions.

---

1. L. H. Sperling, "Interpenetrating Polymer Networks and Related Materials," Plenum Press, New York, 1981.

2. C. C. Han, M. Okada, Y. Muroga, B. J. Bauer, and Q. Tran-Cong, Poly. Eng. Sci., 26, 3 (1986).

3. K. Binder and H. L. Frisch, J. Chem. Phys., 81, 2126 (1984).

SANS STUDIES OF INTERACTING HEMOGLOBIN MOLECULES IN INTACT ERYTHROCYTES

S. Krueger
(University of Maryland, College Park, MD)
and
(National Bureau of Standards, Gaithersburg, MD)

and

R. Nossal
(National Institutes of Health, Bethesda, MD)

Small angle neutron scattering (SANS) was used to investigate interaction forces between hemoglobin (Hb) molecules contained within human red cells. The scattering separately attributable to cell membranes and intracellular Hb was identified, and a series of D_2O-H_2O contrast variation measurements were made in order to establish conditions for which scattering from the cell membrane is minimized (ca. 15% D_2O).

In figure 1, the scattering profile from a normal RBC sample is compared with that from a preparation of RBC membrane fragments. These samples were washed and suspended in 100 % D_2O, conditions where incoherent scattering from hydrogen atoms in the solvent should be minimized. The data indicate that membrane scattering is negligible for $Q \geq 0.06$ Å^{-1}. Scattering cross sections obtained during contrast variation measurements on RBC's are shown in figure 2.

The average intracellular concentration of Hb in RBCs is about 330 mg/ml, so interference scattering must be taken into account in the data analysis. To a first approximation, the differential cross-section per unit volume for protein scattering may be written as (1,2)

$$I(Q) = K N_p (\Delta\rho)^2 V_p^2 P(Q) S'(Q) \qquad (1)$$

where N_p is the number of protein molecules per unit volume in the solution, V_p is the volume occupied by a single protein molecule and $\Delta\rho = |\overline{\rho}_p - \rho_s|$, the "contrast", is the difference between the average scattering density of the protein and that of the solvent. K is the fraction of the solution actually occupied by the protein cores of the cells. P(Q) is the "particle structure factor" representing the scattering from a single core particle averaged over all orientations and normalized such that P(0) = 1, and S'(Q) is the "averaged interparticle structure factor" which accounts for the interference scattering between particles.

Since hemoglobin is a spherical molecule, P(Q) is easily calculated. S'(Q) can be computed by solving the Ornstein-Zernicke equation in a mean spherical approximation (MSA) when the interparticle potential consists of a hard core and a Yukawa potential tail. An analytic solution for this case, which is based on the DLVO theory of interacting colloidal particles, has been provided by Hayter and Penfold (3) and their FORTRAN subroutine has been incorporated into a program which fits the data to the theoretical I(Q) given by Eq. 1.

In order to calculate the protein and membrane match points, MSA fits were made to the large Q (i.e. $Q \geq 0.06$ Å^{-1}) regions of the curves for RBCs in 0, 10, 20, 50, 70 and 100 % D_2O. Because protein scattering cross sections are small compared with membrane scattering in 50, 70 and 100 % D_2O, the MSA fits were somewhat uncertain for those conditions. However, the fitted MSA amplitudes, Amp, are relatively insensitive to slight variations in the shape of the scattering cross sections. A plot of $(\mathrm{Amp})^{1/2}$ vs % D_2O (see figure 3) places the Hb match point at approximately 39 % D_2O, in good agreement with results of earlier studies on Hb. Model calculations of the entire scattering cross section for the protein, $I_p(Q)$, were made for each solution condition by using the parameters of the best fit to the corresponding "large Q" data. The calculated $I_p(Q)$ then was subtracted from I(Q) in each case, yielding the scattering cross-sections $I_m(Q)$ for the membranes alone.

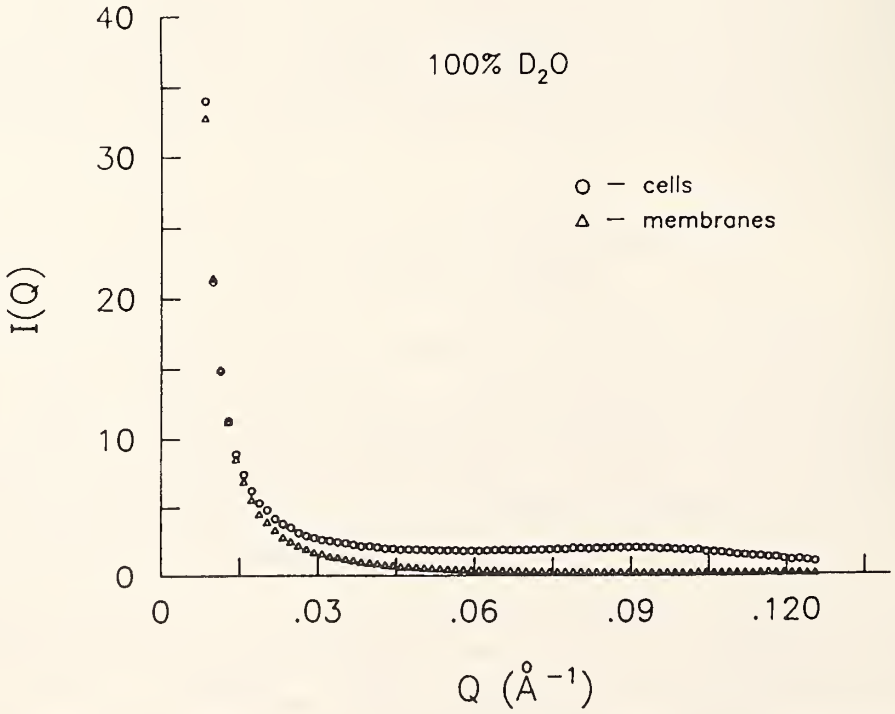

Figure 1. Comparison between scattering from intact RBCs and membranes, showing that the scattering from the Hb within the cells can be distinguished.

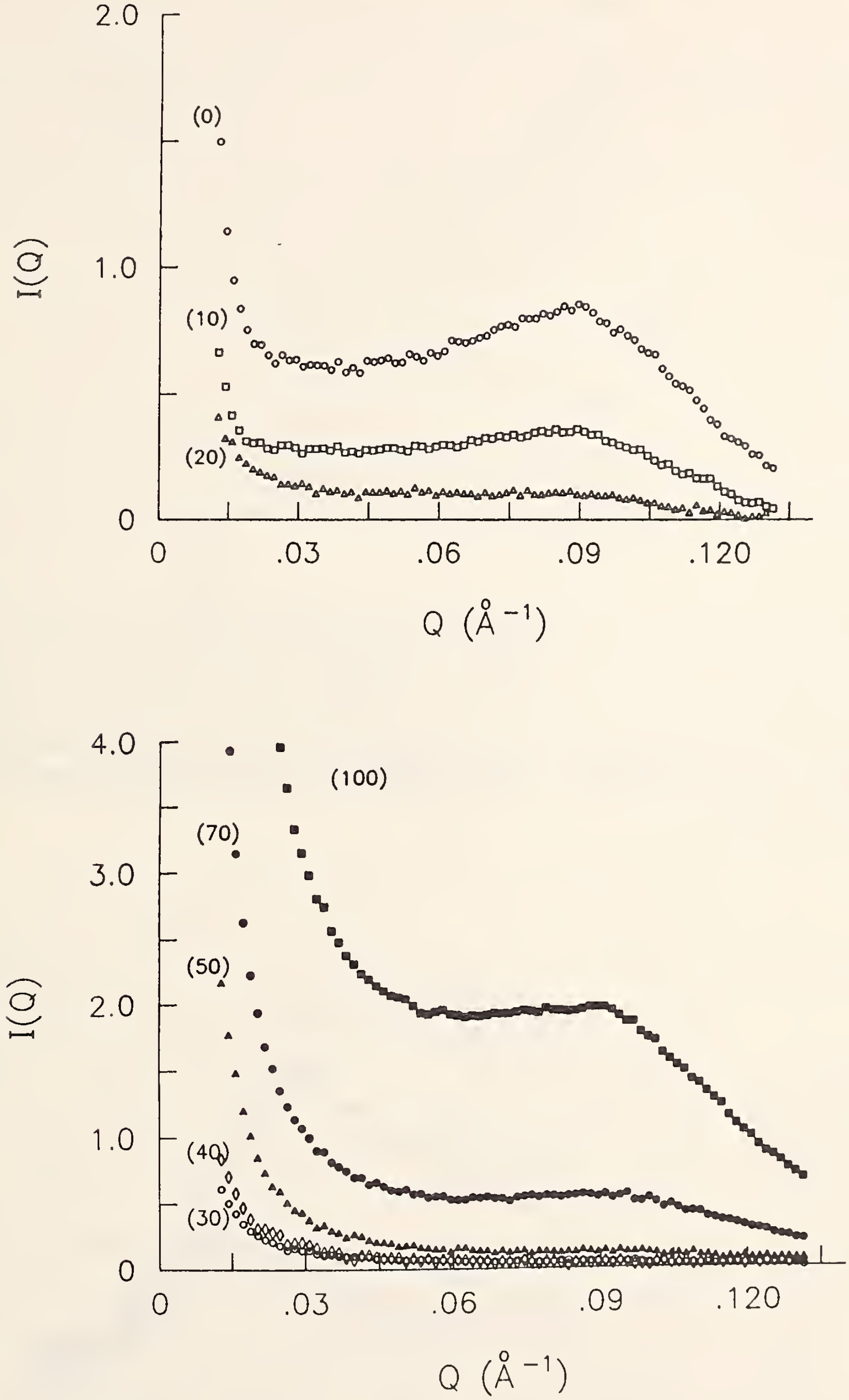

Figure 2. Contrast variation data, taken to establish optimal conditions for observing Hb interactions. a), b) Scattering cross-sections for differing D_2O percentages (in parentheses), plotted on an absolute scale.

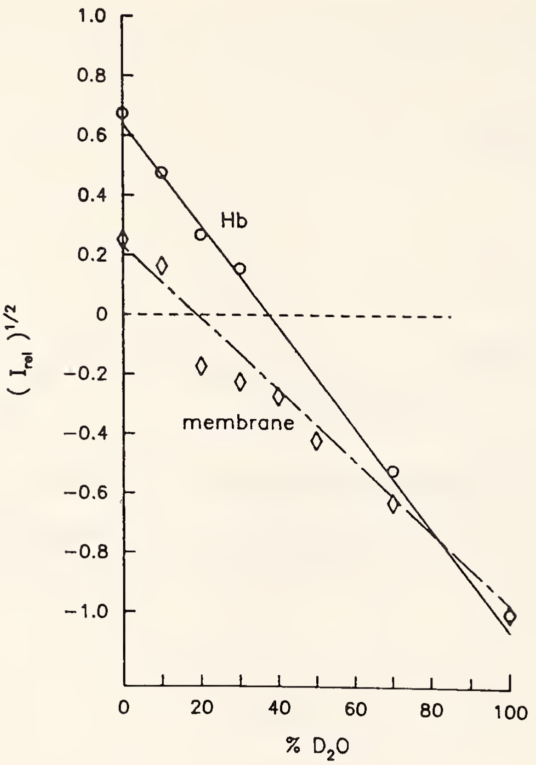

Figure 3. Amplitudes of separate scattering components (normalized to -1.0 at 100 % D_2O concentration), illustrating the approximate membrane and protein match points.

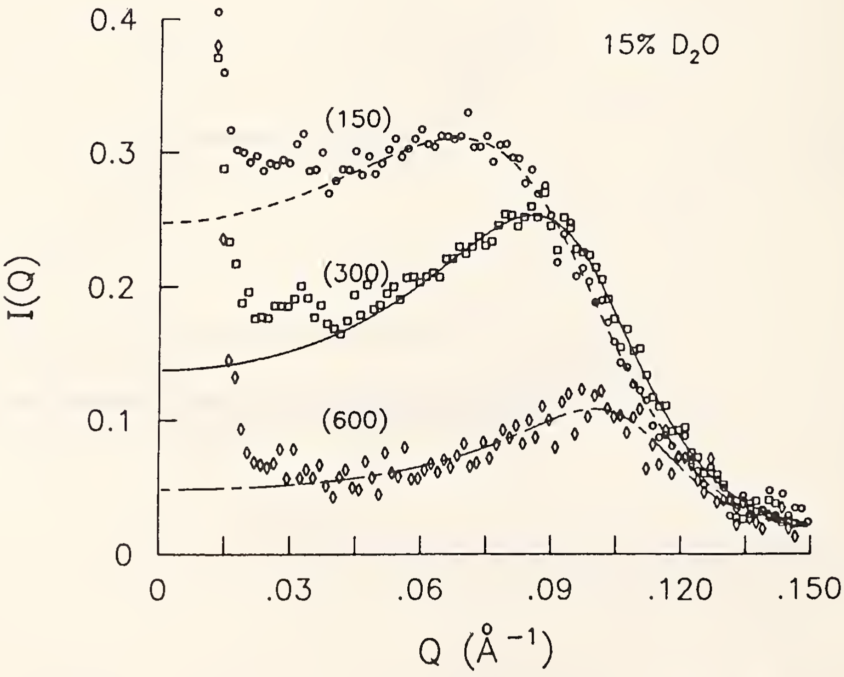

Figure 4. RBCs in 15 % D_2O buffer (pH 7.4) of differing osmolarity (mOsm, in parentheses). The lines represent calculated Hb scattering cross-sections based on the parameters of best fit to the data for Q ≥ 0.06 $Å^{-1}$.

Table 1. Red Blood Cells Under Varying Salt Conditions
15 % D_2O Buffer pH 7.4

	η	Z	R
High Salt (600 mOsm)	.286	20	26.8
Normal Salt (300 mOsm)	.223	12	27.8
Low Salt (150 mOsm)	.166	4	28.4

N_p = number of cells per unit volume remained constant as the salt conditions were varied.

$I_m(Q)$ is fit by using a flat sheet approximation (4) whereby the membrane is represented by a flat sheet with constant thickness, t, and two other, much larger, dimensions. The scattering intensity $I_m(Q)$ can be separated into a factor proportional to Q^{-2} and a second "thickness factor" such that

$$I_m(Q) = \frac{I_o}{Q^2} e^{-Q^2 R_t^2} \qquad (2)$$

A plot of normalized values of $(I_o)^{1/2}$ vs % D_2O, (see figure 3) shows that the membrane "match point" lies between 14 % and 18 % D_2O.

All further experiments were performed with RBCs in 15 % D_2O where the contribution of the membrane to the total scattering is minimized. For illustration, figure 4 shows the scattering profiles for RBCs in normal buffer (300 mOsm) as well as in "low salt" buffer (150 mOsm) and "high salt" buffer (600 mOsm). When the ionic strength of the solution is increased from that of the normal buffer, the cells shrink. Conversely, a decrease in ionic strength causes the cells to swell. In both cases, the concentration of Hb inside the cells changes, producing a corresponding change in the Hb volume fraction η. The volume fraction η, as well as effective Hb radius R and surface charge Z, were determined from the data fitting and are given in table 1.

In addition, oxygenation studies on normal cells were performed, and results contrasted with those of similar studies of erythrocytes obtained from sickle cell disease patients (5).

---

1. D. Bendedouch and S.-H. Chen., J. Phys. Chem. 87:1473-1477, (1983).
2. R. Nossal, C. J. Glinka, and S.-H. Chen, Biopolymers 25:1157-1175, (1986).
3. J. B. Hayter and J. Penfold, Mol. Physics 42:109-118, (1981).
4. G. Porod, In: Small Angle X-ray Scattering. Academic Press, New York, (1982) pp. 18-50.
5. R. Nossal and S. Krueger, Biophys. J. 51, 295a (1987).

COLD NEUTRON PROJECT

J. R. D. Copley, C. J. Glinka, J. Gotaas, G. Greene, M. Kahn,
W. Knill, J. LaRock, C. Majkzrak, C. O'Connor, D. Pierce,
J.M. Rowe, I.G. Schroder, T. Udovic, and R. Williams

1. Cold Neutron Research Facility

The final design for the construction of the Cold Neutron Research Facility, figure 1, has been completed by the Architect/Engineering firm of Burns and Roe. A design package of 150 drawings and 1000 pages of specifications has been produced and will be included in the final solicitation for fixed price construction bids. This solicitation will be issued at the end of July, and bids will be due in late October, with a construction start scheduled for late in 1987. The estimated construction period is 14 months.

The final design incorporates a neutron guide hall of 100 x 200', and an associated office/laboratory addition of 12,000 square feet. The guide hall will be equipped with a full span travelling crane of 20 ton capacity, with a crane hook clearance of 25'. The walls and crane are supported on augured cast-in-place concrete piles, and completely decoupled from the guide hall floor. The floor is slab on grade, supported by 95 percent compacted fill to provide a 2000 lb/sq. ft. floor loading capacity. Services are provided by means of floor trenches, and the floor is effectively decoupled into independent sections by these trenches to minimize vibration transmission. A recessed pit for future installation of a very stable vibration isolation system is provided. Additional independent reinforced concrete beams (7) supported by concrete pilings and decoupled from the rest of the floor are provided for support of the neutron guide tubes and mounting fixtures. The entire building is air-conditioned for temperature and humidity control. The design provides large window areas for maximum natural light. The office and laboratory area is an addition to the existing building which will provide an additional 35 offices, 12 laboratories, a conference room, a terminal room, space for all mechanical equipment (HVAC, etc.), and additional storage space.

2. Neutron Devices

Extensive effort has gone into the development of computer simulation codes to evaluate the performance of devices such as elliptical mirrors, toroidal mirrors, converging guide systems, logarithmic spirals and other neutron focussing systems. The effects of various sources of non-optimum performance such as aberrations have been studied, and configurations to minimize such problems have been developed and studied. The use of computer ray tracing allows easy introduction of realistic estimates of component performance, including surface irregularities, actual reflectivity of mirrors, and misalignment. There are many areas of cold neutron research in which these devices can provide important increases in neutron intensity, and we are currently evaluating alternative configurations for such use.

3. Instrument Improvements

a. Small Angle Neutron Scattering (SANS)

In order to make efficient use of the cold source flux, several upgrades to the current 8m SANS instrument have been implemented during the recent shutdown to install the cold source. The instrument's former 16-bit, 1/4 megabyte data acquisition computer has been replaced with a 32-bit, 6 megabyte machine using a CAMAC interface, paralleling the data acquisition architecture developed for the time-of-flight spectrometer. This new system includes high speed, CAMAC-based histogramming memory that allows rapid acquisition of data in separate memory areas that can be moved into the computer while a new area is being filled, thus enabling real time experiments. The external histogramming memory also frees the computer's cpu to carry out data analysis tasks, such as imaging and circularly averaging the 256 x 256 element data arrays associated with each data set, on-line while the data collection is in progress. The data acquisition software for the new system is based on a suite of programs developed, and proven reliable, for the time-of-flight spectrometer.

Other upgrades include additional shielding added to the detector flight path, the purchase of a second, 64 x64 cm^2 area detector and the implementation of a computer programable circulating bath and resistance heater system to provide improved variability and control of sample temperatures.

b. Time-of-Flight (TOF)

The neutron time-of-flight (TOF) spectrometer became operational during the previous year. The first materials investigated included zeolites, ionic conductors, intercalates, organic compounds, metal hydrides, and high-technology alloys and magnetic materials. Modifications planned for the coming year include (i) vertically curving (i.e., focussing) the second monochromator crystal to

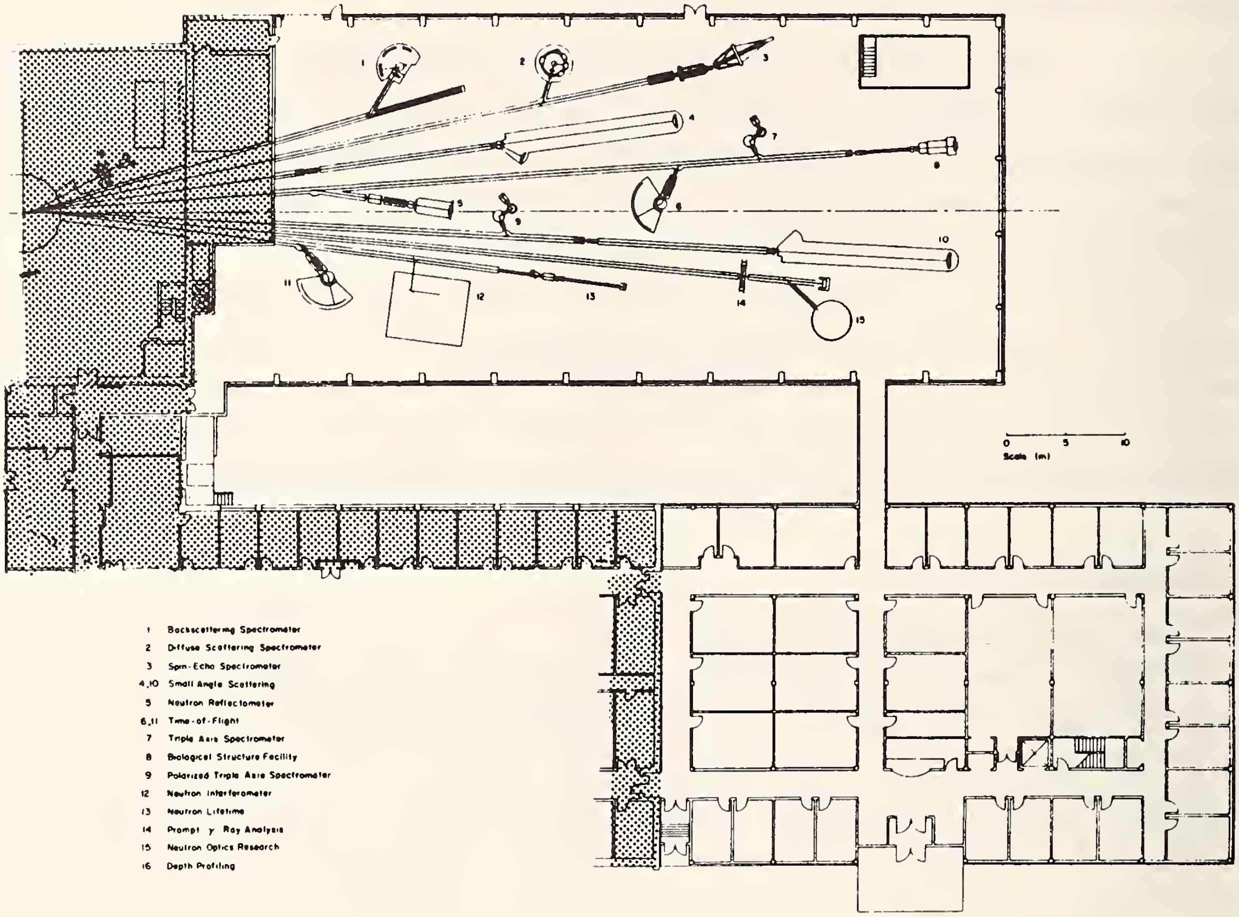

Figure 1. Plan view of Cold Neutron Research Facility. Existing structures are indicated by shading.

substantially increase the neutron flux on the sample; (ii) altering the chopper/sample area shielding design to decrease the sample-monochromator distance thereby increase the neutron flux, the sample-chopper distance to increase the resolution, and the neutron background reaching the detectors; (iii) installing an oscillating radial collimator between the sample and detectors to eliminate parasitic background scattering from the cryostat or furnace walls surrounding the sample; (iv) ganging detectors in pairs to allow utilization of all detectors with the present TOF interface unit during experiments; (v) altering the Be-filter elevator to permanently accommodate the pyrolytic graphite filter as a secondary filter option for incident energies above 5 meV; and (vi) improving the biological shielding from BT-6 to decrease the fast neutron and gamma radiation background levels in the vicinity of the TOF spectrometer.

4. Instrument Design

Several instrument designs are now underway, primarily at a conceptual stage. Design criteria are being developed and estimates of performance based on realistic assumptions are in progress.

a. High Resolution Time-of-Flight Spectrometer

This instrument is being designed to provide approximately 10-15 microvolt energy resolution with an incident wavelength of 6 Angstroms using multiple phased choppers and a sample-detector distance of 4 m. Such an instrument will offer a relatively wide range of wave vectors for quasielastic scattering studies at good resolution. A secondary design goal is the capability for rapid and routine decrease of energy resolution at fixed incident energy, with commensurate increase of intensity to allow for more rapid exploratory studies at the beginning of experiments. Our current estimates indicate that these criteria can be met with satisfactory intensity in a technically achievable design. This instrument will incorporate some of the neutron devices discussed above.

b. High Resolution Small Angle Neutron Scattering Spectrometer

Design of new 30m SANS instrument. Design work is underway for a new high resolution SANS instrument to be built jointly by NBS and the Exxon Research and Engineering Co. for the Cold Neutron Research Facility. With the space available in the CNRF guide hall, an instrument approximately 30m long can be built to resolve small angle scattering at Q-values as low as 0.0005 $Å^{-1}$ with a beam current at the sample of at least 10^4 n/sec. This represents an order of magnitude improvement in Q-resolution over the present 8m SANS instrument. The new instrument would also have a wider Q-range as a result of using two large area detectors, one which can be remotely positioning within an evacuated flight path at distances from 2.5 to 15m from the sample, with the second offset from the beam direction at a fixed distance of 1.5m from the sample to extend the Q-range to nearly 1 $Å^{-1}$. In addition, provisions are being made, through the specification of non-magnetic construction materials and the incorporation of neutron guide fields within the incident beam flight path, to have the option of using a polarized beam.

The principal monochromator for the instrument will be an improved type of mechanical velocity selector recently developed at the Central Institute for Physics in Hungary. This type of selector has been designed to provide not only continuous tunability of the wavelength of the beam over a wide range, but also continuous adjustment of the wavelength spread, $\Delta\gamma/\gamma$, from about 0.05 to 0.25, FWHM. For polarized beam measurements, the velocity selector will either be followed by a polarizing filter or replaced by a double monochromator of multilayer polaring crystals.

We are exploring the feasibility of using ellipically curved, grazing incidence mirrors to collimate and focus the incident beam. Preliminary calculations indicate that substantial gains in beam current at the sample, over what is possible with any type of pinhole collimation, can be achieved if suitable mirrors can be fabricated. We are currently exploring possible sources for such mirrors.

c. Depth Profiling Facility

The neutron depth profiling (NDP) instrument is being designed to take advantage of the two or more orders-of-magnitude increase in signal intensity expected over the existing facility. Drawing from five years of experience at the BT-3 instrument and in collaboration with academic and industrial users of the facility, the new instrument will be constructed at the short cold-neutron guide (NG-0) contained within the reactor confinement building. New features to be incorporated will include: automated sample handling, near real-time spectral processing, goniometer positioning of the sample and detectors, and temperature control of sample. More sophisticated improvements being considered include; in situ ion milling of the sample, medium resolution optical imaging, laser alignment for off-angle positions, and ultimately, focused neutrons for added intensity and spatial specificity. The use of multiple charged particle and/or time-of-flight detectors will improve depth resolution. The increase in signal intensity will permit multidimensional imaging of elemental distributions and routine profiling of nuclides with absorption cross sections for charged particle emission of less than 1 barn.

d. Prompt Gamma Analysis Facility

The neutron capture prompt gamma instrument is expected to show an order of magnitude better sensitivity than existing thermal-beam installations, primarily because of the absence of fast neutrons and gamma rays from the beam. Particular care is being given in the design to the elimination of background lines from H, B, C, and N. The system will allow samples to be irradiated in vacuum or a controlled atmosphere under remote control. The computer based counting system is being designed for high resolution gamma ray spectroscopy at high counting rates. In order to resolve cascade transitions in complex spectra, we intend that two or more high efficiency Compton-suppressed detectors will be operable as a gamma-gamma coincidence spectrometer or as separate single-parameter detectors.

5. Microstructure and Macromolecular Research with Cold Neutrons Workshop

On December 8-9, 1987, NBS will sponsor a workshop on MICROSTRUCTURE AND MACROMOLECULAR RESEARCH WITH COLD NEUTRONS, one of a series of workshops which will focus on the scientific opportunities arising from the cold neutron capabilities of the CNRF. Invited technical talks will cover current areas of research on submicron structures in materials, including macromolecular structures in polymers and biomaterials, and discuss new frontiers which will benefit significantly from the availability of cold neutrons. An important goal of the workshop is to introduce the potential user community to the instruments and techniques planned for the facility, and to provide an opportunity for early input which may guide the ultimate development of the CNRF. For technical information, contact Charles J. Glinka (Reactor Radiation Division, 301-975-6242), James A. Gotaas (RRD, 301-975-6243) or Charles C. Han (Polymer Division, 301-975-6771). For general information about the workshop, please contact Mrs. Kathy Stang, A345 Physics Building, National Bureau of Standards, Gaithersburg, MD 20899.

NBSR COLD NEUTRON SOURCE

R. S. Carter and P. A. Kopetka

The required modifications to the cold source cryostat that were indicated by the tests described in the previous report have been completed and the cryostat has successfully passed a complete series of tests including a one week run at low temperature while hooked up to the refrigerator external to the reactor.

The insertion of the cold source including its outer shield of bismuth and lead was completed July 17, 1987. The various tubing and instrumentation connections will be made during July, and initial tests are expected to start in August.

HYDROGEN IN METALS

R. C. Casella

I have carried out an analysis using a two-well potential for the α-phase motion of hydrogen in yttrium (without pairing), which analysis results in a prediction for the hydrogen/deuterium isotope shift that runs counter to experiment.[1] This result is interpreted as lending further credence to the pairing interpretation of Anderson et al.,[1] since it tends to require an explanation of the neutron scattering data which lies outside the simple picture of an isolated hydrogen atom moving in a potential determined solely by its interaction with the metallic host atoms. This (indirect) inference is further limited by the specificity of the potential employed and the approximate nature of the solutions obtained. The assumed potential is of the form

$$V(\vec{r}) = A\,(x^2 - a^2)^2 + (m\omega_\perp^2/2)\,(y^2 + z^2). \qquad (1)$$

[Eq. (1) is essentially equivalent to the quartic form employed earlier by N. Berk, J. Rush, J. M. Rowe and collaborators[2] for the motion of hydrogen in the β-phase of V_2X, $X = H,D,T$.] I have obtained variational solutions for the motion along x ($x \parallel$ c-axis), employing linear combinations of trial wave functions centered at $x = \pm\ a$, which are of the form of ground-state and first-excited-state oscillator functions, but with the coefficient in the exponent of the gaussian treated as a variational parameter in each case. Initially, analytic solutions were found via perturbative expansion in a parameter $\epsilon = (\epsilon_0/\omega)$, where $\epsilon_0 = (1/ma^2)$ and $\omega = (8Aa^2/m)^{1/2}$. ω is the local oscillator energy for motion along x about ($x = \pm\ a$, $y = 0$, $z = 0$). ($\hbar$ = 1.) For hydrogen in yttrium, setting $a = 0.65$ angstrom, one finds $\epsilon_0 = 9.8$ meV. From the inelastic neutron data, $\Delta = E_1(\parallel) - E_0(\parallel) = 100.1$ meV.[1] If one ignores the small splitting of each level and <u>assumes</u> $\omega \sim \Delta$, then $\epsilon \simeq (1/10)$. Within this small-overlap hypothesis (SOH), I find

$$\Delta = \omega + 3\epsilon_0/8 = \omega(1 + 3\epsilon/8). \qquad (2)$$

Thus, the parameter A in the potential is determined by the hydrogen data. Holding A fixed, one can then predict the corresponding excitation $\Delta(D)$ for inelastic neutron scattering from deuterium in yttrium. I find $\Delta(D) = 70.0$ meV, to be compared with the experimental result, $\Delta(D) = 75.8$ meV. That is, under SOH the anharmonic correction leads to a predicted ratio $\Delta(H)/\Delta(D) = 1.430$, which is larger than the harmonic ratio 1.414, whereas the experimental ratio, 1.321, is smaller.

A somewhat more general analysis, in which the SOH was not made, but still employing variational trial functions of the same analytic form as before, was also carried out using numerical techniques. Of the many solutions obtained of this class, when compared with experiment, the physically allowed solutions reduced to essentially those obtained under SOH, evidencing small splittings about the SOH values.

Short of obtaining agreement with the experimental ratio for a single fixed value of A, any conclusion will be limited by the analytic form of the assumed potential. It is perhaps worth recalling that the theoretical predictions I derived some time ago[3] for the ratio of various cross sections for neutron scattering apply to the general two-well problem, although they remain somewhat difficult to implement experimentally.

---

1. I. S. Anderson, J. J. Rush, T. Udovic, and J. M. Rowe, Phys. Rev. Letters, 57, 2822 (1986).

2. N. F. Berk, A. Magerl, J. J. Rush, J. M. Rowe, and J. L. Provo (unpublished).

3. R. C. Casella, Phys. Rev. B 24, 2913 (1981).

COHERENT NEUTRINO SCATTERING FROM CRYSTALS

R. C. Casella

I have previously demonstrated[1] that for reactor antineutrinos of wavelengths less than or of order crystal lattice constants ($E \gtrsim 10$ keV), the net force exerted by the antineutrino "wind" on a crystal is linear in the number N of nuclei in the target crystal, rather than quadratic in N as postulated in reference 2 in order to explain an observed force ~ 10^{-5} dyne on a crystal in the neighborhood of a reactor, as reported therein.[2] I have subsequently investigated the force exerted by ultralow-energy antineutrinos with wavelengths large compared with the crystal dimension, say, $\gtrsim 1$ cm (i.e., $E \lesssim 10^{-10}$ MeV). Based upon standard nuclear physics, one expects the current density $J[\mathrm{cm}^{-2}\ \mathrm{s}^{-1}\ \mathrm{Mev}^{-1}]$ of such antineutrinos emanating from a fission reactor to be negligible because of phase-space considerations.[3] Nonetheless, since N^2 enhancements can occur at such ultralow energies,[1] I have estimated an upper bound on the force exerted by the reactor antineutrino wind on such a crystal by ignoring the phase-space fall-off at ultralow E, approximating the Avignone-Greenwood spectrum[3] by a simple exponentially falling one of the form, $J = J_0 \exp(-E/E_1)$, with $E_1 \simeq 1.2$ MeV and normalizing the integrated spectrum $\int dE\, J(E)$ to that expected several meters from the core of a 20 megawatt reactor of the NBS type. If one assumes zero-mass neutrinos, then the low energy cross section, as calculated within the standard Glashow-Weinberg-Salam electroweak theory, is proportional to E^2. Moreover, in computing the momentum transfer, an additional factor of E enters. Therefore, extrapolating from the MeV region where typically the cross section for coherent scattering from the nucleons in each nucleus leads to nuclear cross sections $\sim 10^{-42}$ cm^2, I find that, even with an N^2 enhancement, the net force is entirely negligible. I have also considered the effect of possible massive neutrinos, assuming an electron-type neutrino mass of order 10 eV, the upper bound determined from tritium end-point laboratory experiments and as estimated from the timing of the neutrino burst from Supernova 1987A (as observed in the Kamiokande and IMB underground detectors). Again, although considerably larger, the estimated force is entirely negligible. Aharonov et al.[4] have subsequently provided additional arguments supporting my original conclusions.[1]

---

1. R. C. Casella, Nuovo Cimento <u>94A</u>, 42 (1986); R. C. Casella, in <u>Intersections Between Particle and Nuclear Physics -- 1986</u>, ed. D. F. Geesman, AIP Conf. Proc. No. 150, p. 1040, American Institute of Physics, New York (1986).

2. J. Weber, Phys. Rev. C <u>31</u>, 1468 (1985).

3. F. T. Avignone III and Z. D. Greenwood, Phys. Rev. C <u>22</u>, 594 (1980) and F. T. Avignone III, private communication.

4. Y. Aharonov, F. T. Avignone III, A. Casher, and S. Nussinov, Phys. Rev. Letters <u>58</u>, 1173 (1987).

NEUTRON-ANTINEUTRON OSCILLATIONS AND THE POSSIBILITY OF "SQUEEZED STATES" IN NEUTRON INTERFEROMETRY

R. C. Casella

Recently, Yurke[1] has concluded that by employing the output of one interferometer as the input to a second interferometer, the analogue of a "squeezed photon" state can be achieved for the neutrons, despite their fermionic nature, leading to a coherent state for which $\delta\phi \sim 1/N$ rather than $1/\sqrt{N}$, $\delta\phi$ is the precision with which the interferometric phase shift ϕ can, in principle, be measured. If the construction of squeezed neutron states is indeed possible, then despite formidable practical problems associated with "regeneration" upon interaction of the mixed state $|a\ n + b\ \bar{n}>$ with the interferometer "mirrors", the possibility of employing neutron interferometry to detect neutron-antineutron ($n\bar{n}$) oscillations, which I have discussed earlier,[2] is reopened, at least in principle. Motivated by conversations with S. A. Werner, I have begun an investigation of the possibility of constructing such squeezed neutron (or other fermionic) states as well as the general concept of squeezed states.

---

[1] B. Yurke, Phys. Rev. Letters 56, 1515 (1986).

[2] R. C. Casella, Phys. Rev. Letters 53, 1033 (1984).

PATTERSON FOURIER ANALYSIS OF THE ICOSAHEDRAL (Al,Si)-Mn ALLOY

J. W. Cahn
(Institute for Material Science)
and
D. Gratias
(C.E.C.M./C.N.R.S., Vitry, France)
and
B. Mozer

X-ray and neutron diffraction data obtained from single phase icosahedral powder $Al_{73}Mn_{21}Si_6$ are analyzed using a generalized Patterson auto correlation function in 3 dimensions. The icosahedral pattern is quasiperiodic. The local atomic arrangements match those encountered in the prototypic crystalline α phase. Extra peaks in the local icosahedral pattern match those of an icosahedrally rotated α.

SIX-DIMENSIONAL FOURIER ANALYSIS OF ICOSAHEDRAL $Al_{73}Mn_{21}Si_6$ ALLOY

D. Gratias
(C.E.C.M./C.N.R.S., Vitry, France)

and

J. W. Cahn
(Institute for Materials Science)

and

B. Mozer

Fourier analysis of X-ray and neutron diffraction data of an icosahedral alloy are displayed both as a 3D quasiperiodic function and as a 6-D periodic function. The 6-D analysis leads to a simpler description that contains the same information as the 3D analysis: The 6-D function has only two elongated peaks in the unit cell, but each peak contains much chemical detail.

TRIPLE-SHELL SYMMETRY IN ALPHA (Al,Si)-Mn

H.A. Fowler and J. Sims
(Center for Applied Mathematics)

and

B. Mozer

We describe 3-D graphics modeling experiments executed on a calligraphic system. Utilizing precise data from neutron diffraction, a triple icosahedral shell has been identified in the alpha (Al,Si)-Mn phase. These triple shells are centered in the unit cell; the $Pm\bar{3}$ structure is completed by double shells on the cube corners. The triple shell can also be viewed as a composite of twelve coordination icosahedra around the manganese sites on the second (Mackay) shell.

B. Non-RRD Programs

NEUTRON ACTIVATION ANALYSIS OF MICROSCOPIC SAMPLES

R. M. Lindstrom
(Center for Analytical Chemistry)

and

D. J. Lindstrom
(Lockheed EMSCO, Johnson Space Center, Houston, Texas)

An experiment was undertaken to determine the feasibility of neutron activation analysis of very small samples. Johnson Space Center (JSC) is interested in the compositional analysis of individual grains of cosmic dust, with dimensions of 10 micrometers and below, collected in high altitude aircraft flights. The test consisted of a sustained irradiation at high neutron flux in the NBS Reactor, followed by radioassay using a low-background NBS gamma-ray detector (EG&G Ortec, model GEM-40195) installed in the underground Radiation Counting Laboratory at JSC. Neutron activation analysis of such small samples has been reported only once before, in a short article with little experimental detail (reference below).

Samples were individually packaged in quartz tubes. NBS samples were 8 Õg of SRM 1633 Fly Ash (melted to glass on a Pt foil), 15 Õg of K-411 Mineral Glass (SRM 470), and 11 Õg of K-412. JCL samples were Murchison chondrite and Washington University standard glass. The package was irradiated in the G2 tube at a nominal flux of 3.0E14 n/cmõs for 102 hours. The calculated fluence is thus 1.1E20 n/cmõ. A sevenfold increase in sensitivity is possible in future measurements by irradiating for a full fuel cycle. After cooling for four days in the water-filled thimble, the activity was low enough to ship to JSC without special precautions.

The low-level Ty detector was set up in a 4" lead shield in the RCL, 60 feet beneath ground level. The counting room is constructed of welded, selected steel plate surrounded by 3 feet of dunite gravel, a mineral low in K, U, and Th. A cryogenic system that can remove radon from the air supplied to the counting room was not in operation for these preliminary measurements because of high operating expense.

Quartz can be handled without hazard after a week's irradiation, and its transparency is unimpaired by radiation damage. All quartz was somewhat active. NBS quartz contains Sb, and Suprasil cut at JSC with a file contained activities from Cr, Fe, Sc, Co, and Ba. Samples needed to be transferred before counting. The quartz tubes were readily opened by scoring and snapping. Subsamples of as little as 10 ng (determined by the activity ratio from weighable larger pieces) were readily picked from a crushed larger sample using only a sharp pick and a stereo microscope.

The gamma background in the underground shield contains no more than the following components:

1. Pb x-rays, since the shield is not lined with low-Z material.
2. Continuum, peaking around 200 keV with centroid about 350, which is presumably due to the interaction of high energy cosmic rays with the lead shield around the detector.
3. The 511-keV positron annihilation line, from cosmic-ray activation products.
4. Decay products (Pb-214, Bi-214) of 3.8-day Rn-222. This component was reduced by a factor of five by flushing the shield continuously with nitrogen boiling off from the Dewar.
5. A small amount (0.0003 ct/sec) of K-40, not detectable with certainty in an overnight count. The ratio of the counting rate inside the shield to that outside suggests that most of this comes through the the hole in the shield through which the detector is inserted.

None of these components of the background signal is clearly assignable to the detector or Dewar.

The integral background from 100 to 1100 keV for several detectors in several shields is as follows:

Det	Rel eff	Location	Background	Figures of merit	
name	E (%)		B (ct/s)	E/B	E**2/B
Ty	44.7	JSC RCL Pb	0.43	104	4600
Ty	44.7	RCL room	1.29	35	1550
Fran	47.4	NBS B119	1.79	26	1271
Ty	44.7	NBS B119	3.77	12	530
Abby	34.8	NBS B119	1.70	21	710
Sarah	26.3	NBS B119	1.30	20	530
AMD	18.4	Compt sup	1.45	13	230
AMD	18.4	Unsupp	1.52	12	220

Clearly, the combination of the large, low-background Ty detector in the clean lead shield installed in the underground counting room at the RCL is greatly superior to any other combination.

In agreement with calculations, usable signals for several elements were recorded with sample sizes down to 10 ng. In the gamma-ray spectra of the Murchison samples, the major peaks observed are from Fe, Cr, Co, and Sc. Masses of these elements can be determined with impressive sensitivies. For example, amounts of Sc and Co of about 10^-12 grams can be analyzed with an accuracy of better than 5%. With optimized experimental design and long counting times, several additional elements should be analyzable with reasonable precision by INAA in particles of chondritic composition. These include Ir, Zn, Ni, and Se.

Primarily because of shipping delays, we were unable to count the samples until 12-20 days after irradiation. Several elements (Na, Br, La, Sm) could probably have been easily detected if we had been able to count the samples earlier.

Many other elements might be detected if present in higher abundance than in chondritic materials. These include K, Ca, Hf, Zr, As, Sb, Rb, Cs, Sr, Ba, Ta, U, Th, Ag, Au, and the additional rare earths Ce, Nd, Eu, Tb, Yb, and Lu.

A RADIOCHEMICAL PROCEDURE FOR ULTRATRACE DETERMINATION OF CHROMIUM IN BIOLOGICAL MATERIALS

R. R. Greenberg and R. Zeisler

Chromium was recognized as one of the elements essential for optimum human nutrition more than twenty five years ago.[1] However, at elevated levels, some forms of Cr are toxic[2] and possible even carcenogenic.[3] Unfortunately, the accurate determination of Cr in biological materials continues to be one of the more difficult problems in analytical chemistry. In particular, the determination of this element at naturally occurring ultratrace levels in biological fluids such as blood, blood serum, and milk or milk powder frequently leads to erroneous results. The results of an interlaboratory comparison[4] of trace element concentrations in milk powder, conducted by the International Atomic Energy Agency (IAEA), included Cr concentrations reported by 13 different laboratories. These results ranged over five orders of magnitude, and only one laboratory reported Cr concentrations which were within 50 % of the current, best estimate of the actual Cr concentration.[5]

Neutron activation analysis (NAA) is one of the best analytical techniques currently available for trace and ultra-trace level determination of Cr in

Table 1. Preliminary Chromium Concentrations Determined in Human Whole-Blood Samples

Individual	Cr Concentration - ng/g[1]	
BG	0.157 ± 0.023	0.158 ± 0.016[2]
BK	0.267 ± 0.019	
M	0.142 ± 0.019	
T	0.338 ± 0.018	
D	0.148 ± 0.016	
W	0.117 ± 0.025	

---

[1] Fresh weight basis. Uncertainties are 1 sigma counting statistics.

[2] Complete analysis of a duplicate sample.

Table 2. Chromium Concentrations (ng/g) Determined in NBS Standard Reference Materials

Material	This Work[1]	Certified
Bovine Liver (SRM 1577)	80 ± 2	88 ± 12
Milk Powder (SRM 1549)	2.65 ± 0.17	2.6 ± 0.7

---

[1] Uncertainties are $2s/\sqrt{n}$

biological materials. It possesses the sensitivity required to determine sub-ng amounts of Cr, and the nearly blank-free nature of the technique allows chemical dissolution and separation of Cr from the sample matrix (after irradiation) without regard to reagent blank. In addition, NAA is free from chemical interferences, and most types of matrix effects which can interfere with other, non-nuclear, analytical techniques. However, the nuclear interference from the fast neutron reaction Fe-54 (n,alpha) Cr-51, is significant and must be considered when Fe is present in the sample.[6] The interference may be considerable depending on the fast flux of the irradiation facility, and upon the relative amounts of Cr and Fe in the material. The interference from the fast neutron reaction can be minimized, however, by using a highly thermalized facility such as the RT-4 facility of the NBS Research Reactor.[7] Even in matrices with Fe concentrations more than 100,000 times greater than that of Cr, such as whole blood, the interference in RT-4 is smaller than the directly produced Cr-51 activity, and can be accurately subtracted.

To achieve the ultimate sensitivity of NAA, often the most effective approach is to perform a radiochemical separation to isolate the element(s) of interest from other elements which can interfere directly via gamma-ray overlap, or indirectly by elevating the background level of radiation under the peak of interest via Compton events and/or bremsstrahlung. Chromium is particularly susceptible to the latter type of interference in view of the relatively low energy of its 320 keV gamma-ray. A variety of single-element, radiochemical procedures have been developed previously (8-10) to separate Cr from an irradiated biological matrix. These have predominantly been based upon the distillation of chromyl chloride, or upon the liquid/liquid extraction of Cr(VI) into a solution of tribenzylamine (TBA) in chloroform. Separations based upon the former can suffer from low yields[8] unless a relatively complex distillation apparatus is used.[9] However, use of such a piece of apparatus is at least inconvenient, and also provides the potential for cross-contamination of samples, in view of the relatively long half-life of Cr-51. Liquid/liquid extractions of the Cr(VI)/TBA complex are more convenient and use a much simpler apparatus, however, low yields,[8] and/or other problems have resulted in the determination of incorrect Cr concentrations in some matrices.[8,10]

In view of the relative ease of liquid/liquid extraction procedures, investigations have focused on identifying and eliminating earlier problems, and developing a reliable, radiochemical separation procedure, based on extraction with TBA, to determine Cr in biological materials at the ppb and sub-ppb levels. Such a procedure has been developed and includes a two-stage dissolution procedure to minimize the possibility of losses of volatile Cr compounds, the addition of potassium permanganate to oxidize and maintain Cr in the +6 state, two extractions with 5 % TBA in chloroform to quantitatively extract Cr(VI), and a back-extraction into an aqueous solution of sodium hydroxide to provide a stable environment for Cr(VI). The Cr can also be precipitated as barium chromate to improve the counting geometry for samples containing very low levels of Cr i.e., <1 ng.

This procedure has been used to determine the Cr concentrations in whole-blood samples collected, under clean conditions, from six individuals. The results obtained are listed in table 1. Duplicate samples have been run for one person and both values are listed. The apparent Cr produced by the interference from Fe has been determined and subtracted. The uncertainties listed in table 1 represent 1 sigma counting statistics and are typically about 10 % of the Cr concentration. These relatively high uncertainties are not truly representative of the quality of the separation since these samples were processed after decay periods to 2-3 half-lives of Cr-51. This was to allow instrumental measurements using an anti-compton system to be made. In addition, relatively mild irradiation conditions were used: 16 hours at a fluence rate of 2.7 E 13 n/cm^2-s. Since the background radiation under the Cr peak was due to natural sources outside of the sample, and therefore constant, increasing the irradiation time by a factor of two, and reducing the decay time to one half life of Cr-51, should reduce the uncertainty due to counting statistics to a few percent.

Four samples of the Milk Powder, and three samples of the original NBS Bovine Liver (SRM 1577) were analyzed as an additional check of the analytical procedures developed in this work. The results obtained are compared with the certified values in table 2. The values found in this work are within the concentration range certified by NBS.

---

1. W. Mertz, Physiol. Rev. 49 (1969) 163-167.

2. U. S. EPA, Quality Criteria for Water, Washington D. C. (1976).

3. J. C. Arcos, Amer. Laboratory 10 (1978) 29-41.

4. R. Dybczynski, A. Veglia, and O. Suschny, "Report on the Intercomparison Run A-11 of Inorganic Constituents of Milk Powder," IAEA Report - IAEA/RL/68 (1980).

5. A. R. Byrne, C. Camara-Rica, R. Cornelis, J. J. M. de Goeij, G. V. Iyengar, G. Kirkbright, G. Knapp, R. Parr, and M. Stoeppler, "Results of a Co-ordinated Research Programme to Improve the Certification of IAEA Milk Powder A-11 and Animal Muscle H-4 for Eleven "Difficult" Elements," Proc. 2nd Int'l. Workshop on Biological Reference Materials, Neuherberg, FRG, April 24-25, 1986 - in press.

6. R. Cornelis, J. Hoste, and J. Versieck, Talanta 29 (1982) 1029-34.

7. D. A. Becker, J. Radioanal. Nucl. Chem 112 (1987) -in press.

8. R. Stella, N. Genova, M. Di Casa, M. Gallorini, and E. Orvini, J. Radioanal. Chem 34 (1976) 59-63.

9. P. Lievens, R. Cornelis, and J. Hoste, Anal. Chim. Acta, 80 (1975) 97-108.

10. L. T. McClendon, Proc. Trace Substances in Environ. Health-VIII, Columbia, MO (1974) 255-257.

DETERMINATION OF TRACE ELEMENTS IN INTERNATIONAL DIETS

Venkatesh Iyengar
(Center for Analytical Chemistry)

An international project sponsored by the IAEA, and supported by the NBS, the FDA and the USDA is currently in progress (1). This project is designed to assess the daily dietary intake of minor and trace elements by selected target populations in several countries. The countries involved are Australia, Brazil, Canada, China, Iran, Italy, Spain, Sudan, Sweden, Thailand, Turkey and the U.S.A.

Mixed total diets from these countries are being analyzed for caloric energy, phytate and fiber content, and minor and trace elements. Analysis for these constituents are being carried out in selected reference laboratories identified by the IAEA. The NBS is one such reference centers to determine a selected group of inorganic elements.

The U.S. efforts involves both as a collection center and as a reference laboratory. The first part of the project was used to establish the analytical approaches (2,3). An ion-exchange separation method to assay Cd, Co, Cr, Cu, Mn and Mo in foods at low concentration levels has been established at the NBS Reactor Facility. Guidelines have been developed for the preparation of mixed diet reference standards for quality control. The collection of US benchmark samples of mixed diets based on the FDA Total Diet Study scheme is in progress. Until now four such collections have been completed. One portion of mixed diet from each of the four collections has been stored in the National Environmental Specimen Bank.

Three of the four U.S. diets have already been analyzed for minor and trace elements, proximate constituents, phytate and fiber. The results obtained for total mixed diets for several elements show remarkable agreement with the daily intake data calculated from the individual food analysis results of FDA-TDS study (4), thus confirming the validity of this approach for monitoring the dietary intake of minor and trace elements. Recently, a set of 20 samples belonging to Italy, Spain and Turkey has been analyzed. Sample preparation work for another batch of 24 samples is currently in progress. As an example, concentrations of Cd and Mo in the diets from different countries are shown in Table 1. The NBS Bovine Liver (SRM 1577a) was used for quality control during the analysis, and these results are also shown in the Table.

Besides determination of inorganic constitents of foods, Investigations are in progress to study long-term stability of organic nutrients in mixed diets by periodic monitoring of the diet material preserved under liquid nitrogen temperature. Work is also in progress to prepare a mixed diet SRM.

Table 1. Concentrations of Cd and Mo in international diets.
(Results are ug/kg of dry diets, Mean + 1 S.D.)

Country	n	Cd	Mo
Italy	5	39.3 ± 14.3	159.2 ± 51.0
Spain	7	24.9 ± 15.8	199.1 ± 124.2
Turkey	6	18.7 ± 10.9	562.7 ± 279.7
U.S.A.	3	28.9 ± 3.9	272.0 ± 25.5
Reference Material (µg/g, Mean + 2 S.D.)			
SRM 1577a	4	0.41 + 0.04	3.70 + 0.56
(Certified value		0.44 + 0.06	3.50 + 0.50)

---

1. Co-ordinated Research Programme on Human Daily Dietary Intakes of Nutritionally Important Elements as measured by Nuclear and Other Techniques, International Atomic Energy Agency, Vienna, Austria. Report of the First Research Co-ordination Meeting, Gaithersburg, Beltsville and Washington, D.C., March 19-22, 1985.

2. G.V. Iyengar, J.T. Tanner, W.R. Wolf and R. Zeisler Preparation of a mixed human diet material for the determination of nutrient elements, selected toxic elements and organic nutrients, A preliminary report, Sci. Total Environ. 61(1987)235-252.

3. G. V. Iyengar, Dietary intake studies of nutrients and selected toxic elements in human studies: Analytical Approaches. Clin. Nutr. 6(1987)105-117.

4. J. Pennington, B.E. Young, D.B. Wilson, R.D. Johnson and J.E. Vanderveen Mineral content of foods and total diets. The selected minerals in foods survey, 1982-84. J. Am. Diet. Assoc. 86(1986)876-889.

STATUS OF SPECIMEN BANKING ACTIVITIES AT THE NATIONAL BUREAU OF STANDARDS

S. A. Wise, B. J. Koster, R. R. Greenberg, S. F. Stone and R. Zeisler
(Center for Analytical Chemistry)

I. Introduction

Since 1975 the National Bureau of Standards (NBS) and the U.S. Environmental Protection Agency (EPA) have been involved in the development of methods and procedures for environmental specimen banking. In 1975 the Federal Republic of Germany (FRG) and the U.S. EPA agreed to cooperate in the study of environmental specimen banking activities and proposed the establishment of "pilot phase" specimen banks in both countries. The purpose of the EPA/NBS Environmental Specimen Bank Program was to determine the feasibility of long-term storage of environmental and biological specimens for the determination of inorganic and organic constituents. In 1980 a "pilot" environmental specimen bank was established at NBS to evaluate the feasibility of a large-scale National Environmental Specimen Bank. The pilot Environmental Specimen Bank program was to provide working experience in all aspects of specimen banking, e.g., in specimen collection, processing, storage, and analysis.

The approach of the EPA/NBS pilot Environmental Specimen Bank was to gain experience in the collection, storage, and analysis of four types of environmental accumulators: (1) human tissue, (2) marine tissue, (3) food, and (4) air. The goals of the pilot phase were:

1. To develop procedures for the sampling, processing, storage, and analysis of four types of environmental accumulators;
2. To evaluate and improve analytical methods for the determination of trace element and organic pollutants in biological matrices;
3. To evaluate the feasibility of long-term storage of environmental samples under various conditions;
4. To establish baseline data on selected environmental samples, and;
5. To evaluate the potential application of specimen banking for trend monitoring and for providing samples for retrospective analyses as concerns about new pollutants arise and as new analytical techniques are developed.

Since 1980 the EPA-NBS Pilot Environmental Specimen Bank has been involved in the collection, storage, and analysis of the first sample type, human liver tissue. However, the remaining three sample types (i.e, marine, food, and air accumulators) were not incorporated fully into the EPA pilot banking program as originally designed because of funding limitations. During the past year the specimen banking concept at NBS has been modified to reflect current funding levels from EPA and the interest of other agencies in specimen banking activities. The pilot phase is near completion and has been described briefly above and in other publications [1-3]. Several agencies will be sharing the NBS/EPA Specimen Bank facility and will be adapting the procedures developed in the pilot phase. New research has been initiated to study the banking of other specimen types. The current components of these efforts are described in the following sections.

II. Biomonitoring Specimen Bank Research Project

As the "pilot phase" (1980-1986) nears completion, the program will move towards a "project phase" of the Biomonitoring Specimen Bank Research Project. This title reflects the change from solely environmental aspects to the inclusion of specimens of nutritional and medical importance. At present there are five existing specimen banking activities within the NBS specimen banking program, and several other projects are proposed for incorporation into the program in the coming years (see Table I).

EPA Specimen Bank Program

The EPA-NBS Specimen Bank Program will continue to serve as the focal point for specimen banking-related activities during the project phase. The pilot phase of the EPA specimen banking activities resulted in a number of outputs including the following:

1. Development of protocols for the sampling, processing, and storage of environmental/biological specimens (e.g., human liver and marine bivalves); development of cryogenic homogenization procedures for biological specimens;
2. Improved analytical methods for the determination of inorganic and organic constituents in environmental/biological samples;
3. Analytical baseline data for inorganic constituents on 96 liver specimens from three collection periods (1980, 1982, and 1984); analytical data for organic constituents (PCBs and pesticides) on 60 liver specimens from two collection periods (1982 and 1984);
4. An archive of over 500 human liver specimens and a large collection of mussels which are available for future investigations.

The expertise developed during the EPA pilot project has been implemented in other specimen bank projects at NBS as well as by researchers in other programs. For example, sampling and homogenization procedures for human liver and mussels developed in the pilot project were used as the starting point for the development of the protocols used in the National Status and Trends Program sponsored by the National Oceanic and Atmospheric Administration (NOAA) (see discussion below). The existing analytical data base on inorganic and organic constituents in human livers collected from 1980 to the present and the over 400 unanalyzed specimens in the bank represent a substantial resource and a unique opportunity for EPA to investigate pollution trends. During the next year the activities of the EPA-NBS project will be directed towards the evaluation of the analytical data base for possible trends and the evaluation of the compositional stability of the human liver specimens stored under different conditions.

NOAA National Status and Trends Program

In 1985 a specimen banking project was initiated at NBS with the National Oceanic and Atmospheric Administration (NOAA) as part of their National Status and Trends (NS&T) Program to monitor the U.S. marine environment [4]. The NS&T program consists of two monitoring programs: (1) the Benthic Surveillance Project, in which sediment and fish tissue (muscle and liver) are collected annually from approximately 50 coastal sites and (2) the Mussel Watch Project, in which bivalves (mussels and oysters) and sediment are collected annually from approximately 150 coastal sites. As part of the NOAA NS&T program, NBS provides the following specimen banking activities:

1. Develop sampling, homogenization, and storage protocols for sediment, bivalve, fish muscle, and fish liver samples;
2. Archive specimens of sediment and tissue from 12 sites of the Benthic Surveillance Project and mussels/oysters and sediment from 30 sites in the Mussel Watch Project each year; a complete set of samples from all sites will be archived after five years.
3. Analyze selected samples of sediment, bivalves, and fish livers for the determination of selected trace elements (15 elements) and organic compounds (organochlorine pesticides, PCBs, and PAH);
4. Analyze sediment and tissue intercalibration materials as quality assurance exercises.

In addition to the specimen banking activities for the NOAA NS&T program, NBS is involved in the NOAA NS&T program as the laboratory responsible for organic analysis quality assurance activities. These activities include the preparation and distribution of control and/or intercalibration materials and calibration solutions to the various laboratories involved in making analytical measurements for the NS&T program and organizing annual quality assurance workshops to discuss the quality of the analytical data generated within the program. NOAA is also supporting NBS in the preparation of a marine sediment to be issued as a Standard Reference Material for the determination of organic pollutants. Both of these activities complement and support the efforts related to specimen banking of marine specimens.

IAEA/FDA/USDA/NBS Nutrients in Human Diet Program

NBS, the Food and Drug Administration (FDA), and the Department of Agriculture (USDA) are collaborating in a coordinated research program sponsored by the International Atomic Energy Agency (IAEA) to obtain comparative data on the dietary intakes of 23 nutritionally important minor and trace elements in a number of developing and developed countries [5]. In the U. S. effort, which combines the expertise of the three participating government agencies, four aspects are addressed: (1) benchmark total diet samples from the FDA Total Diet Study (TDS) are prepared and analyzed to provide data for the IAEA project; (2) representative portions of these benchmark samples are stored in the NBS specimen bank facility; (3) analytical research is carried out to develop analytical techniques for the determination of a number of constituents in total diet samples and to develop a total diet reference material; (4) the immediate and long-term stability of such total diet samples with respect to organic and inorganic nutrients during handling and storage are investigated.

Several tasks related to the total diet study are included in the expansion of specimen banking activities to this field:

1. Bank aliquots of mixed total diet samples based on the FDA market basket collections;
2. Methods development, analyses, and quality assurance;
3. Intercomparison of analytical methods for trace elements in existing dietary reference materials;
4. Preparation of U.S. mixed diet research material from the 200 different food groups in the FDA Total Diet Study (10 kg); and

5. Determination of long-term stability of trace constituents in the total diet composite.

Future collections of this total diet sample will include the variations in season as well as the four major areas of FDA's TDS. Within several years, a complete inventory of the FDA market basket survey will exist in the proposed Biomonitoring Specimen Bank.

National Cancer Institute (NCI) Chemoprevention Program

As part of a quality assurance program of the National Cancer Institute Chemoprevention Program, NBS is serving as the reference laboratory for the NCI contract laboratories involved in the determination of nutrients in human serum. The following analytes are currently included in the study: zinc, selenium, beta-carotene, retinol, alpha-tocopherol, and ascorbic acid. As part of this program NBS prepares and distributes intercalibration samples to the various laboratories. Since the long-term stability of these nutrients in serum (frozen and lyophilized) is unknown, selected intercalibration serum samples and calibration solutions have been archived under various storage conditions. These samples are periodically removed from the bank and analyzed to determine the stability of these nutrients in the specimens. These stability investigations will provide additional information on the behavior of various matrices with respect to long-term specimen banking.

NOAA Alaska Marine Mammals Tissue Archive

NOAA will be banking selected tissues from marine mammals for the future determination of contaminants associated with offshore oil and gas development. A pilot program has been initiated to develop and implement sample collection protocols for liver, muscle, and adipose tissue from marine mammals. Fur bearing seals will be the first specimen type included in this study. Additional species of Alaska marine mammals will be incorporated into the archive in future years.

III. Analytical Work at the NBSR

Analysis of Human Livers

A representative portion of the samples included in the bank has been analyzed to provide data for real time monitoring, determination of long term stability, and evaluation of today's analytical capabilities. Initially, a combination of four techniques provided a comprehensive data set for 36 human livers. However, several key trace elements were not detectable in all samples or insufficient data was obtained from a particular analytical technique. Frequently, analyses had to be repeated to detect low levels or to confirm results. This expensive approach needed improvement to reduce the amount of sample required and to limit the number of techniques and analytical steps required. In addition, the naturally occurring levels of several pollutant trace elements were approximately one order of magnitude lower than previously reported, thus requiring more sensitive analytical procedures.

Since NAA had been used for the determination of most of the above elements, on individual 1 g (fresh weight) samples, further expansion of NAA and lowering of its detection limits could effectively achieve this goal. Therefore, we modified the instrumental NAA procedures and added radiochemical separation procedures that would provide the additional sensitivity and precision required. The modifications included full usage of the higher fluence rates after the upgrade of the NBSR, as well as application of Compton suppression high resolution gamma spectrometry and multi-element separations in inorganic ion exchange columns (HMD, Carlo Erba). The details of these procedures are described elsewhere [6].

A major part of this work was to determine up to 30 elements for baseline studies in human livers collected during 1982 and 1984. The ranges of elemental concentrations found in the sixty selected specimens are summarized in Table II. As discussed above, improved INAA and RNAA procedures were implemented to lower detection limits and to include additional elements. The significant improvements in detection limits achieved for the low level trace elements Cr, As, Ag, Sn, and Sb are summarized in Table III. These detection limits represent the element concentrations at which, with 95% probability, a sample with the given concentration would generate a detectable signal. The lower detection limits permitted the determination of the aforementioned elements in all 1984 specimens. The nuclear procedures were complemented in an ideal manner by voltammetry. Results for nickel, copper, cadmium and lead from this technique [7] have been included in Table I.

Analysis of Fish Livers

Samples from twelve sites were selected for analysis from the thirty sites collected and banked in the 1985/86 NS&T Benthic Surveillance program. The samples consisted of up to 200 fish liver sections that were cryogenically homogenized and then freeze-dried for analysis. Sequential INAA procedures were used as described previously [8] to determine more than thirty elements in the tissues. The data gives some indication of the variations due to sampling sites and species. For Table IV, we have selected vanadium, chromium, and silver to illustrate these variations and to indicate possible threats to the health of the marine environment.

Table I. Inventory of Specimens in the Biomonitoring Specimen Bank

SAMPLE TYPE	DATE INITIALLY BANKED	NUMBER OF SPECIMENS	RATE OF INPUT	ALIQUOT DESCRIPTION
HUMAN				
EPA:Livers	2/1980	520	35 per year	Left lobe sectioned into A and B replicate samples of approximately 150 grams each, stored double-bagged in teflon.
NCI:Serum	6/1986	991	750-1000 per year	2mL clear or amber ampoule and 5 mL clear glass rubber stoppered bottles containing serum with vitamins and/or nutrients.
MARINE				
EPA:Mussels	3/1983	93	one time collection	Narragansett mussels approximately 70 per bag stored double-bagged in teflon.
NOAA:NS&T	7/1985		MW-30 sites per year BS-10 sites per year	Sediment approximately 150 gram replicate samples stored double-bagged in teflon or teflon jars. Bivalves stored double-bagged in teflon containing 50 mussels with A and B replicates or 30 oysters with A and B replicates. Fish liver and fish tissue stored double-bagged in teflon, approximately 150 gram replicate samples.
MW-Sediment		63		
Bivalves		62		
BS-Sediment		20		
Fish Tissue		18		
Fish Liver		17		
FOOD				
IAEA/USDA/FDA	8/1985	3	1-4 per year	Each diet is divided into 8 aliquots of approximately 750 grams and stored double-bagged in teflon, 4 bags remain in the bank and the remaining 4 are used by other agencies, currently a total of 17 bags are banked.

Table II. Ranges of Trace Element Concentrations (mg/kg fresh weight) in Sixty Selected Human Liver Specimens.

	1982 Collection		1984 Collection	
Element	Low	High	Low	High
Na	720	2265	750	2140
Mg	81.5	171	104	246
Al	0.525	2.22	0.29	7.31
Cl	1019	2418	984	1980
K	1645	3942	1330	3090
Sc	0.000096	0.00093	0.00028	0.00051
V	≤ 0.016	≤ 1.05	0.011	0.026
Cr	≤≤0.01	0.18	0.01	0.12
Mn	0.608	1.964	0.742	2.152
Fe	73.22	441.3	38.6	915
Co	0.026	0.059	≤ 0.017	0.074
Ni	0.0027	0.037	0.0029	0.036
Cu	3.62	17.2	2.60	23.8
Zn	29.3	103	36.97	99.87
As	≤ 0.001	0.0268	0.0022	0.0203
Se	0.327	0.631	0.348	0.838
Rb	1.74	8.07	2.701	8.930
Mo	0.241	1.41	0.332	1.41
Ag	≤ 0.003	0.0347	0.00086	0.0341
Cd	0.28	6.05	0.440	3.268
Sn	---	---	0.050	2.420
Sb	≤ 0.0008	0.0122	0.0013	0.0772
Cs	0.0012	0.019	0.0079	0.0146
La	≤ 0.008	0.417	0.0017	0.0191
Ce	≤ 0.01	0.52	≤ 0.022	0.086
Sm	≤ 0.0009	0.0154	≤ 0.0003	0.0033
Au	---	---	≤ 0.00008	0.06164
Hg	---	---	0.0423	0.329
Pb	0.138	0.926	0.23	1.03
Th	---	---	≤ 0.002	0.0047

Table III. NAA Limits of Detection (μg/kg) for Seven Critical Elements in Human Livers.

	MODIFICATION A			MODIFICATION B		
Element	INAA Normal	INAA Suppressed	RNAA	INAA Normal	INAA Suppressed	RNAA
Cr	10	4	0.5	40	15	1.0
As	30	5	-	10	5	1.0
Se	6	-[a]	-	35	-[a]	0.5
Mo	25	20	-	45	30	40[b]
Ag	4	-[a]	-	40	-[a]	0.7
Sn	300	200	10	3000	2000	30
Sb(^{122}Sb)			-	2	0.7	30
Sb(^{124}Sb)	3	0.8	-			

[a] Due to coincident gamma lines, Ag and Se are not included.

[b] The 739 keV line of ^{99}Mo was used to avoid an additional decay period required for the ^{99}Mo - ^{99m}Tc equilibrium to be established.

Table IV. Selected Trace Elements in Benthic Surveillance Fish Liver Samples Determined by INAA. Concentrations in mg/kg fresh weight; uncertainties are 1σ counting statistics of samples and standards.

Location	Species	V	Cr	Ag
Dana Point	White Croaker	≤ 0.030	0.290 ± 0.004	0.3930 ± 0.0035
Elliott Bay	English Sole	0.644 ± 0.020	2.81 ± 0.03	0.0509 ± 0.0022
Nisqually Reach	English Sole	0.1397 ± 0.0083	4.21 ± 0.03	0.0480 ± 0.0017
Mississippi Delta	Atlantic Croaker	0.0334 ± 0.0082	0.203 ± 0.005	≤0 0.0040
Corpus Christi	Atlantic Croaker	0.072 ± 0.012	0.146 ± 0.005	0.0711 ± 0.0017
Charlotte Harbor	Spot	≤ 0.10	0.125 ± 0.006	0.0791 ± 0.0024
Boston Harbor	Winter Flounder	0.457 ± 0.013	0.140 ± 0.006	0.6187 ± 0.0053
Buzzards Bay	Winter Flounder	0.392 ± 0.012	0.012 ± 0.005	0.1233 ± 0.0023
Bodega Bay	Starry Flounder	0.258 ± 0.011	0.042 ± 0.004	0.1638 ± 0.0020
Southampton Shoal	Starry Flounder	0.290 ± 0.013	0.021 ± 0.005	0.0716 ± 0.0026
Santa Monica Bay	Hornyhead Turbot	0.584 ± 0.033	0.050 ± 0.006	2.510 ± 0.020
St. John's River	Atlantic Croaker	0.0348 ± 0.0085	0.045 ± 0.005	0.0336 ± 0.0021

1. Zeisler, R., Harrison, S.H., and Wise, S.A. (1983), The Pilot National Environmental Specimen Bank - Analysis of Human Liver Specimens, NBS Special Publication 656, U.S. Government Printing Office: Washington, D.C., 135 pp.

2. Zeisler, R. and Wise, S.A. (1985), Quality Assurance and Protocols in Sample Preparation of Biological Samples, In: Biological Reference Materials: Availability, Uses, and Need for Validation of Nutrient Measurements, W.R. Wolf, Ed., John Wiley & Sons, Inc.: New York, NY, pp 257-279.

3. Wise, S.A. and Zeisler, R. (1984), The Pilot Environmental Specimen Bank Program, Environ. Sci. Technol. 18, 302A-307A.

4. Lauenstein, G.G. and Calder, J.A. (1987), Specimen Banking: A Key Element of the National Oceanic and Atmospheric Administration's National Status and Trends Program, Proc. 10th U.S.-German Seminar of State and Planning on Environmental Specimen Banking, Oct. 6-8, 1986, Gloucester Point, VA.

5. Co-ordinated Research Programme on Human Daily Dietary Intakes of Nutritionally Important Trace Elements as measured by Nuclear and Other Techniques, International Atomic Energy, Vienna, Austria. Report of the First Research Coordination Meeting Gaithersburg, Beltsville and Washington, DC, March 19-22, 1985.

6. Zeisler, R., Greenberg, R.R., and Stone, S.F., (1987), Radiochemical and Instrumental Neutron Activation Analysis Procedures for the Determination of Low Level Trace Elements in Human Livers, J. Radioanal. Nucl. Chem., accepted for publication.

7. Stoeppler, M., and Ostapczuk, P., (1986), Report of Analysis, KFA Jlich.

8. Greenberg, R.R., Fleming, R.F., and Zeisler, R., (1984) High Sensitivity Neutron Activation Analysis of Environmental and Biological Standard Reference Materials. Environ. Intern. 10, 129.

ASTM TASK GROUP ON NUCLEAR METHODS OF CHEMICAL ANALYSIS

D. A. Becker
(Center for Analytical Chemistry)

The newly-formed ASTM Task Group (TG) on Nuclear Methods of Chemical Analysis has continued to expand. Formed in 1985, the group now has over 50 members. This TG is part of ASTM Committee E 10.05 (Committee E 10 on Nuclear Technology and Applications, Subcommittee .05 on Nuclear Radiation Metrology) and will address needs for standards and information on the use of nuclear methods for the determination of chemical composition. Initially, the primary interest of most TG members is neutron activation analysis (NAA), and members include scientists from universities, government, and industries (both large corporations as well as small analytical laboratories).

The TG has six subgroups, generally corresponding to analytical interests. These subgroups are listed below along with their current activities:

Forensic NAA: Developing draft method for the analysis of trace elements in bullet lead. When draft is complete, will run round robin using NBS SRM 2416, Lead.

Neutron Generators: Rewriting ASTM Standard Method E 385-80, Oxygen Content Using a 14-MeV Neutron Activation and Direct Counting Technique.

Biology/Medicine/Health: Gathering information to write standard methods for zinc and selenium in biological materials. Instrumental in organizing sessions on zinc analysis at Los Angeles ANS meeting (November, 1987) and on selenium at the San Diego ANS meeting (June, 1988).

Geochemistry/Archeometry: Published listing of gamma-ray lines used by one laboratory for geochemical type samples, in the TG minutes from the New Orleans meeting (January, 1987). Proposed that USGS-Reston compile data on Geochemistry/Archeometry reference materials.

Reactor Facilities: About to initiate research reactor irradiation facilities intercomparison study, using foil techniques to measure thermal and fast neutron fluence. Compiling listing of reactor facilities and laboratories providing irradiation and/or NAA services.

Quality Assurance: Initiates discussions on QA at TG meetings; in particular, held several sessions on multielement standards and reference materials for NAA. Will provide QA guidance for all ASTM NAA standard methods.

Interest and response to this new TG has been excellent, and the TG has furnished improved contacts and communication between scientists working in the field. It is hoped that with further development the TG will provide a substantial force in the further development of NAA and nuclear methods of chemical analysis. For further information on this group and their activities, contact Donald Becker (Chairman) at the address shown above, or by telephone [(301) 975-6283; FTS: 879-6283].

NDP AND FTIR STUDIES OF BOROPHOSPHOSILICATE CVD THIN FILM GLASSES

J.N. Cox, R. Hsu, and P.J. McGregor
(Intel Corp, Santa Clara, CA)

and

R.G. Downing
(Center for Analytical Chemistry)

Borophosphosilicate glass (BPSG) thin films are used as dielectric spacers between metal layers in silicon semiconductor VLSIC technologies. Following deposition and patterning, a controlled "reflow" of the glass, at a temperature low enough to avoid the degradation of other device characteristics, is required to smooth contours produced during the patterning step. The boron and phosphorus are added to reduce the reflow temperature. Prior to the patterning and reflow steps, a "densification" of the glass is often performed near the reflow temperature, as well.

Typically about one micrometer in thickness, these glasses are produced by chemical vapor deposition (CVD). There are several variants of the CVD technique. Reactant gases in some systems are maintained at atmospheric pressure (APCVD), while other reactors are designed for low pressure (LPCVD) depositions. The wafers may stationary (SW configuration), or they may be placed on a moving belt (MW). In the latter case, the wafer may be conveyed through a continuous deposition zone (MW/CZ), or through multiple zones (MW/MZ). The reactant gases typically consist of phosphine, silane or tetraethyl orthosilicate, and oxygen. Boron sources include diborane, trimethyl borate, and boron trichloride.

1. Experimental Goals

This paper summarizes the characterization of various CVD BPSG by Fourier transform infrared spectrophotometry (FTIRS) and Neutron Depth Profiling (NDP). The thin films studied are restricted to levels ranging from 0.0 to 5.0 Wt % for boron and from 0.0 to 7.0 Wt % for phosphorus. FTIRS, which provides chemical bonding information by analyzing the interaction of infrared radiation with the vibrational motions of the constituents of the glass, shows that films in this compositional regime are different chemically and structurally from simple mixtures of the oxides.[1] Furthermore, the different CVD processes produce films that differ chemically from one another. Inhomogeneous distributions of chemical bonds, changes in the relative amounts of these bonds, and internal strains or spectral interferences due to the presence of contaminants, such as water, or of boron and/or phosphorus affect the peak full-width-at-half-maximum (FWHM) and other bandshape parameters.

Neutron Depth Profiling can nondestructively determine the distribution of boron as a function of depth in a thin film.[2] Thus, it can be used to compare the boron profiles produced by reactors that employ SW, MW/CZ, and MW/MZ wafer processing configurations. Also, the physical redistribution of boron during densification and reflow cycles can be observed. Of particular interest is the characterization of the diffusion of the boron from BPSG films into the contiguous layers that initially contain less boron.

2. Results

One result of the study of the spectral bandshape properties of BPSG has been the development of the FTIRS as a monitor for the quantitative determination of boron in "as deposited" films. The required conversion factors, however, are found to differ by as much as 13 % when APCVD MW/CZ films are compared with LPCVD SW films. For certain LPCVD SW and APCVD MW/MZ glasses, no good calibration of the FTIRS for the full range of boron contents has been achieved. For the former film, the problem is attributed to interferences due to variable amounts of water, also detected by FTIRS; for the latter, NDP reveals that the boron content in a nominally 2.0 Wt % film varies with depth by as much as 1.0 Wt %. This variation affects the FTIR bandshape parameters in a complicated fashion. Figure 1 gives the NDP spectrum for this APCVD MW/MZ film.

Also displayed in figure 1 are the profiles following heat treatments (room temperature, 920 C, 1010 C) in a nitrogen ambient. The reflow properties and boron redistribution are observed to limited by the dopant levels in the boron-deficient zones. When an APCVD MW/CZ film of comparable B/P levels, but with a relatively uniform NDP spectrum, is taken through the same temperature treatment, the FWHM of the FTIR peak assigned to the SiO asymmetric stretching vibration is observed to become progressively narrower: 135 to 119 to 121 cm^-1 (+/- 4 cm^-1). This is the typical outcome of a densification cycle, since water and bonding inhomogeneities are removed from the film. In contrast, for the same FTIR peak, the FWHM of the APCVD MW/MZ glass with the profile shown in figure 1 changes from 130 to 114 to 125 cm^-1, respectively. Because the boron in a CVD film is presented as an oxide and is to some extent chemically bound to the SiO host glass network, the NDP and FTIR results suggest that the large chemical potential driving the redistribution of the boron at 1010 C ultimately introduces additional strain into the film, causing the observed increase in the FWHM.

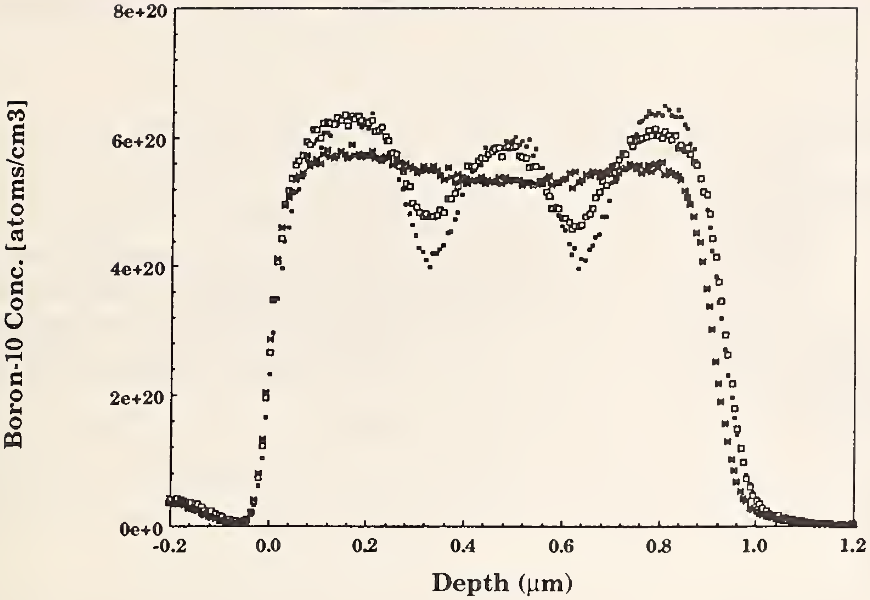

Figure 1. NDP profile of Borophosphosilicate glass film on a silicon substrate: (■) as deposited film; (□) after 920 C, 30 min. anneal in nitrogen; (⧓) after 1010 C, 30 min. anneal in nitrogen.

---

1. A. S. Tenny and J. Wong, J. Chem. Phys., 56, No.11, 5516 (1972).
2. R. G. Downing, R. F. Fleming, J. K. Langland, and D. H. Vincent, Nucl. Instr. and Meth., 218, 47 (1983).

FISSION SPECTRUM AVERAGED CROSS SECTION OF THE ^{93}Nb(n,n')^{93}Nb REACTION

D. McGarry

The following paragraphs discuss the use of the U-235 Fission-Spectrum Facility in the thermal column of the NBS Reactor to measure the fission-spectrum-averaged cross section of the ^{93}Nb(n,n')^{93m}Nb reaction.

The NBS U-235 Fission Spectrum is known as the Cavity Fission Source (CFS) because its geometry is a cadmium-cylinder with U-235 metal disks on the ends which is irradiated in a 30-cm diameter cavity within the graphite thermal column of the NBS Research Reactor. The lower-two portions of figure 1 depict the NBS-CFS. This fission source was used to perform an irradiation, sponsored by the Department of Energy, to measure the integral, spectrum-averaged cross section of the subject niobium reaction.

Because the neutron fluence is produced by fissioning U-235 with thermal-neutrons, the fluence is dependent upon the reactor's power history. The nickel ^{58}Ni(n,p)^{58}Co reaction is used to monitor the absolute fluence in the U-235 spectrum irradiations. The nickel (n,p) response is calibrated by a flux transfer from a known-fluence irradiation in a Cf-252 spectrum. Because high-purity niobium, with less than 2 ppm of tantalum, was only available in wire form, the wire was spiraled together with a nickel-wire monitor as shown in the upper-third view of figure 1. Because the cross sections is only 150 millibarns and the half life of the ^{93m}Nb isotopic state is 16.4 years, the subject irradiation required 30 days.

The nickel wire and nickel disks, 0.025-cm thick and 1.27-cm in diameter, are also used to monitor the axial and radial gradients within the cadmium pill box used in the CFS. Because the disks are carefully repositioned, for each irradiation, relative to the ends of the cadmium pill box (see figure 2), the gradients are repeatable. The axial gradient is shown in figure 3 and is a result of repeated irradiations of carefully-positioned nickel disks. Consequently, knowledge of the relative positions of various 1.27-cm diam. foils permits determination of axial-gradient corrections.

The effects of the radial gradient are shown in figure 4. The line is a least-squares fit to the data points which were obtained by activating 1.27-cm diam. nickel foils and then determining the specific activity of successively smaller-diameter disks punched, or machined, from their centers. If there had been no axial gradient, the best fit would have been a straight line horizontal to the abcissa. The resultant fit is a straight line because the mass ratio is proportional to ratios of the activities, as well as the squares of the diameters.

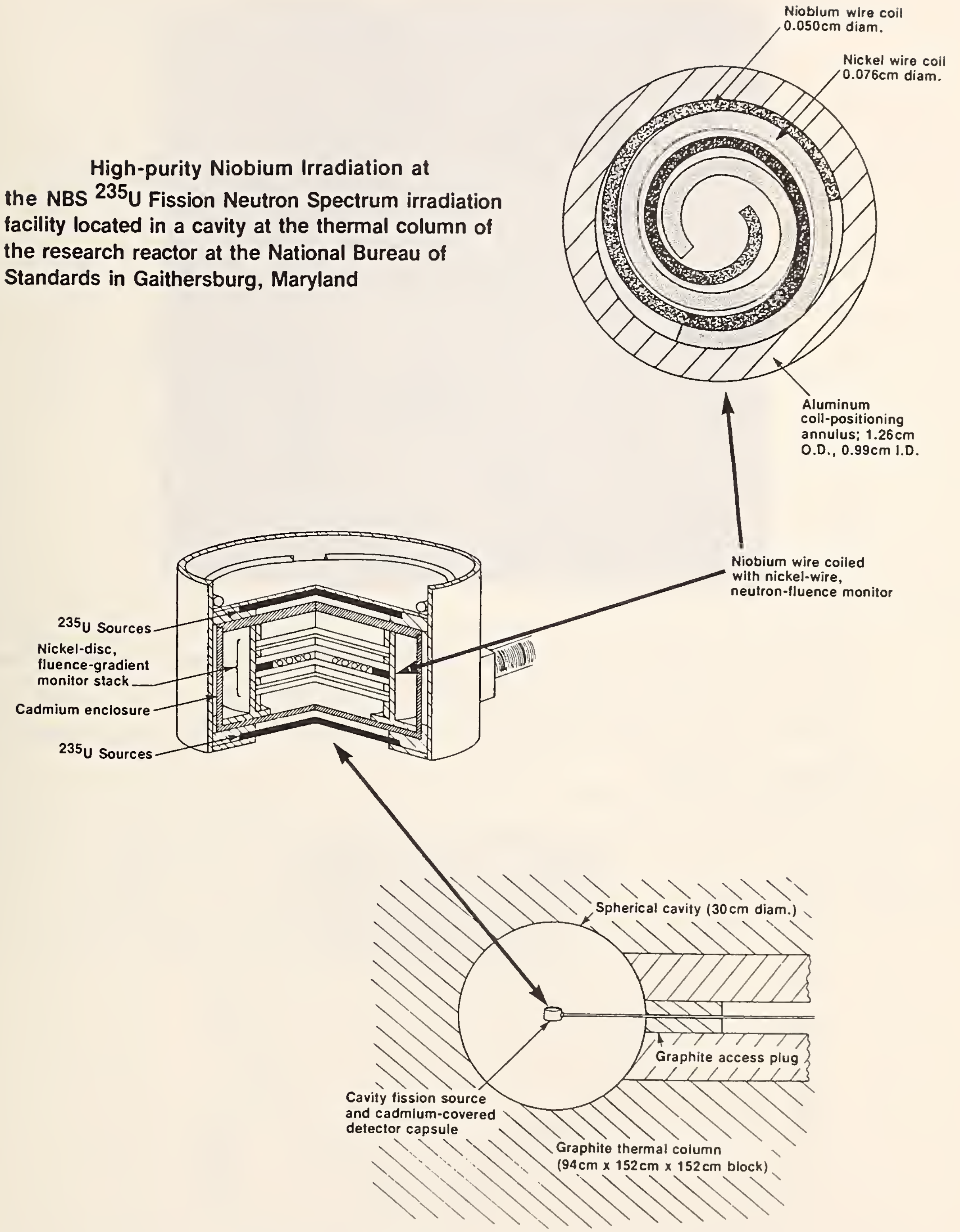

Figure 1. High-purity niobium irradiation at the NBS U-235 Fission Neutron Spectrum irradiation facility located in a cavity at the thermal column of the research reactor at the National Bureau of Standards in Gaithersburg, Maryland.

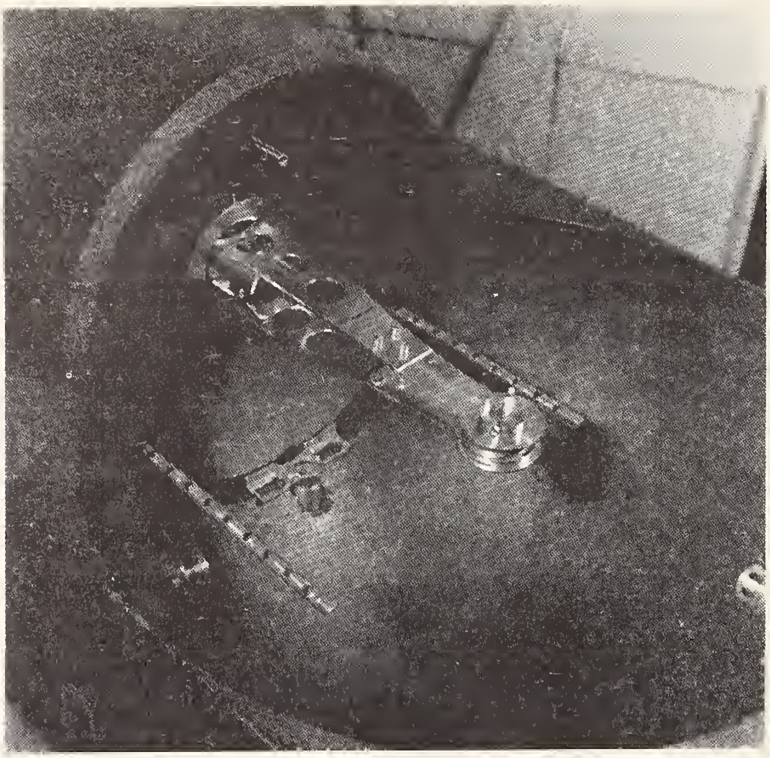

Figure 2. Picture of the spring-tight metal fingers that hold aluminum-encapsulated U-235 metal disc on the top and bottom of a cadmium pill box containing foils and disks to be irradiated in the NBS-CFS. One-half of the graphite piece which forms the 30-cm diam. cavity in the NBSR thermal column is visible.

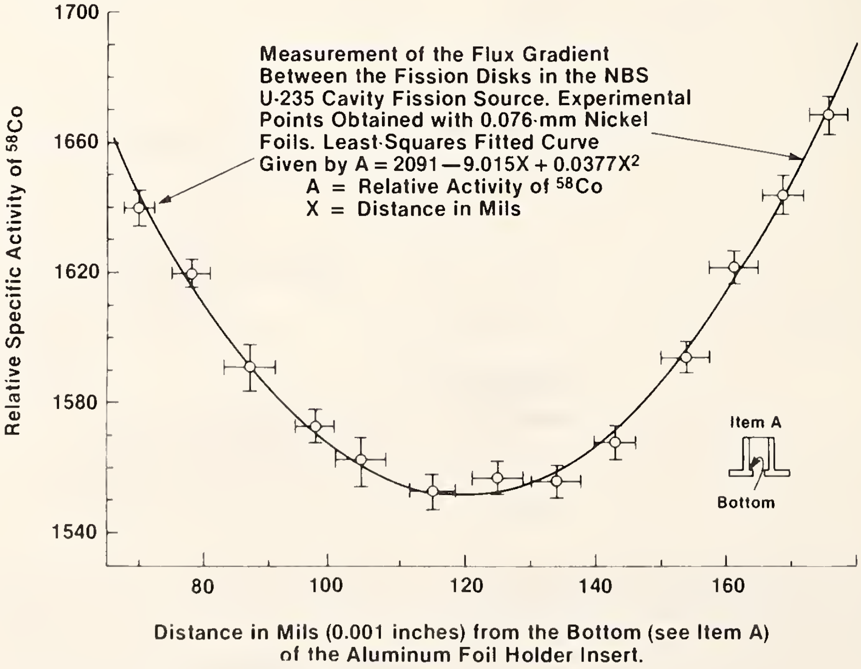

Figure 3. Axial gradient in the NBS-CFS.

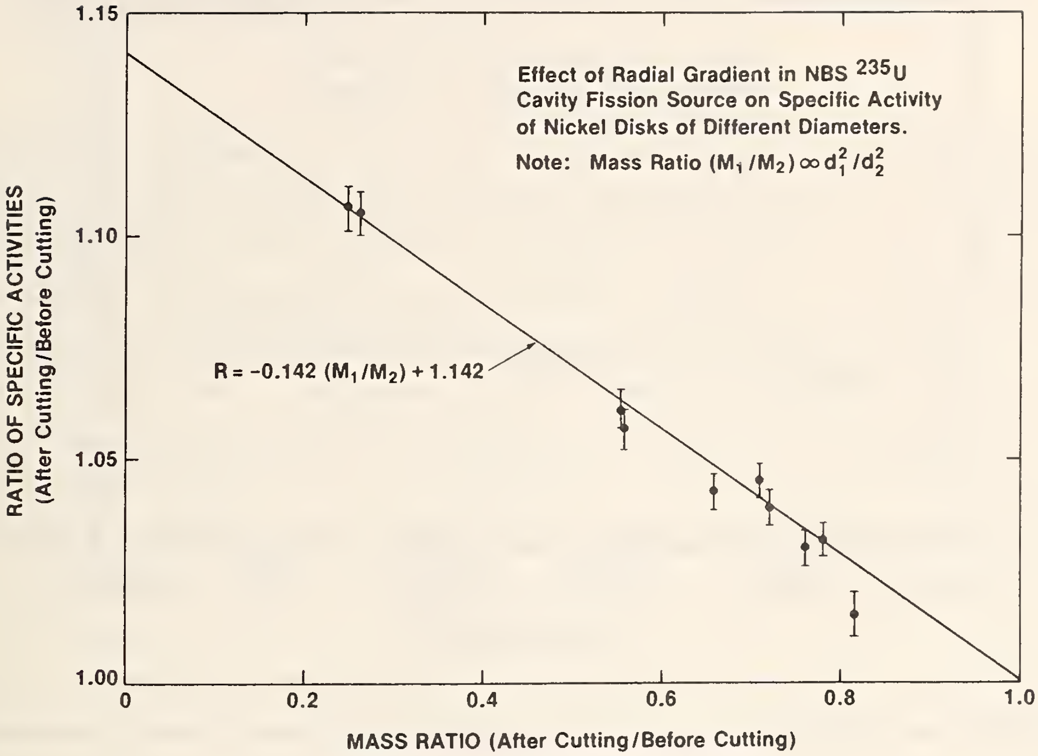

Figure 4. Radial gradient in the NBS-CFS.

To account for the different effects of the radial gradient on the nickel wire and niobium wire, (because each wire section is located at a different radius), numerical integrations of 16 segments of each of these wires were performed. The effect of having a spiraled nickel wire rather than a 1.27-cm diam. disk as a monitor resulted in a 3 % correction.

A $^{10}B(n,\alpha,\gamma)$ COINCIDENCE TECHNIQUE FOR ABSOLUTE NEUTRON COUNTING

D. M. Gilliam and G. P. Lamaze
(Center for Radiation Research)

A preliminary experiment has been carried out to explore the possibility of using a $^{10}B(n,\alpha,\gamma)$ coincidence technique for absolute thermal neutron counting. The motivation for this effort is the need for a highly accurate measurement of linear neutron density for a beam-type neutron lifetime experiment which is being undertaken collaboratively with the University of Sussex (Brighton, England) and the Central Bureau for Nuclear Measurements (Geel, Belgium). The present scheme for absolute counting of the thermal neutrons in a beam involves two steps: (1) determination of the gamma efficiency (including the branching ratio factor) of a germanium gamma-ray detector by means of the alpha-gamma coincidence method (figure 1), and (2) then replacing the thin B-10 target with a thick, "black" B-10 target so that the entire beam is stopped and counted by the calibrated gamma detector. The first step of this scheme was carried out in a preliminary experiment at BT-7. The gamma-ray efficiency obtained by the coincidence method was checked independently by

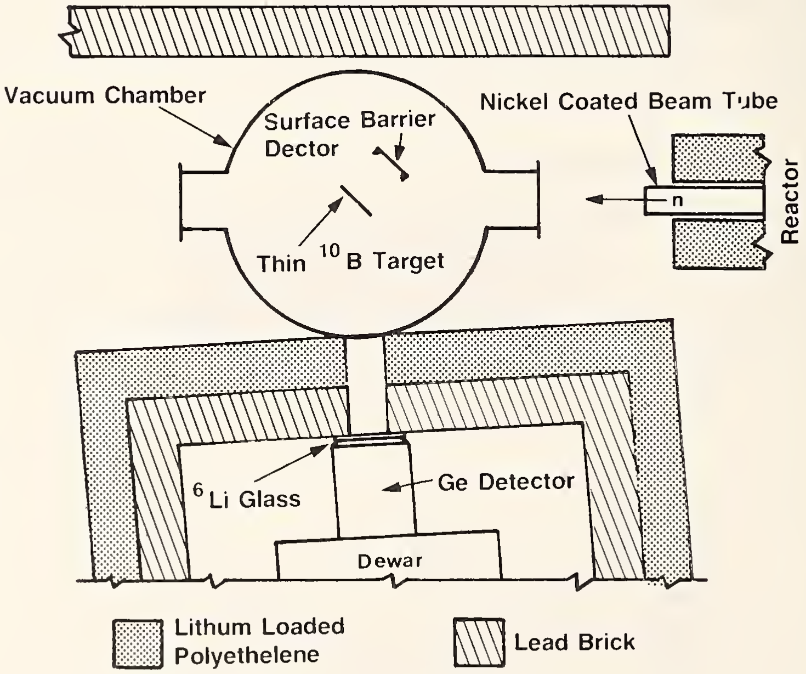

Figure 1. Experimental layout for the $^{10}B(n,\alpha,\gamma)$ coincident measurements. Detectors are in horizontal plane. Due to space limitation, the future arrangement of two germanium detectors will probably be in the vertical plane.

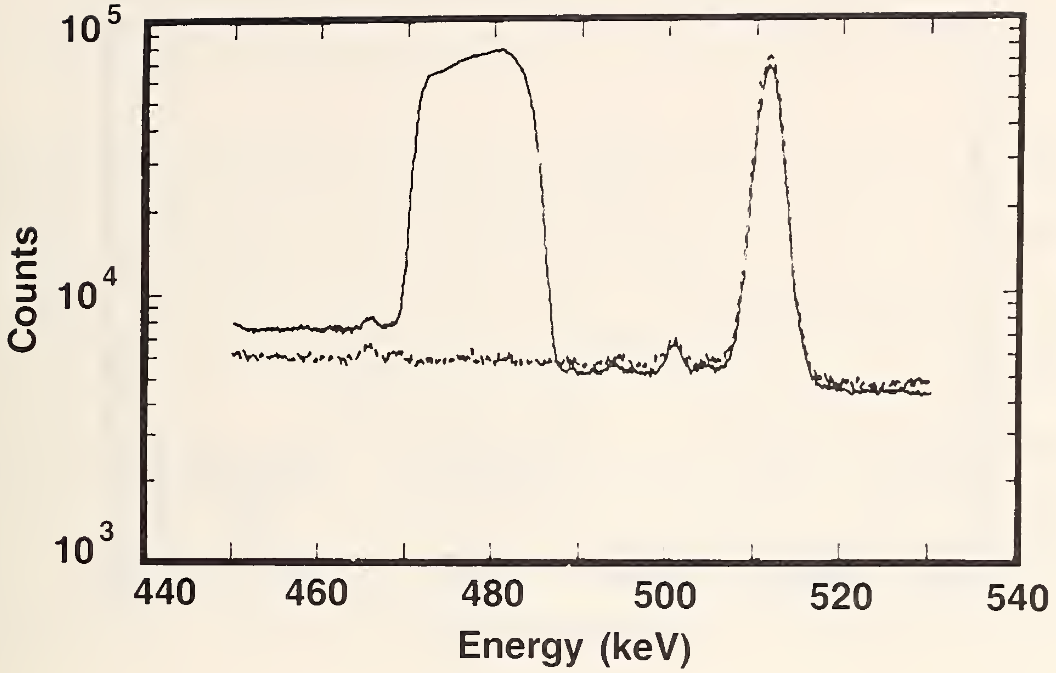

Figure 2. Gamma-ray spectra from B-10 targets on silicon. Dashed line indicates a bare silicon backing.

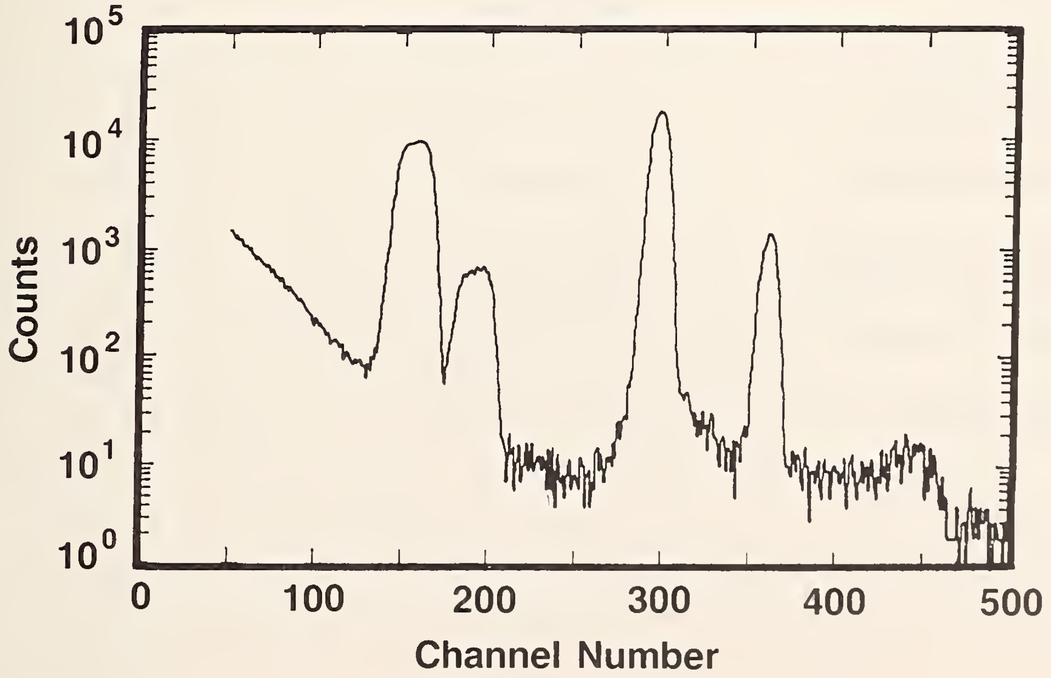

Figure 3. Charged-particle spectrum from B-10 on stainless steel backing.

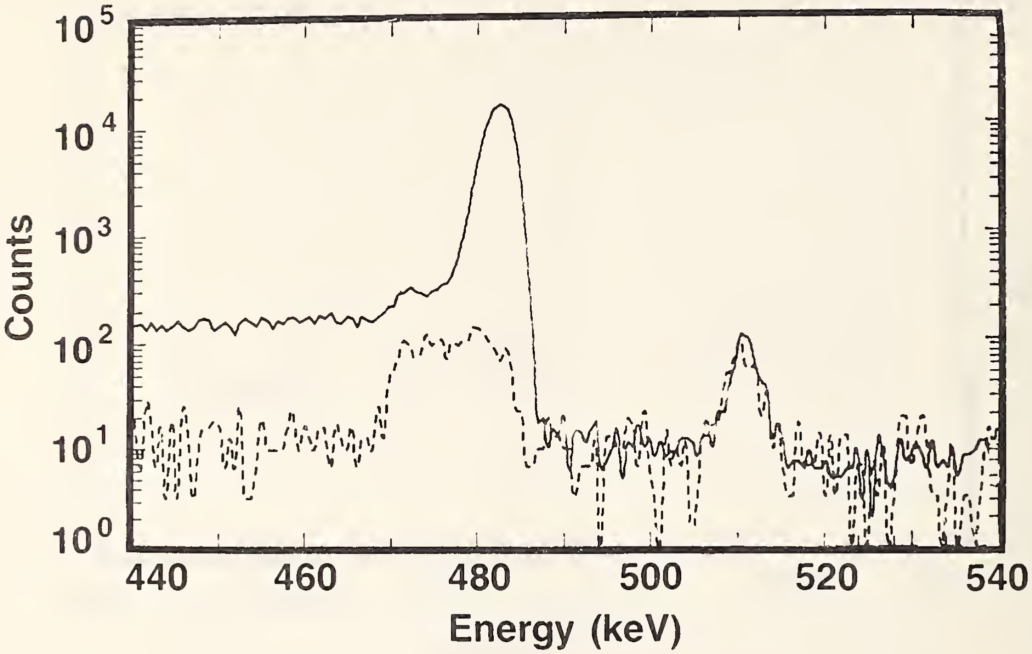

Figure 4. Coincident gamma-ray spectra from B-10 targets on silicon. Dashed line represents the accidental coincident spectrum.

Table 1. Results of Present Measurements

Technique	Efficiency	Uncertainty (1σ)
Coincident Measurement 1	3.266×10^{-4}	± 0.6 %
Coincident Measurement 2	3.249×10^{-4}	± 0.8 %
Coincident Measurement 3	3.261×10^{-4}	± 0.6 %
Coincident Method (Average)	3.260×10^{-4}	± 0.4 % (stat. only)
Gamma Ray Source Method	3.279×10^{-4}	± 1.0 %
Alpha Source Method	3.307×10^{-4}	± 0.8 %

means of calibration with both alpha particle and gamma ray standards. All three of these results[1] for the gamma-ray efficiency agreed within a spread of 1.5 % (table 1).

Figure 2 shows gamma-ray singles spectrum for the thin B-10 deposit compared with the spectrum obtained when substituting a blank silicon wafer backing with essentially zero B-10 content. The spectrum from the blank backing shows that there are no interfering lines in the region of the broad 478 keV peak, which is well separated from the annihilation line at 511 keV. Figure 3 shows the alpha and Li-7 particle spectra, and figure 4 shows the true-coincidence and chance-coincidence gamma-ray spectra.

Although the accuracy of this preliminary measurement is far from the ± 0.1 % goal of the neutron lifetime experiment, the results indicated no problems in principle which would discourage further investment of effort in tests with improved shielding and more careful treatment of electronic dead-time effects.

---

1. G. P. Lamaze, D. M. Gilliam, and A. P. Williams, "Prompt Gamma as a Fluence Rate Monitor in Neutron Beam Experiments," Journal of Radioanalytical Chemistry, to be published.

FILTERED BEAMS

R. Schwartz

In response to questions concerning the purity of the NBS 2 keV filtered beam, the neutron spectrum was carefully measured, using a He-3 spectrometer with a new low-noise preamplifier and pile-up rejection circuitry. The pulse height spectrum is shown in figure 1, where the pulse height analyzer channel numbers have been replaced by the corresponding neutron energies, using the Q-valve for the ^{3}He (n,p) reaction (764 keV). The ordinate is, as labelled, counts/channel, not corrected for the approximately 1/v variation of the He-3 cross section.

Small peaks between 7 keV and 40 keV, previously measured with a proton recoil spectrometer, can not be resolved in this spectrum. Several previously unobserved lines between 70 keV and 550 keV are now seen, however. The total fluence under these newly observed lines is still only about 2 % of the 2 keV line. The rise at ~740 keV is due to pile-up from the main 2 keV peak, and there are no visible peaks at higher energy.

CHARACTERISTICS Ot NBS FILTERED BEAMS

2 keV		24 keV		144 keV	
E_n (keV)	Fluence (%)	E_n (keV)	Fluence (%)	E_n (keV)	Fluence (%)
2	95.6	24	97.1	144	99.7
7	0.6	74	0.2	54	0.33
15	0.6	135	1.6		
29	1.3	280	1.0		
40	0.6	364	0.2		
70	0.11				
129	0.5				
185	0.3				
214	0.10				
255	0.05				
302	0.06				
341	0.07				
385	0.01				
470	0.05				
541	0.03				

Beam Diameter (cm)	1.7	2.5	2.5
Neutron Current (n/s)	1.4×10^6	1.6×10^6	3.1×10^6
<u>Dose Equivalent Rates</u>	(mSv-cm^2/hr)		
MADE (ICRP 21)	51	112	964
H*(10)	31	98	1,260

March 26, 1987

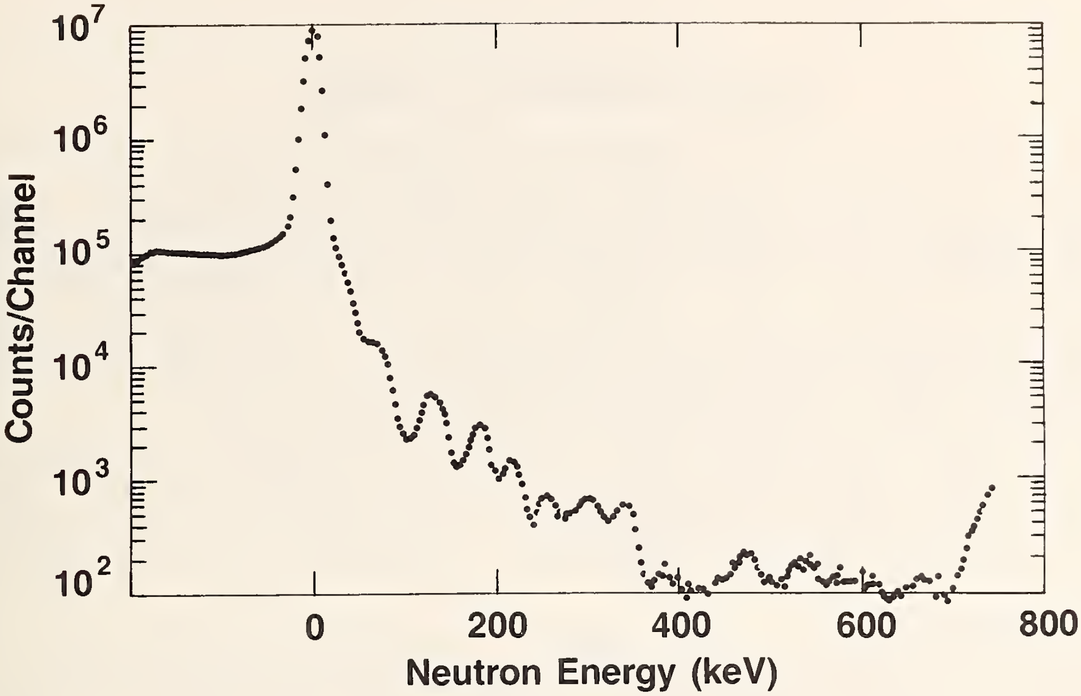

Figure 1. He-3 spectrometer data for 2 REV filtered beam.

The spectral composition of the 2 keV beam, derived from the older proton recoil measurements and these He-3 data, is given in table 1. This is still, by far, the cleanest 2 keV beam at any reactor facility in the world.

The 144 keV beam has been improved by increasing the amount of Ti in the filter. This decreases the 55 keV impurity line from 1.5 % to 0.3 %, with only a slight loss of 144 keV neutrons.

The make-up of all three filtered beams is given in table 1. The 24 keV beam is listed for the sake of completeness: there are no new measurements of this beam.

The filtered beams, together with a thermal column beam, continued to be used for testing radiation protection instrumentation. This included quality control measurements on neutron area monitors for the Naval Surface Weapons Center, dosimeter irradiations as part of the Department of Energy Laboratory Accreditation Program (DOELAP), and testing of a new type of neutron detector developed at the Chalk River Laboratories. This latter testing, done in collaboration with several other laboratories in the United States and England, forms the basis for a paper to be given at the Sixth Symposium on Neutron Dosimetry to be held in Neuherberg, Germany, in October 1987.

C. Reactor Operations and Services

REACTOR OPERATIONS AND SERVICES

T. Raby and J. Torrence

Reactor operations continued at the higher power level of 20 MW for most of the year. The reactor was shutdown in May 1987 in preparation for the installation of the Cold Neutron Source. The shutdown period will also be used for major maintenance including replacement of the shim arms and overhaul of the fuel transfer system. This will considerably reduce future shutdowns.

For the first time in nine years, spent fuel was shipped for reprocessing. It took all this time to get an appropriate spent fuel cask licensed by the NRC. Seven shipments were made to date which were very timely since the storage pool has reached its capacity.

During this period two new senior operators were licensed and a third was hired. This will bring the operating staff to an acceptable level. A summary of the operating statistics for the year is prescribed in the following table. Fuel utilization continues to be excellent.

No. of days at 20 MW	222
On-line time at 20 MW	61%
Average U-235 burnup	66%
No. of Irradiations	1570
Hours of Irradiations	1765
Hours per Irradiation	1.1

2. Irradiation Services

Extensive irradiation services were provided to many users from within and outside NBS. In all, more than 1500 irradiations involving thousands of samples were performed in many areas of research and application.

ENGINEERING SERVICES

J. Nicklas

In addition to normal engineering and design services provided to reactor operations, experimenters and users, the engineering staff is involved in a continuing effort to upgrade the reactor instrumentation in addition to normal surveillance calibrations.

Thirty fuel assemblies, the last numbered S-575 have been inspected and accepted from the DOE contractor by the NBSR staff. An additional 30 fuel assemblies have been fabricated and are awaiting acceptance. Fuel compacts now being made contain 350 gms per element, a change from 300 gm elements. The first 200 plates of the 350 gm elements were radiographed and determined that the process is under control.

The method developed to plug heat exchanger tubes with rubber plugs has been used on several leaking tubes with success. The previous method of pounding metal plugs into the tubes required entry into the bonnet with subsequent high radiation exposure to personnel and was limited to personnel that could enter a 12 inch manhole.

A tool for pulling the fuel transfer arm bearings has been designed and fabricated but has not been tested to date. The original carbon steel bearings are causing an occasional sticking of the transfer arms which causes some loss of feel when transferring fuel.

The second tritium monitor has been installed, tested and completed. Two more modern design differential transmitters have been installed in the process demineralized water system.

The shim arm yokes were fabricated and assembled with the shim arms, bearings, and splines into a complete assembly for installation into the reactor. The last replacement of shim arm assemblies required reuse of the old yokes in a tedious underwater assembly method.

The telescopic cylinder for transferring fuel into and out of the reactor was completely rebuilt with new bearings, seals and end caps. It was not necessary to rebuild the erecting cylinder nor replace the connecting stainless steel lines because they were in excellent condition.

The installation of the 133 kVA uninterruptible power supply for the experimental computer and associated instrumentation was completed and placed in service.

Continued preparing and partially installing new transmitters and venturi at the experimental level for the Cryogenics Bismuth Tip. Also the bismuth tip remote readout meters, lights, push-buttons, and alarms were installed on the console in the Reactor Control Room.

Completed modernizaton of the Reactor Conductivity and the Tritium measurement instrumentation equipment:

Installed a new multipoint recorder on the Tritium Monitor system.

Replaced six conductivity amplifiers with new units. Replaced 11 temperature compensated conductivity cells with associated wiring.

D. Service Programs

NEUTRON ACTIVATION ANALYSIS AT THE FOOD AND DRUG ADMINISTRATION

W. C. Cunningham
(U. S. Food and Drug Administration, Washington, DC)

The Food and Drug Administration (FDA) maintains a neutron activation analysis (NAA) facility in the reactor building of the National Bureau of Standards (NBS). Although this facility is directed by FDA's Center for Food Safety and Applied Nutrition, it provides agency-wide analytical suport for special investigations and applications research. NAA complements other analytical techniques used at FDA and serves as a reference technique and confirmatory quality assurance tool.

During the past year, this facility provided support in all of the areas noted above. Both radiochemical and instrumental NAA procedures were utilized to provide broad multielement information. This methods development and applications research was part of the ongoing FDA effort to improve overall analytical capabilities. The most extensive work was in the application of NAA to the analysis of food supplements. Efforts in this area have increased during the last few years because of increased popularity of these products. Although these food materials are diverse and comlex, approximately 35 different product types have been analyzed by NAA. Element concentrations are examined for label compliance and constituents of possible toxicologic concern. In addition, data for future reference are being compiled on interferences in the analysis, procedure modifications necessary to over come the interferences, and detection limits.

In a paper presented at the 1986 American Nuclear Society Winter Meeting in Washington, DC,[1] this laboratory focused attention on the determination of aluminum in foods by NAA. The paper examined major interferences and discussed ways to overcome or minimize them. It showed that when polyethylene bags were used to contain the food, the detection limit was approximately 0.5 μg/g, using an empty polyethylene bag as the blank. When Whatman filter paper was used as the blank, however, the detection limit was lowered to 0.15 μg/g because of improvement in measuring the precision of the blank. A pre-irradiation separation procedure that was developed in the FDA NAA facility for the determination of aluminum was also employed and findings presented. The procedure utilized Chelex-100 chelating resin and provided a means of achieving detection limits of approximately 0.1 μg/g for most foods.

---

1. W. C. Cunningham and W. B. Stroube, Jr., ANS Transactions, 53, 174-5, (1986).

E. Personnel Roster

REACTOR RADIATION DIVISION
460

R. S. Carter, Chief
T. M. Raby, Deputy Chief
*E. C. Maxwell, Admin. Officer
M. Long, Admin. Assist.
*S. E. Tassey, Secretary
S. C. Shatzer, Clerk-Typist

Neutron Radiography
#T. Cheng
M. Ganoczy

Division Staff
R. Casella
B. Mozer
F. Shorten

REACTOR OPERATIONS

T. M. Raby, Chief
J. F. Torrence, Deputy Chief
C. Harrison, Secretary

Reactor Operations

R. Beasley
M. Bell
N. Bickford
M. Cassells
F. Clark
J. Clark
H. Dilks
L. Lindstrom
M. McDonald
W. Mueller
T. Myers
J. Ring
R. Sprow
R. Stiber
A. Toth
D. Wilkison

ENGINEERING SERVICES

J. H. Nicklas, Chief
C. Harrison, Secretary

Mechanical Design

E.Guglielmo
+J. Heine
J. Sturrock

Electronics
J. Beatty
R. Conway
R. Hayes

NEUTRON CONDENSED MATTER SCIENCE

J. J. Rush, Group Leader
L. Roadarmel, Secretary
+L. Clutter, Clerk-Steno.
*K. Ferrel, Clerk-Typist

Crystallography

#F. Beech
#C. Choi
#V. Himes
J. LaRock (1/2)
A. Mighell
#S. Miraglia
#H. Prask
E. Prince (1/2)
W. Rymes
A. Santoro
*J. Stalick
#D. TranQui

Metal Hydrides and Molecular Materials
#J. Nicol
D. Neumann (1/2)
#S. Trevino
R. Williams (1/2)
T. Udovic (1/2)

Magnetic and Amorphous Materials
R. Erwin
#J. Fernandez-Baca
#T. Giebultowicz
W. Knill
#W. Li
+J. Lynn
J. Rhyne
#M. Spano
#Y. Yu

Advanced Neutron Methods
N. Berk
D. Fravel (1/2)
C. Glinka (1/2)
J. Gotaas
#S. Krueger
E. Prince (1/2)

COLD NEUTRON PROGRAM

J. M. Rowe, Manager
C. O'Conner, Admin. Assist.
P. Grimes, Clerk-Typist

Cold Neutron Program

#J. Copley
D. Fravel (1/2)
C. Glinka (1/2)
*G. Greene
J. Grillo
+M. Kahn
P. Kopetka
J. LaRock (1/2)
D. Neuman (1/2)
I. Schroder
#H. Stanley
T. Thuan
T. Udovic (1/2)
R. Williams (1/2)
D. Pierce

*Part-time
+WAE, Coop, Intermittent
#Guest Scientist, research assoc. (Full Time)

PERSONNEL ROSTER

NON-RRD NBS STAFF LOCTED AT REACTOR

Division 354

D. Brown
C. Campbell
I. Jensen
F. Moore
D. Nelson
J. Shubiak
J. Wang

Division 536

E. Boswell
C. Eisenhauer
D. Gilliam
J. Grundl
G. Lamaze
E. McGarry
R. Schwartz

Division 551

D. Becker
S. Carpenter
G. Downing
K. Fitzpatrick
R. Fleming
C. Grazman
R. Greenberg
J. Langland
R. Lindstrom
G. Lutz
J. Maki
B. Norman
S. Stone
R. Zeisler

GUEST WORKERS AND COLLABORATORS

Division 400

J. Cahn

Division 420

F. Brinckman
J. Blendell
T. Coyle
E. Fuller
K. Hardman-Rhyne
G. Olson
R. Roth
W. Haller

Division 430

R. Fields

Division 440

R. Briber
B. Bauer
C. Chiang
J. Clark
T. Davis
C. Han
R. Waterstrat
W. Wu

Division 450

R. Reno
R. Shaefer
R. Shull

Division 520

G. Greene

Division 541

R. Cavanagh
R. Kelly
T. Madey

Division 543

G. Gillard
R. Harrison
A. Wlodawer

Division 552

B. Koster
L. Sander
S. Wise

PERSONNEL ROSTER

Division 553

C. Poston
H. Rook
C. Stone
J. Small

Division 725

J. Ehrstein

Division 774

H. Hanley
J. Straty

Ames Laboratory

W. Kamitakahara

Armed Forces Institute of Pathology

D. Nagarajan

Army Armament Research and Development Command

C. Choi
H. Prask
S. Trevino

Federal Bureau of Investigation

R. Bilko
J. Haverkost
J. Kilty
P. Kostella
M. Moscop
C. Peters
J. Riley
P. Tangren
P. Thompson

Food and Drug Administration

W. Cunningham
A. Kyah
W. Stroube, Jr.
J. Tanner

National Institutes of Health

J. Bennett
M. Channing
W. Eckelman
M. Geller
R. Finn
R. Frank
A. Katki
M. Neuder
R. Nossel

National Oceanic and Atmospheric Administration

G. Lauenstein

Naval Research Laboratory

K. Grabowski
D. Gubser
N. Koon
S. Lawrence
M. Osofsky
L. Toth
S. Wolf

Naval Surface Weapons Center

J. Cullen
G. Riel
M. Spano

Smithsonian Institution

R. Bishop
M. Blackman
T. Chase
Y. Cheng
J. Mishara
E. Myers
J. Olin

Department of Agriculture

G. Igengar

Argonne National Laboratory

T. Brun

PERSONNEL ROSTER

Battelle Pacific Northwest Laboratories

L. Brackenbush
F. Brauer
G. Endres
M. Failey
R. Sanders

Brookhaven National Laboratory

D. Cox
C. Maryzak

Chalmers University of Technology

L. Sjölin
R. Alenljung

C.N.R.S. Grenoble, France

B. Barbara
C. Chaillout
D. Gignoux
M. Marezio
S. Miraglia
D. Schmitt
D. Tran Qui

CSIRO - Australia

R. Hill

Energy Research Foundation (The Netherlands)

J. Woittiez

Hahn-Meitner Institute (Berlin)

D. Behne

Institut Laue-Langevin Grenoble, France

A. Magerl
R. Pynn
D. Richter
J. Soubeyroux

KFA Jülich, Germany

R. Hempleman
M. Stoepler

ETH, Zurich, Switzerland

I. Anderson

Los Alamos National Laboratory

J. Eckert
R. Robinson
J. Wilkerson
M. Yethridge

Max-Planck Institute

R. Kirchheim
J. Walter

Oak Ridge National Laboratory

J. Hayter
F. Kam

Sandia National Laboratory

J. Schirber
D. Varsick

Alfred University

R. Snyder
R. Zhow

Auburn University

B. Taterchuck

Cambridge University (U.K.)

J. Horton
G. Squire

Carnegie-Mellon University

E. Boltich
W. Wallace

College of William and Mary

E. Schoe
R. Wright

Iowa State University

P. Klavins
H. Ku
R. Shelton
H. Yang

Kyoto University (Japan)

H. Hasegawa
T. Hashimoto
Q. Trancong
S. Sakurai

McMaster University

W. Clarke
R. Barr

Miami University (Ohio)

J. Cantrell

Michigan State University

E. Case
Y. Fan
S. Solin

M.I.T.

J. Didiskein
M. Green
B. Wuensch

Nagoya University

Y. Muroga

Northwestern University

J. Ketterson
C. Sellers
J. Weertman

Ohio University

R. Cappelltetti

Oregon State Graduate School

P. Davis

Princeton University

J. Kolberstein

Purdue University

A. Overhauser

Stanford University

W. Tang

San Jose State University

A. Ling

Stanford Unversity

W. Tang

University of Annecy (France)

J. Bouillot

University of Antwerp (Belgium)

K. Michel

University of California (Irvine)

V. Guinn

University of California (Santa Barbara)

M. Eddy
J. Fint
D. Klingensmith
C. Levi
R. Odette
G. Stucky

University of California (San Diego)

J. Arnold
K. Nishiizumi

University of Cincinnati

H. Jackson
P. Boulchand

University of Delaware

S. Satija

University of Exeter (U.K.)

R. Slade

University of Illinois

J. Borchers
R. Du
J. Cunningham
C. Flynn
S. Landobliger
D. Neumann
M. Salamon
H. Zabel

U. of Illinois (Chicago)

M. Said
J. Kowel

University of Leiden (The Netherlands)

J. Mydosh

University of Maryland

D. Anderson
A. Bates
J. Copley
J. Dodd
J. Fernandez-Baca
A. Fiesel
G. Gordon
F. Guenther
M. Han
D. Herman
J. Hoff
M. Kitto
S. Krueger
C. LeCompte
Q. Li
W. Li
J. Lynn
L. Mackie
L. McCarthy
J. Nicol
J. Ondov
A. Sheffield
P. Sheridan
T. Sullivan
G. Tuncel
S. Tuncel
J. Valette-Silver
W. Waters
Y. Yu

University of Massachusetts

H. Yang

University of Michigan

D. Vincent

University of Milan (Italy)

M. Zocchi

University of Missouri

W. Ching
W. James
T. Little
S. Werner

University of Muenster

F. Kemper

University of Nebraska

D. Sellmyer

University of Nancy (France)

P. Mangin

University of New Hampshire

R. Blakemore

University of Notre Dame

J. Furdyna
T. Giebultowicz

University of Odense

E. Anderson

University of Pennsylvania

P. Davis

University of Peruglia

G. Alberti

University of Rhode Island

D. Andrauskas
S. Hasanain
S. Pickart

University of Vermont

T. Flanagan

University of Virginia

T. Williamson

University of Washington

K. Mottet
W. Zoller

University of Wisconsin

D. Huber

Utah State University

T. Isenhour

Yale Univeristy

D. Ehgelman
J. Flanagan

Swiss Institute for Nuclear Research

I. Anderson

University of Leiden
(The Netherlands)

J. Mydosh

Aerospace Corporation

R. Bowman
J. Knudsen

Alcoa Technical Center

C. Jensen
R. Rioja

Allied Corporation

G. Fish
A. Maeland
J. LaSalle

Atomic Energy of Canada, LTD

W. Lennard

Bell Laboratories

R. Cava
H. Chen
D. Johnson
J. Mitchell
D. Murphy
J. Remeika
W. Rhodes
J. Riley
L. Scheemeyer
S. Sunshine
J. Waszazak
S. Yognasubiamian

Bell-Northern Research Ltd.

F. Shepherd
W. Vandevorst

Bell Communictions Research Laboratories

P. Miceli

Directed Technologies, Inc.

N. Chesser

Eastman Kodak

T. Hossain
M. Landry
J. O'Reilly
C. Swanson

E. I. DuPont de Nemours Co.

D. Corbin
G. Jones
F. Tebbe
C. Torardi

Exxon

R. Busch
J. Dozier
J. Huang
M. Kim
D. Lohse
R. Overfield
S. Sinha

General Electric Co.

L. Provo

W. R. Grace

M. Wax
R. Wormsbecker

GTE Laboratories

M. Downey
G. Hamill
D. Oblas

IBM (Yorktown Heights)

R. Gambino

IBM (San Jose)

G. Hadziioannou
T. Russel

Intel Corporation

N. Cox

Lockheed EMSCO

D. Lindstrom

Mobil Central Research Laboratory

D. Olsen

Motorola, Inc.

S. Wilson

Shell Oil

V. Soni
D. Hart

Westinghouse-Hanford Corp.

W. McElroy

Mobil Solar Research

J. Gregory

F. Publications

COLLABORATIVE PROGRAMS

Alberi, J.; Jeenicke, E.; Ost, R.; Wilson, R.; Schroder, I. G.; Avenier, A.; Bagieu, G.; Benkoula, H.; Cavaigmac, J. F.; Adrisi, A.; Koang, D. H.; and Vignom, B.; "Studies of Parity Violation Using Polarized Slow Neutron Beams," International Conference on Parity Violation in the Nucleon-Nucleon Interactions, Vancouver, BC. May 1987.

Anderson, I. S.; Rush, J. J.; Udovic, T. J.; and Rowe, J. M.; "Hydrogen Pairing and Anisotropic Potential for Hydrogen Isotopoes in Yttrium." Phys. Rev. Lett 57, 2822 (1986).

Anderson, I. S.; Berk, N. F.; Rush, J. J.; and Udovic, T. J.; "Concentration and temperature Dependence of Hydrogen Vibrations along the C-axis for Hydrogen in Yttrium: Evidence of Dynamically-coupled Hydrogen Pairs, "Phys. Rev. B, in press.

Beech, F.; Miraglia, S.; Santoro, A.; and Roth, R. S.; ”Neutron Study of the Crystal Structure and Vacancy Distribution in the Superconductor $Ba_2YCu_3O_{9-\delta}$.” Phys. Rev. B 35, 8778-8781 (1987).

Berk, N. F.; ”Scattering Properties of a Model Bicontinuous Structure with a Well Defined Length Scale.” Physical Review Letters 58, No. 25, 2718 (1987).

Boggs, P. T.; Collins, D. M.; Finger, L. W.; Konnert, J. H.; Prince, E.; and Spiegelman, C. H.; "International Tables for Crystallography, Vol. C, Part 8 Refinement," in press.

Borchers, J.; Sinha, S.; Salamon, M. B.; Du, R.; Flynn, C. P.; Rhyne, J. J.; and Erwin, R. W.; "Magnetic and Structural Characterization of Dy-Y Multilayers," J. Appl. Phys. 61, 4049 (1987).

Borchers, J.; Salamon, M. B.; Du, R.; Flynn, C. P.; Erwin, R. W.; and Rhyne, J. J.; ”Characterization of Structural and Magnetic Order of Er/Y Superlattices." Superrlattices and Microstructures (to be published in 1988.

Bouillot, J.; Rowe, J. M.; and Rush, J. J.; "Structure of the Mixed Crystal $(KCN)_{0.7}(KBr)_{0.3}$ Determined by Neutron Powder Diffraction, Phys. Rev. B., July 1987.

Cahn, J. W.; Gratias, D.; and Mozer, B.; ”Patterson Fourier Analysis of the Icosahedral (Al, Si) - Mn Alloy,” Phys. Rev. Letters, in press.

Carr, M. J.; Chambers, W. F.; Melgaard, D.; Himes, V. L.; Stalick, J. K.; and Mighell, A. D.; NBS/Sandia/ICDD Electron Difraction Database. Technical Report (Sandia), 1987 in press.

Casella, R. C.; "Coherent Scattering of Low Energy Neutrinos from Macroscopic Objects," in Intersections Between Particle and Nuclear Physics -- 1986, ed. D. F. Geesman, AIP Conf. Proc. No. 150, p. 1040, American Institute of Physics, New York, (1986).

Casella, R. C.; "On the Theory of Coherent Neutrino Scattering from Crystals,” Nuovo Cimento 94A, 42 (1986).

Cava, R. J.; Santoro, A.; Johnson, D. W.; and Rhodes, W. W.; "Crystal Structure of the High Temperature Superconductor $La_{1.85}Sr_{0.15}Cu O_4$ above and below T_c." Phys. Rev. B. 35, 6716-6720 (1987).

Cava, R. J.; Santoro, A.; Murphy, D. W.; Zahurak, S. M.; Fleming, R. M.; Marsh, P.; and Roth, R. S.; "The Structure of the Lithium Inserted Metal Oxide δ-LiV_2O_5." J. Sol State Chem., in press.

Cavagnat, D.; Magerl, A.; Trevino, S.; Pesquer, M.; and Vettier, C.; in Dynamics of Molecular Crystals, Ed, J. Lascombe, Elsevier Science Publishers, Amsterdam, p649 (1987).

Choi, C. S.; Prask, H. J.; "Neutron Diffraction Study of Age-Hardened U - 0.75wt% Ti Alloy," J. Nucl. Mater., in press.

Didisheim, J. J.; Prince, E.; and Wuensch, B. J.; "Neutron Rietveld Analysis of Structural Changes in Nasicon Solid Solutions $Na_{1+x}Zr_2Si_xP_{3-x}O_{12}$ at Elevated Temperatures: $x = 1.6$ and 2.0 at 320° C," Solid State Ionics 18 & 19, 944-958 (1986).

Dougherty, D. A.; Choi, C. S.; Kaupp, G.; Buda, A. B.; Rudzinski, J. M.; and Osawa, E.; "Effects of Substituents on the Length of Central $C(sp^3)$- $C(sp^3)$ bond in Anthracene Photodymers and Related Molecules," J. Chem. Soc. Perkin Trans. II, 1063-1070 (1986).

Erwin, R. W.; Rhyne, J. J.; Salamon, M. B.; Borchers, J.; Sinha, S.; Du, R.; Cunningham, J. E.; and Flynn, C. P.; "The Magnetic Structure of Dy-Y Superlattices," Phys. Rev. B 35, 6808 (1987).

Fan, Y. B.; Solin, S. A.; eumann, D. A.; Zabel, H.; and Rush, J. J.; "Phonons in Graphite Intercalated with Potassium and Ammonia," in Graphite Intercalation Compounds, edited by M. S. Dresselhaus, G. Dresselhaus, and S. A. Solin, Materials Research Society, Pittsburgh, 165 (1986).

Fan, Y. B.; Solin, S. A.; Neumann, D. A.; Zabel, H.; and Rush, J. J.; "Elastic Neutron Scattering Study of the Structure of Graphite Intercalated with Potassium and Ammonia," Phys. Rev. B, (in press).

Fernandez-Baca, J. A.; Lynn, J. W.; Rhyne, J. J.; Fish, G. E.; "Spin Dynamics of Amorphous $Fe_{(90-x)}Ni_xZr_{10}$," J. Appl. Phys. 61, 3406 (1987).

Fernandez-Baca, J. A.; Lynn, J. W.; Rhyne, J. J.; and Fish, G. E.; "Study of the Long Wavelength Spin-Wave Energies and Linewidths of the Amorphous Invar Alloy $Fe_{100-x}B_x$," Phys. Rev. (to be published).

Fischer, R.; Neumann, D. A.; Zabel, H.; Morkoc, H.; Choi, C.; and Otsuka, N.; "Dislocation Reduction in Epitaxial GaAs on Si (100)," Appl. Phys. Lett. 48, 1223 (1986).

Fischer, R. X.; Baur, W. H.; Shannon, R. D.; Staley, R. H.; Viga, A. J.; Abrams, L.; and Prince, E.; "Neutron Powder Diffraction Study and Physical Characterization of Zeolite D-rho," J. Phys. Chem., 90, 4414-4423 (1986).

Fischer, R. X.; Baur, W. H.; Shannon, R. D.; Staley, R. H.; Vega, A. J.; Abrams, L.; and Prince, E.; "Neutron Powder Diffraction Study and Physical Characterization

of Zeolite D-ZK-5 Deep-bed Calcined at 500 C and 650 C," Zeolites, 6, 378-387 (1986).

Giebultowicz, T. M.; Rhyne, J. J.; and Furdyna, J. K.; "Mn-Mn Exchange Constants in Zinc-Manganese Chalcogenides," J. Appl. Phys. 61 (8), 3537 (1987).

Giebultowicz, T. M.; Rhyne, J. J.; Furdyna, J. K.; and Debska, U.; "Neutron Diffraction Study of the Wurtzite-Structure Dilute Magnetic Semiconductor $Zn_{0.45}Mn_{0.55}Se$," J. Appl. Phys. 61 (8), 3540 (1987).

Giebultowicz, T. M.; and Holden, T. M.; "Neutron Scattering Studies of the Magnetic Structure and Dynamics of Diluted Magnetic Semiconductors," in Diluted Magnetic Semiconductors, series on Semimetals and Semiconductors, by Academic Press (in press).

Glinka, C. J.; Rowe, J. M.; and LaRock, J. G.; "The Small Angle Neutron Scattering Spectrometer at the NBS," J. Appl. Cryst. 19, 427-439 (1986).

Gotaas, J. A.; Rhyne, J. J.; Wenger, L. E.; and Mydosh, J. A.; "Magnetic Field-induced Transition in $Y_{1-x}Gd_x$," J. Appl. Phys. 61, 3415 (1987).

Gotaas, J. A.; Lynn, J. W.; Shelton, R. N.; Klavins, P.; and Braun, H. F.; "Suppression of Superconductivity by Antiferromagnetism in $Tm_2Fe_3Si_5$," Phys. Rev. B in press.

Hanley, H. J. M.; Straty, G. C.; Glinka, C. J.; and Hayter, J. B.; "Low-Q Neutron Diffraction from Supercooled D-Glycerol," Molecular Physics, in press.

Hempelmann, R.; and Rush, J. J.; "Neutron Vibrational Spectroscopy of Disordered Metal-Hydrogen Systems." Proceedings of NATO Workshop, Rhodes, Greece; Physics B, (in press).

Himes, V. L. and Mighell, A. D.; "A Matrix Approach to Symmetry," Acta Cryst. A43, 375-384 (1987).

Himes, V. L. and Mighell, A. D.; "NBS*SEARCH: A Program to Search NBS CRYSTAL DATA," Crystallographic Databases (to be published) 1987.

Jin, L.; James, W. J.; Lemaire, R.; and Rhyne, J. J.; "Magnetic Structure of $DyFe_3$," Jour. Less-Common Metals, 118, 269 (1986).

Kircheim, R.; Huang, X. Y.; Carstanjen, H. D.; Rush, J. J.; and Udovic, T. J.; "Inelastic Neutron Scattering and Resistivity of Hydrogen in Cold-Worked Palladium." J. Less Common Metals, (in press).

Li, Q.; Lynn, J. W.; and Gotaas, J. A.; "Absolute Measurement of the Ordered Moment in Holmium-rich $(Er_{1-x}Ho_x)Rh_4B_4$," Phys. Rev. B35, 5008 (1987).

Loidl, A.; Knorr, K.; Rowe, J. M.; McIntyre, G. J.; "Glass and Phase Transitions in $(KBr)1-x(KCN)_x$, Phys. Rev. B., in press.

Lynn, J. W. and Rhyne, J. J.; "Spin Dynamics of Amorphous Magnets," Chapter 14 in Spin Waves and Magnetic Excitations, edited by S. K. Sinha and A. S. Borovik-Romanov, North Holland Physics Publishers, in press.

Maeland, A. J.; Lukacevic, E.; Rush, J. J.; and Santoro, A.; "Neutron Powder Diffraction and Inelastic Scattering Study of the Structures of Zr_2Pd, $Zr_2PdD_{1.70}$ and $Zr_2PdD_{1.96}$." J. Less Comm. Metals 129, 77 (1987).

Mangin, P.; Bomazouza, D.; Tete, C.; Rhyne, J. J.; and Erwin, R. W.; "Re-entrant Spin-Glass Properties of α-$(Fe_xCr_{1-x})_{75}P_{15}C_{10}$," J. Appl. Phys. 61, 3619 (1987).

Miceli, P. F.; Youngquist, S. E.; Neumann, D. A.; Zabel, H.; Rush, J. J.; and Rowe, J. M.; "Quasicrystalline and Crystalline Phonon Density of States: Neutron Scattering Measurement on Al_4Mn," in Phonon Scattering in Condensed Matter V, Springer Series in Solid-State Sciences vol. 68, edited by A. C. Anderson and J. P. Wolfe, (Springer-Verlag, Berlin, 1986) p.344.

Miceli, P. F.; Youngquist, S. E.; Neumann, D. A.; Zabel, H.; Rush, J. J.; and Rowe, J. M.; "Neutron Scattering Study of the Vibrational Density of States in Icosahedral and Crystalline $Al_{0.80}Mn_{0.20}$," Phys. Rev. B 34 8977 (1986).

Mighell, A. D.; Stalick, J. K.; and Himes, V. L.; "NBS CRYSTAL DATA: A Comprehensive Database with Chemical, Physical and Crystallographic Data on Solid-State Materials," Crystallographic Databases, edited by G. Bergerhoff, Int. Union of Crystallography, in press.

Neumann, D. A.; Zabel, H.; Rush, J. J.; Fan, Y. B.; and Solin, S. A.; "Quasielastic Neutron Scattering Study of Rotations and Diffusion in $KC_{24}(NH_3)_{4.3}$," (in press).

Nicol, J. M.; Udovic, T. J.; Kelley, R. D.; and Rush, J. J.; "Isotope Dilution Neutron Spectroscopy: A Vibrational Probe of Hydrogen/Deuterium Interactions on Palladium Black, Langmuir, in press..

Nossal, R.; Glinka, C. J.; and Chen, S.-H.; "SANS Studies of Concentrated Protein Solutions. I. Bovine Serum Albumin," Biopolymers, 25, 1157-1175 (1986).

Prask, H. J.; and Choi, C. S.; "Residual Stress Measurements in Armament-System Components by Means of Neutron Diffraction." ASM 1987 Conference on Residual Stress, Cincinnati, OH, in press.

Prince, E.; "Diffraction Patterns from Tilings with Five-fold Symmetry," Acta. Cryst. A43, 393-400 (1987).

Prince, E.; "Applications of Fixed Wavelength Neutron Powder Diffraction," Transactions ACA, 23, in press.

Prince, E.; "Phase Extension by Combined Entropy Maximization and Solvent Flattening," Acta Cryst. A, in press.

Rhyne, J. J.; Erwin, R. W.; Salamon, M. B.; Sinha, S.; Cunningham, J. E.; Borchers, J.; and Flynn, C. P.; "Long-Range Incommensurate Magnetic Order in Dy-Y Multilayers," Invited Paper, Seventeenth Rare Earth Research Conference, Hamilton, Canada, Jour. Less-Common Metls. 126, 53 (1986).

Rhyne, J. J.; Erwin, R. W.; Salamon, M. B.; Sinha, S.; Cunningham, J. E.; Borchers, J.; Du, R.; and Flynn, C. P.; "Occurrence of Long-Range Helical Spin Ordering in Dy-Y Multilayers," Invited Paper, Thirty-first Annual Conference on Magnetism and Magnetic Materials, J. Appl. Phys. 61, 4043 (1987).

Rhyne, J. J.; "Highlights from the Exotic Phenomena of Lanthanide Magnetism," Chapter 76, Handbook on the Physics and Chemistry of Rare Earths, Vol. 11, edited by K. A. Gschneidner and LeRoy Eyring, North Holland Publishing (to be published in 1988).

Rhyne, J. J.; Neumann, D. A.; Gotaas, J. A.; Beech, F.; Toth, L.; Lawrence, S.; Wolf, S.; Osofsky, M.; and Gubser, D. U.; "Phonon Density of States of Superconducting $YBa_2Cu_3O_7$ and the Non-Superconducting Analog $YBa_2Cu_3O_6$," Phys. Rev. B 36, 2294 (1987).

Rhyne, J. J.; Erwin, R. W.; Borchers, J.; Salamon, M. B.; Du, R.; and Flynn, C. P.; "Magnetic Ordering in Rare Earth Multilayers Studied by Neutron Diffraction," Invited Paper, 1987 Metallurgical Society Annual Meeting, Trans. Metallurgical Soc., in press.

Rhyne, J. J.; "Neutron Scattering in Intermetallics," Invited Paper, International Symposium on Magnetism of Intermetallic Compounds, Kyoto, Japan, Jour. Mag. and Mag. Matls., in press.

Richter, D.; Hempelmann, R.; Rush, J. J.; Rowe, J. M.; Eckert, J.; Goldstone, and Tonks, D.; "Localized Vibrations of Hydrogen in Metals." Physica B, (in press).

Rowe, J. M.; "The NBS Cold Neutron Research Facility," NBS Special Publication 711, (1986).

Rowe, J. M.; Rush, J. J.; Schirber, J. E.; and Mintz, J. M.; "Isotope Effects in the PdH system - Lattice dynamics of $PdT_{0.7}$," Physical Review Letters, 57, (1986).

Rowe, J. M.; Rush, J. J.; and Michel, K. H.; "Comment on Dielectric Susceptibility Measurements in $(KCN)_x(KBr)_{1-x}$ Mixed Crystals." Phys. Rev. Lett. (in press).

Santoro, A.; Miraglia, S.; Beech, F.; Sunshine, S. A.; Murphy, D. W.; Scheemeyer, L. F.; and Waszczak, J. V.; "The Structure and Properties $Ba_2Y Cu_3O_6$." Mat. Res. Bull. 22, 1007-1113, (1987).

Schroder, I.; Gilliam, D.; Carlson, A. D.; Bright, S. W.; and Hutchinson, J. M. R.; International U-235 Fission Foil Mass Intercomparision," Transactions American Nuclear Society 53, 473 (1986).

Smith, H. K.; Rhyne, J. J.; Hardman-Rhyne, K. A.; and Wallace, W. E.; "Thermodynamics of Hydrides and Deuterides of R_6Fe_{23} and R_6Mn_{23}," Jour. Less-Common Metls. 130, 421 (1987).

Spano, M. L.; Rhyne, J. J.; Pickart, S. J.; Hasanain, S. K.; Gambino, R. J.; and McGuire, T. R.; "Magnetic Correlations in an Amorphous Gd-Al Spin Glass," J. Appl. Phys. 61, 3639 (1987).

Spano, M. L. and Rhyne, J. J.; "Neutron Scattering Study of the Spin Freezing in Amorphous $Tb_{45}Fe_{55}$ and $Tb_{25}Fe_{75}$," J. Appl. Phys. 61, 4100 (1987).

PUBLICATIONS

Stalick, J. K. and Mighell, A. D.; "Crystal Data Version 1.0 Database Specifications," NBS Technical Note 1229, (1986).

Stalick, J. K. and Mighell, A. D.; "NBS CRYSTAL DATA. A Magnetic Tape of Chemical and Crystallographic Data Compiled and Evaluated by the NBS Crystal Data Center," NBS Tech. Note 1229, U.S. Dept. of Commerce, NBS, (1987).

Stalick, J. K. and Mighell, A. D.; Crystal Data Version 1.0 Database Specifications, American Crystallographic Association Annual Meeting June 22-27, 1986, McMaster University, Hamilton, Ontario (in press).

Torardi, C. C.; Reiff, W. M.; Lazar, K.; and Prince, E.; "Synthesis Structures and Low Temperature Magnetism of the New Lithium and Sodium Insertion Compounds: $LiFe(II)ClMoO_4$ and $NaFe(II)ClMoO_4$," J. Phys. Chem. Solids, 47, 741-750 (1986).

Trevino, S. F. and Tsai, D. H.; "The Simulation of Condensed Matter Chemistry and Detonation," Proc. Army Sci. Conf., West Point (1986), in press.

Trevino, S. F.; "The Rotational Potential of Solid Nitromethane," Quantum Aspects of Molecular Motions in Solids, ed. by A. Heidemann, A. Magerl, M. Prager D. Richter, and T. Springer, p. 9 Springer-Verlag, (1987).

Udovic, T. J. and Kelley, R. D.; "Neutron Scattering Studies of Hydrogen in Catalysts," Hydrogen in Catalysis: Theoretical and Pratical Aspects, (Z. Paal and P. G. Menon, eds.) Marcel Dekker, Inc, New York (1987) pp 167-182.

Udovic, T. J.; Cavanagh, R. R.; Rush, J. J.; Wax, M. J.; Stucky, G. D.; Jones, G. A.; and Corbin, D. R.; "Neutron Scattering Study of NH_4^+ Dynamics During the Deammoniation of NH_4-rho Zeolite," J. Phys. Chem. in press.

Wax, M. J.; Cavanagh, R. R.; Rush, J. J.; Stucky, G. D.; Abrams, L.; and Corbin, D.; "A Neutron Scattering Study of Zeolite Rho." Phys. Chem. 90, 532 (1986).

Werner, S. A.; Giebultowicz, T. M.; and Overhauser, A. W.; "Charge Density Wave Satellites in Potassium?" Physica Scripta (materials of the 1987 European Physical Society Meeting, Piza, Italy), in press.

Wong-Ng, W.; Hubbard, C. R.; Stalick, J. K.; and Evans, E. H.; "Computerization of the ICDD Powder Diffraction Database: Critical Review of Sets 1 to 32," Powder Diffraction, in press.

Yu, H.; Kitano, T.; Kim, C. Y.; Amis, E. J.; Chang, T.; Landry, M. R.; Wesson, J. A.; Han, C. C.; Lodge, T. P.; and Glinka, C. J.; "Uniaxial Deformation of Rubber Network Chains by Small Angle Neutron Scattering," (submitted to Macromolecules).

Yu, S. C.; Lynn, J. W.; and Lau, B. W.; "X-ray Diffraction Studies of Amorphous $(Fe_{1-x}Ni_x)_{77}Si_{10}B_{13}$ alloys.

Zabel, H.; Hardcastle, S. E.; Neumann, D. A.; Suzuki, M.; and Magerl, A.; "Dynamics of Two-dimensional Melting on a Periodic Substrate," Phys. Rev. Lett. 57, 2041 (1986).

PUBLICATIONS

INDEPENDENT PROGRAMS

Bowman, R. C., Jr., Robertson, R. E., Knudsen, J. F., and Downing, R. G., "Studies of Boron Implantation through Photochemically Deposited SiO2 Films on Hg(1-x)Cd(x)Te", Soc. Photo Optical Instru. Eng. Proc. 686, 18-25 (1986).

Bowman, R. C., Jr., Marks, J., Downing, R. G., and Knudsen, J. F., "Effects of Boron Implantation on Silicon Dioxide Passivated HgCdTe", Mat. Res. Soc. Symp. 90, 279-286 (1087).

Fleming, R. F. and Lindstrom, R. M., "Precise Detemination of Aluminum by Instrumental Neutron Activation (to be published).

Gilliam, D. M., Hocken, D., Humphreys, J. C. and Lamaze, G. P., "Neutron Sensitivity of LiF Chip Gamma Dosimeters at Megagray Doses", Proc. of the ASTM-EURATOM Symposium on Reactor Dosimetry (in press).

Greenberg, R. R., and Zeisler, R., "A Radiochemical Procedure for the Determination of Chromium in Biological Materials", J. Radioanal. Nucl. Chem., (in press).

Grundl, J., "Derivation of Neutron Exposures Parameters from Threshold Detector Measurements", Proc. of the ASTM-EURATOM Symposium on Reactor Dosimetry (in press).

Lamaze, G., Gilliam, D. M., Williamson, T. G., "Calibration of a Neutron Driven Gamma Ray Source", Proc. of the ASTM-EURATOM Symposium on Reactor Dosimetry (in press).

Lamaze, G. P., Gilliam, D. M., and Williams, A. P., "Prompt Gamma as a Fluence Rate Monitor in Neutron Beam Experiments", J. of Radioanal. Chem. (in press).

Lindstrom, R. M., Zeisler, R., and Rossbach, M., "Activation Analysis Opportunities Using Cold Neutron Beams", J. Radioanal. Nucl. Chem. 112, No. 2 (1987).

Lindstrom, R. M., "Nuclear Analytical Methods in Standards Certification", to be published in proceedings of IAEA Advisory Group Meeting on Comparison of Nuclear Analytical Methods with Competitive Methods (1987).

McGarry, E., Ruddy, F., Gold, R., Kellogg, L. S., Preston, C. C., Roberts, J. H., "Updated PCA Physics-Dosimetry Results and Analyses", Proc. of the ASTM-EURATOM Symposium on Reactor Dosimetry (in press).

Riley, J. E., Jr., and Lindstrom, R. M., "Determination of Boron in Borosilicate Glasses by Neutron Capture Prompt Gamma-Ray Activtion Analysis", J. Radioanal. Nucl. Chem. 109, 109-115 (1987).

Schwartz, R. B., "Neutron Personnel Dosimetry Calibrations at NBS", NBS Special Publiction, NBS 250-12, (1986).

Williams, J. G., Cogburn, C. O., Hodgson, L. M., Apple, S. C., McGary, E. D., Lamaze, G. P., Gilliam, D. M., Schima, F. J., Rogers, J. W., Gehrke, R., Baker, J. D., Wheeler, F. J., "Measurements of Fission Spectrum Averaged Cross Sections for the ^{93}Nb(n,n')^{93m}Nb Reaction", Proc. of the ASTM-EURATOM Symposium on Reactor Dosimetry (in press).

PUBLICATIONS

Williamson, T. G., Ayers, T. A., Hammersten, W. L., Lamaze, G. P., Schima, F. J., "Measurement of the ^{93}NB(n,n') Fission Spectrum Cross Sectin", Proc. of the ASTM-EURATOM Symposium on Reactor Dosimetry (in press).

Williamson, T. G., Lamaze, G. P., Gilliam, D. M., Eisenhauer, C. E., "Iron and Cadmium Capture Gamma Ray Photofission Measurements", Proc. of the Am. Nucl. Soc. Topical Conf. on Radiation Shield ing and Dosimetry (in press).

Zeisler, R., Stone, S. F., "Analysis of Marine Bivalves and Sediments", Trans. Am. Nucl. Soc. 53:201 (1986).

Zeisler, R., Stone, S. F., and Sanders, R. W., "Sequential Analysis of 45 Trace Elements in Marine Bivalves", Anal. Chem. (in press).

Zeisler, R., Greenberg, R. R., and Stone, S. F., "Radiochemical and Instruemtnal Neutron Activation Analysis Procedures for the Determination of Low Level Trace Elements in Human Livers", J. Radioanal. Nucl. Chem. (in press).

NBS-114A (REV. 2-80)

U.S. DEPT. OF COMM. **BIBLIOGRAPHIC DATA SHEET** *(See instructions)*	1. PUBLICATION OR REPORT NO. NBS/TN-1240	2. Performing Organ. Report No.	3. Publication Date November 1987

4. TITLE AND SUBTITLE

NBS Reactor: Summary of Activities July 1986 Through June 1987

5. AUTHOR(S)

Frederick J. Shorten, Editor

6. PERFORMING ORGANIZATION *(If joint or other than NBS, see instructions)*

NATIONAL BUREAU OF STANDARDS
U.S. DEPARTMENT OF COMMERCE
GAITHERSBURG, MD 20899

7. Contract/Grant No.

8. Type of Report & Period Covered
July 1986 through
June 1987

9. SPONSORING ORGANIZATION NAME AND COMPLETE ADDRESS *(Street, City, State, ZIP)*

Same as item #6 above.

10. SUPPLEMENTARY NOTES

☐ Document describes a computer program; SF-185, FIPS Software Summary, is attached.

11. ABSTRACT *(A 200-word or less factual summary of most significant information. If document includes a significant bibliography or literature survey, mention it here)*

This report summarizes all those programs which use the NBS reactor. It covers the period for July 1986 through June 1987. The programs range from the use of neutron beams to study the structure and dynamics of materials through nuclear physics and neutron standards to sample irradiations for activation analysis, isotope production, neutron radiography, and nondestructive evaluation.

12. KEY WORDS *(Six to twelve entries; alphabetical order; capitalize only proper names; and separate key words by semicolons)*

activation analysis; crystal structure; diffraction; isotopes; molecular dynamics; neutron; cold neutrons; neutron radiography; nondestructive evaluation; nuclear reactor; radiation.

13. AVAILABILITY

☒ Unlimited
☐ For Official Distribution. Do Not Release to NTIS
☒ Order From Superintendent of Documents, U.S. Government Printing Office, Washington, D.C. 20402.
☐ Order From National Technical Information Service (NTIS), Springfield, VA. 22161

14. NO. OF PRINTED PAGES

197

15. Price

* U.S. Government Printing Office: 1987 0-201-490 (60174)

NBS Technical Publications

Periodical

Journal of Research—The Journal of Research of the National Bureau of Standards reports NBS research and development in those disciplines of the physical and engineering sciences in which the Bureau is active. These include physics, chemistry, engineering, mathematics, and computer sciences. Papers cover a broad range of subjects, with major emphasis on measurement methodology and the basic technology underlying standardization. Also included from time to time are survey articles on topics closely related to the Bureau's technical and scientific programs. Issued six times a year.

Nonperiodicals

Monographs—Major contributions to the technical literature on various subjects related to the Bureau's scientific and technical activities.

Handbooks—Recommended codes of engineering and industrial practice (including safety codes) developed in cooperation with interested industries, professional organizations, and regulatory bodies.

Special Publications—Include proceedings of conferences sponsored by NBS, NBS annual reports, and other special publications appropriate to this grouping such as wall charts, pocket cards, and bibliographies.

Applied Mathematics Series—Mathematical tables, manuals, and studies of special interest to physicists, engineers, chemists, biologists, mathematicians, computer programmers, and others engaged in scientific and technical work.

National Standard Reference Data Series—Provides quantitative data on the physical and chemical properties of materials, compiled from the world's literature and critically evaluated. Developed under a worldwide program coordinated by NBS under the authority of the National Standard Data Act (Public Law 90-396).
NOTE: The Journal of Physical and Chemical Reference Data (JPCRD) is published quarterly for NBS by the American Chemical Society (ACS) and the American Institute of Physics (AIP). Subscriptions, reprints, and supplements are available from ACS, 1155 Sixteenth St., NW, Washington, DC 20056.

Building Science Series—Disseminates technical information developed at the Bureau on building materials, components, systems, and whole structures. The series presents research results, test methods, and performance criteria related to the structural and environmental functions and the durability and safety characteristics of building elements and systems.

Technical Notes—Studies or reports which are complete in themselves but restrictive in their treatment of a subject. Analogous to monographs but not so comprehensive in scope or definitive in treatment of the subject area. Often serve as a vehicle for final reports of work performed at NBS under the sponsorship of other government agencies.

Voluntary Product Standards—Developed under procedures published by the Department of Commerce in Part 10, Title 15, of the Code of Federal Regulations. The standards establish nationally recognized requirements for products, and provide all concerned interests with a basis for common understanding of the characteristics of the products. NBS administers this program as a supplement to the activities of the private sector standardizing organizations.

Consumer Information Series—Practical information, based on NBS research and experience, covering areas of interest to the consumer. Easily understandable language and illustrations provide useful background knowledge for shopping in today's technological marketplace.
Order the **above** *NBS publications from: Superintendent of Documents, Government Printing Office, Washington, DC 20402.*
Order the **following** *NBS publications—FIPS and NBSIR's—from the National Technical Information Service, Springfield, VA 22161.*

Federal Information Processing Standards Publications (FIPS PUB)—Publications in this series collectively constitute the Federal Information Processing Standards Register. The Register serves as the official source of information in the Federal Government regarding standards issued by NBS pursuant to the Federal Property and Administrative Services Act of 1949 as amended, Public Law 89-306 (79 Stat. 1127), and as implemented by Executive Order 11717 (38 FR 12315, dated May 11, 1973) and Part 6 of Title 15 CFR (Code of Federal Regulations).

NBS Interagency Reports (NBSIR)—A special series of interim or final reports on work performed by NBS for outside sponsors (both government and non-government). In general, initial distribution is handled by the sponsor; public distribution is by the National Technical Information Service, Springfield, VA 22161, in paper copy or microfiche form.

U.S. Department of Commerce
National Bureau of Standards
Gaithersburg, MD 20899

Official Business
Penalty for Private Use $300